The behaviour of powders under failure prone conditions: An experimental and numerical investigation.

Rolland, Samuel Andre

Swansea University
Prifysgol Abertawe

The Behaviour of Powders under Failure Prone Conditions

An Experimental and Numerical Investigation

A thesis submitted in partial fulfilment of the requirements of
the Degree of Doctor of Philosophy in Engineering
at Swansea University
by Samuel André ROLLAND,
2007

Supervisors: Prof D.T. Gethin, Prof R.W. Lewis

ProQuest LLC.
789 East Eisenhower Parkway
P.O. Box 1346
Ann Arbor, MI 48106 – 1346

Declaration

This work has not previously been accepted in substance for any degree and is not being concurrently submitted in candidature for any degree.

Signed (candidate)

Date 30/01/2008

Statement 1

This thesis is the result of my own investigations, except where otherwise stated. When correction services have been used, the extent and nature of the correction is clearly marked in a footnote(s).
Other sources are acknowledged by footnotes giving explicit references. A bibliography is appended.

Signed (candidate)

Date 30/01/2008

Statement 2

I hereby give consent for my thesis, to be available for photocopying and for interlibrary loan, and for the title and summary to be made available to outside organisations.

Signed (candidate)

Date 30/01/2008

Abstract

The Behaviour of Powders under Failure Prone Conditions

This work investigates the behaviour of powders under failure prone conditions. Experimental investigations were carried out to explore the low pressure region of the yield surface defined in the $P - Q$ plane for a ferrous and an alumina powder. A new method based on high speed video acquisition and image analysis was developed to avoid contact measurement techniques in the simple compression test and to investigate the fracture initiation in the diametral compression test. The data reduction from the simple compression test was compared to loading curve analysis technique to obtain the yield stress and the elastic parameters can also be derived. The latter are compared to results from previous experimental studies by authors using different techniques. The data from the diametral compression test was analysed and the images were used to observe the conditions of crack initiation. The resulting data combined with the yield points obtained by the well documented instrumented die technique were used to establish the yield surfaces. The yield surfaces were obtained by modifying an elliptic model and exhibit different characteristics in the low pressure range for the ferrous powder and the alumina powder.

The development of a three invariant model was carried out and used to evaluate the impact of Lode dependency on the compaction process. The formulation of the model is fully laid out and its performance was benchmarked against existing code. The impact of the Lode dependency was then explored in two numerical case studies. The compaction, ejection and unloading of a cylinder and a multilevel part were simulated. The impact of the new model on tool forces, density and stress distributions were quantified, showing that the major effect were in the peak values of the stresses. It is therefore concluded that it is of interest to take into account the Lode dependency when investigating possible causes of defects.

The conditions of fracture initiation were then explored by means of two case studies. First a cylindrical component was used to explore ejection and unloading scheme with a particular attention to delamination. Then a multilevel component was analysed. SEM images of samples are used in combination with simulations to define the conditions of failure observed in some multilevel parts. This led to the definition of a formulation for a failure risk index. This aims to indicate fracture propensity based on an empirical approach. The criterion was based on stresses and takes into account material and kinematic variability. Finally it was tested against the experimental data and found to give a good agreement with the experimental data.

Acknowledgements

I would like to thank the following people who have helped me in the work undertaken in this thesis:

Professor D. T. Gethin, my supervisor for his invaluable advice and support. Professor R. W. Lewis for his advice and the experienced point of view that he shared on this work.

Dr D. Korachkin whose help and technical discussion was much appreciated in setting up the experimental parts of this work.
Dr. P. Mosbah whose guidance and expertise was indispensable for the numerical implementations undertaken in this thesis.
AEA Technology, and in particular Dr J. Tweed for managing the Studio Project and the J1 Industrial Advisory Group (DTI funded projects which sponsored the work in this thesis) and Dr D. Guyoncourt for his technical insight and valuable discussion. GKN SinterMetal, Dr R. Maassen in particular for receiving me to collect experimental data used in this work.
The technical staff of the School of Engineering, in particular P. Matthews, A. Jolly and the workshop technicians for their help in setting up experiments.

I also wish to thank my parents, for their continued support and confidence.

Finally, and most importantly, I wish to thank my wife Charmaine, for her patience when I came home late and for her understanding every time my work seemed to take most of our time.

To Charmaine

Contents

List of Figures

List of Tables

Chapter 1

Introduction

Powder compaction is an attractive manufacturing process, when suitable, to produce components with economic advantages. Research in powder compaction looks to improve the production method by extending the knowledge of granulate materials behaviour and embedding this knowledge in design tools. In particular computational methods can be used to predict the outcome of the process, thus cutting long and costly development time.

Computational methods applied to powder compaction have been implemented since the early 1990s, mainly based on work from the field of soil mechanics, exploiting the similarities between consolidation and densification in porous and granular media. Simple components are simulated reliably, and the need for more advanced models is increasing, in particular, a deeper exploration of the powder behaviour in conditions dominated by shear. These conditions adversely affect the compaction process resulting in low density regions and sometimes fractures.

This work aims to explore the powder behaviour in such conditions. The particular compaction method studied is cold uniaxial die pressing. It was financed by industrial partners who also brought forward some of the case studies therefore its outcomes are largely driven by industrial requirements in the development of testing methods and software.

First, the experimental part of the work first looks at simple tests that can be used to characterise powders: the unconfined compression test and the diametral compression test. However a new approach is used to analyse the results by image

processing techniques that were developed to analyse the results. The information from these experiments help understand the yield and fracture properties of powder compacts. The information collected from these tests can be used to calibrate constitutive models that are used for computational simulations.
Then, the next part of this study then investigates the effect of three dimensional states of stress in powder compacts. The mathematical basis for a numerical implementation is developed. A comparison is carried out between models to evaluate the influence of complex conditions. Finally, an investigation of the factors that lead to the initiation of fractures was carried out. In particular, the state of stress and the evolution of plastic deformations were examined, leading to the development of a criterion for fracture propensity in powder compacts. These developments are validated by a set of case studies.

1.1 The Powder Manufacturing Industry

Powder manufacturing (PM) is a production route through which components are produced from a loose granular material by subjecting it to pressure. A wide range of applications make use of powder compacted components. Mechanical and structural products include gears, connecting rods and bearings, which are manufactured from ferrous and hard powders. Components for the control of friction also represent an important share of the powder manufactured parts, such as bushes and brake pads, showing that friction can be minimised or enhanced by exploiting properties of copper alloys, polymers or ceramics. Hard metals and ceramics, which are difficult to work on with machining processes advantageously exploit the properties of powder compaction for the production of tools tips for machining and also the mining industry. Powder manufactured components are also used in the medical environment where ceramics are pressed into prosthetics. Finally, tabletting is also a process based on the pressing of powder in the pharmaceutical and food industry. Some of the products from powder manufacturing processes are illustrated in Figure 1.1.

The strong point of this production route lies in its economic advantages regarding manufacturing costs and its high material utilisation: 95% (Figure 1.2 from the Eu-

Figure 1.1: examples of powder manufactured parts, on the left, mechanical components from GKN and on the right, a femoral head

ropean Powder Metallurgy Association - EPMA). This is made possible by the near finished dimensions that can be obtained from the process. Also, powder manufacturing processes are the only efficient way to obtain some properties, for example a controlled porosity to either impregnate a bush with lubricant or produce filters.

Powder metallurgy was developed as industry in the early twentieth century based on the production of tungsten lamp filaments. The powder metallurgy sector grew rapidly during the second World War, driven by the adoption of the process for the production of ferrous structural parts. It is now an established manufacturing process, particularly popular in the automotive sector [Cap00]. Published figures in the industry show that north American car manufacturers lead the way in automotive PM product usage [New04b] and although European cars include less PM parts, European manufacturers are increasing the amount of powder manufactured products, pushed in by new technologies [New04a].

The PM market is largely dominated by north America, followed by Europe and Japan, but new countries are emerging in the sector, already overtaking Japan with their combined shipments, Figure 1.3. These countries are mainly, China, Russia, India and Iran, whereas powder shipments for the main producing nations have been stagnating since 2000 [New04b]. The net effect is a 10% yearly growth in this

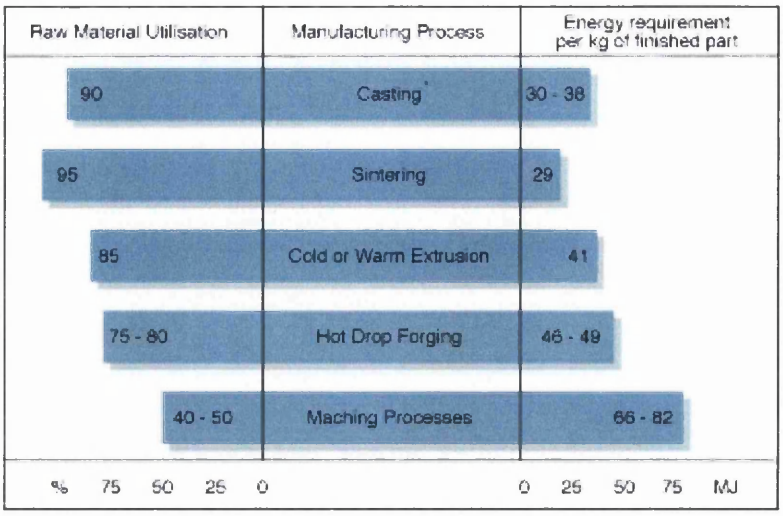

Figure 1.2: Raw material utilisation and requirements of various manufacturing processes [EPM07a]

industry sector.

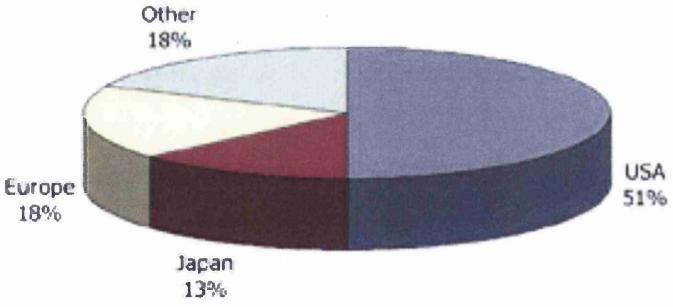

Figure 1.3: Global powder shipments in 2003 [New04a]

1.2 The Powder Compaction Manufacturing process

The PM industry covers the activities from the production of the powder until the finished product is obtained (Figure 1.4). The powder is obtained by various methods such as mechanical grinding, electrolysis, atomisation or chemical processes. The powder then needs to be blended with the desired alloying elements and additives (binders or lubricants) required to obtain the desired properties. The mix is then pressed to the desired shape. The more traditional ways of producing the compact are die pressing, isostatic pressing and metal injection moulding. Temperature is an important variable of the process and divides PM methods into two general families: hot and cold compaction processes. Warm compaction is sometimes added to this classification, carried out at intermediate temperatures, but it is not widespread. The production method studied in this thesis is cold die compaction. It can be subdivided into the die filling, pressing and ejection steps, of those three steps the investigation will be restricted to the pressing and ejection phases. The result of the compaction is called the green compact. In this state it has neither acquired its final mechanical properties nor dimensions. A few exceptions exist, for example in the pharmaceutical and food industries. For these processes, the product is in its final state as it comes out of the die.
Most compacts need to be sintered. Sintering is a heat treatment by which the compact acquires cohesion in its crystalline arrangement. Previous cohesion in the green state was only the result of grain interlocking and in some cases cold welding. After sintering at a temperature usually half of the melting temperature, the compact can be considered as a continuous material, whether solid or porous. The final finishing operations can then be carried out, such as machining, coating, surface and heat treatments or any other necessary operation.

The powder compaction manufacturing process also has its limitations. This study concentrates on uniaxial die compaction and associated geometrical limitations arise. This is essentially due to the pressing motion of the tools. The EPMA gives an overview of good design practices for powder manufactured components [EPM07a]. Other limitations are due to the granular nature of the basic material. If cohesion is to be obtained, pressure is an important parameter and shear motion

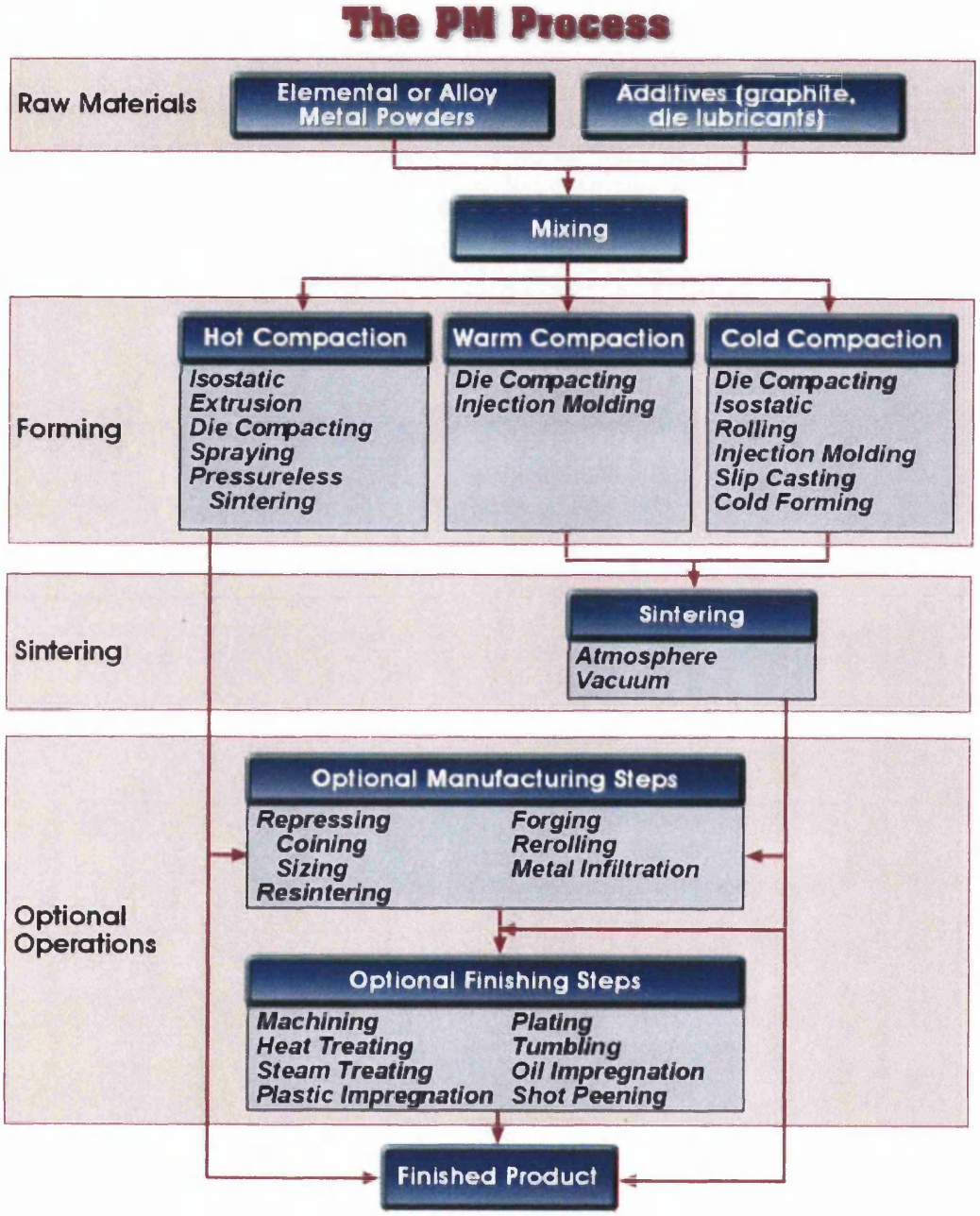

Figure 1.4: The PM process [MPI07]

inside the die can destroy the fragile integrity of a green component. Finally, the need for sintering also brings the need for a homogeneous density field throughout the part. If this condition is not fulfilled, shrinkage associated with sintering will not be uniform leading to out of tolerance geometry or enforcing additional finishing operations with associated cost penalty. The issues are particularly aggravated in complex or close tolerance part geometries and are particularly relevant to ceramic or hard metal parts, which are compacted to a low relative density and subsequently shrunk by sintering, in contrast with ferrous parts which are compacted to very high relative densities and are therefore less affected by shrinkage. The ability to predict the likelihood of such defects is particularly attractive because it can lead to near right first time manufacturing. Simulation promises to play a key role in achieving this and will be discussed more fully in the next section.

1.3 The Role of Modelling in the PM Industry

Numerical simulation is nowadays an important tool in the design of a new product. Computational methods are widely used to check the suitability of a part for its purpose - with fluid, structural or thermal considerations. Some more advanced optimisation techniques can even refine a design. These applications all aim to improve the design of the part with a focus on its conditions of use. Computational simulation of manufacturing processes are not as widely spread in the industry. They are mostly a basis for joint research between academia and industrial partners. This may be because, from a manufacturer's point of view, failure of a component in service is taken into account by trying to completely prevent it, leading to the use of safety factors and the implementation of maintenance plans. On the other hand, failure during the manufacturing process is essentially viewed as a statistical process. It has to be asked how much can be invested in the process to improve it before it becomes cheaper to simply throw away the faulty parts. Some numerical research in manufacturing techniques makes use of statistical techniques based on variations of a set of parameters [RSL95].

The design stage is where numerical simulations can have an impact, as they do not require the use of machine tools that could be employed in production, thus resulting in a loss of income. Projects such as Modnet [PM 99] and Dienet [BF06],

in Europe, have shown the progress in numerical modelling capabilities [Cal06], but also outline the separation between industrial partners and numerical work centres. The latter are often academic institutions. The conclusion of the Dienet project shows that numerical modelling is not yet widely implanted in industry [BF06]. It must be highlighted that very good results are obtained in this European programme by numerical codes regarding density distribution and predictions of the tool forces have improved a lot over the last decade. However the industry still hasn't adopted computational methods in its design process: the three main reasons quoted are computational time requirements, the expertise needed to use the models and, to a certain extent, the outcomes of the simulations are not entirely satisfactory. The first points can be addressed by expertly tuning code and the second partly by improving user interfaces. The second point and the third one also raise questions on the quality of the input data. Good results can only come out of a model if it is appropriately calibrated to reflect the behaviour of the considered material. The techniques for the calibration of the model can be themselves complex and expensive. Finally better tools for the interpretation of the output from such models need to be developed. Once stresses and density fields are computed, only crack propagation can influence the evolution of the compact in the models currently in use and published. The essential data is therefore present, which emphasizes the need for better exploitation tools.

As mentioned above, before being widely adopted by the industry, a simulation system needs to be well calibrated yet simple to use. The complexity of models that reflect the behaviour of a powder can be such that the collaboration between the industry and research organisations is a necessity. Databases could provide the necessary information for the use of modelling tools, making the simulation software more usable by eliminating the time consuming experimental phase. An initiative comparable to the Global Powder Metallurgy Property Database developed by the Metal Powder Industry Federation (MPIF), the Japanese Powder Metallurgy Association (JPMA) and EPMA, would be useful to ease and promote the use of numerical tools in industry. Finally this collaboration is also an opportunity to convey expectations regarding the outcomes of the simulations between users and developers. Recent projects such as the Dienet thematic network showed, in particular, that improvements regarding stresses on the tools and the development of

fracture prediction capabilities are high on the list of expectations.

Numerical simulations have another crucial role, outside the industry. They can be used as a research tool to investigate powder compaction. Many phenomena need to be investigated, such as anisotropy, yield behaviour and fracture mechanisms. The compaction of powders has been simulated reliably since the late 1990s [PM 99]. This is however in a context where the powder undergoes an essentially uniaxial deformation in oedometric conditions. Further detail on these conditions is given in Chapter 5. These conditions are only encountered homogeneously throughout the material in the ideal case of a frictionless compaction. This region of the yield surface can be considered a safe zone for the reliability of the simulations. It is interesting to also explore what happens when the stresses stray from this ideal path. Such conditions can arise due to geometrical features (corners), tooling limitations or important friction. More often, they occur during the ejection phase of the compaction cycle. This is the stage of the compaction cycle that has received the least attention.

The present study looks at these conditions, with a view to characterise the powder behaviour under low confining pressure, as well as in out-of-plane stress conditions. The studies of stress states outside the oedometric conditions are rare to date. Most authors make the deliberate choice of only using simple yield functions. A study by Mosbah *et al.* [MKSK97] shows that the behaviour of powders is dependent on the Lode angle. This particular point will be reviewed in Chapter 2 and developed in Chapter 4. Little work followed in the computational field to explore how this influences the compaction process. The development of fractures has been investigated by several authors. Most work is based on fracture propagation derived from other applications of fracture mechanics [TA06]. It is important to also have an insight into the initiation of cracks. Coube [Cou98] and Mori *et al.* [MSSO99] have explored different methods to predict the onset of fracture based respectively on the volumetric strain and the maximum principal stress.

A good investigation of the low pressure region of the yield surfaces and the initiation of fracture must rest on data relating to these conditions. This thesis therefore includes a part on experimental work and the development of data exploitation tech-

niques as well as the numerical developments that relate to the observations.

1.4 Context and Scope of the Work

The present work was carried out in close collaboration with the industry. Although this was essentially a research oriented project, there were also deliverables in terms of knowledge transfer to the industry and regarding the exploitability of the outcomes. This involved writing a graphical user interface and the associated training material. The research aim of the project is to determine the conditions in which the powder compaction process fails to produce a sound component with a view to predict numerically the outcome of a compaction. The scope of the work is limited to the cold die compaction process. This sets out several challenges. the first one is in the determination of the condition of fractures. The literature gives several indicators on the likely conditions. However a more detailed investigation is required to characterise precisely the behaviour of powders in these conditions. This was done experimentally and numerically. The challenges involved in the development of numerical defect prediction lie in the need for an accurate model regarding the material behaviour in these conditions. The first step to take is therefore the gathering of experimental data, including the validation of the concerned experiments. To ensure that the simple tests mentioned in the first section of this chapter can be used to characterise powders, imaging techniques were used to analyse the tests. The work of Shima *et al.* was used as a basis to explore the impact of Lode dependency in powders. Although was shown to be Lode dependent, no published work documents how this influences the outcome of a compaction cycle. To conclude this work, case studies are used to explore cases known to put the compacts' integrity at risk. They used to document the evolution of stresses and density in the areas of the compact which can be of concern and to establish the performance of a defect prediction model.

1.5 Structure of the Thesis

As stated above, the present work aims to investigate and characterise the conditions of defect appearance in parts produced by the cold uniaxial powder compaction process. This includes the pressing and ejection stages but excludes the filling of the die and the sintering phases. The organisation of this thesis is outlined below, detailing the original work undertaken to achieve the specified target.

Chapter 2 presents a literature review on the powder characterisation methods and the associated modelling techniques.

In Chapter 3, experimental results and their interpretation techniques are developed to explore the behaviour of powders in situations where the powder compaction process may fail. The work in this chapter is focused on checking the conditions of yield or failure in the unconfined compression test and the Brazilian disc test. They are well documented tests but their results are dependent on the way in which the data is exploited. The use of new image analysis techniques specifically contrasts the results from the analysis of the loading curve of the test and those obtained by taking into account the state of the compact (e.g. strain measurements or observation of fractures). The results from the test are then used to establish a new yield surface that reflects the findings in the final section of the chapter.

Chapter 4 is dedicated to the study of numerical models for the powder compaction process. The emphasis is put on the development of the constitutive equation relating stresses and strains. In particular, a new constitutive model is developed to investigate what happens when the compaction does not remain a simple uniaxial deformation. The constitutive relationship is based on a Lode dependent associated plasticity model. Thus, the chapter first introduce a modified CamClay model, then the development of the new Lode-dependent model. Its performance is evaluated and examples of a cylinder and a stepped component are used to illustrate the differences introduced by the Lode dependency.

Chapter 5 introduces a method to predict the failure of a component during the compaction and ejection cycle. It is based on a statistical approach for several reasons. First, the experimental results show that even if the experiments appear to have a very good reproducibility in terms of maximum load and elastic properties, the stress levels at which fractures appear are much less precise and suggest that

they are distributed statistically. This is illustrated with two case studies. The resulting defect occurrence criterion is shown in this final chapter of investigation as a proof of concept based on the finding from the previous chapters, which could be further developed by more extensive experimental data to calibrate the statistical distribution employed.
Chapter 6 brings a closure on this work with the conclusions regarding the work undertaken and its outcomes. Recommendations are also made on the ways to build upon the present work for future developments and exploitation.

Throughout the chapters, illustrations will be found with images from numerical simulations. The components studied in this work are all axisymetrical, and therefore as a convention, only half of the part is shown. The centre line is on the left and the outer surface on the right. Another convention used in this work is that compressive values of the pressure are positive for and tensile values are thus negative.

Chapter 2

Literature Review

The literature to date is reviewed in this chapter. It aims to present the work carried out to date, which the present thesis extends. Modelling the behaviour of powders in the compaction process requires a good understanding of the granular media. It is possible to consider powder as a continuum or to consider each individual particle that constitutes it. These different approaches lead to several possibilities in the modelling of powder compaction exposed further in the section on simulation techniques. Consequently, the choice of approach, whether micromechanical or macromechanical leads to the necessity to characterise different properties of the powder.

Essentially, powder compaction is carried out by gross deformation of a media, with a reduction in volume that can exceed 2:1, this is particularly important when choosing a modelling technique. The desired effect is the permanent deformation of the media into the shape of the die. This involves an elastic deformation, which will be recovered as the component comes out of the tool set and a non-recoverable deformation which ensures that the powder is effectively packed and cohesive. The techniques employed to characterise the deformation conditions of powders in the forming process are reported in the first section of this chapter. Following experimental characterisation, the data must be put in an exploitable theoritical form. This is the role of constitutive models, which are used to determine the response of a powder to imposed conditions. The most important material models for powder compaction are reviewed in the second section of this work. Once models are es-

tablished, they need to be set within a mathematical framework to be exploited. A review of possible solutions are presented with a strong emphasis on the finite element method, as it is the scheme employed in this work for numerical modelling. A different approach, known as discrete modelling is also presented for its interesting perspective on powder forming simulation by reproducing the discrete nature of the material. Finally, a section is dedicated to the review of the work carried out on fracture in powder compaction. This section gathers experimental observations and some numerical work. It also includes numerical developments that are not directly related to powder forming but that can be of interest as they are generic methods to simulate the development of cracks.

2.1 Experimental Characterisation Techniques

The techniques for the characterisation of the plastic behaviour are reviewed first in this section, as plasticity is the dominant phenomenon in powder compaction and the basis of powder manufacturing. In continuum mechanics, the most common plasticity models are based on a stress limit known as the yield stress. The research on powder compaction concentrates on this mode of determination of the onset of plasticity. Characterising plasticity for powders is therefore the search for the stress limit from which a permanent deformation is achieved. It is important to characterise powders in a range of conditions rather than for a set compaction scheme as the state of the material throughout a compact is not homogeneous, especially in multilevel components and in the presence of friction.

It is expected that the stress limit to reach plasticity is a function of the density of the material. The techniques employed are largely derived from civil engineering, with tests for soils (oedometric test) and building materials such as concrete and plaster (Brazilian disc tests). It must also be noted that manufacturing parts from powder is most widely applied to components that have plane strain situations, either by axial symmetry or their small dimension. This generalisation has an important consequence regarding the characterisation of plasticity for powders: this reduces the number of variables from the three principal stresses to the hydrostatic and deviatoric stresses P and Q. Arguably, the plane deformation conditions are invalidated when complex features are introduced, which raises the question of

the validity of a yield model based on two stress measures only. As a consequence, the use of models derived from such experiments can be difficult to exploit in the simulation of complex multilevel parts.

2.1.1 Measurement of The Yield Properties of Powders

Closed die compaction tests

The instrumented die test is a technique inspired from the oedometric test for soils. It consists of compressing a sample in a cylindrical die under the displacement of the tool forming one of the end of the cylinder. The instrumentation on the test bench has been refined with years of research to improve the quality of the data obtained from such equipment. The particular technical choices vary according to the research organisation. Two designs are proposed by AEAT [GTG+01] and UWS [Cam00], but the data collected from the instrumented die tests always consists of axial and radial stresses and the tool displacement. The difference lies in the implementation of the radial stress measurement: AEAT uses three pins whereas a set of five strain gauges was employed by the system developed at Swansea University.
To test a particular powder, the loose material is introduced in the die and compacted up to its maximum green density. During this process, the stresses are recorded and considered to constitute the yield conditions of the powder at the considered density. This test is very important, as it can represent the stress path followed by powder in an ideal case of uniaxial compression. When the friction is neglected, all the volume in the die is deformed homogeneously and strictly proportionally to the displacement of the compacting tool. The data exploitation technique differs according to the design of the experimental equipment. It needs to take into account the height of the compact at the time of each measurement depending on the location of the sensors in the die. Korachkin demonstrated the calibration procedure with cylindrical rubber plugs compressed in the die [Kor06]. Friction must also be accounted for during the test. Bocchini introduces an indirect method for the calculation of the friction coefficient during a die compaction test [Boc95]. The result of the test can be plotted in the $P - Q$ plane chosen to represent the yield surface.

Triaxial tests

A more complex evolution of the instrumented die test is the so called triaxial test. It consists of compacting powder in a rubber sleeve under hydraulic pressure as well as from the end under the displacement of a tool. This is a triaxial test as the deformation taking place is axial, radial and circumferential, but only two independent directions are really used as radial and circumferential deformations are equal in cases of axial symmetry. It is sometimes referred to as a biaxial test for this reason. The test can be carried out with different methods of measurement of the deformations. Direct measurements involve a deformation sensor based on strain gauge or displacement transducers immersed in the hydraulic fluid to retrieve the radial deformation [SRKW+77, CBL+94, BAC94, SC07]. An indirect measurement can also be carried out by measuring the change in the volume of hydraulic fluid in the chamber around the specimen [Koe71, MK79]. Dorémus *et al.* [DGM+95] and Sinka *et al.* [SCML00, SC07] recently used the test to establish the yield limit of steel powders, respectively with an indirect and a direct measurement method of the radial deformation. This technique has great advantages as it can be used to vary the ratio of axial to radial deformation resulting in a wide range of sampling points for the definition of a yield stress limit. The die compaction can theoretically be reproduced with this test by maintaining a hydraulic pressure such that no change in fluid volume occurs. The radial stress is directly given by the hydraulic pressure maintained around the sample and the axial stress is the compaction force divided by the section of the sample. Despite the apparent simplicity of the approach, this experiment presents major difficulties. Friction between the powder and the rubber sleeve is difficult to characterise. There is also the difficulty of compensating the forces induced on the tools from the friction of the sleeve and the hydraulic pressure applied on the 'footing' of the compact. This renders the test complex to analyse. Also, very specialised equipment is required for the test, making it impractical in industry for a company producing parts from uniaxial pressing. Finally, both direct and indirect measurement methods have their drawbacks. With an indirect measurement method, Mosbah highlighted that the rubber sleeve needs to reliably seal the oil out: the rubber can be porous in such measure that it has no consequence at low pressure but at high pressure, it may not completely isolate the powder from the

hydraulic fluid [Mos95]. The seal between the punches and the sleeve is also critical. The direct measurements come with the challenge of using a sensor immersed in a high pressure fluid. Although this could have been a problem in the early tests, the technology is now available to overcome this issue. However, the position of the measurement is critical as the radius will be different at different axial positions on the compact. To obtain more regular measurements, precompacted samples can be used instead of loose powder, but this implies a lower threshold for the characterisation of the powder. The approach with precompacted samples, as exploited by Cameron, gives good results as it avoids the footing issue at the tip of the punches, however it involves bringing samples to their yield limit and repeating this process from different densities [Cam00]. This is a lengthy process and can only be carried out to characterise powder above the density at which cohesion is reached. The technique employed by Sinka and Cocks can be used to characterise powders from the tap density [SC07]. It only requires a single run to characterise a powder along a particular loading path, in the same manner as the instrumented die test. This is much more effective but generates a wide foot at the contact between the contact and the punches where hydraulic pressure may interfere with the results.

Dorémus used the results from the triaxial test to calibrate a Drucker-Prager model reviewed in the next section [DGM+95], but Sinka *et al.* questioned the existence of the critical state with shear failure following their investigation as the powder appears to yield plastically rather than fail in shear mode in their experiments, supporting single surface models such as the modified CamClay model[SCML00]. Cameron also found a good agreement between the experimental data and a modified CamClay model, reviewed in the next section [Cam00]. Finally, the approach taken by Sinka and Cocks showed that density may not be the most appropriate state variable to describe the evolution of yield surfaces and suggests the use of work per unit volume instead[SC07]. This approach was motivated by a good conservation of normality between the plastic flow vectors and the contours of constant works. Smooth constant work surfaces were obtained whereas the isodensity surfaces were difficult to characterise. It was however necessary to express the stresses with respect to the original configuration and thus use Kirchhoff stresses, which are seldom used in engineering applications. Cauchy stresses are commonly employed instead. This also assumes that the initial conditions from the characterisation tests

are always repeated in the situations that need to be simulated, which is difficult to achieve in practice.

The true triaxial test was developed and exploited in the 1980s by Shima and Mimura [SM86]. This is the only reference to a triaxial testing technique in the literature to date in which all directions of the deformation can be independently set. The experimental apparatus consists of 6 wedges placed in a box. The displacements are controlled and the shape of the wedges is designed so that as they are pushed together, a rectangular-prismatic volume is compressed between them. The equipment is complex and require very good precision in the tool manufacture and the control of their displacement to avoid lock up of the device. The friction is taking place between the tools and the powder and also among the tools themselves making the data reduction complex. Mosbah *et al.* [MKSK97] concludes from experiments that the shape of the elastic envelope for powders is influenced by the third deviatoric stress invariant. This finding was later also confirmed by Shima and Kotera [SK98].

Shear box test

The shear box test was documented by Jenike [Jen64]. It has therefore also come to be known as the Jenike cell test. It can be carried out on powders that have already been compacted in a die. By analogy to soil mechanics, pre-compaction is equivalent to the consolidation of soils. The samples can be subjected to an axial load during the shear test or not, which requires further instrumentation to monitor the corresponding radial stresses. The load to which the sample is subjected can be used to obtain a variety of data points to test the yield limit in different conditions. This testing method was explored by Cameron [Cam00] to define yield limits under high shear stresses.

Unconfined compression test

The unconfined compression test is a very simple test to produce a different set of data points. It can be considered as belonging to the same category as a biaxial test without a confining pressure. It may also be encountered in the literature as the simple compression test or the free standing compression test. This test originates from concrete testing [AST00, Des69]. It requires the manufacture of samples that have achieved cohesion. It can therefore not be used to characterise the powder from very low densities. For example, it is possible to use the instrumented die and the triaxial tests from a tap density of 3.2g/cc for the DistaloyAE, a ferrous powder from Högan"as. This powder does not achieve a cohesion that can sustain ejection from the die at densities below 5.35g/cc. The difficulty in this test lies in finding the appropriate point of the loading curve to reflect when the sample is considered to have yielded. The difficulty increases as the material is more ductile. Additional measurements need to be taken for ductile material and a technique is developed in Chapter 3 of this work to ensure the capture of the yield condition.

Brazilian disc test

The Brazilian disc test is also called the diametral compression test. It is a long established test on rocks, concrete and plaster. The test itself is a very basic procedure as it simply consists of crushing a cylindrical sample radially. The interpretation of the test however is very complex. Due to the position of the sample, the stress distribution is not homogeneous and is very complex with stress concentrations at the contact between the tools and the compact. The first analysis of the test was given by Hertz at the end of the 19^{th} century [Her95] as a solution for radial contact. However because of the point load assumption, it predicts infinite stresses at the contacts. It was later refined by Hondros [Hon59] to take into account the area of contact between the tools and sample. Experimental and numerical work followed to study the influence of the type of contact and its width. It is generally accepted that the ratio of the contact width to the sample diameter should not exceed 0.2. Flat contacts can also be used in conjunction with the solution by Hondros, although it was originally calculated for a contact on an arc of a circle [Fah96]. The

validity of a yield point calculated from the diametral compression test can also be argued. It is difficult to detect localised changes in the deformation field, which will invariably occur due to the particular stress distribution in the sample. This makes the test well suited for brittle materials, in which rupture will be easy to detect, but not advisable for a ductile material as the onset of plastic deformation can be undetected and modify the stress distribution, thus invalidating the calculation of the stresses for the yield condition. In the study by Procopio *et al.*, plastic deformations were found to influence the location where the fracture originates [PZC03]. Ernst defined a brittle failure as one that occurs before permanent deformation of the sample at the macroscopic level can be observed [Ern99]. A study is conducted in this work regarding the results of the Brazilian disc test and their applicability in Chapter 3, with attention to the fracture condition (brittle or ductile) according to the definition by Ernst.

The three and four point bending tests can also be used to characterise the elastic envelope of powders. Kraft mentions that the tests could be exploited in such a way [Kra03]. However, the literature shows that it is rarely done. The more common application of the bending tests is the study of the evolution of the bending strength with respect to another process parameters, for example, the relative density [DFA+01], or the nature and quantity of binders, [E. 05].

2.1.2 Measurement of the Elastic Properties of Powders

The elastic properties of powders are particularly influential on the recovery of the compact. This is critical during the unloading and the ejection of the part as it will undergo a recovery of the elastic deformations as it comes out of the die. This process can cause difficulties as the material undergoes a radial recovery, which is very localised at the edge of the die.The concentration of the radial springback can induce high shear stress levels, sometimes tensile stresses too, threatening the integrity of the compact. The elastic properties of powder are therefore critical and need to be explored. The development of the shear and tensile stresses are investigated in

Chapter 5 of the present work.

Several methods are available for the investigation of the elastic parameters of powders. It can be done during the die compaction test, the triaxial test or the simple compression test. These are theoretically easy tests to process as they involve homogeneous deformations and stresses. The results however show that discrepancies can arise between the different methods. The reasons for the discrepancies are largely due to the method adopted, in which friction, die rigidity and other parameters can interfere with the results. This is investigated further in Chapter 3 of this thesis.

Since the mid-1990s, a popular method to evaluate the elastic properties of powders is the axisymmetrical triaxial test. By combining the data between the pressure and the deformations from the test, it is easy to derive an elasticity modulus for the powder. Mosbah and Bouvard, Pavier and Doré mus and Dorémus *et al.* used this technique to determine the elastic properties of the powder by imposing loading and unloading cycles during a triaxial compaction [MB96, PD99, DTA01].

Further studies, by Guyoncourt, Korachkin and also in this work show that the values of Young's modulus from the triaxial test are largely overestimated [Guy05, Kor06]. This is also acknowledged by Pavier [Pav98]. This is because it does not take into account the friction between the powder and the rubber sleeve. The interaction of the hydraulic pressure on the end of the punch is also neglected. The tests by Guyoncourt showed that the elastic properties of powders can also be altered when measured during a compaction cycle due to creep. This is understandable as the load observed at the end of a compaction decreases when the punches are maintained in position. The results of the tests therefore depend on the time left for the compact to settle in the die before taking the measurements of elastic properties. Guyoncourt therefore chose to use the axial recovery of the compact and a calibration from the radial pressure and friction to derive an axial elasticity modulus. The radial recovery is then used to calculate Poisson's ratio. This approach is very complex and requires a very meticulous calibration of the experimental apparatus. Guyoncourt's study is also the only one found in this literature review that takes into account the deformation of the die as most authors consider the toolset much stiffer than the powder and therefore assume its deformation negligible. The values for Young's modulus of a comparable ferrous powder were one third of those found by Pavier [PD99]. The same method was also applied to a zirconia powder and a

cellulose powder. The discussion of the results states that the assumed isotropy of Young's modulus probably results in overestimated results as the compact is stressed radially as well as axially.
An instrumented die approach is set out by Cunningham *et al.* for the measurement of the elastic properties and applied to a pharmaceutical powder [CIS04]. This approach is used by Korachkin, as well as the derivation of Young's modulus from the simple compression tests [Kor06]. The conclusion of this study is that the instrumented die test yields values of the elastic modulus twice as large as those from the simple compression test. This can be explained by several factors: the assumption of isotropy, again, may influence the results and, because the results are based on the elastic recovery of the sample in the axial direction, the friction with the die interferes with the measurement.
It could be deduced that the value of Young's modulus is most reliable from the simple compression test but the data from the test needs to be analysed carefully to identify the elastic region of the stress-strain response curve. Several methods are investigated and contrasted in the present work to establish the best data reduction method in Chapter 3.

The characterisation of powders is very well established in the conditions of closed die compaction. However, under dominating deviatoric stresses or high shear conditions, little exploration was carried out to know whether powder materials fail under large shear strains or deform plastically, except for a pharmaceutical excipient [PZC03]. The present work looks to fill the gap in the literature to date by investigating this issues for a ferrous and a ceramic powder and presents the development of the associated techniques. Chapter 3, consequently validates the simple compression test and the Brazilian disc test with restrictions regarding the data reduction method to be employed.

2.2 Constitutive Relationships

The constitutive relationships used to replicate the behaviour of powders during compaction are derived from elasto-plastic modelling. Elasto-plasticity is a good

basis to model powder compaction, as it as a forming process based on the non recoverability of deformations. This justifies the use of elasto-plastic constitutive relationships, even in the case of ceramic powders, in which each grain is essentially crushed and interlocked without much deformation. The models are usually borrowed or derived from soil mechanics. Powder models have a lot in common with some geophysical material models and they are grouped into granular media and porous material models. The difficulty in powder compaction is that, due to the extent of the deformation, the material starts as a granular media and, eventually, the aim is to obtain a continuum that would behave like a solid, or a near-solid porous media. The behaviour of a solid is very different from that of a granular or porous media. For example, pressure dependency is not commonly a feature of the elasto-plastic characteristics of solids. It is therefore a challenge to represent accurately the range of behaviours that can be exhibited during a powder compaction cycle.

Historically, the models used to model the behaviour of powders during compaction emerged from geomechanics. Those original models can be classified in two main groups: porous material models and granular material models, as presented by Khoei *et al.*[Kho05].

2.2.1 Porous Material Models

Key developments in porous material modelling were introduced by Green, Sima and Oyane and Gurson [Gre72, SO76, Gur77]. Green's model introduced pressure dependency and the evolution of the yield surface with the void ratio of the material. The evolution of the yield surface is governed hardening coefficients – C_1 and C_2 in the equation below. These coefficients are functions of a hardening parameter, such as the relative density or volumetric strain. Shima and Oyane proposed an approach based on relative density and Gurson developed a model on the nucleation of voids intended for the ductile failure of porous materials.

Plasticity models for porous materials are essentially based on the von-Mises yield criterion. Because it is originally formulated for fully dense materials, it has to be

modified to reflect the dependency of the material response upon the void fraction and the pressure. A generalised formulation of these models can be written as:
$C_1 J_2 + C_2 I_1^2 = {\sigma_y}^2$,
in which J_2 is the second deviatoric invariant, I_1 is the hydrostatic stress and σ_y is a measure of the yield stress. C_1, C_2 and σ_y can be functions of the porosity, void ratio or density as chosen to reflect the hardening. The models of this family can are plotted as an ellipse in the P-Q plane, centred on the origin. This is a drawback for the modelling of powder behaviour, as they are cohesionless materials at low density and cannot sustain high tensile stresses before sintering. This means that this category of models is best suited for simulations starting from high relative densities or low void ratios, and the simulation of recompaction after sintering as they imply a cohesive strength equal to the compression strength.

2.2.2 Granular Material Models

The granular material models are based on two main approaches. One possibility is to use a shear failure envelope as in the Mohr-Coulomb criterion or the Drucker-Prager model. The other one is to use a single surface cap model, consisting of a closed surface in the P-Q plane. The successful use of the Mohr-Coulomb envelope was reported by Tran [TLGA93] and the Drucker-Prager model was used with good results in [PM 99].
The shear failure lines are used in models such as the Mohr-Coulomb [Cou76] and the Drucker-Prager model [DP52]. The elastic domain is then completely closed by a compaction cap, dependent on a state variable, most generally density in powder applications. Both these models were originally intended for geomechanical applications. Several models based on a shear failure envelope and compaction cap have been developed. The most referenced ones are those by DiMaggio and Sandler, and Desai [DS71, Des80].
When the cap is reached, plastic flow occurs. In the case of associated models, the plastic flow is normal to the cap and compaction occurs. The shear failure envelope also defines a limit to the elastic domain, and when reached, the material flows plastically without volumetric change. Tran demonstrated the applicability of

the Mohr-Coulomb model with two different compression caps: one elliptic and the other spherical. The results were judged satisfactory for a prediction of density in a bush and stepped component.

This classical approach to shear failure was modified by Coube and Riedel [CR00]. In this work, the flow rule was altered to obtain a gain in volume when plasticity was obtained on the shear failure line, with a view to capture material damage.

One of the drawbacks of this type of model is that at the intersection between the cap and the failure line, a discontinuity in the yield surface occurs. This discontinuity must be passed if the material changes its plastic flow from a compacting regime to a shear failure while remaining plastic. Mathematically, this involves special ways of treating the discontinuity such as patching both surfaces together with an intermediate function or using an especially adapted method to return to the yield surface as shown by Crisfield [Cri97]. Single surface cap models have the advantage of a continuous cap surface, which removes the difficulty encountered with failure envelope and cap models. Roscoe and Schoffield introduced a critical state model expressed in the hydrostatic-deviatoric plane [RST63]. It is based on the linear evolution of an elliptic cap with density and a critical state line, on which the material is deformed at constant volume. This was the source of several evolutions such as the CamClay model by Schoffield and Wroth[SW68] and the more general formulations of the modified critical state model by Zienkiewicz *et al.* and Lewis and Schreffler [ZHL77, LS87]. Finally, a new model was introduced by [Khoei, 2005], making use of a single surface to define the elastic domain and potentially including the influence of the third deviatoric invariant.

These models, essentially for soil mechanics, were successfully adapted by Mosbah and Bouvard for the simulation of the compaction and ejection of a cylinder [MB96]. The modifications were based on the modified CamClay model suggested by Lewis and Schreffler [LS87]. Specific hardening rules were defined to govern the evolution of the yield surface. The values from the simulation for residual stresses and ejection forces were deemed high by Mosbah and Bouvard, in comparison with experimental data. Their recommendation in the closure to their work was that including the influence of the third deviatoric invariant could be a solution as it would decrease the load bearing capability of the material in non-oedometric conditions.

A review of the performance of different models was published by the Modnet research group [PM 99]. The Drucker-Prager model and the modified CamClay model were used in four independent tests showing a good agreement and density predictions within 0.5g/cc of experimental results for a ferrous powder with a solid density of 7.6g/cc. More recently similar studies was carried out in the Dienet project, in which the correlation between the experimental figures and simulation results were improved from the Modnet project [CCI+04, CJK+05]. This is, however, largely down to improved calibration techniques, and the differences between the different models are still minor. This can be explained by the fact that in all these simulations, the calibration data is common to all models and the material remains on the compacting end of the yield surface compaction cap for the Drucker-Prager or at a higher hydrostatic stress than the critical state in the modified CamClay.
Finally, Khoei *et al.* introduced applications of the single surface three invariant model [KAAL06]. The conclusion did not emphasise the results from the simulation as much as the ability of the developed model to reproduce characteristics from other types of constitutive equation. In particular, it can take the shape of a smoothed cone-cap model such as the Drucker-Prager or make use of the third deviatoric stress invariant, although the latter feature was not exploited.

2.2.3 Multisurface Models

More advanced models have been developed by using several nested yield surfaces. Multisurface plasticity models were introduced by Mroz *et al.* [MNZ79]. It consists of an elastic core and several hardening surfaces. The elastic core moves in the space in which it is defined (the principal stress space for example) according to kinematic hardening rules. The elastic core comes into contact with subsequent hardening surfaces, thus modifying the hardening rules as new surfaces become active. The state of stress always lies at the contact point between the yield surfaces and the flow rule is associated.
This type of model has several advantages. The kinematic hardening rules enable the anisotropic representation of the plastic phenomena in material, although this does not address anisotropic behaviour that could occur elastically. This type of

model can also reflect the irreversibility of deformations at very low density levels by entering plastic deformations when the stress reaches the limit of the elastic core region and yet start isotropic hardening related to densification when subsequent surfaces are reached.
Successful implementations of multisurface models are reported in the literature by Häggblad and Oldenburg and Bortzmeyer respectively applied to ferrous and ceramic powders. [HO94, Bor92]

2.2.4 Endochronic Plasticity Model

The final type of plasticity model introduced is the endochronic plasticity model. This model was introduced by Valanis and Lee [VL84]. It uses a pseudo time variable which evolves with the deformation history of the material. No yield surface is employed to describe the plasticity phenomenon. The constitutive equation is formulated as an integral of the so called hereditary functions, which define the material behaviour.
This type of model circumvents the problems related to the discrimination of the elastic and plastic part of the deformations as it postulates that any deformation has a plastic contribution. This can theoretically be exploited at low densities as the powder undergoes non recoverable deformation under very low stress. However, the endochronic approach is difficult to use as it requires a characterisation process which can discriminate the elastic and plastic deformations throughout the density range.
The endochronic plasticity model is rarely encountered in applications to powder forming due to the complexities laid out above. Häggblad found that the endochronic plasticity model compared favourably with cap and multisurface plasticity models [H91]. The latest implementation is presented by Khoei *et al.* [KMB02] showing excellent agreement with experimental data collected by Dorémus [DGM+95].

Various constitutive models, employed in the numerical modelling of the powder compaction process, were presented in this section. The constitutive models define

the stress-strain relationships and consist of a yield limit, which is often used to define the direction of the plastic flow. In this case the model is then referred to as an associated model. This is further explained in Chapter 4 with the detailed developments of a three-invariant constitutive model.

2.3 Numerical Modelling of Powder Compaction

researchers have used a number of approaches for the numerical simulation of powder compaction. The two important groups illustrated in this chapter are based on macromechanical and micromechanical approaches. The first option looks at the simulation of the compacted components as the continuous mapping of properties over a domain (the part geometry). This is illustrated here under the title of Continuum Models. The second approach considers the granular nature of the material and attempts to reproduce its behaviour by replicating its geometry on a microscopic scale. Both approaches can be used and compared in particular for the evaluation of constitutive equations [RLG04] and friction mechanisms [CG01].

2.3.1 Continuum Models

Early empirical models for the prediction of loads and density distributions appeared in the 1920s with Walker's work [Wal23]. This was a simple correlation between the volume and the applied pressure. More models followed, proposed by Heckel then Kawakita and Lüdde [Hec61, KL71]. These were particularly applied to metallic and pharmaceutical powders. They rely on experimental observation of compaction and only provide a compaction curve of pressure against volume or porosity. The equations are simple, but this also means that a limited number of powders can be represented with reasonable accuracy. The simple relationship between pressure and the state variable also means that the conditions in which these models are applicable are limited to cylinder, as the models consists of empirical rules defining density profiles as a function of the distance from the die wall and the height in the component for a given axial load. These limitations progressively resulted in this type of solution being abandoned for research, although they are still used in the industry to estimate the pressing capacity required to produce simple components

and thus are still sometimes investigated in professional publications. For example, Denny recently provided a comparative review of the Heckel and Kawakita equations for powder compaction [Den02]. The recent development of a new phenomenological equation was presented by Panelli and Filho [PF01], showing that empirical models are still developed but the increasing computing power available at reasonable costs means that the focus in research is on more complex models integrated within resolution methods by simulation of the evolution of the compact observed as a discretised domain. The predominant method is finite element analysis, but other possibilities are available such as finite volumes.

The finite element method is based on the spatial discretisation of the studied domain with a mesh. The resolution is carried out by the solving equilibrium equations over the domain. This work makes use of the finite element method with an updated Lagrangian mesh. The meshing scheme is important. It defines the reference configuration in which stresses and deformations are expressed. Eulerian and Lagrangian are the possible approaches, in which the meshes are respectively attached to the space and the material. The former solution is not applied to powder compaction due to the large deformations incurred and its inability to represent appropriately large material displacement. The Lagrangian options still have problems with degenerated elements due to very large deformations. Remeshing schemes have been investigated to solve his problem [KMB02]. Adaptations of the finite element method, the extended finite element method, was also investigated by Khoei *et al.* to improve the results in areas where strong gradients and discontinuities occur [KSAS06]. A popular alternative is the Arbitrary Eularian-Lagrangian (ALE) approach, in which a Lagrangian mesh is used as well as a background Eulerian mesh. The Lagrangian mesh is updated at each time step and the results are stored over the Eulerian domain. This is particularly interesting in the cases of large deformations as the elements in an updated Lagrangian scheme can be grossly deformed and thereby induce numerical errors in the calculations. The mixed scheme helps to maintain the condition of the elements while tracking the deformations [KAAL06]. The appropriate stress and strain measured need to be used, according to the discretisation scheme adopted. For the updated Lagrangian scheme used in the present work, the Cauchy stress and log strains are used.

The theory of the finite element method for non linear problems is very well laid out by Crisfield [Cri96]. Other references are also available by Zienkiewicz, pioneer in the field of computational mechanics or by Belytschko [ZT00, BLM00]. These are textbooks rather than research material, the reader is therefore referred to these works as the details of the finite element methods will not be reviewed in detail here. The thematic European research networks Modnet and Dienet have both demonstrated the capability of the finite element methods to simulate the powder compaction process. Brewin and Federzoni highlighted the improvements made over the period that they cover in replicating the density distributions and loads generated in the compaction [BF06]. They concluded that good results are obtained from the finite elements method and the main future source of improvement is the refinement of the constitutive models rather than a radical change in simulation technique. Improving the constitutive models could come from better calibration or the use of new constitutive equations.

2.3.2 Discrete Models

It is possible to simulate the compaction of powders with discrete models. Discrete models do not make use of a mesh to cover the compaction domain. Instead of considering the compact as a continuum, an attempt is made to capture the particulate nature of powders. Cundall introduced a first model with rigid particles with contact laws governing interactions [Cun79]. This approach was justified by the large proportion of the deformation of the granular media represented by the simple rearrangement of the particles. This is however not sufficient for ductile powders. Fleck developed a rigid perfectly plastic model for the particles, complementing the contact laws [Fle95]. This was used as a basis for the development of a constitutive equation at the macro-mechanical level that could be used in a continuum model. More recently, Shima and Kotera presented a model investigating the influence of the shape of the particles in the pressure-density relationship [SK98]. The particle dynamics method was used and, to simulate deformable particles, an empirical law was used to describe the interaction behaviour when the overlap between the particles was over a threshold value. Up to this threshold, the contacts were considered Hertzian. It was shown that the non spherical particles requires a higher pressure

to be compacted to a set density level. The interpretation given by the authors is that this is due to the easier rotation of spherical particles.

A series of papers from the University of Wales, Swansea pioneers the use of the combined finite-discrete element method [RGK+00, GDR+01, GLR03, RLG04]. The method is based on the simulation of particles as finite element domains. Ransing *et al.* demonstrated the capability of the model to reproduce the behaviour of particulate materials [GDR+01]. The particles are represented by circular finite element domains in plain strain conditions. A spring and dashpot interaction law between the particles is specified and the constitutive equation for the deformation of the particles assumes the form proposed by Fleck *et al.*[Fle95] or Gurson [Gur77], depending on the density. The finite-discrete element model compares favourably with the continuum approach and the Gurson model in a compaction test for a ferrous powder. The final publication in this series mentioned here [RLG04] also included the fracture of brittle particles. It was demonstrated to successfully simulate the compaction of particles of mixed nature and behaviour with particular reference to pharmaceutical applications. Using the same method, Cameron and Gethin investigated the frictional interactions between particles and a non smooth wall [CG01]. The study concentrated on the effect of particle size and surface roughness. In 2005, Lewis *et al.* carried out an extensive review of elastic and viscoelastic rheology models for the particles [LGYR05]. The study included the simulations of different shapes of particles and mixes of particles with different rheology models, sizes and material properties. The most important outcome of this publication was that it demonstrated the capability of the CDFEM to simulate an amalgamation of different materials. Although a modest number of particles is used due to the time consuming contact search, this is a very important achievement, in particular for pharmaceutical applications.

Additionally, a completely different approach to discrete modelling is taken by Khoei *et al.* [KSA07]. The reproducing kernel method is a discrete simulation technique in which the properties at each node are propagated to its neighbours by means of a kernel function. It does not attempt to simulate the deformations of the powder particles. It is effectively a mesh-free method for the simulation of a continuum. The main advantage is that the problems encountered with mesh degeneration are avoided, which is not negligible in the simulation of a process based on large de-

formations. Its main drawback lies in the search for the neighbours of each node, which is computationally demanding.

2.4 Fractures in Powder Compaction

The development of fractures in powder compacts is very difficult to assess. Because observations carried out with traditional techniques (microscope, SEM) can only look at a section rather than a 3-D reconstitution of the material, they can only be identified by a line rather than a fracture plane. Due to the granular nature of the material, the line can by hard to differentiate from the normal interstitial gaps left between the material grains after compaction. Publications on the conditions of fractures are mainly in professional literature and are mostly concerned with creep, fatigue and possible ways to improve the service lifetime of industrial components. They are mainly particular case studies with a phenomenological study rather than investigations of more general conditions of fracture initiation. A typical example was published by Kabatova *et al.* [KDW06].

Sources of fractures in powder compacts were listed by Zenger, introducing a classification of fractures by cause [Zen98]. The first cause introduced is improper material integrity, then interparticle shifting, improper elastic strain release and finally high tensile/shear stress. These categories are simplified and revised by Ernst, who identified two types of cracks: tension and shear cracks [Ern99]. Fractures caused by improper material integrity are not referred to. These causes can be the presence of contaminants in the powder, or trapped air in the mass of powder. The tension cracks are caused by the very low tensile strength of the green compacts because completely cohesive state for most compact materials is only achieved during sintering. Examples are provided showing that the fractures are typically brittle. No macroscopic deformation is observed and micrographs show that the interlocking that the grains build up during compaction appears to have been pulled apart without deforming the grains. This category overlaps Zenger's improper elastic strain release and high tensile stress sections.

The shear fractures are introduced by an analogy with fluid flows. The shear deformation in powders, unlike in fluids, is limited by how much the grains can be deformed before they separate. A case in which the material grains break is not

considered and it is indeed unlikely as it is a safe assumption that the bond between grains in powder pressed material is much weaker than the grains. Examples of shear cracks are shown. These fractures do not open but the grain of the material along the crack is deformed either side of the crack line. So called dead water cracks are given as an example, where a a multilevel component is compacted under the displacement of a single tool or the displacement of tools in a non synchronised and proportional fashion. This leads to the separation of layers in the powder, comparable to the separation that occurs in a fluid around a corner. This analogy is the origin of the name chosen for cracks formed in such conditions. Ernst's shear fracture category covers interparticle shifting and high shear stresses in Zenger's causes of cracks.

The development of numerical crack models relies on work developed in the context of general fracture mechanics. Griffith's theory is the first attempt to formalise the development of fractures by bringing together a phenomenological explanation and a mathematical framework [Gri20]. He presents a criterion for the creation governing the growth of the crack surface. This criterion is based on the release of the elastic energy through the creation of new crack surfaces. This energy is used to overcome the atomic forces which ensure the material's crystalline structure. Griffith's criterion was developed in a linear elastic context, making it applicable to brittle materials only. It is expressed as an energy release rate.
An approach based on the release of accumulated energy was exploited experimentally by Jonsn [JH07]. In the diametral compression test, an estimation of the crack length was given and combined with the recorded press displacement and force to determine the fracture energy of ferrous compacts.
The notions of stress concentration factors was then introduced following Westergaard's solution for stresses near a geometric singularity [Wes39], which identifies and analyses 3 modes of fracture: tension, shear and antiplane cracks. This is an important step in the development of fracture mechanics as it reflects the local stress configuration at the tip of a crack.
With the development of non-linear mechanics, a more general formulation for an energy release rate was required. The J-integral characterises the change in potential energy per crack length increment. It is calculated around a crack tip and has been shown to be path independent.

Several crack growth criteria and associated remeshing techniques were reviewed by Bouchard *et al.* in a series of two papers [BBCT00, BBC03]. In particular the crack propagation criteria explored were the maximal circumferential stress criterion, the strain energy density criterion and the maximal energy release rate criterion. The study is valuable for the insight in simulations of crack growth but is not directly applied to powder compaction. It is a very good overview of the techniques available for crack growth, but in the particular field of powder compaction, the granular nature of the material may require more attention to the study of fracture initiation rather than propagation in a first approach.

In simulations, Mori *et al.* demonstrated the use of a simple maximum stress criterion for the prediction of fracture initiation in powder compacts based on the maximum principal stress [MSSO99]. The simulations were carried out with a rigid-plastic model for the compaction and an elastic model for the ejection of the compact. A correlation is observed between experimental results and numerical predictions but the simplification of the model and some assumptions on material properties for the die and the powder lead to the conclusion that refinements are necessary.

Coube and Riedel modified a Drucker-Prager model to include a dilating behaviour when the shear failure line is reached. As a result, the loss of density is used as an indicator that fracture is likely to take place in dilating areas of the compact [CR00].

Finally, Tahir and Ariffin published a study of the propagation of a crack in a two level component [TA06]. The stress intensity factors are calculated and an algebraic expression of the fracture toughness in mode I and II is proposed. This technique is derived from methods employed for the simulation of fractures in rocks [QZS+03]. The results are in very good agreement with the location of experimentally observed fractures but the initiation of the crack had to be assumed by inserting a defect in the mesh. This is because the calculation of the stress intensity factor requires knowing the length of an existing crack. This highlights the fact that a lot of attention was given to fracture growth due to the influence of geomechanics but the particular crack initiation conditions proper to powders still need investigation. This is one of the aim of the present work and Chapter 5 of this thesis introduces a fracture initiation criterion supported by case studies.

2.5 Closure

A review of the literature to date was presented. It focuses on the aspects investigated in the present work: powder characterisation, numerical modelling techniques and investigating fractures in powder compacts. It highlights some of the developments that could be carried out and sets the background for the work in this thesis. The present work investigates, in particular, tests in dominant shear conditions carried out with the necessary checks on the nature of the failure (brittle or ductile) to apply the appropriate data reduction technique. Few investigations exist relating to the Lode dependency of powders and no work was found regarding the potential influence that it could have on the compacted components. Chapter 4 of this thesis is dedicated to the development of such a model, its analysis and numerical experiments that illustrate the impact of the Lode dependency. Finally, the conditions of fracture growth are well documented in other domains than powder compaction and have been successfully applied to powder compaction simulation. There is however little documentation on the initiation of fractures. The present work develops a fracture initiation criterion, rather than a fracture propagation model, based on observations from experimental and industrial backgrounds.

Chapter 3

Experimental Data

3.1 Introduction

This chapter presents the experiments during which data was collected to establish the behaviour of powders. These experiments are necessary to calibrate the constitutive models reviewed in Chapter 2, so that the simulation actually reflects the physical behaviour of the material considered. Each experiment is used to define points on the yield surface defined as a function of stresses. Some tests are well documented, in particular the die compression tests and axisymetrical triaxial tests. As explained in the section for experimental techniques of Chapter 2, few authors have carried out true triaxial tests because of their complexity. Each test measures the behaviour of the powder under particular stress conditions. Some examples are shown in Figure 3.1. In this work, a set of three simple tests are used: the unconfined compression test, the Brazilian disc test and the uniaxial compression test. The aim of the investigation is to establish a convenient way of characterising a powder that can be employed in an industrial context if necessary. There are a few examples where these tests have been applied to powders previously as an extension of principles applied in geomechanics. However these explorations have been limited in their scope in that they have been used in an attempt to calibrate models that are rooted in geomechanics rather than to develop material models that are appropriate for powder compaction processing. The significant challenge that is presented in this work is that the tests are aimed at establishing a powder yielding

model under conditions where dilation might be present. These types of test present challenges in the determination of actual yielding as well as data reduction that is needed in order to establish a yield surface that will capture both compression and shear induced mechanisms.

As a consequence of the need for more detailed data under shear and low pres-

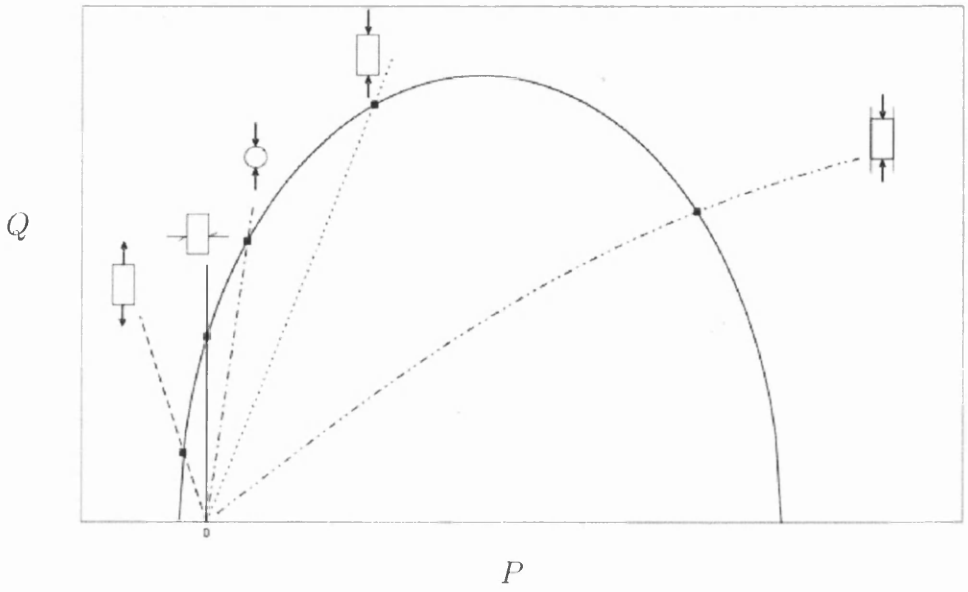

Figure 3.1: Tests in the P-Q plane, from left to right: tensile test, shear test, diametral compression test, unconfined compression test and die compaction test

sure yield conditions, the work laid out in this chapter looked to calibrate, and re-formulate if necessary, the yield surface. To do so the simple compression and Brazilian tests were investigated with attention to different data reduction techniques to ensure the suitability and appropriate exploitation of the recorded information. Finally, the well-documented instrumented die test complements the low pressure tests to establish the yield surfaces of the ferrous and ceramic powder studied in this chapter.

3.2 Unconfined Compression Test

Several properties of the powder can be investigated with the unconfined compression test. It can be exploited to derive elastic properties of the powder, such as Young's modulus and Poisson's ratio. It can also be used to look for points on the yield surface. During the unconfined compression test, the material fails under conditions dominated by shearing. Pavier and Dormus used the yield point of the test to characterise the shear failure line of a Drucker-Prager model [Pav98], and it can also be used in a single surface model such a the modified Cam-Clay model to characterise the dilating side of the yield surface. The difficulty of this test is to detect failure. Several approaches have been taken by authors in the past. Mosbah *et al.* used the dilatancy of the compact detected with strain gauges glued to its sides [Mos95]. In contrast, Pavier and Dormmus used the appearance of visible cracks to determine whether failure had occurred [Pav98, Dor03]. Both of these experiments have problems, strain gauges interfere with the surface strength of the compact and the detection of cracks implies the need to observe surface failure. The current work seeks to overcome these problems and thus in the present work a classical data acquisition technique is complemented by the analysis of images collected during the compression experiment.

3.2.1 Experimental Procedure

The unconfined compression test is very simple in principle. A cylindrical sample is placed between the platens of a press and compacted axially until complete failure of the compact is observed. Typically, the displacements and loads are recorded. In the present case, images of the experiment were also recorded to track the evolution of the compact during the test. Several factors can influence the quality of the experiment. The first one is the parallelism between the surfaces of the compact and the press platen. Other experimentalists made the choice of correcting the ends of the cylindrical samples by abrasion before the experiment [Mos95, Pav98]. The choice in this work was to maintain the integrity of the compact. This is justified by the fragility of green components and any operation can introduce additional stresses. To compensate, the top platen of the press is mounted on a ball and socket

arrangement and care was taken to align this parallel with the top of the compact. Friction between the platens and the ends of the compact can influence the deformation of the sample during its compression. Mosbah and Dormus *et al.* tested several lubrication methods to avoid a barrelling effect with the conclusion that the differences between lubricants were negligible [Mos95, DTA01]. During the present set of experiments, an ISO VG 68 lubricant was used.

The aspect ratio of the compacts used for the test can influence the results but exploration of this aspect is not the focus of this study and was deliberately excluded. A range of specimens with height to diameter (H/D) ratios from 1 to 2.5 were tested by Dorémus *et al.*[DTA01]. The deviation between the higher and lower H/D ratio is of the order of 10%. All compacts in the present study have a height and diameter of 18mm. This choice of a 1:1 height to diameter ratio benefits the homogeneity of the density throughout the compacts. Two materials have been tested. The first one is DistaloyAE supplied by Hgans with 1% Kenolube lubricant by weight. The second one is a spray dried spherical alumina powder containing an organic binder. The experiment was conducted on a Dartec hydraulic press for the ferrous samples and on an electro-mechanical Hounsfield testing machine for the alumina ones. The tests on the alumina samples generated forces up to 550N and the load cell on the Hounsfield has a working range up to 1kN. This machine resolves forces with 0.5% accuracy and displacements at 0.01%. The Dartec press was used for the ferrous samples. Even at the lowest density the force level is 14kN. Its accuracy is 0.5% on forces above 0.5kN (equivalent to 2MPa with the samples used in this study) but no calibration information was available regarding displacement measurement accuracy on the Dartec press, however the readout suggests a displacement resolution of 0.01mm. In both cases, the measurements were taken by making use of the data acquisition capabilities in the control system of the testing equipment.

A Kodak EM system was used to record images of the experiment. It can take 1000 pictures per second at a basic resolution of 240x200 pixels. With variations due to adjustments particular to each test, such as setting the focal distance, this resulted in a resolution between 0.083mm and 0.09mm per pixel. This resolution was further improved using image exploitation techniques explained in section 3.2.3. The data from the experiment, once analysed is expected to give an insight into the elastic properties of the powder and its yield behaviour under conditions dominated by

deviatoric stresses.

3.2.2 Data Exploitation Technique: Data from the Press

The initial outcome of the experiments is a data set of force against the displacement of the top platen. The data is presented in Figure 3.2 plotted as axial stress against axial strain. The curve has four identifiable regions. This division is supported by other authors' observations [Mos95].

In region 1 of the compression curve, contact surfaces are established. This phase

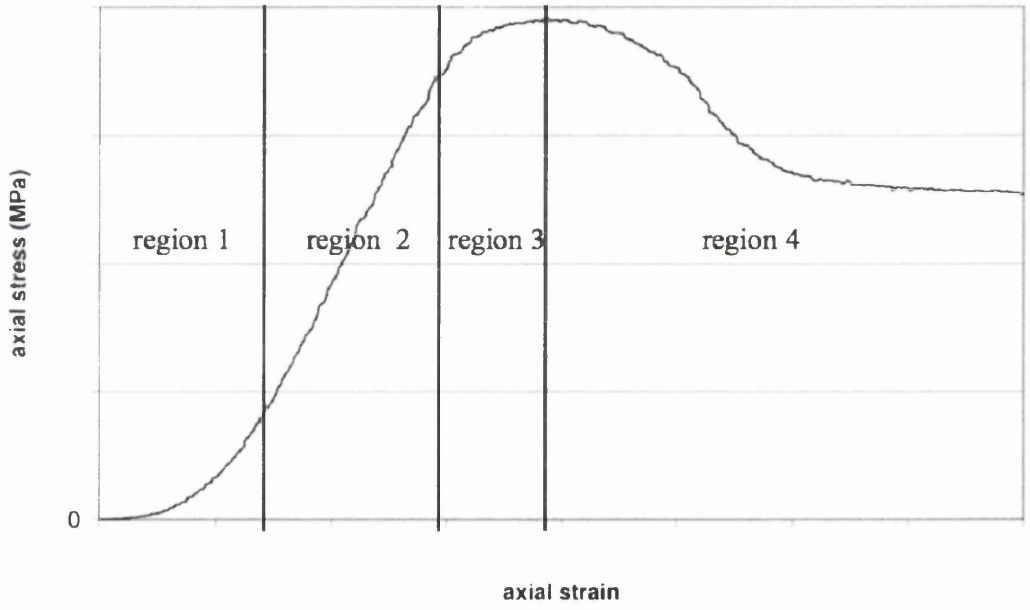

Figure 3.2: Typical plot of the axial stress against axial strain for an unconfined compression test

is made complex by the occurrence of several phenomena and their effects are extremely difficult to separate. Because ideally flat and parallel surface do not exist, there is first of all the establishment of the contact between the tool and the compact. It is also expected that the powder undergoes plastic deformations sporadically throughout the sample due to local regions of lower densities, because an ideally homogeneous compact cannot be obtained. Mosbah carried out cyclic load-

ings of compacts up to a maximum load level below yielding that remains constant throughout the cycles [Mos95]. This showed that the initial non linear behaviour of the powder can largely be attributed to the settlement of contacts with plastic deformations. After a few cycles, all deformations are recoverable within a cycle below the yield strength. The slope found follows the one observed in region 2 of the first cycle. This result is exploited in the present work by concentrating on the region 2 of the loading curve, thus avoiding the need to cycle the load.

The second region is dominated by elastic deformation. It consists of linear deformation taking place according to Hooke's law of elasticity.

In the third region, non recoverable deformations take place. The stresses throughout the compact build up in a non-linear fashion until the initiation of the complete collapse of the compact by fracture. The final failure of the component is considered to occur when the load decreases in region 4, although the fracture is certainly initiated before then.

The maximum admissible stress can be obtained easily from the graphs. Because the behaviour of powders is pressure dependent, the yield information obtained from this test is only relevant to the conditions of the present test. This is taken into account in the formulation of the yield surface (in Chapter 2 and section 5 of this chapter).

The yield conditions can be obtained from the experiment. The onset of plasticity is likely to be progressive throughout the compact due to localised stresses at the contacts or heterogeneity in the samples. This raises the question as to when yielding really occurs. Several criteria can be used: the loss of linearity, the onset of dilatancy or the initiation of a fracture if the material is considered to fail in a brittle manner.

When the data acquired from the press is examined, it is possible to define a range over which the stresses and strains are linearly related. Because of noise in the measurements, it becomes necessary to choose an tolerance interval 2δ within which the behaviour is considered linear Figure 3.3. Two tests were carried out to investigate the impact of this choice. The criterion chosen is the deviation of the strain from a linear elastic law for a given stress. The elastic law was obtained by carrying out a linear regression on the data set to obtain Young's modulus. The boundaries of the linear region are adjusted so that all points within the interval satisfy the

relationship:

$(1-\delta)\frac{\sigma}{E} < \epsilon < (1+\delta)\frac{\sigma}{E}$

This operation was carried for $\delta = 1\%$ and $\delta = 2\%$.

It is difficult to obtain consistent data with this technique if a lot of noise is in-

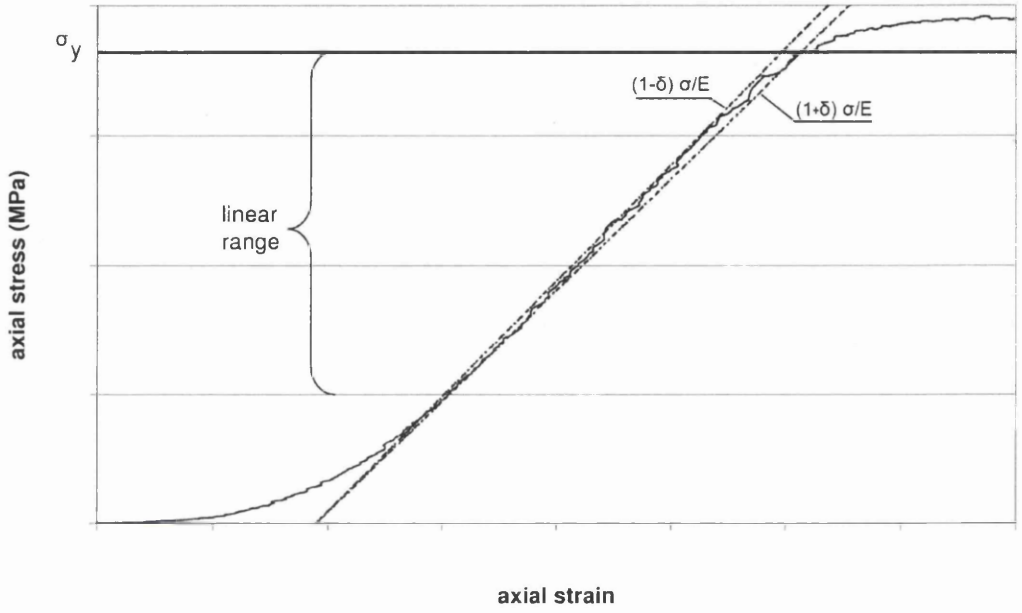

Figure 3.3: Definition of the linear range with tolerance δ

cluded in the acquired data. The present data set was affected by noise from other electrical equipment in the laboratory where the tests on the ferrous material were carried out. The press used for the tests on the alumina samples was located in a different laboratory, in which there was far less electrical noise. The sampling frequency used for the data acquisition is 50Hz and considered high enough to enable the use of a smoothing filter on the data to reduce the impact of undesirable signals without any significant alteration to the essence of the collected data (Figure 3.4). A median filtering technique described by Russ was applied by embedding it in the data processing spreadsheet [Rus90].

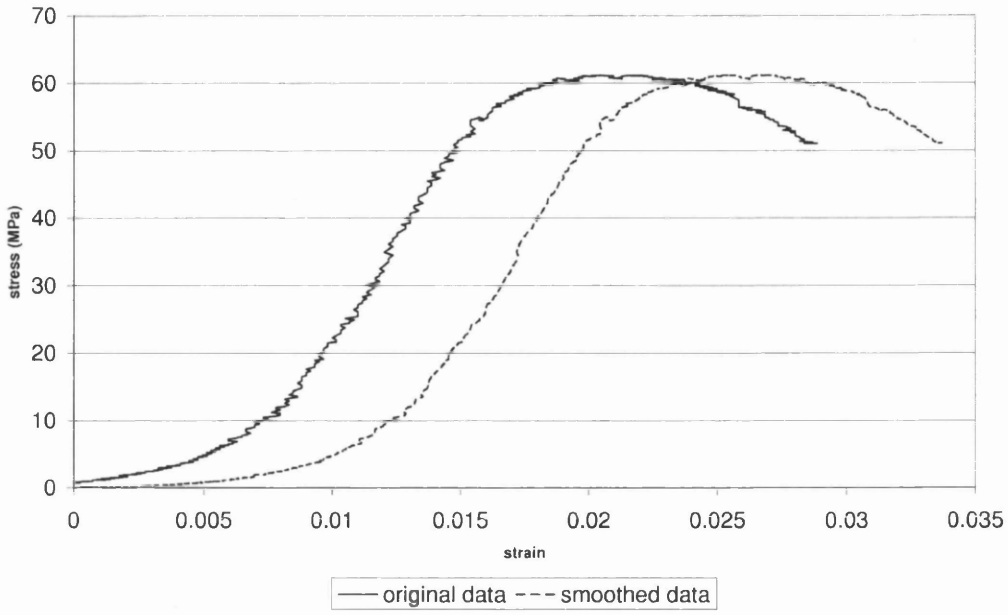

Figure 3.4: Effect of the smoothing filter on the data set, the unfiltered data is shifted by -0.005 strain units for clarity

3.2.3 Data Exploitation Technique: Images

It is possible to observe the evolution of the compact failure using digital imaging techniques. It is arguable whether ductile or brittle failure occurs under the conditions of the simple compression. The criterion used by Ernst is the formation of fracture without observable large scale deformations, for example [Ern99]. It is consistent with the use of constitutive equations that define the Drucker-Prager model to consider that the failure is brittle, as the stress locus for the test lies on the shear failure line. Therefore the use of the conditions under which fracture is detected can be used to define the shear failure line, and this is the approach taken by Pavier and Doremus [Pav98, Dor03]. This, however does not account for any plastic yielding that may occur. Also if the fracture is initiated internally, it is only detected when it reaches the surface of the compact. Further, the failure obtained by Doremus and Pavier in the test, show a diagonal fracture, whereas a conical pattern was obtained in the experiments conducted within this study Figure 3.5. Both failure patterns are due to shear stresses. The conical failure pattern can be expected due to the

axisymetrical nature of the component, whereas in the diagonal failure plane, a defect must have been present so that a particular plane was privileged for the growth of the crack.

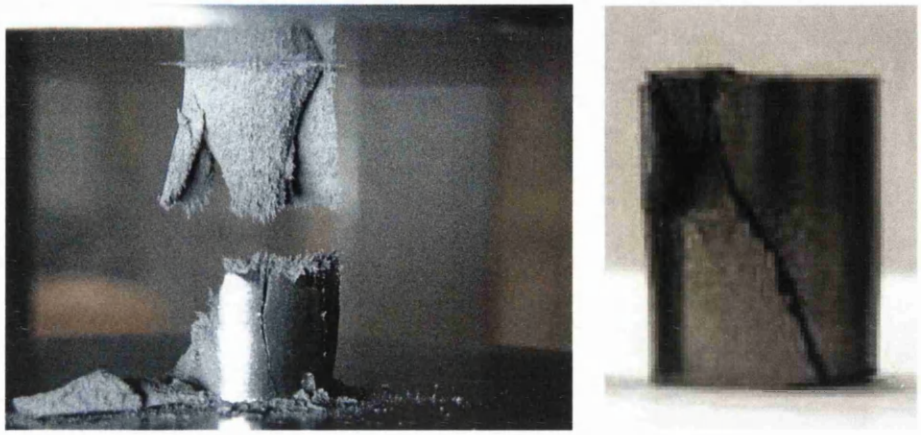

Figure 3.5: Left: conical failure pattern obtained in the present set of experiments, right: diagonal fracture from Doremus

The choice of the imaging technique used in this work follows results obtained by Mosbah [Mos95]. It is concerned with measuring the radial deformations but through a non contact method, in contrast with Mosbah's work, which used glued strain gauges. This choice is motivated by the argument that gluing strain gauges to green samples modifies the behaviour of the powder by addition of a bonding substance in the area where the glue permeates into the compact. The essential advantage of the technique used here is that it does not interfere with the observed phenomenon at all. The strain measurements may then be used to compute the evolution of volumetric strain to detect the presence of yielding before the complete failure of the compact. It is also a coherent approach to validate (or reject) the elliptic model that had been historically implemented in the code for continuum analysis of powder compaction used by the research group in Swansea.
The experimental set-up is very simple but the data exploitation of images is the main challenge of this particular experimental procedure. Dedicated software was written to process the images and track the contours of the compact to follow the deformations during the compression. The images recorded during the experiment

are black and white so the program written to analyse the pictures is based on the grey levels of the pixels. Because of the light reflecting off the cylindrical samples, as seen in Figure 3.6, the traditional technique of setting a threshold between the level of the background and that of the part could not be used. Instead, a method based on contrast between neighbouring pixels was used within a predefined area where it is known that the edge is located.

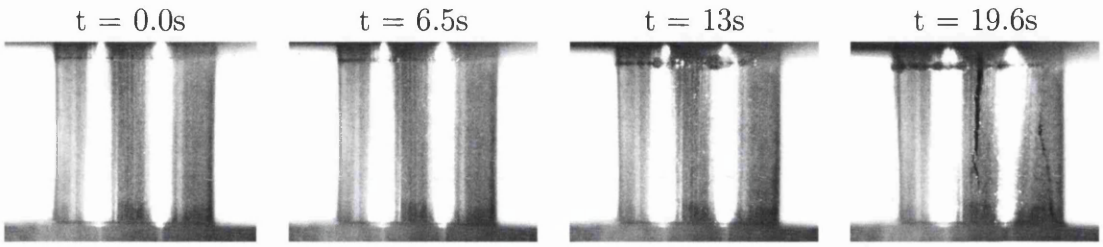

Figure 3.6: Aspect of a ferrous compact throughout the test

To improve the results derived from the basic resolution of the camera, a technique of interpolation for edge tracking at sub-pixel level was used [ELM88]. Without specific information available regarding the CCD response, a linear scale was used in which the brightness of the pixel is used directly to determine the location of the edge within the pixel, as illustrated in Figure 3.7. This technique does not result in a discrete resolution enhancement to produce a higher resolution image although it is one of its possible applications with further processing. A continuous function was fitted to the resulting discrete curve to obtain the radial strain values as shown in Figure 3.8.

3.2.4 Results for a Ferrous Powder

Data from the Press

The loading curves from the press are plotted as axial stress against axial strain (Figures 3.9 to3.12). Some data sets are widely out of the norm, they are shown in the graphs below: one data set in Figure 3.10 labelled A and one in Figure 3.11

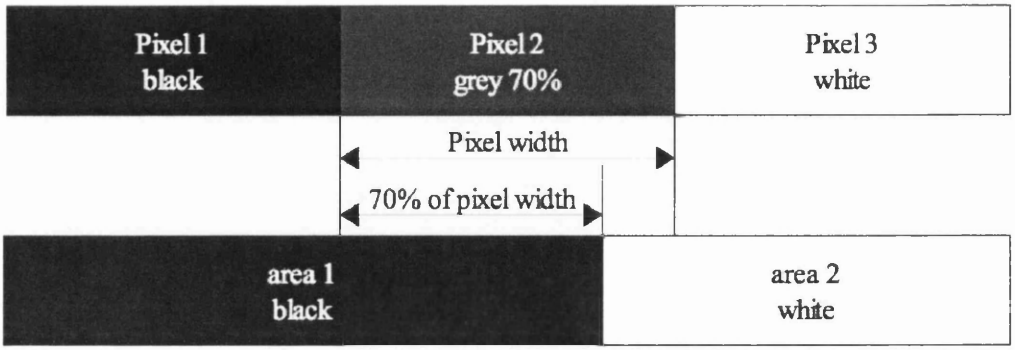

Figure 3.7: Pixel interpolation technique by fill level: a simple example for a linear CCD response

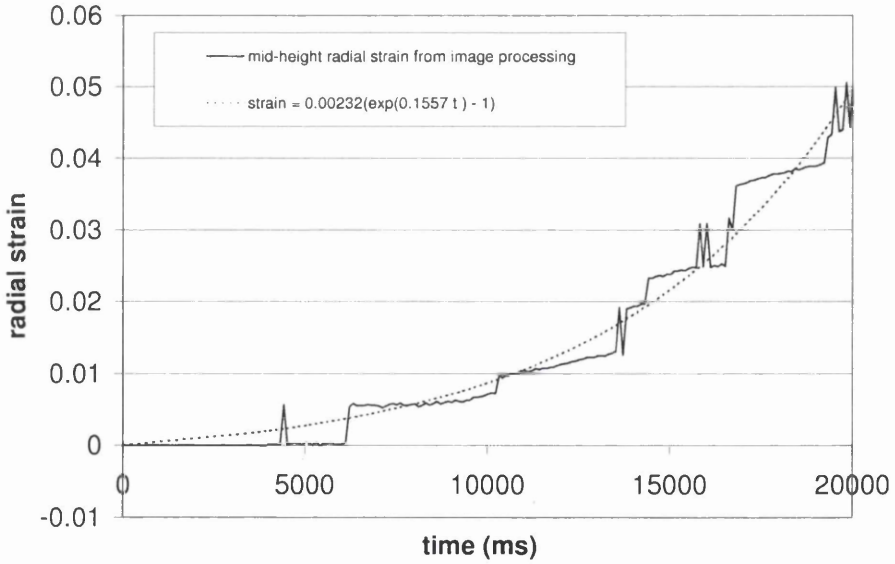

Figure 3.8: Evolution of radial strain with time during the unconfined compression test

labelled B. Those samples were considered damaged and are therefore discarded for future analysis.

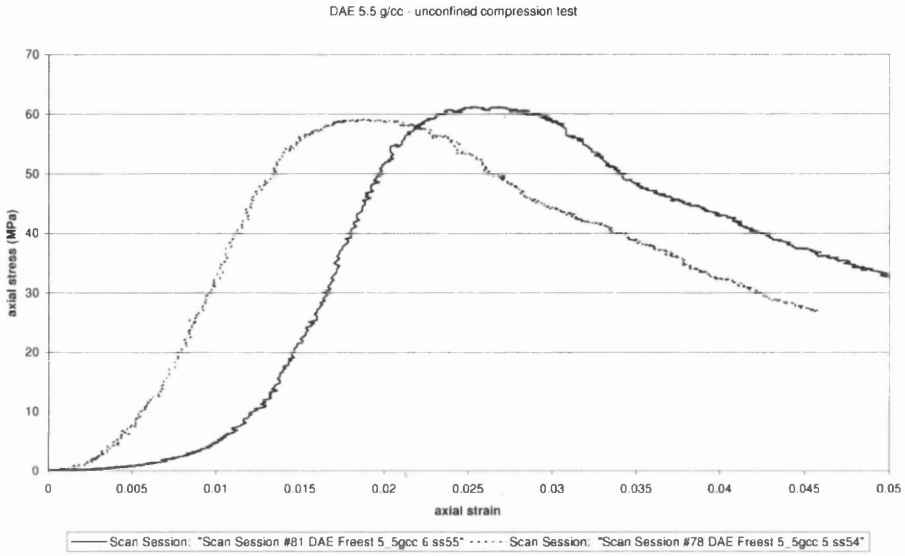

Figure 3.9: Plot of stress against strain for the unconfined compression test, DistaloyAE, 5.5g/cc nominal density

Young's modulus was calculated by applying the linearity interval method previously introduced. Changing the tolerance on the linearity criterion has little impact on Young's modulus (Table 3.1). The highest density groups only undergo a variation of the order of 1.5%, although at 5.5 g/cc, the variation is 13.5%. Figure 3.13, shows that the elasticity modulus can be considered to vary linearly over the studied range.

Table 3.1: Young's modulus according to the density and the linearity interval threshold

	5.45g/cc	5.95g/cc	6.31g/cc	6.73g/cc
1% linear interval	5387 MPa	7699 MPa	8360 MPa	8902 MPa
2% linear interval	4743 MPa	7766 MPa	8277 MPa	9130 MPa

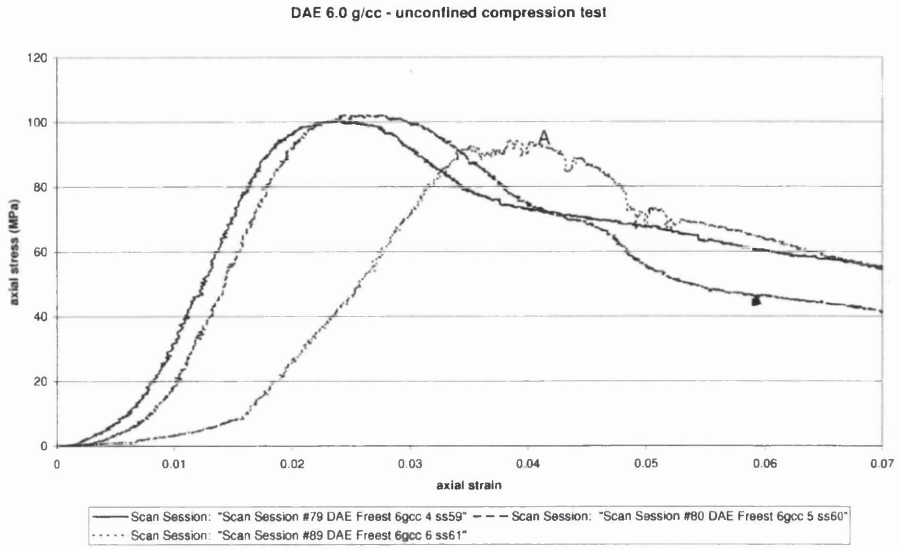

Figure 3.10: Plot of stress against strain for the unconfined compression test, DistaloyAE, 6.0g/cc nominal density

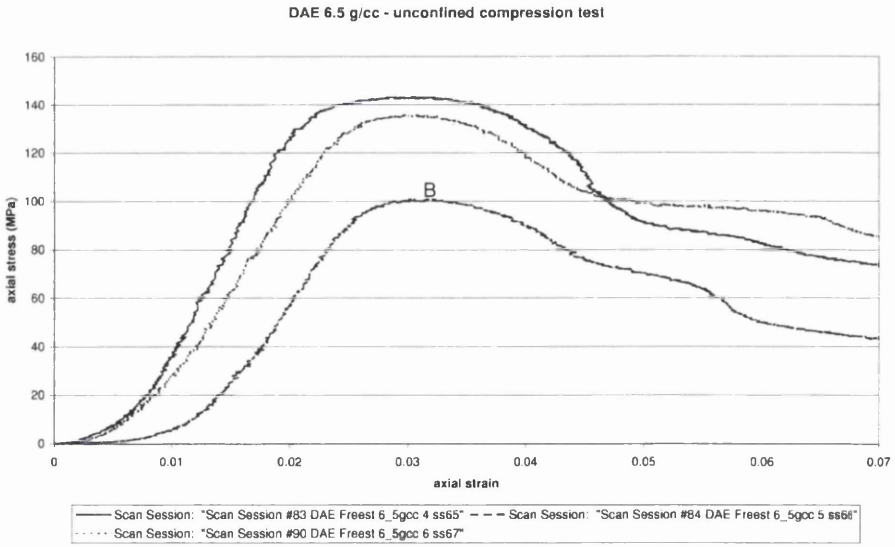

Figure 3.11: Plot of stress against strain for the unconfined compression test, DistaloyAE, 6.5g/cc nominal density

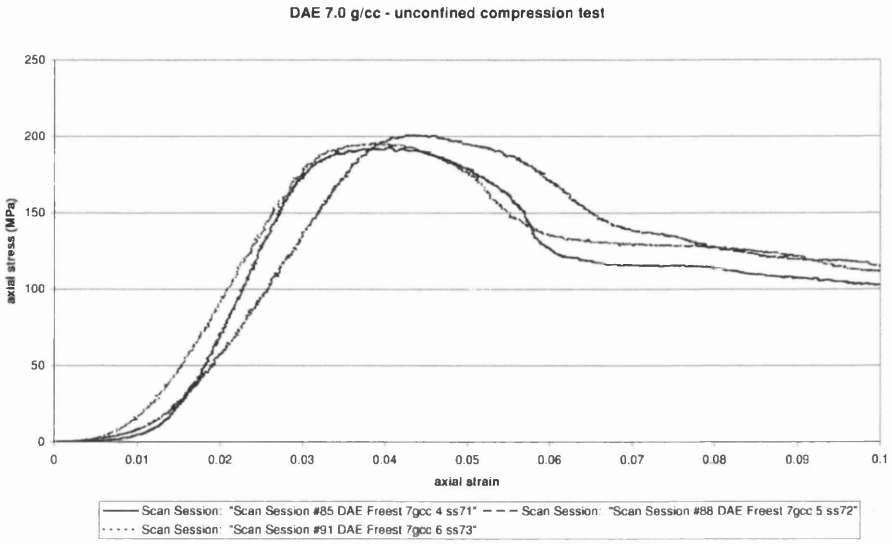

Figure 3.12: Plot of stress against strain for the unconfined compression test, DistaloyAE, 7.0g/cc nominal density

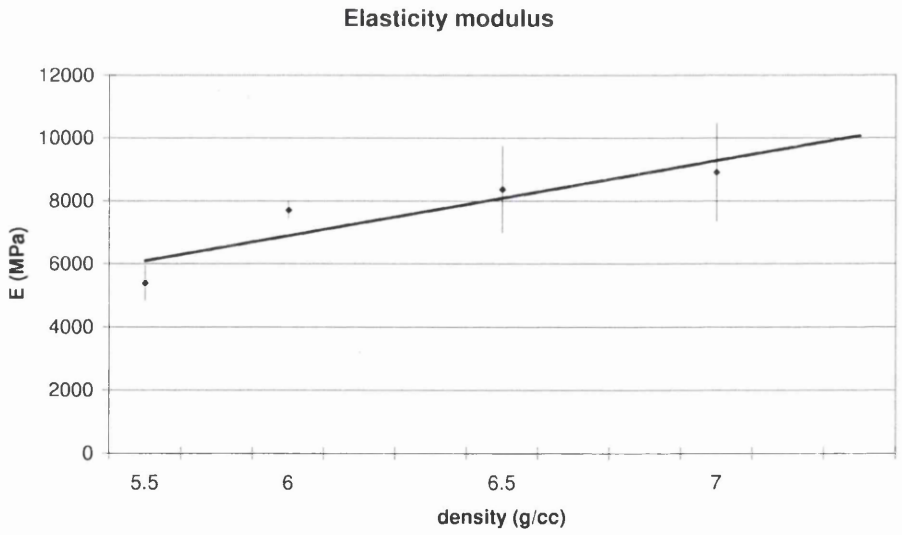

Figure 3.13: Young's modulus and deviation from the 1% linearity interval technique.

Several factors contribute to the larger variation in E at low density when changing the linearity tolerance. The lower density group only consisted of two tests, due to the difficulty in keeping the samples intact between their production and the test. Also the displacements are smaller, which could lead to a higher noise to signal ratio on the displacement sensors. The observation in Figure 3.13 of the deviation of Young's modulus within the density groups shows that at 5.5 g/cc, a 10% deviation is observed. Higher densities show a deviation of 17%. It is undeniable that difficulties arise at low densities due to the fragility of the compact. This problem has also been encountered by other authors in compaction tests [DTA01, Jon06]. The simple compression test has the added difficulty that the sample must be ejected and handled, implying that the samples need to have reached a sufficient cohesion to be tested. Despite these difficulties, values of Young's modulus could be derived. These will be compared later with values that have been derived from other test methods.

There are a number of ways in which the yield stress can be defined. As a logical continuity of the linearity interval method employed, it is deduced as the stress at which the data points come out of the chosen linearity interval (σ_y in Figure 3.3). By applying this to the data set, its evolution can be approximated with a linear function of density over the observed density range. As expected, tightening the interval on the linearity criterion reduced the yield stress. The variations in the yield stress follow the observations about Young's modulus: the impact of tightening the linearity criterion decreases with increasing density. The variations between samples within each density group also show that at lower densities, it is much more difficult to obtain a consistent result with a 50% difference in the yield stress between the samples at 5.45g/cc down to a 1.5% deviation at 6.73g/cc for a 1% tolerance on linearity. Figure 3.14 shows that the maximum stress and the yield stress are not proportionally related but have a constant difference. In the case where a 1% linearity interval is used to find the yield stress, this difference is 30MPa.

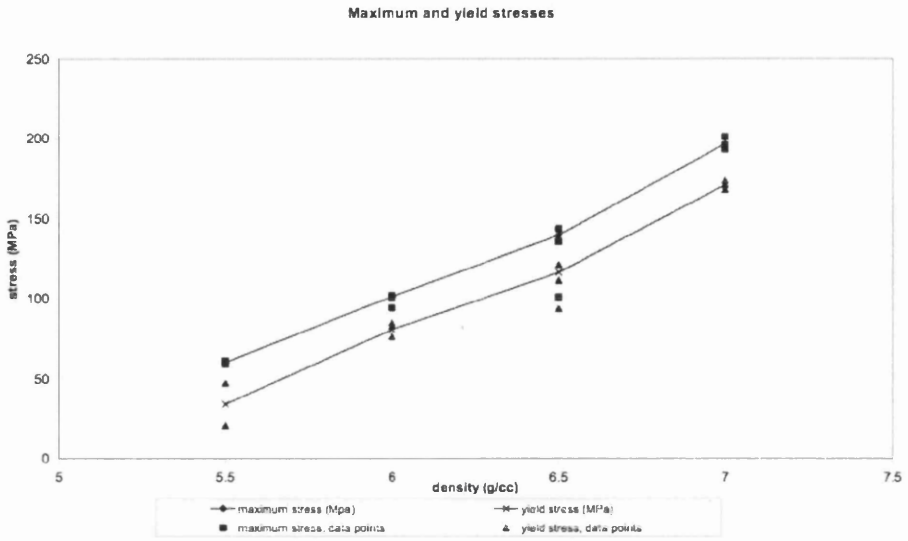

Figure 3.14: Maximum stress and yield stress from the 1% linearity interval technique.

Analysis of the Images

The image analysis technique introduced previously was used to track the radial deformation during the compression of the sample. Plotting the strains and stresses show consistency with the axial stress and strain recorded by the data acquisition system on the press. The radial strains also present a linear range that coincides with that of the axial strains when plotted against stresses (Figure 3.15).

The volumetric strain was then calculated from the axial and radial strains. When plotted against the axial strain, it appears that at the start of the compression, the sample is consolidated at first then this is followed by an increase in volume (Figure 3.16). This highlights the existence of dilatancy. This phenomenon is predicted by the theory of plasticity in granular media, and it occurs as plastic yielding is reached under dominantly deviatoric conditions. The point at which dilatancy starts the minimum in Figure 3.16 may be used to define the yield point. This is itemised in Table 3.2 where it is compared with the yield stress values obtained by the linearity interval technique. It is apparent that the onset of dilatancy occurs consistently below the thresholds chosen for the linear intervals and also that the differences between the values obtained using different methods decrease as density increases.

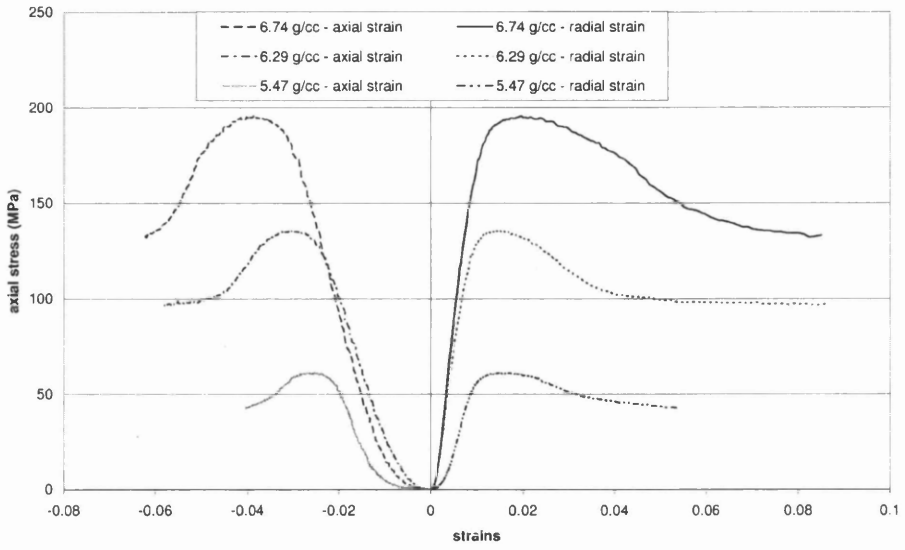

Figure 3.15: Axial stress against axial and radial strains for ferrous samples.

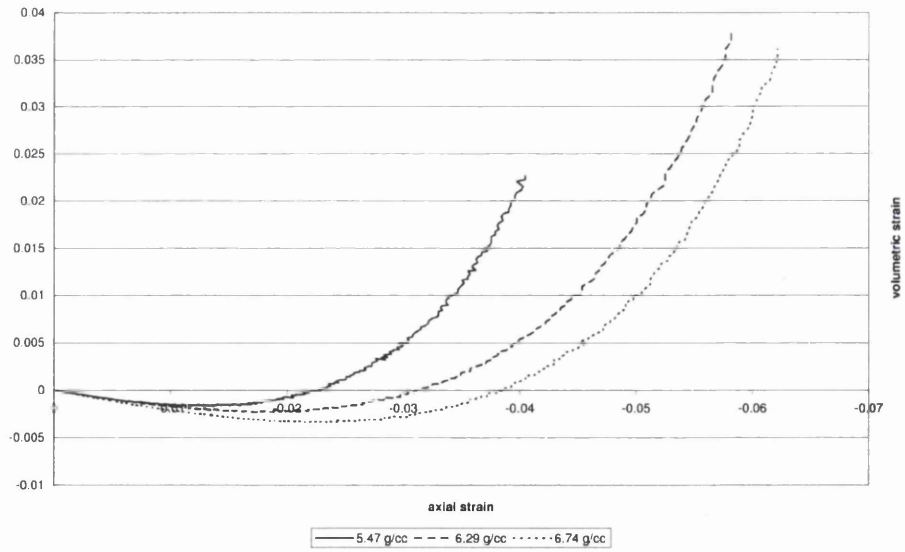

Figure 3.16: Evolution of the volumetric strain against the axial strain in ferrous samples.

The data gathered by image analysis can also be used to re-evaluate Young's mod-

Table 3.2: Values of yield stress according to the criterion used (values from the linear interval method are used as the basis for the variations)

Density (g/cc)	Onset of dilatancy	1% linear interval	2% linear interval
5.45	13.5 MPa	21 MPa (-36%)	34 MPa (-60%)
6.30	89.1 MPa	111 MPa (-20%)	122 MPa (-27%)
6.75	144.0 MPa	173 MPa (-17%)	182 MPa (-21%)

ulus, E, and calculate Poisson's ratio, ν. An optimisation procedure was used to calculate E and ν from the experiment over the linear range up to the yield point indicated by the onset of dilatancy. To calculate the elastic parameters, the incremental form of Hooke's law in the axisymmetrical case gives:

$d\epsilon_y = \frac{1}{E} d\sigma_y - \frac{\nu}{E} (d\sigma_r + d\sigma_\theta)$

$d\epsilon_r = \frac{1}{E} d\sigma_r - \frac{\nu}{E} (d\sigma_y + d\sigma_\theta)$

For the unconfined compression test, there are no radial and circumferential stresses so after simplification Young's modulus and Poisson's ratio are expressed as:

$$E = \frac{d\sigma_y}{d\epsilon_y} \tag{3.1}$$

$$\nu = \frac{d\epsilon_y}{d\epsilon_r} \tag{3.2}$$

The differences in elasticity modulus are shown in Table 3.3, below, where the higher limit of the elastic regime is defined by the onset of dilatancy.

By changing the range over which the elastic parameters are calculated, important

Table 3.3: Poisson's ratio and comparison of Young's modulus according to the criterion used.

	Poisson's	Elasticity modulus, E (MPa)	
Density (g/cc)	ratio ν	Onset of dilatancy	1% linear interval
5.45	0.315	3161	4990
6.30	0.309	7235	7389
6.75	0.308	9931	7982

variations are observed. Changing the upper limit of the elastic range to the onset

of dilation of the sample has brought down the values at low densities and increased the value in the higher density range.

3.2.5 Result for an Alumina Powder

Data from the Press

The same tests were repeated with an alumina powder. A Hounsfield electro-mechanical testing machine was used to match the sensitivity of the data acquisition to the expected forces. The acquired data is shown in Figures 3.17 to 3.20. It was of better quality than the data from the ferrous samples, due to the location with far less electrical noise of the Houndsfield press. The collected information was therefore processed without the use of any smoothing filter. The application of the linearity interval technique was limited to the 1% interval as the results with the 2% interval differ vary significantly from the values that can be obtained when radial deformations are taken into account.

Between the samples of each density group, Young's modulus shows variations of

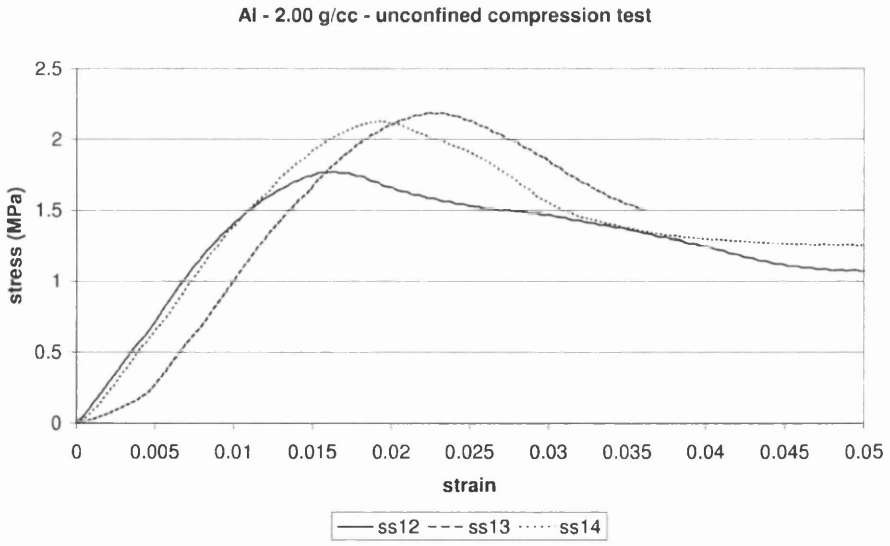

Figure 3.17: Plot of stress against strain for the unconfined compression test, Alumina, 2.00g/cc nominal density

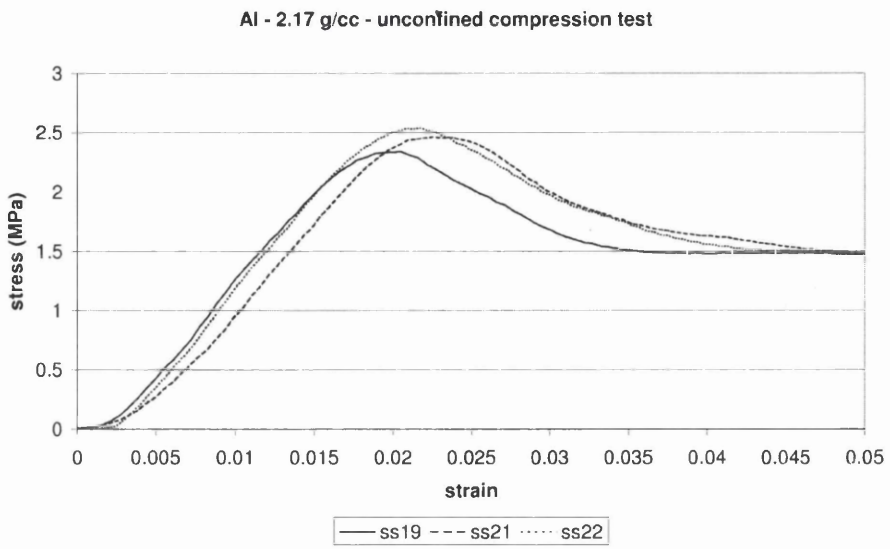

Figure 3.18: Plot of stress against strain for the unconfined compression test, Alumina, 2.17g/cc nominal density

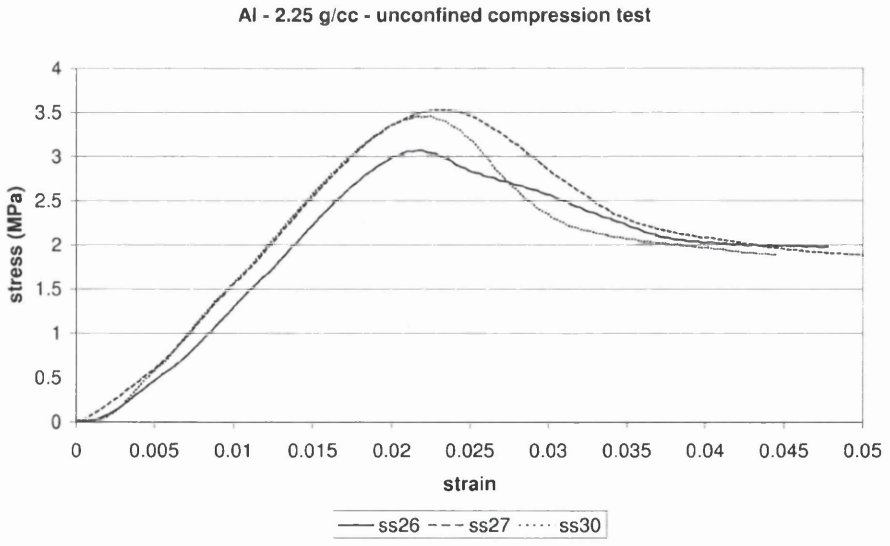

Figure 3.19: Plot of stress against strain for the unconfined compression test, Alumina, 2.25g/cc nominal density

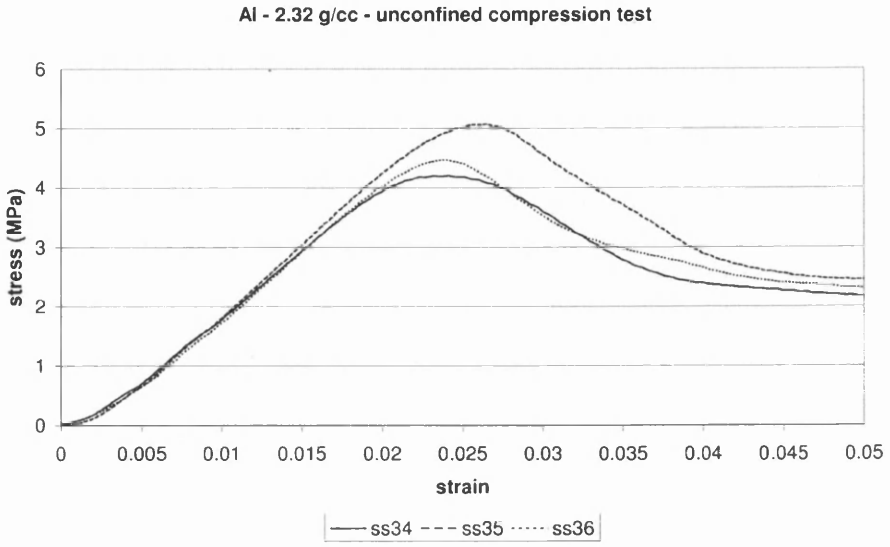

Figure 3.20: Plot of stress against strain for the unconfined compression test, Alumina, 2.32g/cc nominal density

14% at the lowest density and 4% for all other densities. However using this analysis, the variations of the yield stress and maximum stress do not show any consistent pattern (Table 3.4). Note that given the small size of the sample, the variation was calculated by using the sample standard deviation formula rather than the simple standard deviation.

There is a consistent increase of the properties measured in Table 3.4. Figure

Table 3.4: Young's modulus, yield stress and maximum stress with the variations within each density group

Density (g/cc)	E (MPa)	deviation	Yield stress (MPa)	deviation	Maximum stress (MPa)	deviation
2.07	127.01	14%	1.62	18%	2.03	11%
2.14	148.42	4%	2.18	2%	2.45	4%
2.23	193.88	4%	2.85	11%	3.35	7%
2.30	234.44	4%	4.07	9%	4.58	10%

3.21 shows that the evolution of Young's modulus can be considered linear over the studied range. An exponential evolution could also be used, particularly due to the inflexion in the lower density range. The evolution of the maximum and yield stresses can be assimilated to an exponential function of density.

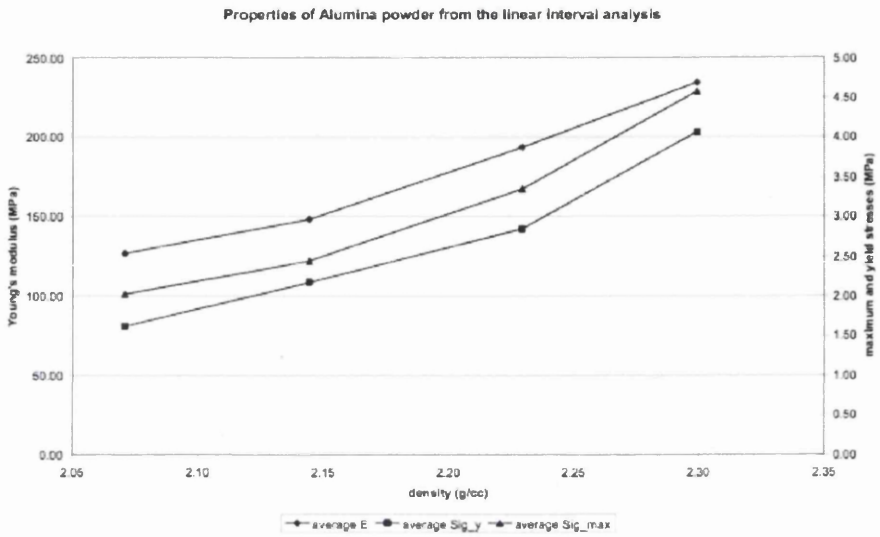

Figure 3.21: Properties of alumina powder from the linearity interval technique with a 1% threshold

Analysis of the Images

It was much more difficult to obtain exploitable results from the images of the alumina samples. This was due to the colour of the sample and their reflective surface. Focus adjustments and obtaining satisfactory contrast with these samples was extremely difficult. Imaging recognition techniques are well known to be subject to light variations and this particular series of test corroborates these claims. Only two tests could be reliably analysed with image processing techniques. Similar trends are observed with the alumina powder as were observed on the ferrous one in the evolution of strains and stresses (Figure 3.23). In particular the change from a compression to an expansion, highlighting the occurrence of dilatancy for this powder as well (Figure 3.24).

Due to the reflective nature of the component on a cylindrical surface, it was very difficult to obtain exploitable data from the imaging system. The use of a matt coating by spraying on the sample should be considered for further investigation to obtain a more comprehensive data set across the alumina density range, or even for application to other ceramic materials which give a very shiny surface finish. Figure 3.22 illustrates the blurry edge in the alumina samples images.

Using the onset of dilatancy as the upper limit of the elastic region to calculate E

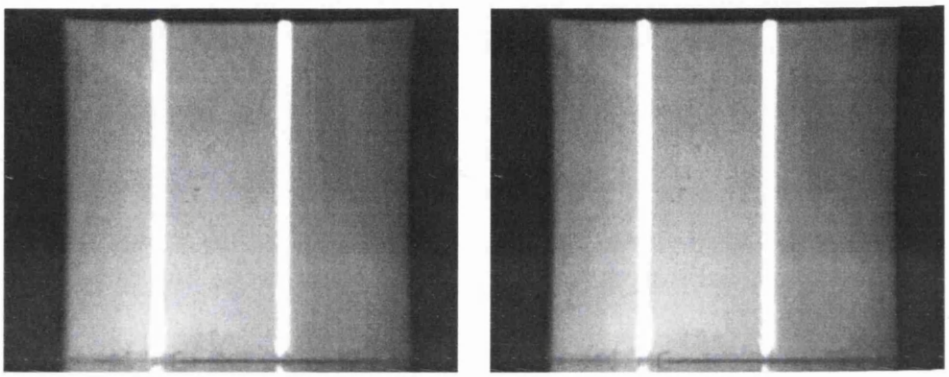

Figure 3.22: Alumina sample and detail of the left edge.

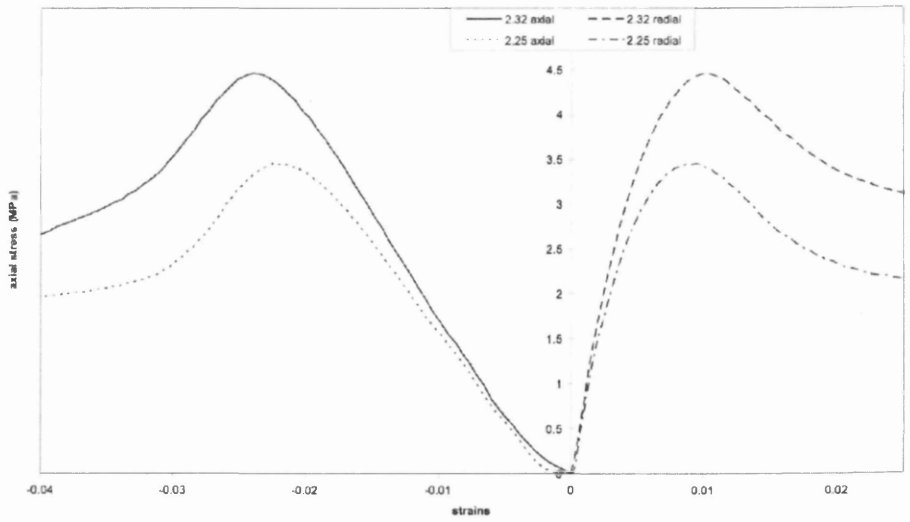

Figure 3.23: Axial stress against axial and radial strains for ceramic samples.

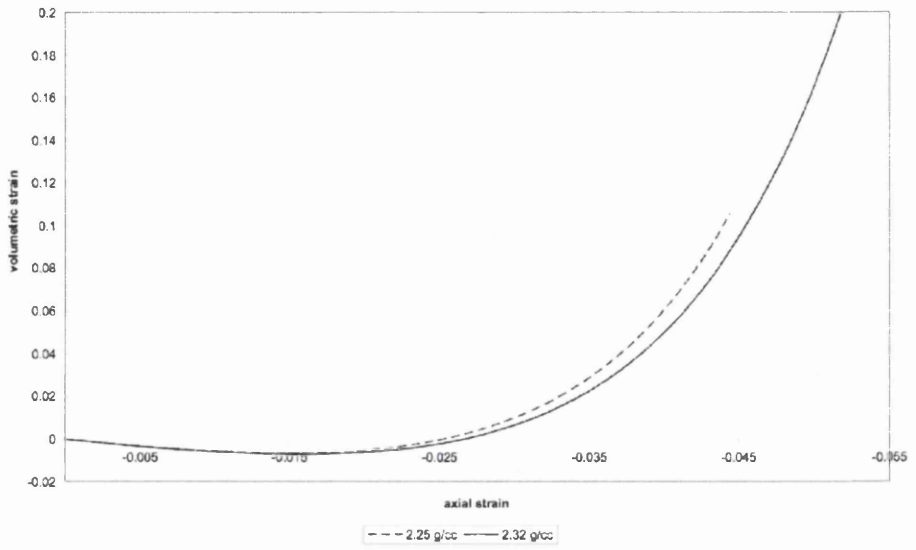

Figure 3.24: Evolution of the volumetric strain against the axial strain in ceramic samples.

and ν yields values of Young's modulus within 1% of those previously obtained and itemised in Table 3.4: 199.8MPa at 2.23g/cc and 235.3MPa at 2.3g/cc. Poisson's ratio, ν, was calculated and exhibits high values, showing that the alumina compacts have little volume variation during the elastic phase of the deformation, corroborated by Figure 3.23. The values are laid out in Table 3.5. The values of the yield stress are significantly lower when taken at the beginning of dilatancy than those from the the linearity interval technique (10.5% at 2.23g/cc and 22.9% at 2.30g/cc).

Table 3.5: Elastic properties of the alumina powder

density	Yield Stress	Young's modulus	Poisson's ratio
2.23g/cc	2.55MPa	200MPa	0.45
2.30c/cc	3.10MPa	235MPa	0.46

3.2.6 Discussion

The method used demonstrate the use of combined mechanical test data and image analysis techniques to obtain the elastic properties and yield points from the unconfined compression test. The results from these tests may be compared with other work reported in the literature. The results from by Dorémus, in which elastic data was obtained from the axisymetrical triaxial compression test, show much higher values of Young's modulus (Table 3.6)[Dor03]. However, less lubricant (0.6% weight) was used in the powder used in the tests carried out by Doremus. It is expected that admixed lubricant would decrease the stiffness of the green powder compact, which is confirmed by observations in Korachkin's work [Kor06]. Doremus measured the elastic parameters during a triaxial test, which can also influence the results. This is supported by the fact that at high densities (6.8 g/cc and above) the values of Young's modulus are approaching those of the solid material, about 155GPa, given for powder type FD-0400 in the PM Database, online [EPM07b]. Guyoncourt found values for the DistaloyAE powder mix between 59 and 73 GPa for densities between 6 g/cc and 6.85 g/cc, which are also higher than the values found in the present work (Figure 3.25[Guy05]. These values were calculated from data obtained during a uniaxial compression test.

Several factors can explain the differences between experimentalists' results. The

Table 3.6: Values of Young's modulus from different studies for the compacted DistaloyAE powder.

	5.5 g/cc	6.3g /cc	6.8 g/cc	7.0 g/cc
This study	3161 MPa	7235 MPa	9932 MPa	13015 MPa
Doremus	35869 MPa	66111 MPa	109101 MPa	138513 MPa

tests performed by Dorémus and Guyoncourt were both confined tests, whereas the present work uses unconfined samples. Friction effects can interfere with the results from the test, in the former cases whereas the sole area of friction in the free standing test is the contact disc between the press platens and the sample. Also, Doremus computes the bulk modulus, K, from deformations and pressure and then the elasticity modulus. When using this method with the data collected in the present

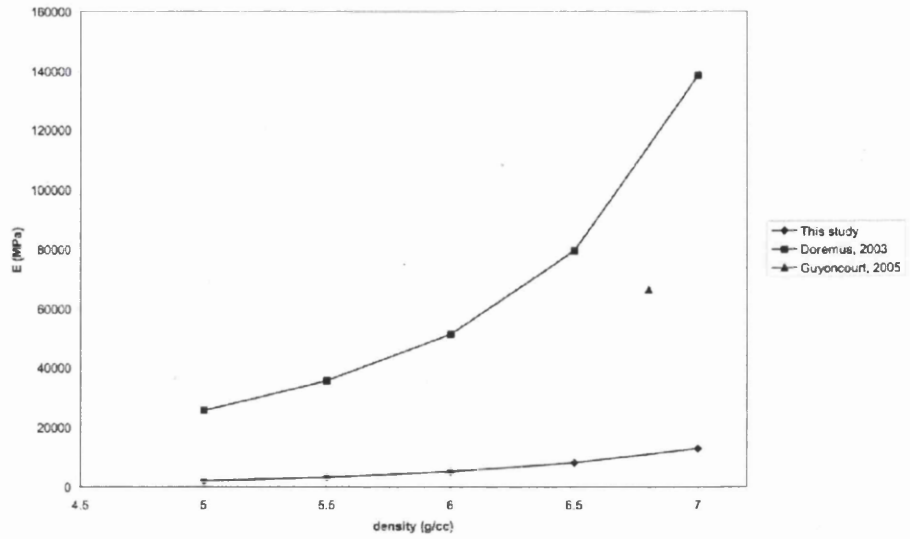

Figure 3.25: Values of the elasticity modulus for the DistaloyAE powder from three studies.

work, values of E are also found to increase by 50% but it is judged less reliable to do so because it adds the imprecision from the image processing to calculate the volumetric strain. Although the camera provides good data regarding the evolution of the radial strains, the readings are more accurate on the data acquisition system. This is why Hooke's law is the preferred method of calculating Young's modulus. The outcome of the different reduction methods are exposed in Table 3.7, based on the results found in this study for the ferrous powder.
The values obtained for Poisson's ratio also differ from those given by Doremus. It

Table 3.7: Young's modulus from different calculation methods, P is the hydrostatic or mean stress

Density	ν	$K = \frac{dP}{d\epsilon_{vol}}$	$E = 3K(1-2\nu)$	$E = \frac{d\sigma_y}{d\epsilon_y}$
5.5g/cc	0.315	2614 MPa	2893 MPa	3161 MPa
6.3g/cc	0.309	12242 MPa	13992 MPa	7235 MPa
6.8g/cc	0.308	14549 MPa	16740 MPa	9932 MPa

is found in the present study at a consistent values of 0.3, whereas it was found to increase from 0.08 to 0.15 by Dorémus [Dor03]. Korachkin found comparable values

to those from Dorémus but argues that the measurements taken in a die may not be accurate, as they are taken during the elastic recovery of the compact when it is unloaded [Kor06]. It can be affected by friction, which would cause the compact to recover only partially and thus introducing inaccuracies in the calculation of Poisson's ratio.

Finally, the comparative evaluation of the test can show that the yield stress found could differ according to the method used to process the data. Because Dorémus determined that yield has occurred when a fracture was visible, his values are closer to those from the linear range method as shown in Table 3.8. Unlike the elasticity modulus, the differences are much less significant when density increases. The changes in the values of the elastic parameters found between authors mainly has a significance for the predicted elastic recovery of a compact, when carrying out simulations. An overestimated value of Young's modulus will result in very little elastic recovery predicted, and conversely, a more compliant elasticity modulus will result in large elastic recoveries. Poisson's ratio will affect the pressure transmission between the axial and radial load in an elastic loading regime.

The elastic data obtained from the tests show that the methods employed yield

Table 3.8: Evolution of yield stress with density from different studies.

	5.5g/cc	6.3g/cc	6.8g/cc
This study (onset of dilatancy)	13.47 MPa	89.14 MPa	143.95 MPa
This study (linear interval)	33.92 MPa	116.35 MPa	170.96 MPa
Dorémus	49.34 MPa	100.88 MPa	175.23 MPa

results trends that are comparable to those obtained by others authors. However it would be possible to gain in accuracy by improving the experimental apparatus. A higher resolution camera in particular would reduce the degree to which deformations must be approximated at the sub-pixel level. A data acquisition system collecting channels others than those of the hydraulic press would also bring an improvement as a separate LVDT would measure the distance between the platens

rather than the displacement of the crosshead of the press. Measuring from the press can indeed lead to imprecisions as it does not take into account the deformations of the press itself. This issue is raised here for a critical analysis of the experimental procedure but no major differences are anticipated as the forces in the test (50kN maximum) are not near the maximum capacity that the press is built to apply (250kN).
The evolution of the strains during the test is similar to those found by Mosbah [Mos95]. The exact values are not comparable, though, as the powder used was only recorded as a generic ferrous powder. The results may also be different because of the technique employed. The main advantage of an optical measurement is that there is no interference with the powder's behaviour unlike glued strain gauges, which can considerably change the response of the powder at the location of the measurements.
The alumina powder exposed the main problem of the method. A good knowledge of image acquisition techniques, especially regarding lighting conditions, is required to obtain pictures that are more easily exploitable.

3.3 Brazilian Disc Test

The Brazilian disc test, also called the diametral compression test explores a very different region of the yield surface from those explored with triaxial or uniaxial tests. It is the only simple test that induces tensile forces in the compact without all the preparation required for a direct tensile test on a green compact. Because of the tensile stress and the direction of the compression it is important to be aware of the impact that anisotropy can have on the results, as a consequence of the material properties developed during a uniaxial compaction scheme or through the influence of the Lode angle, explored in the next chapter, to which granular materials are subjected. The challenges in the Brazilian disc test are associated with the non uniformity of the stress distribution. This discards the tests as a means to explore the elastic properties of the material and introduces the necessity to monitor the compact with careful considerations of the conditions of fracture initiation. The first outcome of the test concerns the mode of failure of the compact. It can be brittle or ductile. This can be explored by locating the initiation of the fracture on the

force-displacement curve from the test. Different approaches to the stress analysis due to the contact between the sample and the press platens are also explored.

3.3.1 Theoretical Background for the Analysis of Contacts

Two solutions are documented for the calculation of the stresses in the compact, first according to HertzHertz and then by Hondros.

Hertz's solution, from 1895, is a two dimensional elastic analysis of the stresses in the test in plane stress conditions. It shows that tensile stresses arise perpendicular to the diameter of the compression. Therefore the conditions of fracture initiation are very different from those observed in the simple compression test, for which theory only predicts the development of compressive and shear stresses, although it is important to note that residual stresses in the compact are not taken into account by the theoretical solutions.

Hondros, in 1959, extended Hertz's solution to make provision for a finite contact area instead of using an idealised contact on a point. The difference in the approach is exploited in the present work by retrieving the contact area that developed during the test from the images and using it to contrast the calculated fracture initiation stresses.

Equations 3.3, 3.4 and 3.5 give the stress distribution along the compression axis of the compact in the configuration solved by Hertz (point load):

$$\sigma_x = \frac{-2P}{\pi t}\left[\frac{x^2\,(R-y)}{\left((R-y)^2+x^2\right)^2} + \frac{x^2\,(R+y)}{\left((R+y)^2+x^2\right)^2} - \frac{1}{2R}\right] \tag{3.3}$$

$$\sigma_y = \frac{-2P}{\pi t}\left[\frac{(R-y)^3}{\left((R-y)^2+x^2\right)^2} + \frac{(R+y)^3}{\left((R+y)^2+x^2\right)^2} - \frac{1}{2R}\right] \tag{3.4}$$

$$\sigma_x = \frac{-2P}{\pi t}\left[\frac{x\,(R-y)^2}{\left((R-y)^2+x^2\right)^2} + \frac{x\,(R+y)^2}{\left((R+y)^2+x^2\right)^2} - \frac{1}{2R}\right] \tag{3.5}$$

P is the load applied, R the radius of the sample and t the thickness of the sample. In this solution, the circular section of the sample is in the x-y plane with the compression taking place along the y-axis. Vertically, along the y-axis, the horizontal

stress is constant and tensile, and the vertical stress is compressive and reaches its minimum for $y = 0$. As the contact is idealised as a point load, it tends to infinity at the contact points (Figure 3.26). In contrast, the solution proposed by Hondros uses distributed loads thus avoiding the infinite stresses at the contacts (Figure 3.27).

Although it can be argued that the solution given by Hondros is intended for a load

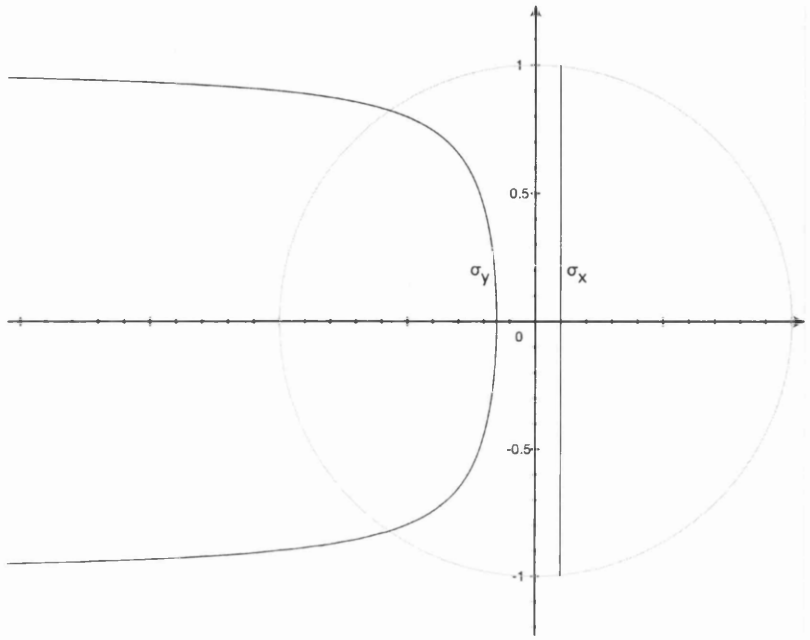

Figure 3.26: Stresses along the compressed diameter according to Hertz

distributed over an arc rather than a flattened contact, Fahad carried out numerical experiments demonstrating that *the stress distribution in the flattened disc case is essentially identical to the case where an arc was used* [Fah96]. It is therefore used to calculate the maximum tensile stress of the compact, given the absence of an analytical solution for a case with flat contacts. The stresses are not calculated over the whole surface of the component but only along the vertical and horizontal diameters. The following form of the solution was given by Procopio *et al.* [PZC03]:

$$\sigma_{\theta y}, \sigma_{\theta x} = \frac{\pm P}{\alpha \pi R t} \left[\frac{(1 - r^2/R^2)\, sin\,(2\alpha)}{1 \mp 2r^2/R^2 cos\,(2\alpha) + r^4/R^4} \mp tan^{-1} \left(\frac{1 \pm r^2/R^2}{1 \mp r^2/R^2} tan\,(\alpha) \right) \right] \tag{3.6}$$

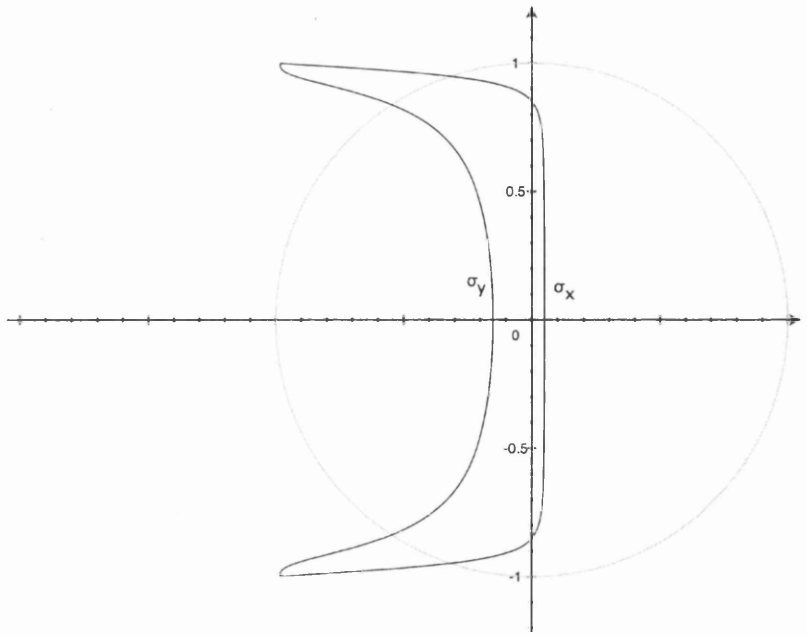

Figure 3.27: Stresses along the compressed diameter according to Hondros

$$\sigma_{ry}, \sigma_{rx} = \frac{\mp P}{\alpha \pi R t} \left[\frac{(1 - r^2/R^2)\, sin\,(2\alpha)}{1 \mp 2r^2/R^2 cos\,(2\alpha) + r^4/R^4} \pm tan^{-1} \left(\frac{1 \pm r^2/R^2}{1 \mp r^2/R^2} tan\,(\alpha) \right) \right] \tag{3.7}$$

$$\tau_{r\theta} = 0 \tag{3.8}$$

The index θ indicates circumferential stresses, and r indicates radial stresses. The second index, x or y, is used to indicate the axis along which the stress distribution is calculated, respectively horizontally and vertically. The loading angle α is shown in Figure 3.28.

The solutions from Hondros and Hertz converge to the same tensile stress in the centre when the contact area tends to zero:
$\sigma_t = \frac{P}{\pi R t}$
Also, for the application of the same load, the solution for the tensile stress given by Hertz and Hondros differ by a factor dependent only on the contact angle:

$$\frac{\sigma_{tHondros}}{\sigma_{tHertz}} = \frac{sin\,(2\alpha)}{\alpha} - 1 \tag{3.9}$$

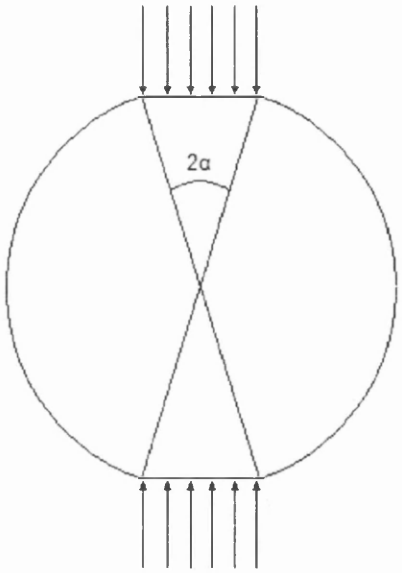

Figure 3.28: Definition of the contact angle α.

The difference between the tensile stresses obtained by considering a point or distributed load is illustrated in Figure 3.29 as the ratio between the stresses at the centre.

3.3.2 Experimental Procedure

The test was carried out in its simplest form. The samples obtained from compaction were placed between the platens of a press and compressed across their diameter. Because of the difficulties associated with handling green compacts, in particular at low densities, the contact areas between the samples and the punch were not prepared in any way. Surface preparation by forming a flat area by abrasion has been shown to result in lower values of the fracture stress by [Fahad, 1996] in a study on plaster samples.

The absence of surface preparation implies a high stress concentration region at the contact or a localised deformation to form the contact surface at the start of the test. Because the study is on porous material, the material is very ductile under compressive loads. The consequences of this deformation on the initiation of the

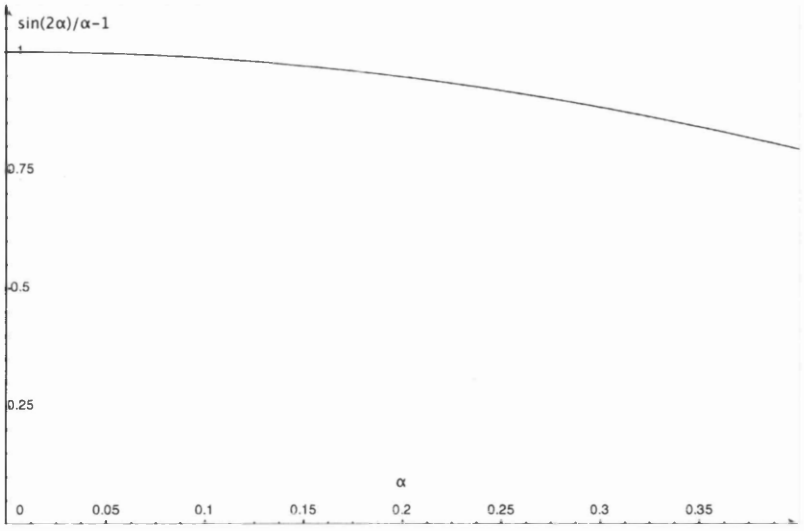

Figure 3.29: Variation of the tensile stress values found at the centre of the sample according to the calculation method — contact angle in radians.

tensile fracture is discussed in a further section.

Two materials were tested in this study. A ferrous powder, DistaloyAE, with 1% weight admixed Kenolube and an alumina powder. The samples are all 18 mm in diameter and 18 mm in height. The aspect ratio of the compact influences the calculated fracture stress of the compact. As the height of the compact increases, the plane stress assumption in the calculation by Hertz's equation may not hold any more. Dorémus *et al.* examined the influence of the aspect of the compact with a values from 0.25 to 2 for the ratio H/D. The lowest value for the fracture stress was obtained for H/D = 0.25 and the highest was 30% greater for H/D=2 [DTA01]. The ratio H/D = 1 was chosen in this work. It is a compromise between minimising heterogeneous density in the axial direction due to friction and a good stability of the compact between the press platens, which can influence the results.

As in the unconfined compression test, different presses were used to adjust the range and sensitivity of the equipment to the expected forces. The tests on the alumina samples were carried out on a Hounsfield electro-mechanical testing machine and the tests on the ferrous samples on a Dartec hydraulic press. The maximum force recorded was 220N for the alumina samples and 5.67kN for the the ferrous samples. The control system of each press was used for data acquisition and the tests were

recorded with the Kodak EM high speed digital capture system at a rate of 1000 images per second.

3.3.3 Detection of Fracture: Image Processing Techniques

Several image processing techniques have been explored to try and obtain the clearest indicator of the very start of the fractures. Strategically, they can be classified into two categories, the first one is image enhancement, and the other one is based on the comparison of images captured during the test.

The first method consists of enhancing contrast by remapping the image from the grey scale to the harmonic colour scale. The harmonic colour scale is the one commonly used for post-processing mapped numerical results such as those from finite element simulation. It ranges from red to blue. The output from this technique is illustrated in Figures 3.30.b and 3.30.c. Several approaches were used to cut out contrasts in unnecessary areas of the picture such as the background by capping the brightness values that are translated into the colour spectrum. For example, in Figure 3.30.b, the brightness values from 0 to 1 were mapped from blue to red, whereas in Figure 3.30.c, a threshold of 0.3 and a cap of 0.7 were applied. Unfortunately, no clear result was obtained by this method.

The second method consists of highlighting contours by reassigning a colour to each pixel that corresponds to the difference in grey value with its immediate neighbours to the left and above. The result from this modification can be an image in grey scale (Figure 3.30.d) or on the harmonic colour scale (Figure 3.30.e). This method introduces a delay in the detection of the crack due to the need for a sharp contrast between pixels, which translates in a requirement for the width of the cracks to represent a major fraction of the pixel dimension in which it propagates. As the resolution of the camera is low, this means that the crack is only noticed when the crack is already quite opened (0.09mm with the resolution of the camera used for this work). This is a good method to follow the propagation of an already opened fracture but it is difficult to find the precise moment of fraction initiation.

Finally the third method consists of subtracting the original picture from the one considered at any time of the test. As the pictures are grey scale pictures, this is

done by taking the difference in grey level or brightness of each pixel. Two parameters are then used to modify the brightness value of the pixel: centre and saturation (Figures 3.30.f and 3.30.g). The centre is used to specify what value will be assigned to a pixel which has no difference in brightness between the image considered and the original one, and the saturation is used to enhance the contrasts. The value obtained is then translated into a colour of the harmonic scale as exposed in the first image processing technique.

To account for the change in height of the compact during the test, each pixel was remapped by using the original height of the compact and the speed of the press platen. Another challenge was encountered when processing the images by this method: the lights used in the experiment were incandescent lights. Their luminosity varies with the current that flows through them. The impact on the resulting images was that they were not directly comparable. To compensate, a first attempt was made by correcting the brightness of the image with a function of the form:

$\delta B = |k \times \sin(f)|$

where B is the difference in brightness. It is measured as the difference in average brightness between the lightest image and the darkest one in the image capture session. f is the frequency, 50Hz in this case, and k is an amplitude parameter chosen to minimise the variation in the overall brightness between images. This approach however did not provide a very good result. There are two reasons for this: the background is not flat hence affected differently by the change in lighting conditions. Furthermore, hysteresis effects in the light filament makes the luminous response different from the function that governs the current flowing through it. A second approach was taken to reduce the impact of light variations by sampling an area of the picture, before carrying out the image subtraction routine. The average brightness of the sampling area was calculated and the brightness of each pixel shifted by this amount. The patch chosen for sampling is situated in the compact rather than on the background area of the picture thus making the images readable. The counterpart of this technique is that the background that was not affected by the light variation was now changing colour. This is only a minor side effect of the method, as the background is not of any interest for the purpose of detecting the cracks. This was the most successful technique to detect the initiation of fracture through image analysis. Using this method fractures were detected much earlier

than with the previous image enhancement techniques. The observation of variations in the images can be put in a form that is more objective to detect fracture. To do so, the brightness value and position of the pixel undergoing the largest variation in each picture was also logged as tabulated data. Figure 3.31 shows the largest variation in one of the samples. The correlation between the tabulated data and the appearance of fracture on the images is excellent, confirming the sudden modification in the patterns on the surface of the compact. In the example illustrated by Figure 3.31, fracture intiation is considered to occur at $t = 4208ms$ of the test, shown by the image 4208.
Examining the original images when clear fractures are evident also confirmed that the position of the cracks coincided with the initiation sites detected by the procedures set out above. This provides substantial support for the image analysis methodology developed.

3.3.4 Results for a Ferrous Powder

The forces and displacement information recorded during the test were converted to stress against normalised displacement. The normalised displacement is the ratio of displacement to the diameter of the compact. Some authors also call it diametral strain [PZC03]. The test was carried out for nominal densities of 5.5, 6.0, 6.5 and 7.0g/cc, values that are similar to those used for the unconfined compression test. The analysis of the collected data shows that the loading curve (Figure 3.32) can be divided into five regions.

In the first region of the compression curve, the contacts between the platens of the press and the compact are established. A non-linear elastic contribution may be present but it is mostly an initial plastic process establishing the contact areas. Because no preparation was carried out for the contact areas, a stress concentration occurs at the point where the platen initially touches the compact. It is certain that the stresses reach the yield condition of the powder locally due to the high stress level at the contact, as shown in Appendix C. The stresses then decrease as the contact surface grows. Thus, further local densification was also achieved.
The onset of fracture invariably occurs within the linear region of the curve, while

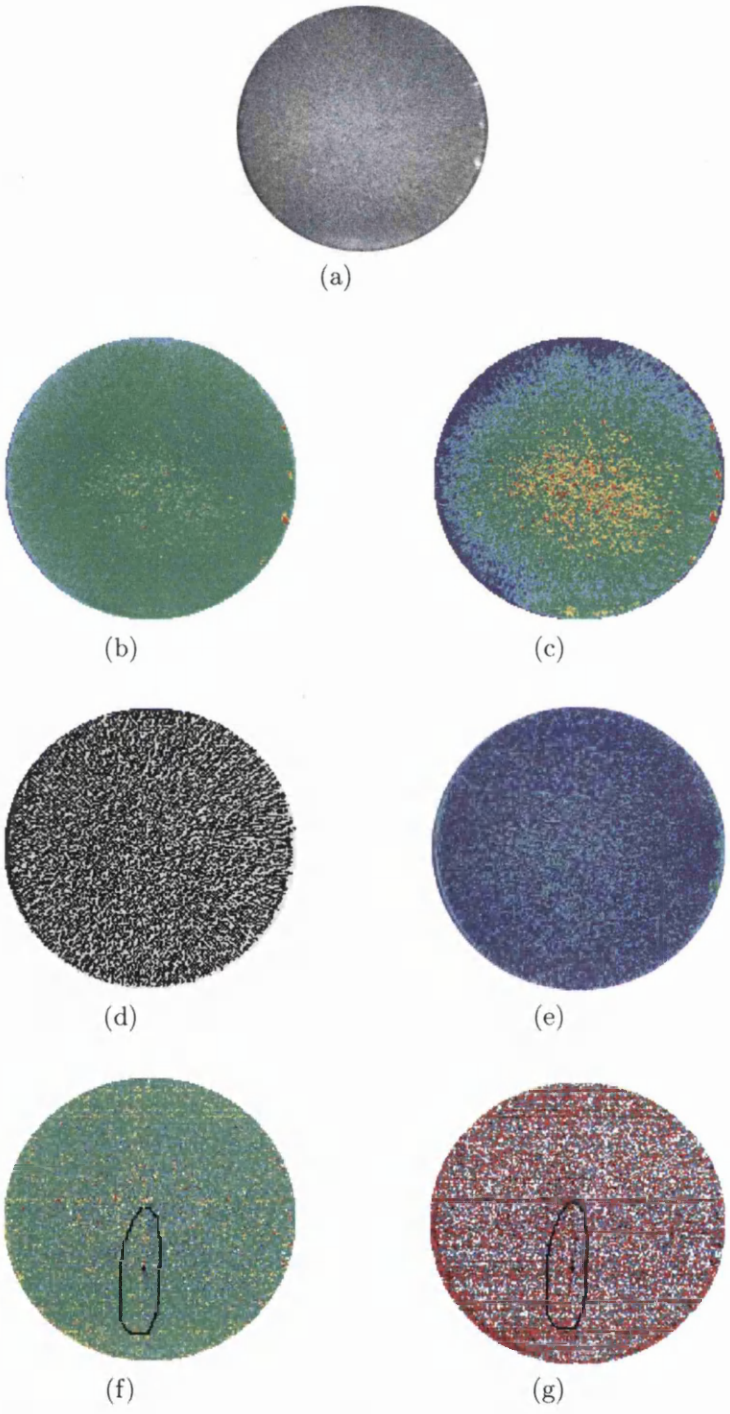

Figure 3.30: Original picture (a), processed by contrast enhancement of brightness levels (b and c), contour search in black and white (d) and colour (e) and by image subtraction (f and g)

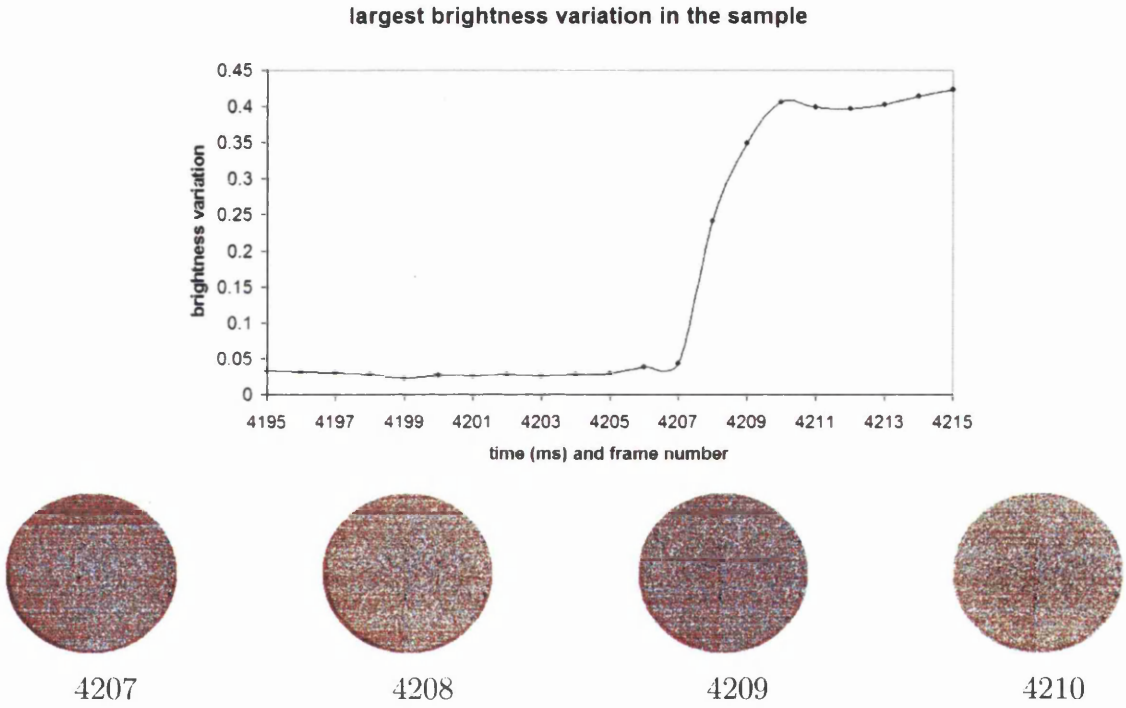

Figure 3.31: Difference in brightness at the point of greatest variation in the captured sequence of images, example at 6.5 g/cc, ferrous component. A line appears in the sample (image 4208), as the jump in brightness variation occurs indicating fracture.

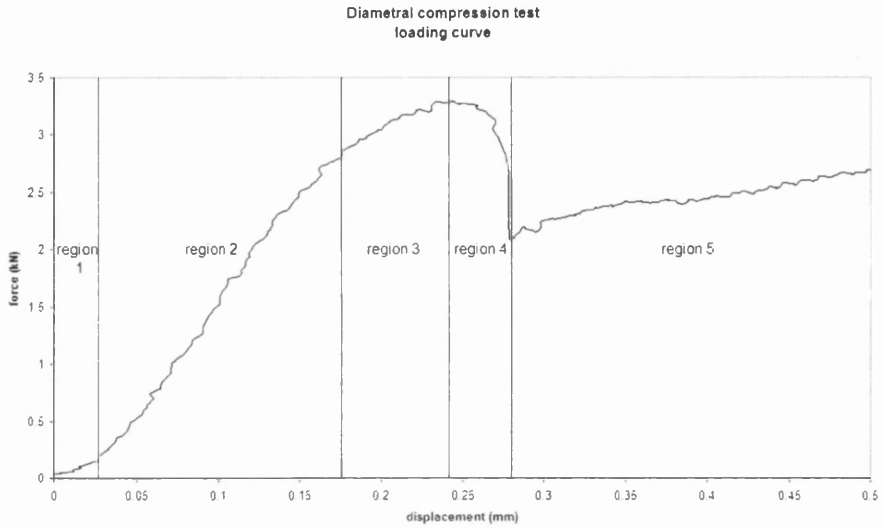

Figure 3.32: Typical loading curve for a Brazilian disc test.

the compact's response to the imposed platen displacement remains linear. This highlights the difference between what happens locally, where stress concentration may occur, and the overall characteristic of a component. A technique based on a linearity interval devised in the previous section can be employed to define the yield point of the compact. This technique was used on the force-displacement curves with a 3% interval. Such a large interval is required because of the noise in the collected data. Unlike the materials that are conventionally seen as continua, the granular nature of the material remains here and induces irregularities in the component's response so the technique needs to be adapted. The results from this measurement are later contrasted with the onset of fracture obtained from the observation of images acquired with a high speed digital camera during the test. In both cases, the stresses can be calculated using the analytical solution either by Hertz or Hondros. The third stage of the test is non-linear again as the compact gives way. This third stage is also subject to interpretation. It can be seen as the stable growth of the crack as suggested by Jonsèn or it may be a plastic phenomenon [Jon06]. It is likely to be more complex even with both phenomena occurring at the same time.
Finally, in region 4 the compact collapses completely and the force falls away when imposing further displacement. The maximum load reached during this test can be

used to verify the consistency of the properties of the compacts. It can be particularly useful to compare the repeatability of the maximum, which reflects an overall property of the samples, and the spread in the failure data, which can be seen essentially as a statistical indicator as it is linked to the weakest point of the compact. It is therefore also a measure of the consistency in the compaction of the test samples. Jonsèn identified a fifth region in which each half of the failed disc is then reloaded [Jon06]. This evidently is subject to the stability of each half of the compact once it has split and this rarely occurred in the present work as most of the split compacts' halves rolled onto their side. Thus this region does not always yield meaningful data.

The relationship between the evolution of stresses and the appearance of cracks can be unclear. As the loading curves combined with the detection of fracture initiation, shown in Figures 3.33 to 3.36, indicate, fracture begins earlier than the start of the stage considered as that of crack growth indicated in Figure 3.32, making the interpretation of the test from the loading curves difficult. Finally the images recorded can also give an insight into the mechanisms of fracture by defining the location of the crack initiation. Procopio *et al.* showed with simulations that if plastic yielding occurs, the stress concentration will be shifted along the compressed diameter [PZC03]. In the experimental context, however, local defects can influence the actual point of crack initiation. Figures 3.33 to 3.36 show the loading curves from each test and include a point that indicates the detection of fracture on the recorded images.

The maximum load sustained by the compacts (Figure 3.37) shows that the data is homogeneous despite evidence of damaged compacts in figures 3.34, 3.35 and 3.36[1].

The points when the linearity condition at 3% deviation is breached were noted and the corresponding values of the tensile stress at the centre of the compact were calculated using the Hertz solution and are plotted in Figure 3.38 as the yield condition. This figure shows that the detection of fractures from the images gives failure

[1]Compacts believed to be faulty show a loading curve with important saw-toothed irregularities, probably due to the powder failing around the contact area. The data series 57, 6.0g/cc, shows the variability of the experimental process as it failed with a fracture originated in the centre of the compact as predicted by the theory but very early in the test under a low force. This early failure may be the result of a fault in the compact material introduced during compaction or handling resulting in localised stresses.

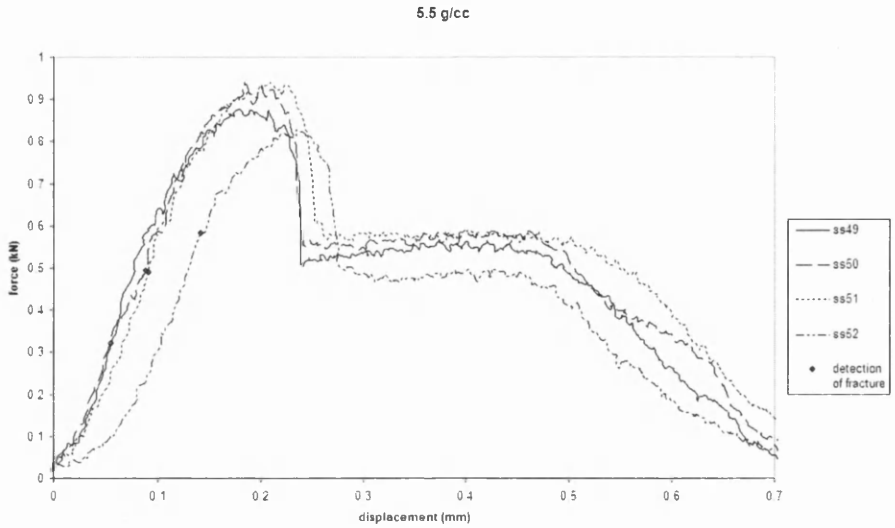

Figure 3.33: Loading curves for the ferrous samples at 5.5g/cc with detection of failure from images.

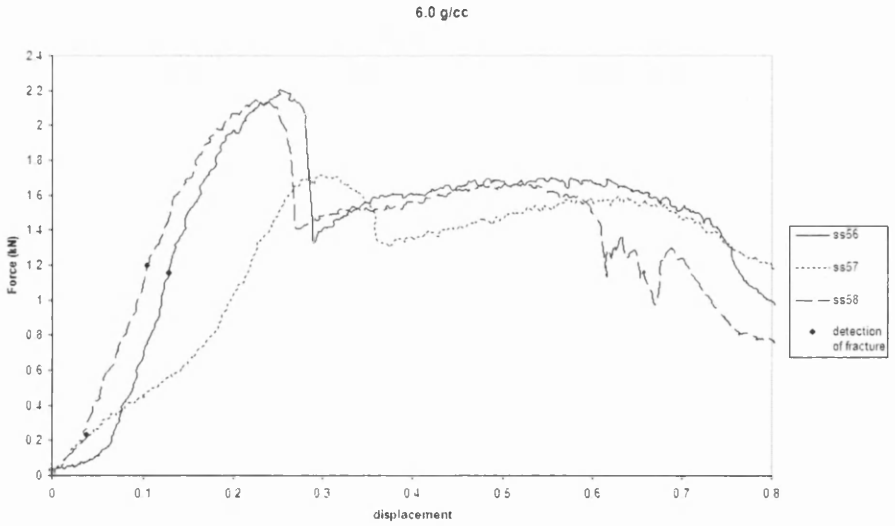

Figure 3.34: Loading curves for the ferrous samples at 6.0g/cc with detection of failure from images.

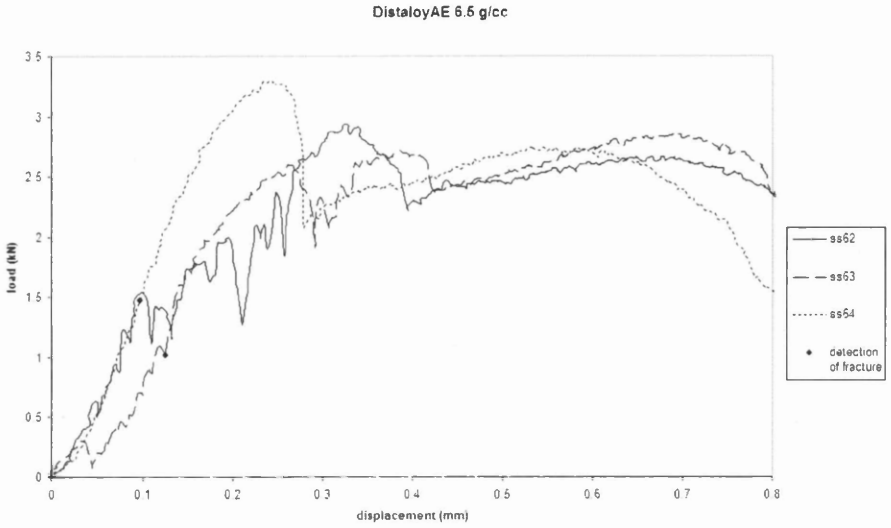

Figure 3.35: Loading curves for the ferrous samples at 6.5g/cc with detection of failure from images.

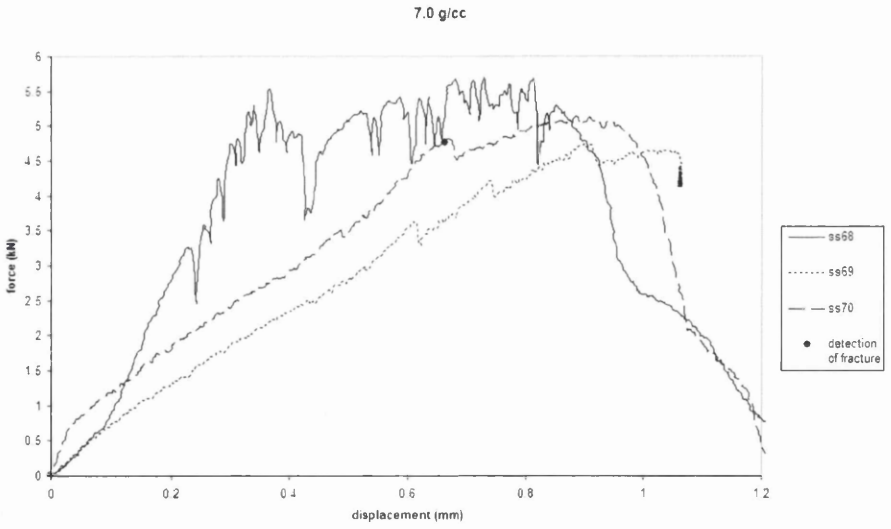

Figure 3.36: Loading curves for the ferrous samples at 7.0g/cc with detection of failure from images.

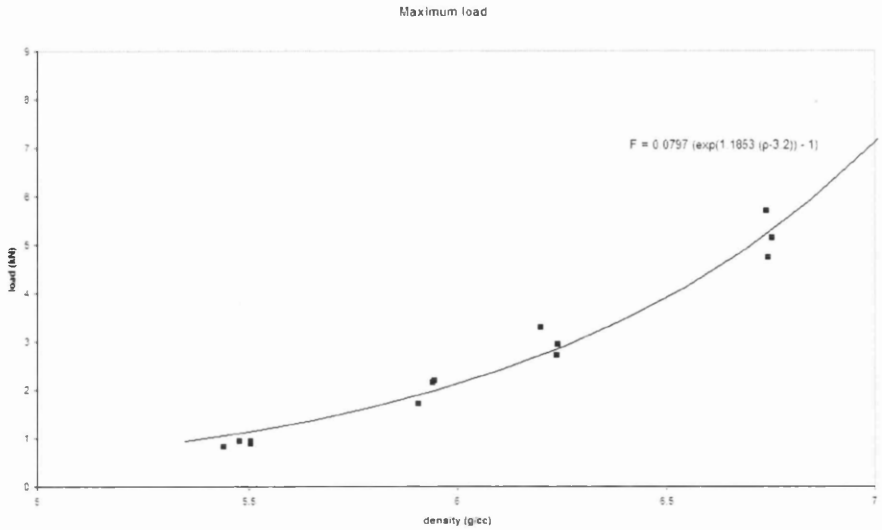

Figure 3.37: Maximum load in the Brazilian disc test.

points before the linearity criterion is breached, plotted as the fracture initiation stress. Consistently, the tensile stress derived from the fracture initiation obtained from image analysis falls below the value derived from the loading curve analysis. The values of the stresses derived from the contact models are only applicable to the non fractured component, therefore this comparison is only valid in order to evaluate both methods, as it is shown that the compact is already fractured when it reaches the yield limit at the upper end of the linear interval.

The values presented above have been calculated by a method which assumes a point load. In contrast, the calculation according to Hondros requires knowledge of the contact area or loading angle. This is retrieved from the images by a pixel count, and then used as a ratio of the number of pixels at the contact to the number of pixel across the diameter of the compact. The results are shown in Table 3.9. As can be expected, the contact area decreases with the increasing stiffness of the compact when the density is higher. The ratios between the stresses obtained by Hertz and Hondros are calculated as set out in equation 3.9 and plotted in Figure 3.29.

The variation between the different contact cases are very small. The largest difference in the tensile stress at the detection of failure is less than 5%, which is negligible

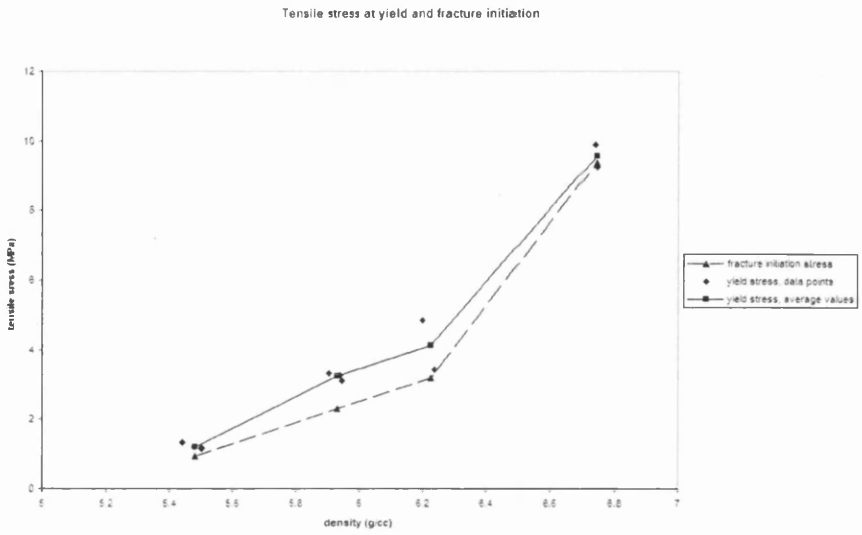

Figure 3.38: Maximum load in the Brazilian disc test.

compared to the variability of the measurements between samples (typically around 20%).

The variability of the load at which cracks occur compared to the good repeatability of the test with regard to the maximum load supported by the compact highlights the statistical nature of fracture initiation. Figure 3.39 sums up the different criteria and the variability in the ratio between the crack initiation load and the maximum load between 50% at low density and 91% at high density. The use of the maximum load to calculate the tensile strength of the ferrous samples is therefore inappropriate at low densities as it grossly overestimates it.

3.3.5 Results for an Alumina Powder

The Brazilian disc test on alumina samples provides an insight into the behaviour of a typical ceramic powder. The components exhibit a linear elastic behaviour, which is the major part of the loading curve, and the force then drops suddenly. This is shown in figures 3.40 to 3.43. It indicates a brittle behaviour of the powder. The tensile stress reached at the centre of the compact is lower than 1MPa, which shows

Table 3.9: Details of the contact widths measured from the images and related change in the maximum calculated tensile stress for ferrous samples.

density	test	contact width/radius $\approx \alpha$ (rad)	$\frac{\sigma_{tHondros}}{\sigma_{tHertz}}$
5.0g/cc	49	0.172	0.96
	50	0.201	0.95
	51	0.190	0.95
	52	0.187	0.95
6.0g/cc	56	0.148	0.97
	57	0.139	0.97
	58	0.117	0.98
6.5g/cc	62	0.118	0.98
	63	0.116	0.98
	64	0.135	0.98
7.0g/cc	70	0.087	0.99

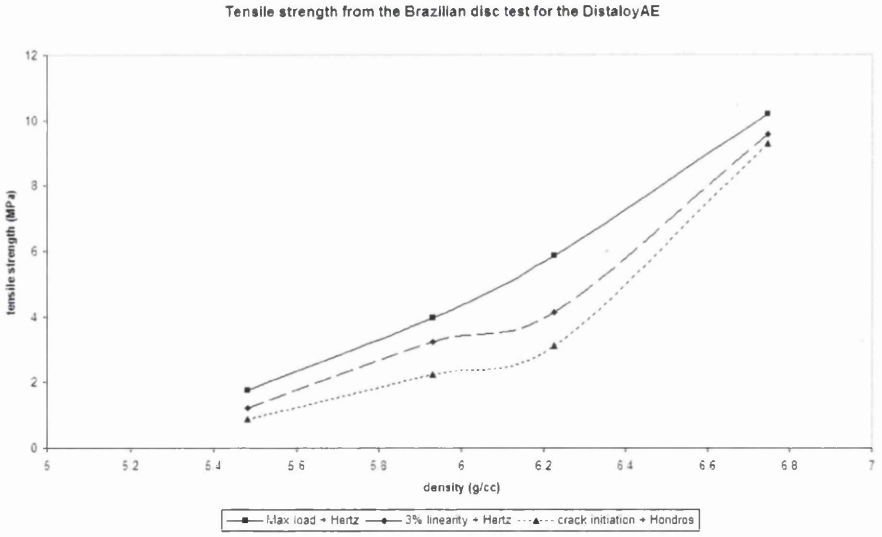

Figure 3.39: Maximum tensile stress for different criteria applied to ferrous sample tests.

that this powder does not achieve strong interparticle bonds.

The images show that fracture occurs when the load is close to reaching its

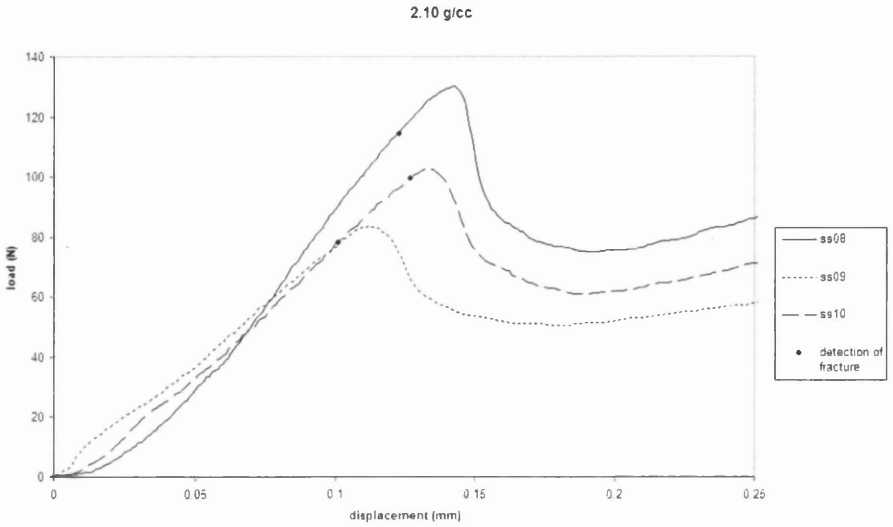

Figure 3.40: Loading curves for the alumina samples at 2.10g/cc with detection of failure from images.

maximum. The non linear region of the loading curve is very short, making it very difficult to identify a crack growth period. The images confirm this by showing a very fast growth of the crack line. It only takes 10 ms from the detection of the initial fracture to the moment when the crack is shown along the whole diameter of the sample. The frequency of the data acquisition system was 50Hz, so within the resolution of the equipment, the propagation of the crack can be considered instantaneous. The maximum load indicates a good correlation with the density from 2.17g/cc (Figure 3.44). It is also apparent that because the alumina powder is very light with a tap density of 0.9g/cc, any inaccuracy when weighing the amount of powder used to produce the samples has a proportionally large impact on the final density of the compact. It is therefore more appropriate to consider the data as individual data points covering a density range than in groups with a nominal density as was done with the DistaloyAE powder.

The yield of the component can be detected by using the linearity interval technique, previously exposed. The threshold was set to $\pm 1.5\%$. It is lower than in

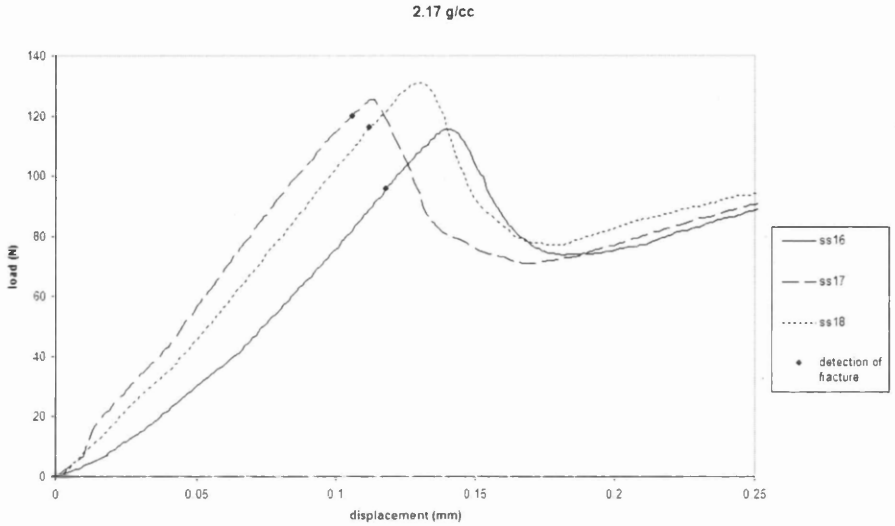

Figure 3.41: Loading curves for the alumina samples at 2.17g/cc with detection of failure from images.

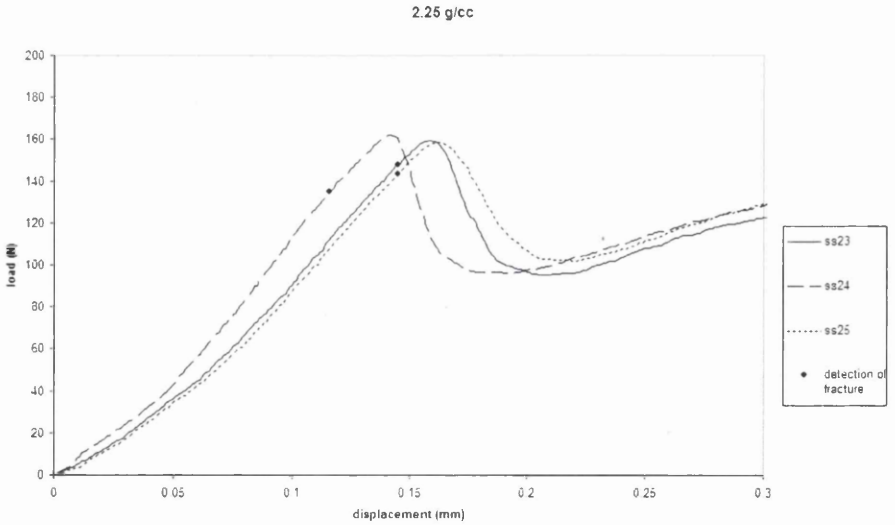

Figure 3.42: Loading curves for the alumina samples at 2.25g/cc with detection of failure from images.

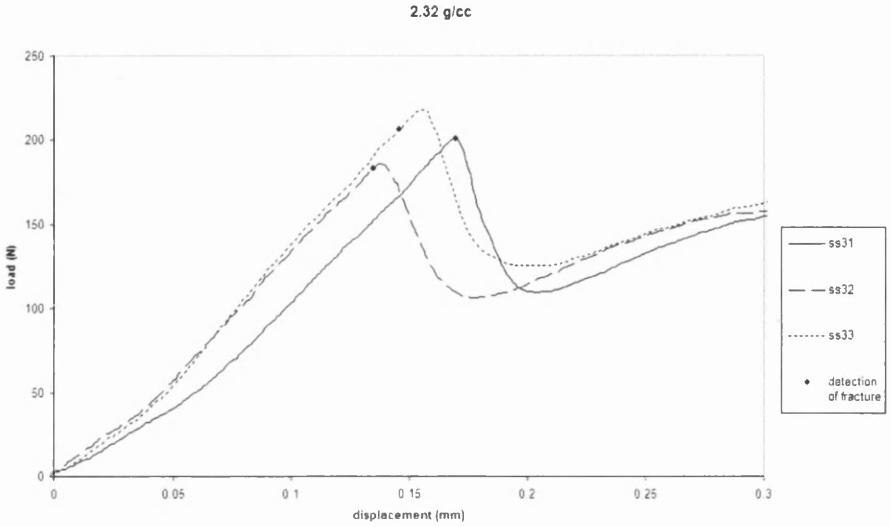

Figure 3.43: Loading curves for the alumina samples at 2.32g/cc with detection of failure from images.

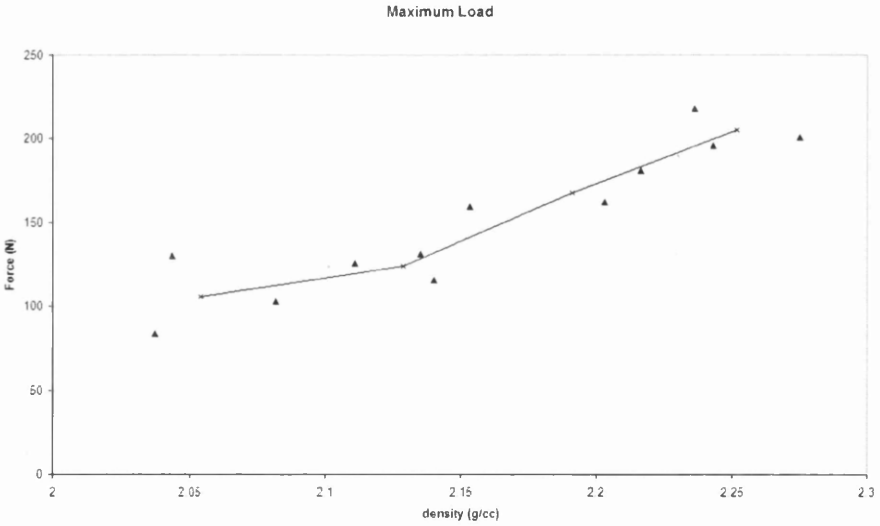

Figure 3.44: Maximum Load with data and averages grouped by nominal density.

the study of the ferrous powder due to the absence of noise. Despite the lower threshold, the yield stress is within 1% of the maximum load in 10 out of 12 cases, with exceptions at 2.216 g/cc and 2.243g/cc where the yield of the component was calculated respectively at 86.7% and 94.6% of the maximum load (Figure 3.45). It is also visible that the functions fitted to the maximum load and the fracture load can be correlated by a factor of 0.9.

The study of the contacts shows that a decrease in the contact area occurs with

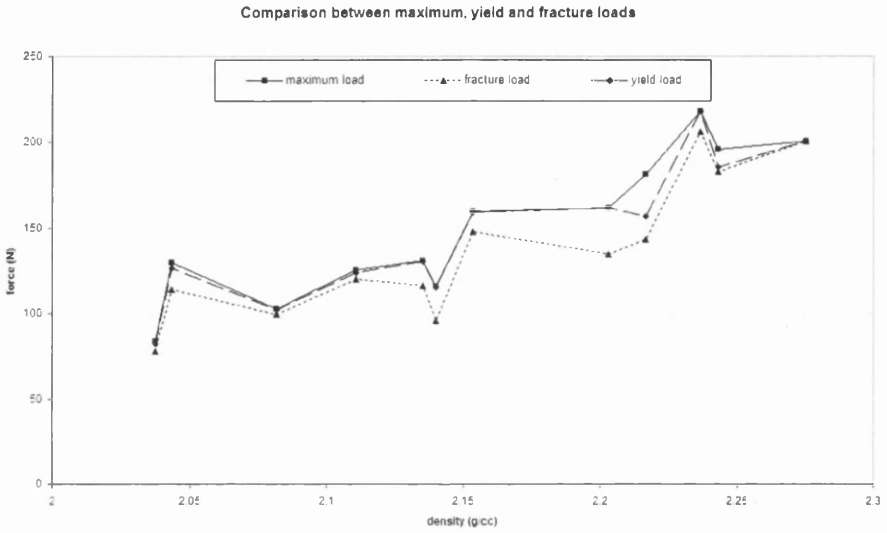

Figure 3.45: Compared values found for the maximum, yield and fracture loads for the alumina samples.

rising density but it is less marked than in the case of the ferrous powder (Table 3.10). The largest contact has a measured width of 12.2% of the compact's diameter at 2,04g/cc and the smallest contact has a width of 9.1% of the compact's width at 2.15g/cc. Such small contact areas result in a very small difference between the tensile stresses calculated by Hertz's and Hondros's solutions. All variations arising from changing the calculation method are within 2%. Figure 3.46 summarises the different value of the tensile strength found from the diametral compression test with different criteria. It shows again that using the apparent yield of the component or the maximum load gives very close values for the brittle alumina powder. The fractures however appear consistently before yielding is observed at 90% of the

maximum load on average. The ratio between the maximum load and the fracture initiation load is however difficult to characterise as it varies between 79% and 100% without clearly identifiable trends.

Table 3.10: Details of the contact widths measured from the images and related change in the maximum calculated tensile stress for alumina samples.

test	density (g/cc)	contact width/radius $\approx \alpha$ (rad)	$\frac{\sigma_{tHondros}}{\sigma_{tHertz}}$
9	2.037	0.116	0.98
8	2.043	0.122	0.98
10	2.082	0.120	0.98
17	2.111	0.104	0.99
18	2.135	0.096	0.99
16	2.140	0.107	0.98
23	2.157	0.091	0.99
24	2.203	0.099	0.99
25	2.216	0.097	0.99
33	2.236	0.103	0.99
32	2.243	0.108	0.98
31	2.275	0.099	0.99

3.3.6 Discussion

The study of DistaloyAE and alumina by the diametral compression test highlights the difference in behaviour between these powders. DistaloyAE has very distinct non linear regions at the start and the end of its loading curve, whereas with alumina, those regions are smaller in extent. This shows that the ferrous compacts are ductile and subject to yield in regions where high compressive stresses develop. The alumina samples, on the other hand, have a brittle behaviour and reach fracture without large plastic deformations taking place throughout the compact. This observation is supported by the propagation of the fractures in the compacts. In the alumina compacts, the fracture initiation occurs when the load is close to its maximum, and the maximum is reached when the fracture is completely propagated through the

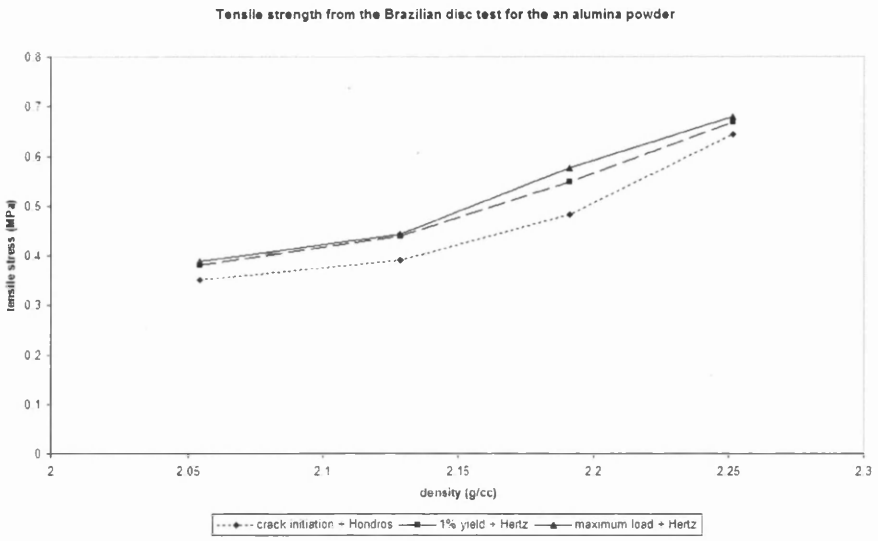

Figure 3.46: Maximum tensile stress for different criteria applied to alumina sample tests.

compact along the diameter. When the load reaches its maximum value in the case of the ferrous compacts, a wedge shaped region has appeared with a base at the contact with the platens and pointing to the centre of the sample. This indicates shear is present and additional fractures are taking place. The stress distribution predicted by Hondros shows that the horizontal stress component along the vertical diameter is not positive from the centre to the contacts. Instead it becomes negative at a radius dependent on the contact angle. The videos show a good correlation with this prediction: the ferrous samples develop a wider contact area and the tension fracture does not propagate totally across the samples. Instead they meet the shear fractures, and each half of the compact is split (Figure 3.47). In the case of the alumina compact, the fracture goes all the way to the top of the compact, which is consistent with a smaller contact angle (Figure 3.48).

These results show that the non linearity in the third region of the loading curve (Figure 3.32), is not related to the growth of the tensile fracture but to its widening and the evolution of the contacts.

Although in this series of tests no particular measure was taken to prepare the contacts with the platens, the tensile strength values for the DistaloyAE discs are

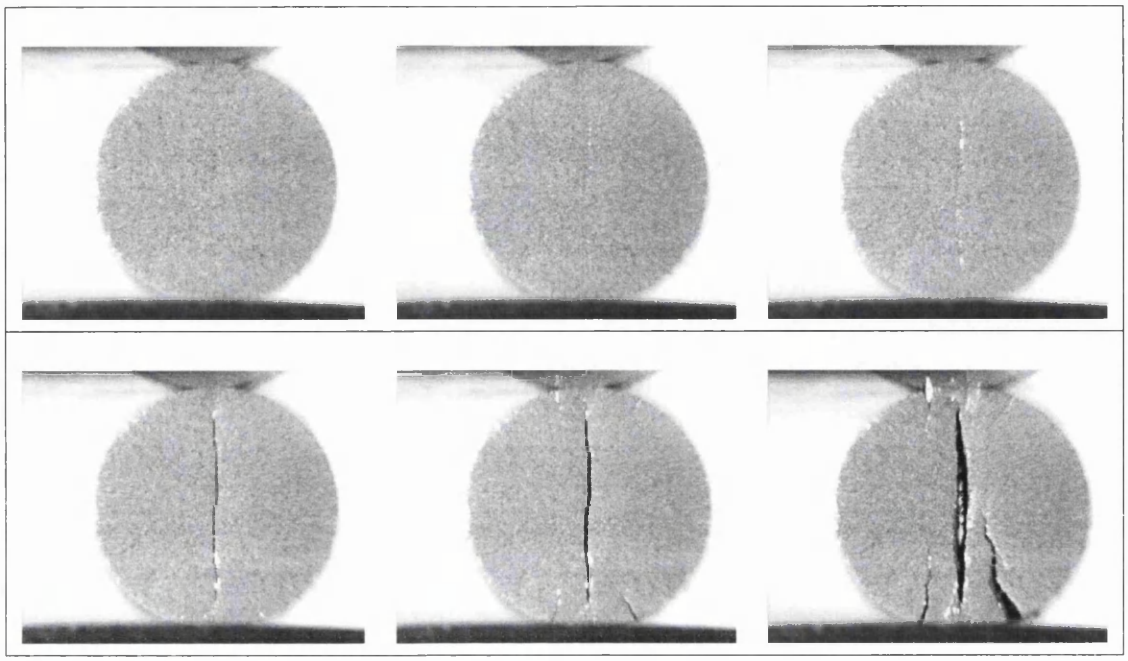

Figure 3.47: Fracture growth in a DistaloyAE sample

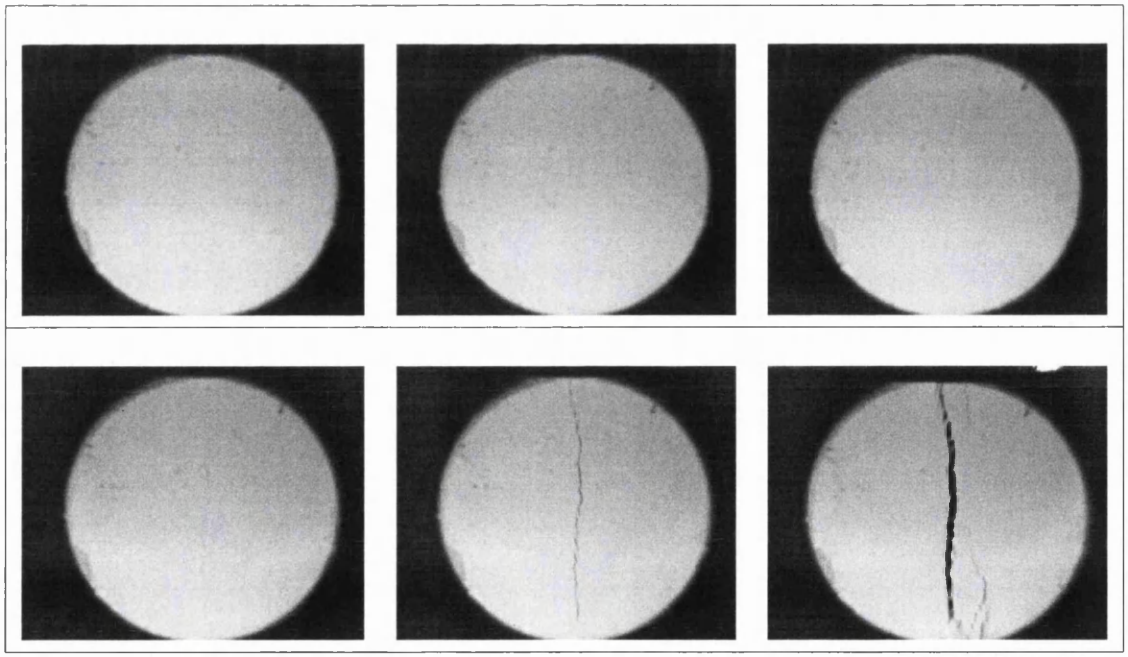

Figure 3.48: Fracture growth in an alumina sample

very close to results found by Dorémus and Jonsèn, who prepared the contacts, as shown in (Figure 3.49) [Dor03, Jon06].

In this series of tests, the development of the image analysis technique by image

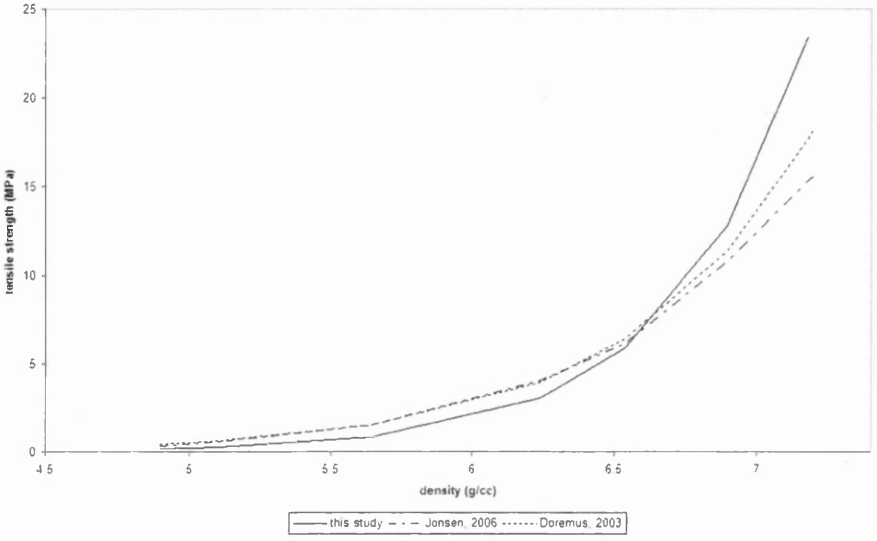

Figure 3.49: Comparison between the results obtained in this work and previous studies.

subtraction proved very useful, as it can show a fracture that may not be visible on the original image. This can be due to the thickness ratio of the samples. The fracture may start invisible from the filmed end of the compact but a displacement in the face of the compact changes the reflection of the light on its surface and can be easily detected by the image subtraction technique. This is illustrated below with the original picture and the resulting image processed by the brightness subtraction technique (Figures 3.50). The saturation multiplies the brightness difference found between the picture at the start of the test and the analysed picture. In some cases, the result is out of range, it is then plotted white.

The Brazilian test is a test that is difficult to interpret due to the complexity of the stress distribution generated within the sample. It has been shown that in the context of powder characterisation, a good correlation is obtained in the results between the stresses at the centre of the compact when the component's behaviour

(a) Image captured at time t

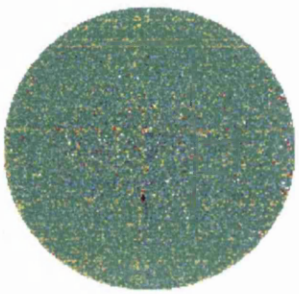

(b) Image at time t subtracted from the image at the start of the test — saturation 15

(c) Image at time t subtracted from the image at the start of the test — saturation 50

(d) Image at time t subtracted from the image at the start of the test — saturation 100

Figure 3.50: Results from the use of different saturation levels

becomes non linear and the onset of fracture. This correlation holds in the cases of brittle and ductile powders. However, two observations must be made regarding the test. First, the results of the tests are certainly influenced by the anisotropy of the compact due to uniaxial compaction. Further literature on the effects of material anisotropy is available in Korachkin's thesis [Kor06]. Also,the stresses induced by diametral compression imply that Lode's angle is not zero. The consequences of this are investigated further in Chapter 4 with the development of a three-invariant model and a study of its impact on the resulting stresses in the compacts.

3.4 Instrumented Die Test

The die compaction test consists of the uniaxial pressing of a cylindrical compact. It has been used to characterise powder for several years and is well documented in the literature. It is now a proven and reliable technique to calibrate constitutive models under the conditions of closed die compaction. It was used in this study to obtain a consistent data set, in which all the information was collected from the same batch of material. This is why data was recorded as the samples were prepared for the unconfined and diametral compression tests. The instrumented die technique was used for the development investigation but not developed further than already reported in the literature, therefore only the results are exposed and for further details, the reader is referred to the review in Chapter 2 or the literature readily available [GTG+01, Cam00, Kor06].

The radial and axial stresses are retrieved from the data acquisition system as well as the displacement of the punch. The effects of friction are taken into account by measuring the load at the top and at the bottom of the compact and with information from the shear plate experiment documented by Cameron and Korachkin [Cam00, Kor06]. However, friction is considered to have a negligible impact on the density distribution for this particular experiment and the density of the compact is therefore calculated from the volume and the mass of the powder in the die.

The model is based on a formulation in the hydrostatic deviatoric plane, so this is the format in which the data is used. Figure 3.51 shows the evolution of the hydrostatic stress, P, with density (also know as pressure or mean stress). The relationship

between the pressure and the density for the DistaloyAE was established, in the present work, by curve fitting as:

$$P = 35.056\left(e^{0.734(\rho-3.84)} - 1\right) \tag{3.10}$$

Plotting the deviatoric and hydrostatic stresses shows an equally good repeatability (Figure 3.52). The hydrostatic and deviatoric stresses can be related by:

$$Q = 172.651 \tanh\left(\frac{0.769P}{172.651}\right) \tag{3.11}$$

The equations 3.10 and 3.11 were obtained by curve fitting after inspection of the

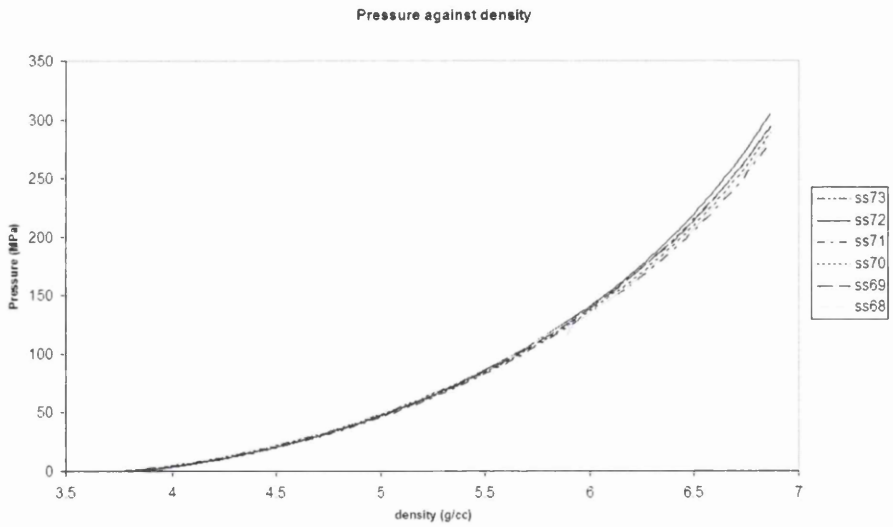

Figure 3.51: Pressure against density for DistaloyAE in a die compaction.

experimental data and the coefficient were calculated by the least square method. Figure 3.53 shows the resulting characteristic curves for a uniaxial compression test. The match between the experimental values and the fitted curve is considered very good, with a match within 5% from a density of 4.2g/cc.

The Alumina powder has a behaviour which is typical of brittle powders. First a phase of deformations at low stresses occurs followed by a sharp increase in the pressure as the density rises (Figure 3.54). This type of behaviour was reported by

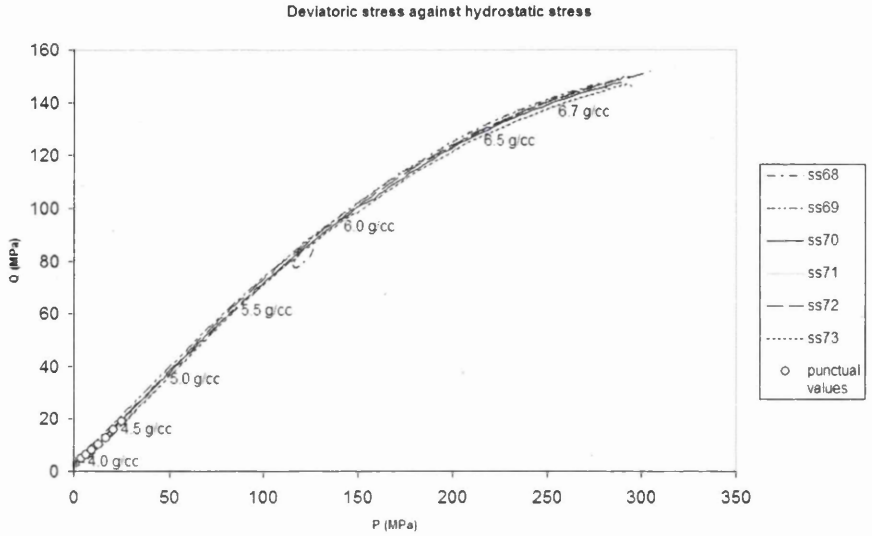

Figure 3.52: Deviatoric stress against pressure for DistaloyAE in a die compaction.

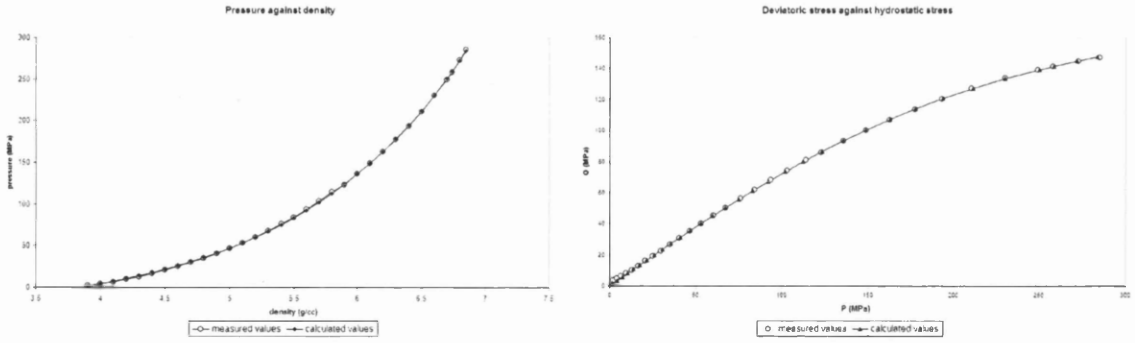

Figure 3.53: Characteristic curves for DistaloyAE in a die compaction.

Guyoncourt but with application to zirconia powder [GTG+01]. The data recorded experimentally is more scattered than in the ferrous case with 6% deviation on average, with a maximum of 11.7% at 2.3g/cc.
To describe the pressure-density relationship in alumina, a different form was used for the equation, from the one employed in the case of the ferrous powder:

$$P = 0.0356\,(\rho - 0.295)^{14.223} + 1.615 \tag{3.12}$$

It is notable that the best form for the equation is cannot be assumed *a priori*. It must be adapted for the material studied, for example, the present study highlights the difference in behaviour between the ferrous and the ceramic powders with the use of an exponenial equation for the former material and a power law for the latter, to describe the pressure-density relationship. Hydrostatic and deviatoric stresses in the uniaxial test for the alumina powder are almost linearly related, as shown in Figure 3.55, it can be described by the function :

$$Q = 0.937P^{0.979} - 0.200 \tag{3.13}$$

Equation 3.12 reflects the evolution of pressure with density within 5%. The error

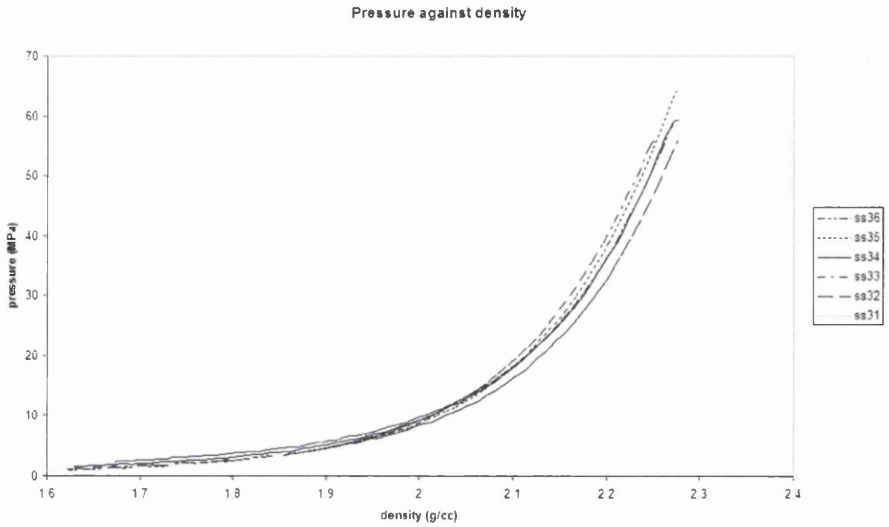

Figure 3.54: Pressure against density for alumina in a die compaction.

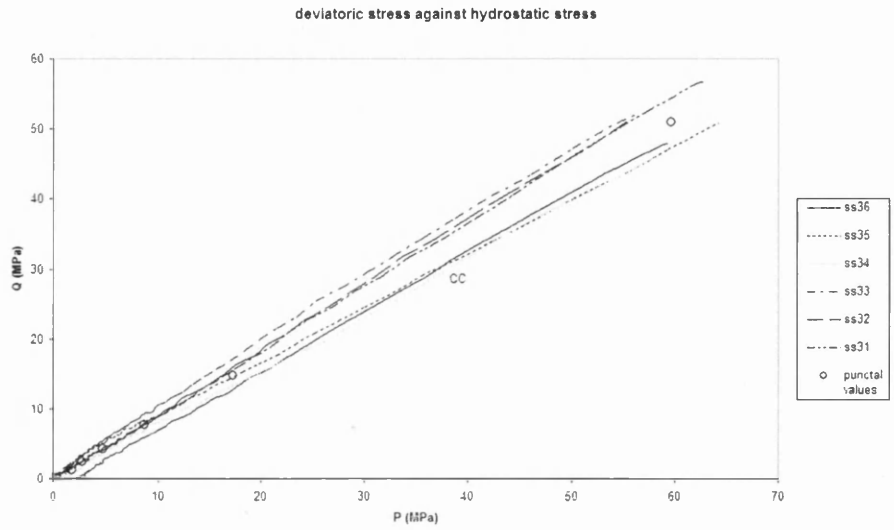

Figure 3.55: Deviatoric stress against pressure for alumina in a die compaction.

on the deviatoric stress, however varies greatly with the density range. At 1.68g/cc, the error is 44% and it decreases to 5% at 1.78g/cc. In absolute values, this only represents a 0.5MPa variation at 1.68g/cc and is caused by the curve fitting scheme, which emphasises accuracy at high densities. The match between the experimental data and the calculated values is shown in (Figure 3.56).

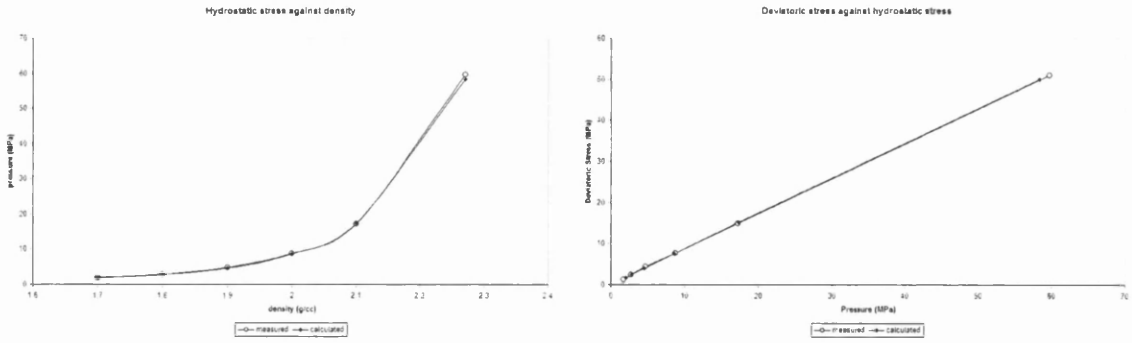

Figure 3.56: Characteristic curves for alumina in a die compaction.

3.5 Establishing the Yield Surfaces

The experiments introduced in the previous sections were chosen to characterise the behaviour of powders over a range of deviatoric and hydrostatic states of stress. From this information it is possible to derive a material model when the conditions of compaction deviate from the theoretical uniaxial compression path. A finite element code was developed at Swansea University for the simulation of powder compaction as a continuum. It uses a constitutive model based on elliptic yield surfaces defined in the plane of hydrostatic-deviatoric stresses. The yield function can be expressed as:

$$f = \frac{(P - P_1)^2}{P_0^2} + \frac{Q^2}{Q_0^2} - 1 = 0 \tag{3.14}$$

This model is a simplified implementation of the model proposed by Mosbah [MB96]. The provision for cohesion made in the original version was abandoned and the terms used for the hydrostatic coordinate of the centre of the ellipse and its hydrostatic semi-axis length are both equal to P_0 in the numerical version of the code. This configuration of the yield surface can easily be calibrated with the die compaction test. The results obtained from this model are good for the simulation of components manufactured in conditions close to uniaxial compaction [PM 99].
The coefficients can be calculated analytically from the experimental data by enforcing yield condition and the flow rule at the stresses recorded during the die compression test. The yield condition in the die compression test gives:

$$f = \frac{1}{P_0^2}\left(\frac{\sigma_z^D + 2\sigma_r^D}{3} - P_0\right) + \frac{\left(\sigma_z^D - \sigma_r^D\right)^2}{Q_0^2} - 1 = 0 \tag{3.15}$$

The superscript D indicates the values measured in the die compression test.
The flow rule is $\dot{\epsilon}^p = \dot{\lambda}\frac{\partial g}{\partial \sigma}$, in which is the plastic multiplier and g is the plastic potential. Because the tools are much stiffer than the powder, it can be assumed that the die is totally rigid, thus there is no radial deformation. The model used is associated, as calibration of a non associated model requires data about the plastic flow of the material, which is unavailable. Associating the plastic potential and the yield surface translate mathematically as $g = f$, therefore, in a closed die compaction,

the derivative is:

$$\frac{\partial g}{\partial \sigma_r} = \frac{\partial f}{\partial \sigma_r} = 0$$

$$\frac{\partial f}{\partial \sigma_r} = \frac{4}{3P_0^2}\left(\frac{\sigma_z^D + 2\sigma_r^D}{3} - P_0\right) + \frac{\left(\sigma_z^D - \sigma_r^D\right)}{Q_0^2} = 0 \tag{3.16}$$

From equations 3.15 and 3.16, the coefficients can be calculated:

$$P_0 = \frac{3\left(P^D\right)^2 + 2P^D Q^D}{P^D + 2Q^D} \tag{3.17}$$

$$Q_0 = \sqrt{\left(Q^D\right)^2 \frac{\frac{3}{2}Q^{D(P^D)^2}}{2P^D + \frac{2}{3}Q^D}} \tag{3.18}$$

Figures 3.57 and 3.58 however show that this model does not reproduce accurately the values found experimentally for the yield at low pressure.

It is possible to alter the shape of the yield surface to obtain a better match between experiments and the theoretical yield surface. This can be achieved by modifying its equation in the form:

$$f = \frac{\left(P - P_1\right)^2}{P_0^2} + \left(\frac{P - (P_1 - P_0)}{2P_0}\right)^n \frac{Q^2}{Q_0^2} - 1 = 0 \tag{3.19}$$

The choice of this equation form is motivated by the need to deviate from the ellitptic shape so that the apex of the curve may move in the hydrostatic direction. Khoei proposed a single surface cap model based on a quadratic function of the stress invariants, however its basis was not elliptic [Kho05]. This leads to the necessity to adopt limits in a computational implementation to avoid negative values of the deviatoric stress, which are not physically possible. The elliptic basis of the model proposed in this work avoids this problem.

The calibration of this model now requires the definition of four constants, P_0, Q_0, P_1 and n. This can be achieved by solving a set of equations that place each test on the yield surface A fourth equation can be obtained from the die compaction test. If the tools are assumed to be rigid, then no radial deformation takes place. In the

absence of radial stress, this gives: $\frac{\partial g}{\partial \sigma_r}$. The plastic potential, g, can be defined as:

$$g = \frac{(P - P_1)^2}{P_0^2} + \frac{Q^2}{Q_0^2} - 1 = 0 \tag{3.20}$$

This makes the model non-associated, however it simplifies the calibration by reducing the number of terms in the calculation of the derivative. A more complex function could not be exploited due to the lack of information on plastic potential. By making use of the coefficients from the yield function, it also ensures that the plastic potential is defined for all acceptable stresses.

This model was calibrated by using the yield conditions in the die compression test, the unconfined compression test (superscript C), the Brazilian disc test (superscript B) and the flow rule in the die compression test as objective function expressed in a vector form in equation3.21. From this, an optimisation routine was programmed to calculate the values of the coefficients with a Newton-Raphson scheme over a range of densities by solving for each considered density value:

$$\begin{bmatrix} \frac{(P^D-P_1)^2}{(P_0^D)^2} + \left(\frac{P^D-(P_1^D-P_0)}{2P_0}\right)^n \frac{(Q^D)^2}{Q_0^2} - 1 \\ \frac{(P^C-P_1)^2}{(P_0^C)^2} + \left(\frac{P^C-(P_1^C-P_0)}{2P_0}\right)^n \frac{(Q^C)^2}{Q_0^2} - 1 \\ \frac{(P^B-P_1)^2}{(P_0^B)^2} + \left(\frac{P^B-(P_1^B-P_0)}{2P_0}\right)^n \frac{(Q^B)^2}{Q_0^2} - 1 \\ \frac{\partial g}{\partial \sigma_r} = \frac{4(P^D-P_1)}{3P_0^2} - \frac{}{Q_{2Q^D}^2} \end{bmatrix} = \begin{bmatrix} 0 \\ 0 \\ 0 \\ 0 \end{bmatrix} \tag{3.21}$$

The resulting yield surfaces obtained for DistaloyAE and alumina powders are shown in Figure 3.57 and Figure 3.58. The difference in the low pressure region is noticeable, but there is also a significant change in the highest deviatoric stress that can be sustained by the powder. In the examples shown below, for DistaloyAE the difference in the highest admissible deviatoric stress at 5.1g/cc is 17.5% and 19.5% at 2.27g/cc for the alumina powder. These values correspond to a relative density of 0.65 in both cases.

The observation of the yield surfaces of the DistaloyAE and the alumina powder highlights the differences between the behaviour of ferrous and ceramic powders. The low pressure region of the ferrous yield surfaces are well developed resulting in

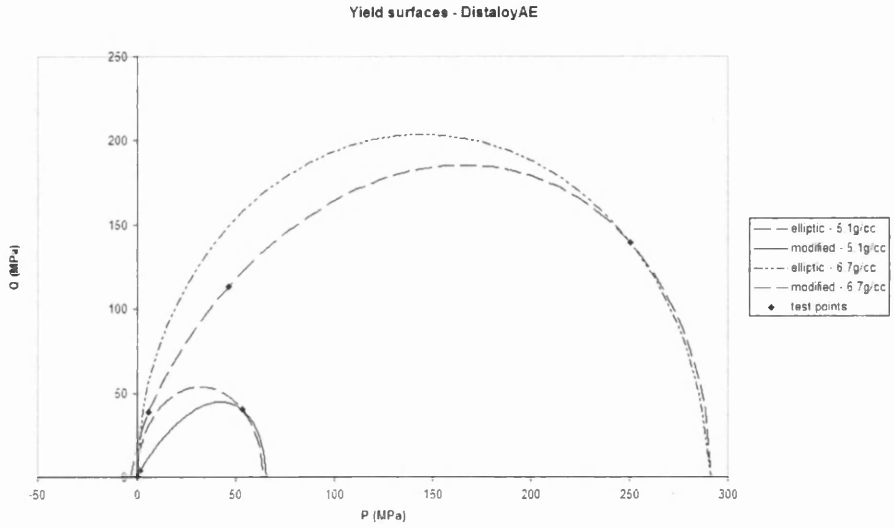

Figure 3.57: Yield surfaces for the DistaloyAE powder.

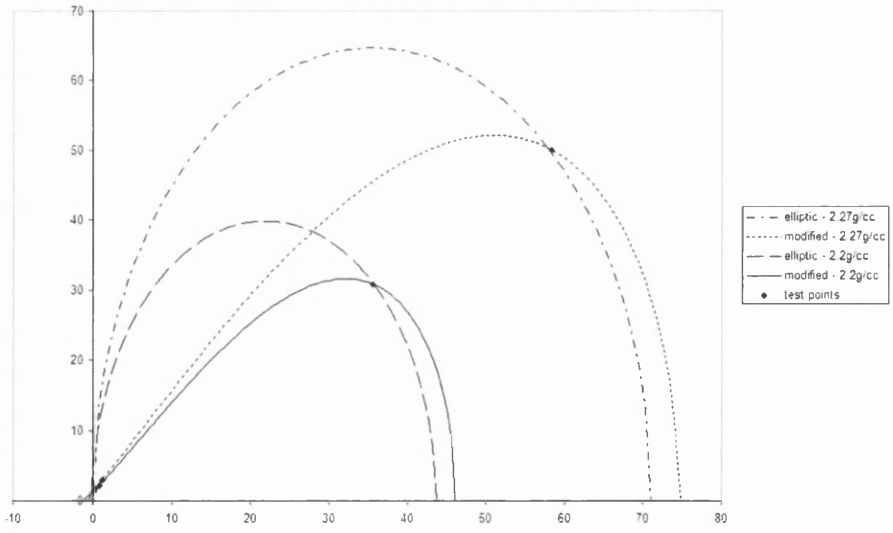

Figure 3.58: Yield surfaces for the alumina powder.

a nearly elliptic yield surfaces. Cohesion is also developed as density increases. On the other hand, there is very little variation between the low pressure region at low and high density for the alumina powder.

It is visible that the yield surfaces obtained are very different according to the material. the alumina powder exhibits a yield surface which can be suitably described by a model such as the Drucker-Parger model, in which the shear failure envelope and the compaction cap are described separately. The ferrous powder, however, seem to exhibit a more ductile behaviour under high deviatoric stresses in which the shear failure is not an appropriate representation of the phenomenon. Instead, an elliptic model is more appropriate, even though the present study shows that this could be refined. This is most likely caused by the range of relative density exploited in the compaction process. Ferrous powders are compacted to relative density of 0.9 or more and undergo little shrinkage during sintering. Ceramic powders, however are compacted to lower relative densities, typically 0.7 for alumina. The shrinkage during sintering is not negligible. The fragility of ceramic compacts in low pressure conditions is also observed in the data from Dorémus, in which a zirconia powder was tested [Dor03]. The deviatoric stresses achieved in the Brazilian disc test and unconfined compression test are respectively lower than 5% and 10% of the deviatoric stresses in the die compaction test. This is also true in the case of alumina. In the case of the DistaloyAE, for comparison, the ratio between the stresses in the unconfined compression test and the die compaction test is of the order of 80% and 30% for the Brazilian disc test.

Once the yield surface parameters have been calculated for a number of densities, a function may be fitted to define them over the density range investigated. The optimisation solver provided in Microsoft Excel was used to obtain the optimal match. The functions used are:

$$P_0 = K_1 \left(\ln \left(1 - \left(\frac{\rho - \rho_0}{\rho - \rho_{max}} \right) \right) \right)^{K_2} \tag{3.22}$$

$$P_1 = K_3 \left(\ln \left(1 - \left(\frac{\rho - \rho_0}{\rho - \rho_{max}} \right) \right) \right)^{K_4} \tag{3.23}$$

$$Q_0 = K_5 \tanh \left(\frac{K_6 P_0}{K_5} \right) \tag{3.24}$$

$$n = K_7 \left(e^{K_8(\rho - \rho_0)} - K_9 \right) \tag{3.25}$$

The coefficients are K_0 to K_9. The limit densities rho_0 and ρ_{max}, can be specified as the loose powder density and the solid density. They can also be considered as variables to improve the correlation between the equations and the experimental data. The evolution of the coefficients defining the yield surfaces is illustrated in Figure 3.59 for the DistaloyAE and in Figure 3.60 for the alumina powder.

It is interesting to note the evolution of the cohesion of the powder measured

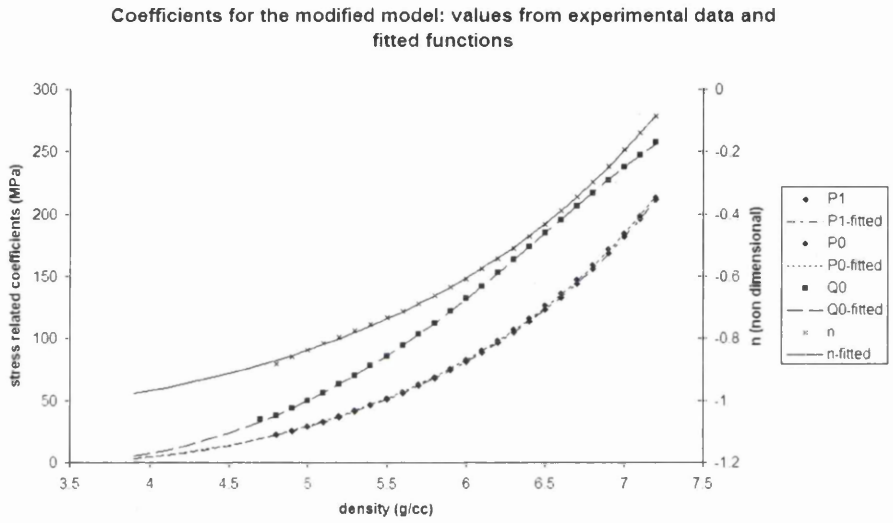

Figure 3.59: Model parameters against density for the DistaloyAE powder.

as the pure hydrostatic stress at yield. A comparison with a modified CamClay model in which the centre and the hydrostatic semi-axis are independent (equation 3.14) shows the inability of a simple ellipse, as proposed by Mosbah, to reflect cohesive properties with a calibration from the diametral or unconfined compression test. When calibrated against either low pressure test, the elliptic model does not develop any cohesion. Figures 3.61 and 3.62 show the evolution of the intersection between the yield surface and the pressure axis at the tensile end of the yield surface, respectively for the DistaloyAE and alumina powders. The pressure is considered positive in compression and the plots show that with a modified CamClay model as expressed in equation 3.14, the powder cannot sustain low compressive stresses any

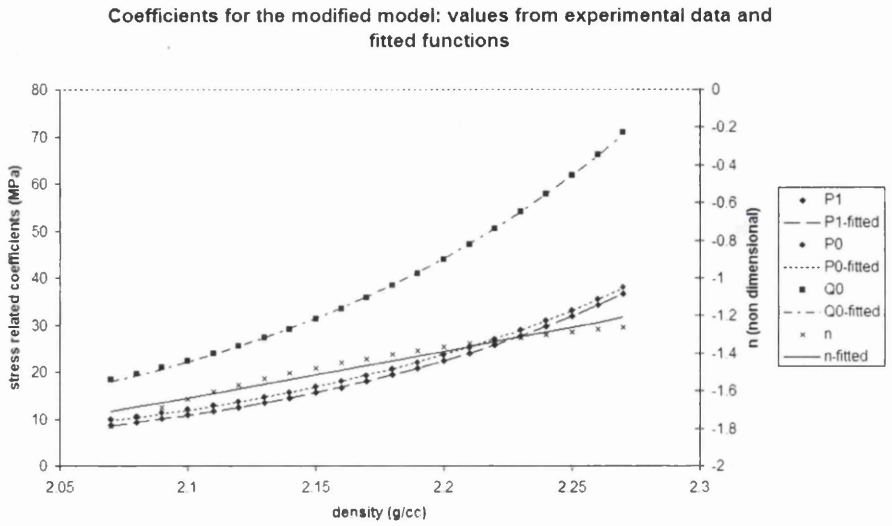

Figure 3.60: Model parameters against density for the alumina powder.

more, as density grows. This cannot be upheld as a valid model and justifies the use of a model without a cohesion term when the simple elliptic shape of the modified CamClay is chosen. In some cases, the cohesion does not follow a monotonous evolution. This is due to the calibration method. Instead of a direct measurement of the cohesion, the intersection between the hydrostatic axis and the yield surface is governed by the growth of the surface in the hydrostatic and deviatoric direction. This makes the evolution of cohesion a difficult parameter to control in the studied models with the available calibration data.

This study demonstrates the ability of the modified elliptic model proposed in this chapter to reflect the yield behaviour of the studied powders at low pressure and to develop cohesion as the density increases. More tests can be carried out to obtain more complex yield surfaces but it is interesting to keep the model simple for usability. Four parameters are used to describe the yield surfaces. They may be described by very complex functions requiring many material constants. However this is only a curve fitting exercise, which can be carried out by modern spreadsheet programs.

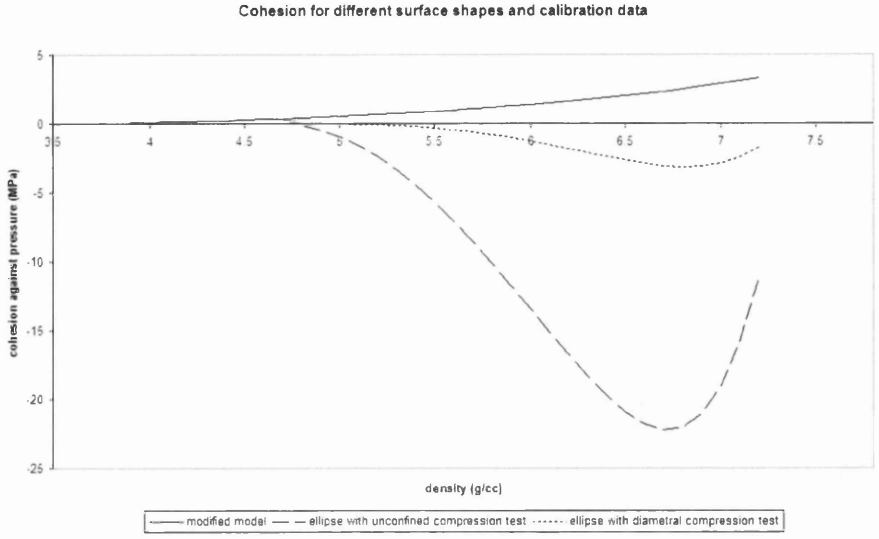

Figure 3.61: Cohesion for the DistaloyAE powder calibrated for the modified Cam-Clay and the *skewed elliptic* model with the experimental data from the present work.

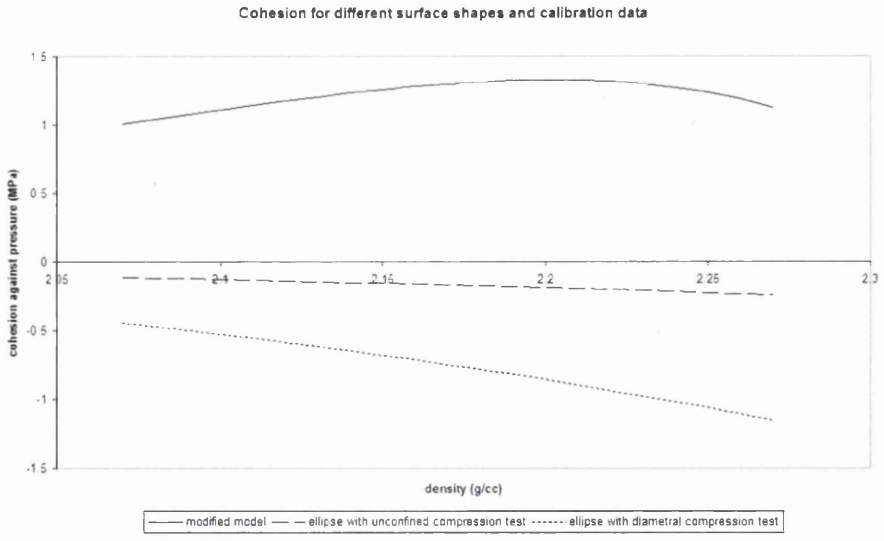

Figure 3.62: Cohesion for the alumina powder calibrated for the modified CamClay and the *skewed elliptic* model with the experimental data from the present work.

3.6 Closure

In this chapter, a new formulation for the yield surface of compacted powders was derived. It is able to reflect more accurately the behaviour of powders yielding under low pressure. The new formulation compares favourably with the modified CamClay formulation. The new formulation is capable of assuming a shape close to that of a Drucker-Prager model when required (with the alumina powder for instance) but can also keep a shape close to an ellipse to represent the yield behaviour of a ferrous powder. As a single surface model, it also simplifies an eventual computational implementation, as highlighted in Chapter 2.
To obtain the information necessary to devise the new constitutive model, an experimental investigation was carried out. The use of high speed image capture combined with the developed image analysis technique to detect fracture in the Brazilian disc test and to measure radial strain in the simple compression test, showed that the data reduction solely from the loading curves is insufficient in most cases. It did show that the Brazilian disc test can be analysed from the loading curves only in the case of brittle materials like the alumina samples. This can be interpreted as the consequence of the rupture under tensile stresses in a material which develops little cohesion and highlight a much greater pressure dependency in the alumina samples than in the ferrous components. Image processing is shown to be a good measurement tool to avoid contact measurement methods as green compacts are very fragile.

Further investigation can be suggested to improve the knowledge of the powder behaviour. In particular, a series of tests in a shear box could give an insight into the shape of the yield surface in the intermediate pressure range. Although anisotropy is certainly developed in the powder properties by the uniaxial compaction process, it was not investigated in the present study, which focuses on the characterisation of the yield surface. It would be of interest to quantify its impact, which can be expected to vary according to the type of powder.

Chapter 4

Study of the influence of the Lode Dependency in Powder Compaction

4.1 Introduction

A variety of constitutive equations are used in the literature to model the behaviour of powders in the compaction process. A set of constitutive equations for a classical elasto-plastic formulation consists of a yield surface, which sets a limit on the elastic domain for stresses and a flow rule, which defines the direction of the plastic material deformation. Associated models are the general rule in powder compaction modelling, which means that the plastic potential function and the yield function are coincident in the stress domain. Their formulation is based on the use of the first stress invariant and the second deviatoric invariant, with few exceptions [Kho05]. These formulations reflect the pressure dependency of the yield properties of powder. However, when friction and complex geometries are introduced in a component, the uniaxial state of deformations in the components is not upheld [CR00]. This can exacerbate the three dimensional variations that exist within the part and hence the neglect of the third deviatoric stress invariant may be important. This may be particularly important for more complex multilevel and three dimensionally shaped components.

Experiments in the field of geomechanics and concrete show that in three dimensional states of stress, the strength of porous and granular media cannot be reduced to two variables. In particular, the third deviatoric stress invariant influences the shape of the yield surface. Its impact is generally introduced by means of the Lode angle, defined in Figure 4.1.

In a comparison of numerical simulations with experiments, Mosbah *et al.* showed that good results were obtained in the compaction of cylindrical components, but residual stresses after unloading and ejection forces are found to be higher than the experimentally measured values [MB96]. At the time, this was attributed to the influence of the third deviatoric stress invariant. An experimental investigation followed these conclusions, which deduced that the Lode angle has an influence on the admissible stresses in elasto-plastic deformation, and this was further confirmed by Shima [MKSK97, SK98]. Both works lead to the conclusion that the use of a two invariant formulation for plasticity modelling was incomplete but did not directly attribute the high stress levels observed in computational results to the influence of the third deviatoric invariant. The present work builds on the existing modified CamClay model developed at Swansea University to include the dependency on the third deviatoric invariant through the Lode angle and investigate its impact on the compaction and ejection. First, the previously existing model is introduced and the modifications to include the third deviatoric stress invariant brought to the code are exposed. Both models are then examined to evaluate their performance and solutions.

The constitutive equations used to model the behaviour of powders are generally based on the pressure and the deviatoric stress. They are linked to the stress invariants by the following relationships:

$$I_1 = -3P \tag{4.1}$$

in which P is the pressure positive in compression and the first stress invariant:

$$J_2 = \frac{Q^2}{3} \tag{4.2}$$

in which Q is the deviatoric stress and $J_2 = \frac{\bar{\sigma}_{ij}\bar{\sigma}_{ij}}{2}$ is the second deviatoric invariant. The deviatoric stresses in a matrix notation are given by:

$$\bar{\sigma}_{ij} = \sigma_{ij} - \frac{I_1}{3} I_{ij}$$

where I is the identity matrix. The third deviatoric stress invariant is given by:

$$J_3 = \det(\bar{\sigma}_{ij}) \tag{4.3}$$

It is a mathematical property of the deviatoric stress matrix and this representation is not employed as such, because it has no physical meaning. It is represented as the Lode angle for the purpose of implementation and is given by:

$$\alpha = \frac{1}{3} \arcsin\left(\frac{-3\sqrt{3}J_3}{2J_2^{3/2}}\right) \tag{4.4}$$

The Lode angle takes values between -30°and 30°.

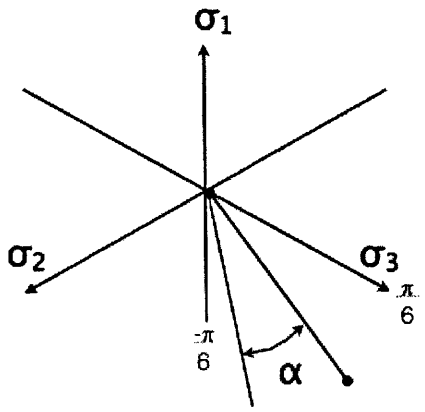

Figure 4.1: Lode angle, α, defined in the triaxial principal stress plane.

4.2 Mathematical Basis of Elasto-Plasticity

The mathematical basis of elasto-plasticity is set out fully by Crisfield [Cri96]. In powder compaction, yield models are particularly challenging due to their dependence on density or potentially other state variables such as work. Included for completeness, classical elasto-plasticity yield models are based on an elasticity domain, the decomposition of strains and a yield criterion. It is assumed that the strain increments can be decomposed in their elastic and plastic fractions, $\Delta\boldsymbol{\epsilon}^e$ and $\Delta\boldsymbol{\epsilon}^p$:

$$\Delta\boldsymbol{\epsilon} = \Delta\boldsymbol{\epsilon}^e + \Delta\boldsymbol{\epsilon}^e$$

The strain decomposition can be substituted into Hooke's law of elasticity:

$$\Delta\boldsymbol{\sigma} = \boldsymbol{C}\Delta\boldsymbol{\epsilon}^e = \boldsymbol{C}\left(\Delta\boldsymbol{\epsilon} - \Delta\boldsymbol{\epsilon}^e\right) \tag{4.5}$$

In which $\boldsymbol{C}$ is the matrix of elastic coefficients. The set of admissible stresses is governed by a yield function f. Plastic flow occurs if $f = 0$. The function f cannot take a positive value as it defines the set of admissible stresses. If $f < 0$, plastic loading does not occur and there is no plastic flow. In this case the behaviour is elastic and the stresses can be updated by:

$$\boldsymbol{\sigma}_k = \boldsymbol{\sigma}_{k-1} + \Delta\boldsymbol{\sigma} = \boldsymbol{\sigma}_{k-1} + \boldsymbol{C}\Delta\boldsymbol{\epsilon} = \Delta\boldsymbol{\sigma} = \boldsymbol{\sigma}_{k-1} + \boldsymbol{C}\Delta\boldsymbol{\epsilon}^e$$

When plastic loading occurs, it is governed by a flow rule:

$$\Delta\boldsymbol{\epsilon}^p = \lambda\frac{\partial g}{\partial\boldsymbol{\sigma}}$$

in which g is the plastic potential function and the plastic multiplier. In this work, the plastic potential and the yield surface are considered associated, so $f = g$. Additionally, the model is rate independent, so the equivalence between the rate equations and the incremental form can be exploited. From the flow rule and Hooke's law, the stress-strain relationship can be written in the case of plastic loading:

$$\Delta\boldsymbol{\sigma} = \boldsymbol{C}\left(\Delta\boldsymbol{\epsilon} - \lambda\frac{\partial f}{\partial\boldsymbol{\sigma}}\right) \tag{4.6}$$

This expression leads to the formulation of the elastic prediction for the incremented stresses and to the basis for a return to the yield surface when the elastically incremented stresses is not in the elastic domain:

$$\boldsymbol{\sigma} = \boldsymbol{\sigma}_0 + \boldsymbol{C}\left(\Delta\boldsymbol{\epsilon} - \lambda\frac{\partial f}{\partial \boldsymbol{\sigma}}\right) \tag{4.7}$$

in which the elastically predicted stress is $\boldsymbol{\sigma}^e = \boldsymbol{\sigma}_0 + \boldsymbol{C}\Delta\boldsymbol{\epsilon}$. The return to the yield surface is carried out through an iterative process. The plastic multiplier must be positive and satisfy the yield function. The equations involved can be highly non linear and the success of the return to the yield surface is dependent on the yield function, which must be formulated to ensure the unicity of the solution.

4.3 Modified CamClay Model

As discussed in Chapter 2, there are a number of yield surface forms that may be adopted. Common forms include an ellipse e.g. modified CamClay by Lewis and Schrefler or Mosbah *et al.* [LS87, MB96], and two-surface models such as the Drucker-Prager model enclosed by a shear failure envelope and a compaction cap [CR00]. In the modified Cam-Clay model available in the literature, the yield surface can be expressed as a function of the pressure and deviatoric stress:

$$f = \frac{(P - P_1)^2}{P_0^2} + \frac{Q^2}{Q_0^2} - 1$$

For convenience of use when introducing the third deviatoric stress invariant, this can be rewritten as a function of the first stress invariant and the second deviatoric stress invariant:

$$f = 27J_2 + M\left(I_{1-I_c}\right)\left(I_1 - I_0\right) \tag{4.8}$$

in which $I_0 = -3\left(P - P_1\right)$, $I_c = -3\left(P_{1-P_0}\right)$, and $M = \frac{Q_0^2}{P_0^2}$. I_0, I_1, and M are the hardening coefficients. They are functions of the density which is used as a hardening variable. The model is associated, thus the derivative of the plastic potential for the

flow rule is:

$$\frac{\partial f}{\partial \sigma_{ij}} = 27\bar{\sigma}_{ij} + M\left(2I_1 - I_0 - I_c\right)\delta_{ij}$$

where δ_{ij} is the Kronecker delta function. The stress increments in equation 4.6 can be written in a tensor form as:

$$\Delta\sigma_{ij} = C_{ijkl}\left(\Delta\epsilon_{kl} - \lambda D f \sigma_{kl}\right) \tag{4.9}$$

The development of the term $C_{ijkl}Df\sigma_{kl}$ from the equation above gives:

$$C_{ijkl}\frac{\partial f}{\partial \sigma_{kl}} = \frac{E}{1+\nu}\frac{\partial f}{\partial \sigma_{ij}} + \frac{\nu E}{(1-2\nu)(1+\nu)} tr\left(\frac{\partial f}{\partial \sigma_{mn}}\right)\delta_{ij}$$

With $tr\left(\frac{\partial f}{\partial \sigma_{mn}}\right) = 3M\left(2I_1 - I_0 - I_c\right)$, this leads to:

$$C_{ijkl}\frac{\partial f}{\partial \sigma_{kl}} = \frac{E}{1+\nu}\left(27\bar{\sigma}_{ij} + M\left(2I_1 - I_0 - I_c\right)\delta_{ij}\right) + \frac{3\nu E\left(2I_1 - I_0 - I_c\right)}{(1-2\nu)(1+\nu)}\delta_{ij}$$

$$C_{ijkl}\frac{\partial f}{\partial \sigma_{kl}} = \frac{27E}{1+\nu}\bar{\sigma}_{ij} + \frac{ME}{1-2\nu}\left(2I_1 - I_0 - I_c\right)\delta_{ij} \tag{4.10}$$

In a fully implicit integration, the stress is considered at the end of the step and substituting equations 4.9 and 4.10 into equation 4.7 gives:

$$\sigma_{ij} = \sigma^e_{ij} - \lambda\left[\frac{27E}{1+\nu}\bar{\sigma}_{ij} + \frac{ME}{1-2\nu}\left(2I_1 - I_0 - I_c\right)\right] \tag{4.11}$$

Equation 4.11 can be split into the hydrostatic and deviatoric contributions. The hydrostatic part is given by:

$$I_1 = I_1^e - \lambda\frac{3ME}{1-2\nu}\left(2I_1 - I_0 - I_c\right)$$

From this, the expression for λ is:

$$\lambda = \frac{\left(I_1^e - I_1\right)(1-2\nu)}{3ME\left(2I_1 - I_0 - I_c\right)} \tag{4.12}$$

The deviatoric contribution in equation4.11 is:

$$\bar{\sigma}_{ij} = \bar{\sigma}^e_{ij} - \lambda \frac{27E}{1+\nu} \bar{\sigma}_{ij}$$

Substituting λ gives:

$$\bar{\sigma}_{ij} = \bar{\sigma}^e_{ij} - \frac{(I^e_1 - I_1)(1-2\nu)}{3ME(2I_1 - I_0 - I_c)} \frac{27E}{1+\nu} \bar{\sigma}_{ij}$$

$$\bar{\sigma}_{ij} = \frac{(2I_1 - I_0 - I_c)\,\bar{\sigma}^e_{ij}}{(2I_1 - I_0 - I_c) + 9\frac{(I^e_1 - I_1)(1-2\nu)}{M(1+\nu)}} \tag{4.13}$$

It is notable that the deviatoric stresses are obtained as a scaled value of the elastic deviatoric stresses. Finally, substituting equation 4.13 into equation4.8 gives:

$$f = 27(2I_1 - I_0 - I_c) + MI_1(I_1 - I_0 - I_c)\left[(2I_1 - I_0 - I_c) + 9\frac{(I^e_1 - I_1)(1-2\nu)}{M(1+\nu)}\right]^2 \tag{4.14}$$

The Kuhn-Tucker condition applied to the expression of λ gives, from equation 4.12:

$$\frac{(I^e_1 - I_1)(1-2\nu)}{3ME(2I_1 - I_0 - I_c)} \geq 0 \tag{4.15}$$

By definition the stresses are bound by the yield surface, therefore from equation 4.14:

$$27(2I_1 - I_0 - I_c) + MI_1(I_1 - I_0 - I_c)\left[(2I_1 - I_0 - I_c) + 9\frac{(I^e_1 - I_1)(1-2\nu)}{M(1+\nu)}\right]^2 \leq 0 \tag{4.16}$$

If the yield condition is not reached, no plastic flow takes place, therefore for all $f < 0$, $\lambda = 0$ and the Kuhn-Tucker condition is verified. If plastic flow occurs, the admissible stresses lie on the yield surface, $f = 0$ and $\lambda > 0$. This can be expressed as an equality known as the consistency condition:

$$\lambda f = 0 \tag{4.17}$$

The analysis of the expression of λ in 4.12 gives an interval for the solutions to equation 4.16 so that the consistency condition is satisfied. Noting that $\nu \leq 0.5$, this means that $(1 - 2\nu)$. Also M is a squared quantity, therefore positive, and E is Young's modulus, thus positive by definition so the term $(3ME)$ is always positive. The sign of the term $(I_1^e - I_1)$ is defined by:

$$\begin{aligned} (I_1^e - I_1) > 0 \text{ for } I_1^e > I_1 \\ (I_1^e - I_1) = 0 \text{ for } I_1^e = I_1 \\ (I_1^e - I_1) < 0 \text{ for } I_1^e < I_1 \end{aligned} \tag{4.18}$$

The sign of the term $(2I_1 - I_0)$ is defined by:

$$\begin{aligned} (2I_1 - I_0) > 0 \text{ for } I_1 > I_0/2 \\ (2I_1 - I_0) = 0 \text{ for } I_1 = I_0/2 \\ (2I_1 - I_0) < 0 \text{ for } I_1 < I_0/2 \end{aligned} \tag{4.19}$$

From the inequalities 4.18 and 4.19, the inequality 4.15 is satisfied for the following conditions:
for $I_1 > I_0/2 : I_1^e > I_1 > I_0/2$
for $I_1 < I_0/2 : I_1^e < I_1 < I_0/2$
It can be shown that equation 4.14 of the fourth degree in I_1 has two solutions in the interval $[0; I_0]$. To return to the yield surface, it can be solved by the *regula falsi* method, using the appropriate starting interval to ensure $\lambda > 0$. This interval can be further reduced to minimise the number of iterations:

$$\begin{aligned} \text{for } I_1^e > \tfrac{I_0}{2} : 0 > I_1 > \tfrac{I_0}{2} \\ \text{for } I_1^e < \tfrac{I_0}{2} : 0 < I_1 < \tfrac{I_0}{2} \end{aligned} \tag{4.20}$$

It is notable that the return to the yield surface is obtained by solving a single equation for the scalar value of I_1, whereas the general case for the return to the yield surface by an implicit scheme is given by a set of equations solved to obtain the stress vector update, as shown by Crisfield or Simo [Cri96, SH98]. This type of solution is developed in the next section for the three-invariant model as the approach presented in this section cannot be used when the third stress invariant is included. The return mapping of the stresses to the yield surface in the present

case is efficient as it does not require the calculation of the derivatives of the yield surface and hardening coefficients in its computational implementation.

4.4 Development of the Three-Invariant Model

Within this work, a model was developed to investigate the effect of the third deviatoric invariant. The mathematical basis for its implementation in a finite element code is first introduced below. Its effect is expressed through the Lode angle. This is followed by the evaluation of the numerical implementation. Following the experimental work showing evidence of variations in the yield limit of powders according to the loading direction in the triaxial principal stress plane [MKSK97, SK98], simulations are then presented to assess the changes in density, stresses or compaction forces occurring when the yield surface is altered with the Lode angle.

4.4.1 Yield Surface Formulation

Several possibilities exist to introduce the influence of the third invariant in a constitutive model. The Mohr-Coulomb yield criterion can be used in conjunction with a compacting cap surface. The maximum shear stress approach of the Mohr-Coulomb means that it is defined by planes in the space of principal stresses (Figure 4.2.a). This makes the model difficult to exploit due to the singularities at the intersection of the yield surface planes. Methods of overcoming this difficulty by using a smoothing function at the singularity have been presented by Nayak and Zienkiewicz and Owen and Hinton [NZ72, OH80]. Crisfield demonstrates an especially adapted return mapping algorithm for cases in the neighbourhood of several yield surfaces [Cri97]. These procedures are computationally heavy and require an implementation very specific to the model considered which is difficult to generalise.
A more recent approach with a single surface formulation is proposed by Khoei [Kho05]. Although the third deviatoric invariant is included in the formulation, it was not tested and explored within the case studies published, thus its influence was not quantified. Furthermore, the term reflecting the Lode angle is added to

the formulation rather than implemented as a multiplicative term of the maximum deviatoric component. This implies that the Lode angle can also influence the value of the maximum hydrostatic stress. A key problem is that it is very difficult to calculate the value of the Lode angle by numerical means under very small small deviatoric conditions. Retaining the influence of the Lode angle on the deviatoric stress only makes it possible to ignore the impact of the Lode angle when the stresses are close to hydrostatic conditions (within the machine's precision) avoiding dividing by a term close to zero in equation 4.4.

Based on this consideration it was decided that to introduce the impact of the third invariant into the existing model, the ratio of the deviatoric to hydrostatic semi-axis length should be modulated by κ, a function of the Lode angle:

$$f = 27J_2 + M\kappa^2 \left(I_{1-I_c}\right)\left(I_1 - I_0\right) \tag{4.21}$$

Equation 4.21 includes the influence of the Lode angle through the term κ. Expressions to reflect the inclusion of this term have been reported in the literature, in particular, Bardet provides a comprehensive review of options [Bar90]. However, the difficulty remains of matching the parameters with the actual material response. This difficulty arises due to the sparseness of experiments relating to the behaviour of powders with respect to the Lode angle.

In an effort to keep the function without introducing complexity artificially that could not be matched to experimental data, its formulation was designed after inspection of the data from the experimental investigation by Mosbah *et al.* [MKSK97]. It may be defined as:

$$\kappa = (1 - \beta)\cos^2\left(3\frac{\theta}{a}\right) + \beta \tag{4.22}$$

When combined with the basic yield surface, it modulates the shape of the yield surface in the π-plane such that the modified CamClay model, for $\beta = 1$ (Figure 4.2.b), becomes dependent on the Lode angle (Figure 4.2.c). To obtain a peak value in compression, the Lode angle is remapped as θ defined between 0 and $\frac{\pi}{3}$. The modification only rotates the reference so that θ is 0 when the stresses lie on the

compressive section of a principal stress axis:

$$\theta = \frac{-1}{3}\left(\arccos\left(\frac{3\sqrt{3}J_3}{2J_2^{3/2}}\right) - \pi\right)$$

It is possible to simplify the expression for κ by using the relationship $\cos^2\left(\frac{\pm a+\pi}{2}\right) = \frac{1-\cos(a)}{2}$. This results in:

$$\kappa = \frac{(1-\beta)}{2}\left(1 - \frac{3\sqrt{3}J_3}{2J_2^{2/3}}\right) + \beta \tag{4.23}$$

κ alters the yield function so that the ratio of the semi axis lengths in the $P-Q$ plane vary between β and 1:
for $\theta = 0$, this ratio is 1,
for $\theta = \frac{\pi}{3}$, this ratio is β.
The formulation of the yield function, however, does not ensure the convexity of the yield surface. This is a requirement in classical plasticity formulation to ensure a correct return to the yield surface when plastic flow occurs. The minimum value of β for this formulation of κ that ensures convexity is 0.78. This is illustrated in Figure 4.2.c and d.

To obtain the direction of the plastic flow, as the associativity of the model is retained, the derivative of the yield function is necessary. It is given by:

$$\boldsymbol{n} = \frac{\partial f}{\partial \boldsymbol{\sigma}} = \frac{\partial f}{\partial I_1}\frac{\partial I_1}{\partial \boldsymbol{\sigma}} + \frac{\partial f}{\partial J_2}\frac{\partial J_2}{\partial \boldsymbol{\sigma}} + \frac{\partial f}{\partial J_3}\frac{\partial J_3}{\partial \boldsymbol{\sigma}}$$

$$\boldsymbol{n} = \frac{\partial f}{\partial \boldsymbol{\sigma}} = M\kappa^2\left(2I_1 - I_0 - I_c\right)\frac{\partial I_1}{\partial \boldsymbol{\sigma}} + 27\frac{\partial J_2}{\partial \boldsymbol{\sigma}} + 2M\kappa\left(I_1 - I_0\right)\left(I_1 - I_c\right)\frac{\partial J_3}{\partial \boldsymbol{\sigma}}$$

The derivative of κ is:

$$\frac{\partial \kappa}{\partial \boldsymbol{\sigma}} = \frac{\partial \kappa}{\partial J_2}\frac{\partial J_2}{\partial \boldsymbol{\sigma}} + \frac{\partial \kappa}{\partial J_3}\frac{\partial J_3}{\partial \boldsymbol{\sigma}}$$

$$\frac{\partial \kappa}{\partial \boldsymbol{\sigma}} = \frac{9\left(1-\beta\right)\sqrt{3}}{8J_2^{5/2}}J_3\frac{\partial J_2}{\partial \boldsymbol{\sigma}} - \frac{3\left(1-\beta\right)\sqrt{3}}{4J_2^{3/2}}\frac{\partial J_3}{\partial \boldsymbol{\sigma}}$$

$\frac{\partial I_1}{\partial \boldsymbol{\sigma}}$, $\frac{\partial J_2}{\partial \boldsymbol{\sigma}}$ and $\frac{\partial J_3}{\partial \boldsymbol{\sigma}}$ are standard derivatives. They are included in Appendix A for completeness.

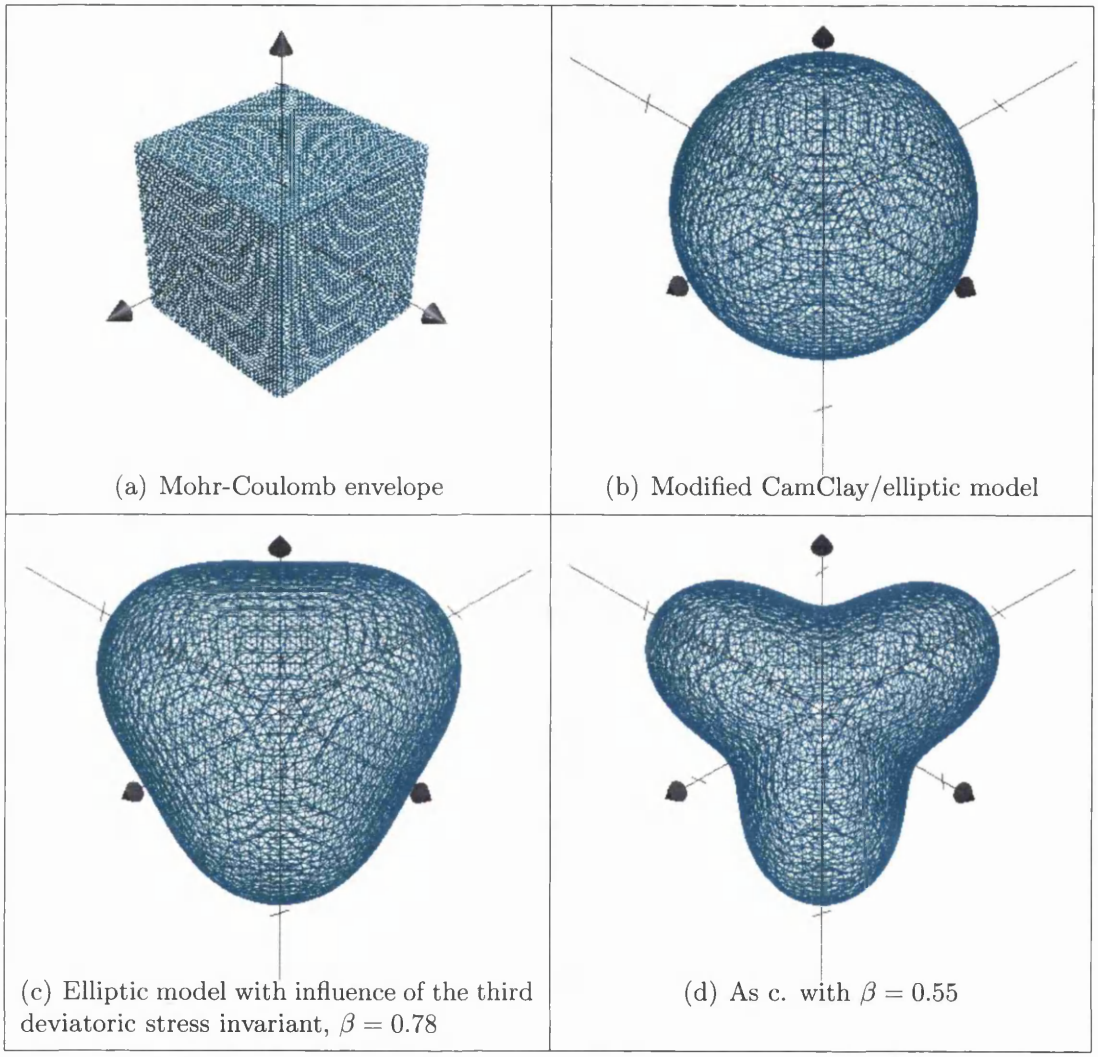

(a) Mohr-Coulomb envelope

(b) Modified CamClay/elliptic model

(c) Elliptic model with influence of the third deviatoric stress invariant, $\beta = 0.78$

(d) As c. with $\beta = 0.55$

Figure 4.2: Yield surfaces for several yield criteria in the principal stress plane.

4.4.2 Hardening

In this work, the yield surface is assumed to evolve with the density ρ, which is related to the change in volume as illustrated in Figure 4.3.

With large deformations, the strain increments can be defined as:

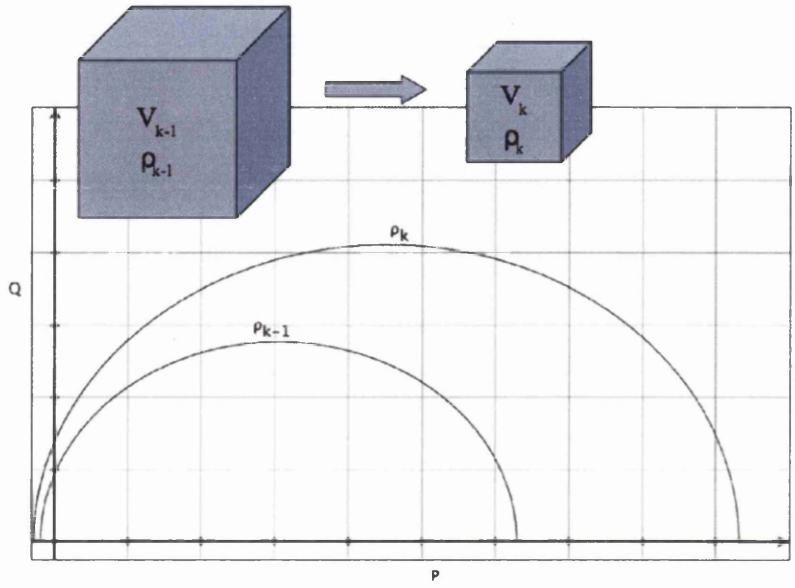

Figure 4.3: Hardening: growth of the yield surface with the change in density.

$$(\Delta\epsilon_i)_k = \int_{(u_i)_{k-1}}^{(u_i)_k} \frac{du}{u} = \ln\left(\frac{(u_i)_k}{(u_i)_{k-1}}\right)$$

The subscripts k and $k-1$ indicate the time step in the overall deformation. The volumetric strain, for a vector expression is therefore:

$$\Delta\epsilon_k^v = \ln\left(\frac{v_k}{v_{k-1}}\right) \tag{4.24}$$

Ensuring mass conservation gives, in an incremental form: $v_k \rho_k = v_{k-1} \rho_{k-1}$, equivalent to:

$$\frac{\rho_k}{\rho_{k-1}} = \frac{v_{k-1}}{v_k} \tag{4.25}$$

Equations 4.24 and 4.25 can be combined to obtain:

$$\rho_k = \rho_{k-1} e^{-\Delta \epsilon_k^{pv}}$$

$$\left. \frac{\rho}{\epsilon^{pv}} \right|_k = -\rho_{k-1} e^{-\Delta \epsilon_k^{pv}} \tag{4.26}$$

The derivatives of the yield function with respect to the strain can be calculated to take into account the evolution of the yield surface:

$$\frac{\partial f}{\partial \epsilon^{pv}} = \left(\frac{\partial f}{\partial M} \frac{\partial M}{\partial \rho} + \frac{\partial f}{\partial I_0} \frac{\partial I_0}{\partial \rho} + \frac{\partial f}{\partial I_c} \frac{\partial I_c}{\partial \rho} \right) \frac{\partial \rho}{\partial \epsilon^{pv}}$$

in which:

$$\frac{\partial f}{\partial M} = \kappa^2 \left(I_1 - I_0 \right) \left(I_1 - I_c \right)$$

$$\frac{\partial f}{\partial I_0} = -M \kappa^2 \left(I_1 - I_c \right)$$

$$\frac{\partial f}{\partial I_c} = -M \kappa^2 \left(I_1 - I_0 \right)$$

4.4.3 Integration of the Model

When the stresses are elastically incremented to the elastically predicted stress $\boldsymbol{\sigma}^e$, if it lies outside the elastic domain, it needs to be remapped to the yield surface. Several possibilities exist for the return to the yield surface. The explicit scheme, illustrated in Figure 4.4, makes use of the derivative calculated where the elastic increment of the stress crosses the yield surface. It is conditionally stable as it may not return towards the yield surface when large steps are used. Note that it is necessary to find the point $\boldsymbol{\sigma}^a$ where the elastic increment crosses the yield surface. It returns to the point $\boldsymbol{\sigma}_{f3}$ in the example given below. A fully implicit scheme remaps

the elastically incremented stress in such a way that the orthogonality of the return path is ensured at the final remapped stress point $\boldsymbol{\sigma}_{f1}$. Implicit solutions exist such as illustrated in Figure 4.4, resulting in the remapped point $\boldsymbol{\sigma}_{f2}$.

In the present case, the return to the yield surface is carried out using a fully

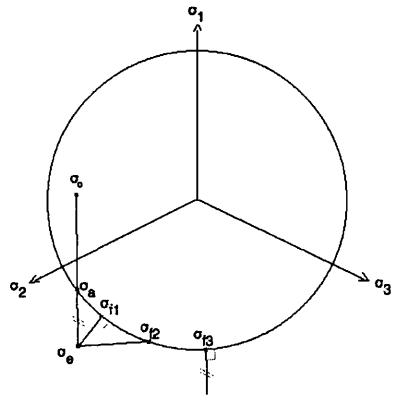

Figure 4.4: Results of different techniques for the return to the yield surface.

implicit, or backward Euler scheme. This type of scheme is well documented and is unconditionally stable. It was therefore the choice for the development and implementation of this model and other possibilities were deliberately left aside. Although an index notation was used for its simplicity in the developments of the simple elliptic model, a tensor notation is adopted in this section, for its brevity as the calculations involved are more complex.

For any state of stress $\boldsymbol{\sigma}_0$, at the start of the loading step, located within or on the yield surface, a strain increment can be applied such that the stress at the end of the step is $\boldsymbol{\sigma}_f$:

$$\boldsymbol{\sigma}_f = \boldsymbol{\sigma}^e - \boldsymbol{C}\boldsymbol{\lambda}\boldsymbol{n}_f \tag{4.27}$$

The yield function must also satisfy:

$$f(\boldsymbol{\sigma}, \epsilon^{pv}) = 0$$

In equation 4.27, $\boldsymbol{\sigma}^e$is the elastically incremented stress vector:

$$\boldsymbol{\sigma}^e = \boldsymbol{\sigma}_0 + \boldsymbol{C}\Delta\boldsymbol{\epsilon}$$

The volumetric plastic strain increment is:

$$\Delta\epsilon_f^{pv} = \lambda \boldsymbol{n}_f \boldsymbol{J} \tag{4.28}$$

Equations 4.27 and 4.28 can be set as a residual vector minimised through an iterative process. The expression for the residual at the n^{th} step of minimisation is:

$$\boldsymbol{r}_n = \begin{bmatrix} \boldsymbol{\sigma}_n - \boldsymbol{\sigma}^e + \lambda \boldsymbol{C}\boldsymbol{n}_n \\ \Delta\epsilon_n^{pv} - \lambda \boldsymbol{n}_n \boldsymbol{J} \end{bmatrix}$$

The updated residual is:

$$\boldsymbol{r}_{n+1} = \boldsymbol{r}_n + d\boldsymbol{r}_n \tag{4.29}$$

Additionally the yield function must be satisfied and is updated by:

$$f_{n+1} = f_n + df_n \tag{4.30}$$

The change in the residual and the yield function is calculated from a Taylor expansion of the incremental terms in equations 4.29 and 4.30:

$$d\boldsymbol{r}_n = \begin{bmatrix} d\boldsymbol{\sigma}_n + d\lambda_n \boldsymbol{C}\boldsymbol{n}_n + \lambda_n \boldsymbol{C}\left(\frac{\partial \boldsymbol{n}_n}{\partial \boldsymbol{\sigma}} d\boldsymbol{\sigma}_n + \frac{\partial \boldsymbol{n}_n}{\partial \epsilon^{pv}} d\epsilon_n^{pv}\right) \\ \\ d\epsilon_n^{pv} - d\lambda_n \boldsymbol{n}_n \boldsymbol{J} - \lambda_n \left(\frac{\partial \boldsymbol{n}_n \boldsymbol{J}}{\partial \boldsymbol{\sigma}} d\boldsymbol{\sigma}_n + \frac{\partial \boldsymbol{n}_n \boldsymbol{J}}{\partial \epsilon^{pv}} d\epsilon_n^{pv}\right) \end{bmatrix} \tag{4.31}$$

$$df_n = \frac{\partial f_n}{\partial \boldsymbol{\sigma}} d\boldsymbol{\sigma}_n + \frac{\partial f_n}{\partial \epsilon^{pv}} d\epsilon_n^{pv} = \boldsymbol{n}_n d\sigma_n - H d\epsilon_n^{pv} \tag{4.32}$$

By setting the updated residual vector to $\boldsymbol{0}$, the updates for a Newton-Raphson scheme on the stresses and volumetric plastic strain are obtained by substituting equation 4.31 into 4.29:

$$\begin{bmatrix} \boldsymbol{I} + \lambda_n \boldsymbol{C} \frac{\partial \boldsymbol{n}_n}{\partial \boldsymbol{\sigma}} & \frac{\partial \boldsymbol{n}_n}{\partial \epsilon^{pv}} \\ \\ -\lambda_n \frac{\partial \boldsymbol{n}_n \boldsymbol{J}}{\partial \boldsymbol{\sigma}} & 1 - \lambda_n \frac{\partial \boldsymbol{n}_n \boldsymbol{J}}{\partial \epsilon^{pv}} \end{bmatrix} \begin{bmatrix} d\boldsymbol{\sigma} \\ \\ d\epsilon^{pv} \end{bmatrix} + d\lambda_n \begin{bmatrix} \boldsymbol{C}\boldsymbol{n}_n \\ \\ -\boldsymbol{n}_n \boldsymbol{J} \end{bmatrix} + \boldsymbol{r}_n = \boldsymbol{0}$$

$$\begin{bmatrix} d\boldsymbol{\sigma}_n \\ \\ d\epsilon_n^{pv} \end{bmatrix} = -d\lambda_n \begin{bmatrix} \boldsymbol{I} + \lambda_n \boldsymbol{C} \frac{\partial \boldsymbol{n}_n}{\partial \boldsymbol{\sigma}} & \frac{\partial \boldsymbol{n}_n}{\partial \epsilon^{pv}} \\ \\ -\lambda_n \frac{\partial \boldsymbol{n}_n \boldsymbol{J}}{\partial \boldsymbol{\sigma}} & 1 - \lambda_n \frac{\partial \boldsymbol{n}_n \boldsymbol{J}}{\partial \epsilon^{pv}} \end{bmatrix}^{-1} \begin{bmatrix} \boldsymbol{C}\boldsymbol{n}_n \\ \\ -\boldsymbol{n}_n \boldsymbol{J} \end{bmatrix} \tag{4.33}$$

$$- \begin{bmatrix} \boldsymbol{I} + \lambda_n \boldsymbol{C} \frac{\partial \boldsymbol{n}_n}{\partial \boldsymbol{\sigma}} & \frac{\partial \boldsymbol{n}_n}{\partial \epsilon^{pv}} \\ \\ -\lambda_n \frac{\partial \boldsymbol{n}_n \boldsymbol{J}}{\partial \boldsymbol{\sigma}} & 1 - \lambda_n \frac{\partial \boldsymbol{n}_n \boldsymbol{J}}{\partial \epsilon^{pv}} \end{bmatrix}^{-1} \boldsymbol{r}_n$$

Substituting equations 4.32 and 4.33 into 4.30 gives the iterative update $d\lambda$ for the plastic multiplier:

$$d\lambda_n = \frac{f_n - \begin{bmatrix} \frac{\partial f_n}{\partial \boldsymbol{\sigma}} & \frac{\partial f_n}{\partial \epsilon^{pv}} \end{bmatrix} \begin{bmatrix} \boldsymbol{I} + \lambda_n \boldsymbol{C} \frac{\partial \boldsymbol{n}_n}{\partial \boldsymbol{\sigma}} & \frac{\partial \boldsymbol{n}_n}{\partial \epsilon^{pv}} \\ \\ -\lambda_n \frac{\partial \boldsymbol{n}_n \boldsymbol{J}}{\partial \boldsymbol{\sigma}} & 1 - \lambda_n \frac{\partial \boldsymbol{n}_n \boldsymbol{J}}{\partial \epsilon^{pv}} \end{bmatrix}^{-1} \boldsymbol{r}_n}{\begin{bmatrix} \frac{\partial f_n}{\partial \boldsymbol{\sigma}} & \frac{\partial f_n}{\partial \epsilon^{pv}} \end{bmatrix} \begin{bmatrix} \boldsymbol{I} + \lambda_n \boldsymbol{C} \frac{\partial \boldsymbol{n}_n}{\partial \boldsymbol{\sigma}} & \frac{\partial \boldsymbol{n}_n}{\partial \epsilon^{pv}} \\ \\ -\lambda_n \frac{\partial \boldsymbol{n}_n \boldsymbol{J}}{\partial \boldsymbol{\sigma}} & 1 - \lambda_n \frac{\partial \boldsymbol{n}_n \boldsymbol{J}}{\partial \epsilon^{pv}} \end{bmatrix}^{-1} \begin{bmatrix} \boldsymbol{C}\boldsymbol{n}_n \\ \\ -\boldsymbol{n}_n \boldsymbol{J} \end{bmatrix}} \tag{4.34}$$

For the next iteration, the updated values are:

$$\boldsymbol{\sigma}_{n+1} = \boldsymbol{\sigma}_n + d\boldsymbol{\sigma}_n$$

$$\epsilon_{n+1} = \epsilon_n + d\epsilon_n$$

$$f_{n+1} = f_n + df_n$$

Some derivations are omitted here for brevity and clarity. They are in Appendix A, in particular the derivatives of the yield function and the hardening coefficients are developed.

4.5 Formulating the Tangent Modular Matrix

In finite element procedures, it is necessary to compute the tangential modular matrix. This matrix relates the strain and stresses in the formulation and is used to compute the stiffness matrix for the resolution of the equilibrium equations. The code used in the present work uses an updated Lagrangian scheme with Cauchy or true stresses and logarithmic strains. Detailed developments are available in a number of published works [Cri96, BLM00]. Three different possible ways of formulating the tangent modular matrix are presented below. The first is the classical form of the tangent modulus, then the consistent tangent modulus is presented and finally an approach based on the response to a perturbation is introduced. The definition of the tangent modular matrix $\boldsymbol{C}_t$ is expressed for an elastic loading case by:

$$\Delta\boldsymbol{\sigma} = \boldsymbol{C}_t \Delta\boldsymbol{\epsilon} \tag{4.35}$$

The time derivative of 4.35 gives the form used as a basis for the derivation of the tangent modular matrix:

$$\dot{\boldsymbol{\sigma}} = \boldsymbol{C}_t \dot{\boldsymbol{\epsilon}} \tag{4.36}$$

4.5.1 Classical Formulation of the Tangent Modular Matrix

The equation 4.5, for plastic loading cases, can be expressed with the time derivative, or rate terms, as:

$$\dot{\boldsymbol{\sigma}} = \boldsymbol{C}_t \left(\dot{\boldsymbol{\epsilon}} - \dot{\lambda} \frac{\partial f}{\partial \boldsymbol{\sigma}} \right) \tag{4.37}$$

Also, in the case of plastic loading, the stresses remain on the yield surface. Therefore, rate expression of the plastic loading condition is:

$$\dot{f} = \left(\frac{\partial f}{\partial \boldsymbol{\sigma}} \right)^T \dot{\boldsymbol{\sigma}} + \frac{\partial f}{\partial \epsilon^{pv}} \dot{\epsilon}^{pv} = 0$$

$$\boldsymbol{n}^T \dot{\boldsymbol{\sigma}} - H \dot{\epsilon}^{pv} = 0$$

For a vector expression of strains and stresses, the plastic volumetric strain rate is: $\dot{\epsilon}^{pv} = \dot{\boldsymbol{\epsilon}^p}\boldsymbol{J} = \dot{\lambda}\boldsymbol{n}^T\boldsymbol{J}$, so that:

$$\boldsymbol{n}^T\dot{\boldsymbol{\sigma}} - \dot{\lambda}H\boldsymbol{n}^T\boldsymbol{J} = 0 \tag{4.38}$$

Substituting the stress increment from the elastic relationship, equation 4.37, into equation 4.38 gives:

$$\boldsymbol{n}^T\boldsymbol{C}\left(\dot{\boldsymbol{\epsilon}} - \dot{\lambda}\boldsymbol{n}^T\right) - \dot{\lambda}H\boldsymbol{n}^T\boldsymbol{J}$$

Rearranging to solve for $\dot{\lambda}$ yields:

$$\dot{\lambda} = \frac{\boldsymbol{n}^T\boldsymbol{C}\dot{\boldsymbol{\epsilon}}}{\boldsymbol{n}^T\boldsymbol{C}\boldsymbol{n} - H\boldsymbol{n}^T\boldsymbol{J}} \tag{4.39}$$

From equations 4.5 and 4.36: $\dot{\boldsymbol{\sigma}} = \boldsymbol{C}_t\dot{\boldsymbol{\epsilon}} = \boldsymbol{C}\left(\dot{\boldsymbol{\epsilon}} - \dot{\boldsymbol{\epsilon}}_p\right)$

$$\dot{\boldsymbol{\sigma}} = \boldsymbol{C}\left(\boldsymbol{I}\frac{\boldsymbol{n}\boldsymbol{n}^T\boldsymbol{C}}{\boldsymbol{n}^T\boldsymbol{C}\boldsymbol{n} - H\boldsymbol{n}^T\boldsymbol{J}}\right)\dot{\boldsymbol{\epsilon}}$$

therefore:

$$\boldsymbol{C}_t = \boldsymbol{C}\left(I - \frac{\boldsymbol{n}\boldsymbol{n}^T\boldsymbol{C}}{\boldsymbol{n}^T\boldsymbol{C}\boldsymbol{n} - H\boldsymbol{n}^T\boldsymbol{J}}\right) \tag{4.40}$$

4.5.2 Formulation of the Consistent Tangent Modular Matrix

This formulation of the tangent modular matrix is qualified as consistent due to its consistency with the fully implicit approach. The derivative of equation 4.27 gives the rate equation:

$$\dot{\boldsymbol{\sigma}} = \boldsymbol{C}\dot{\boldsymbol{\epsilon}} - \dot{\lambda}\boldsymbol{C}\boldsymbol{n} - \lambda\boldsymbol{C}\left(\frac{\partial\boldsymbol{n}}{\partial\boldsymbol{\sigma}}\dot{\boldsymbol{\sigma}} + \frac{\partial\boldsymbol{n}}{\partial\epsilon}\dot{\epsilon^{pv}}\right)$$

$$\dot{\boldsymbol{\sigma}} = \left(\boldsymbol{I} + \lambda\boldsymbol{C}\frac{\boldsymbol{n}}{\boldsymbol{\sigma}}\right)^{-1}\boldsymbol{C}\left(\dot{\boldsymbol{\epsilon}} - \dot{\lambda}\boldsymbol{n} - \lambda\frac{\partial\boldsymbol{n}}{\partial\epsilon^{pv}}\dot{\epsilon}^{pv}\right)$$

with $\dot{\epsilon}^{pv} = \dot{\lambda}\boldsymbol{n}^T\boldsymbol{J}$, $\boldsymbol{R} = \left(\boldsymbol{I} + \lambda\boldsymbol{C}\frac{\partial \boldsymbol{n}}{\partial \boldsymbol{\sigma}}\right)^{-1}\boldsymbol{C}$ and $N = \boldsymbol{n} + \lambda\frac{\partial \boldsymbol{n}}{\partial \epsilon^{pv}}\boldsymbol{n}^T\boldsymbol{J}$, so

$$\dot{\boldsymbol{\sigma}} = \boldsymbol{R}\left(\dot{\boldsymbol{\epsilon}} - \dot{\lambda}\boldsymbol{N}\right) \tag{4.41}$$

For the stresses to remain on the yield surface, the loading condition is:

$$\dot{f} = \frac{\partial f}{\partial \boldsymbol{\sigma}}^T \dot{\boldsymbol{\sigma}} + \frac{\partial f}{\partial \epsilon^{pv}}\dot{\epsilon}^{pv} = 0$$

$$\boldsymbol{n}\dot{\boldsymbol{\sigma}} = H\dot{\epsilon}^{pv}$$

$$\boldsymbol{n}^T\boldsymbol{R}\left(\dot{\boldsymbol{\epsilon}} - \dot{\lambda}\boldsymbol{N}\right) = H\dot{\lambda}\boldsymbol{n}^T\boldsymbol{J}$$

$$\dot{\lambda} = \frac{\boldsymbol{n}^T\boldsymbol{R}}{\boldsymbol{n}^T\boldsymbol{R}\boldsymbol{N} + H\boldsymbol{n}^T\boldsymbol{J}}\dot{\boldsymbol{\epsilon}}$$

substituting $\dot{\lambda}$ into equation 4.41 gives:

$$\dot{\boldsymbol{\sigma}} = \boldsymbol{C}_{ct}\dot{\boldsymbol{\epsilon}} = \boldsymbol{R}\left(\frac{\boldsymbol{n}^T\boldsymbol{R}}{\boldsymbol{n}^T\boldsymbol{R}\boldsymbol{N} - H\boldsymbol{n}^T\boldsymbol{J}}\right)\dot{\boldsymbol{\epsilon}}$$

$$\boldsymbol{C}_{ct} = \boldsymbol{R} - \frac{\boldsymbol{R}\boldsymbol{n}^T\boldsymbol{R}}{\boldsymbol{n}^T\boldsymbol{R}\boldsymbol{N} - H\boldsymbol{n}^T\boldsymbol{J}} \tag{4.42}$$

4.5.3 Formulation of the Tangent Modular Matrix by Perturbation

The final possibility for the formulation of the tangent modular matrix exploits its definition. This follows the principles of establishing sensitivity as in optimisation studies by computing a response to a perturbation. A small strain increment is applied in each direction individually after the stresses corresponding to the current time step have been calculated. This results in a loop with $(n + 1)$ iterations in which n is the number of degrees of freedom per gauss point in the analysis. The first loop is devoted to the calculation of the stresses at the end of the step, then at the end of each loop, only the variation is recorded that corresponds to the strain

perturbation: for $j = 1$ to n

$$C_{tij} = \frac{\partial \sigma_{ij}}{\partial \epsilon_{ij}} \text{ for } j = 1 \text{ to } n \tag{4.43}$$

The subscript j indicates the iteration number in the loop for the calculation of the tangent modular matrix. This also provide a consistent notation with equation 4.43. The main advantage of this method is that, by definition, the resulting matrix is consistent with the method of return to the yield surface for a sufficiently small perturbation. This comes at a cost, as the return to the yield surface needs to be carried out once for the imposed strain increment at the time step of the problem then another n times to calculate the tangent moduli. It is important to notice that the tangent modulus does not reflect the local derivative, but it is based on a forward difference form.

4.6 Analysis of the New Three-Invariant Constitutive Equations

The new constitutive equation was implemented then tested and this is described in this section. To do so, it is possible to examine its behaviour by isolating it from the finite element program within which it is designed to work normally. This results in a simple program that takes in initial stresses and strains, strain increments and outputs stresses after the strain increment has been applied. In effect, this is the procedure applied to each integration point of the finite element scheme. By carrying out this type of test, it is possible to study the impact of the method employed to return to the yield surface and its performance, using the *regula falsi* or Newton-Raphson scheme. Finally it provides an insight into the behaviour of a Lode dependent model with a controlled input.

4.6.1 Performance of the Return Mapping Scheme

This test case consists of the application of a strain increment:
$[\delta\epsilon_{xx}; \delta\epsilon_{yy}; \delta\epsilon_{zz}; \delta\epsilon_{xy}; \delta\epsilon_{yx};]^T = [0.0; -0.1; 0.0; 0.0; 0.0]^T$
at a density of 5.1g/cc, with no initial stress. This corresponds to a uniaxial strain, such as one that may be encountered in an idealised, friction free die compression. The elastic prediction of the stress gives $I_1 = -5000MPa$ and $\sqrt{J_2} = 888.231MPa$. The return paths to the yield surface are shown in Figure 4.5.

The remapping paths are very different according to the technique employed. The

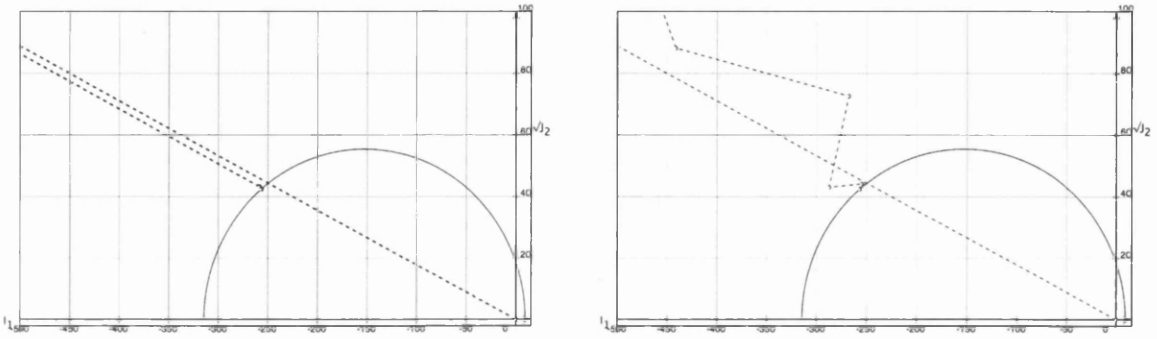

Figure 4.5: Return to the yield surface with the *regula falsi* (left) and with the fully implicit Newton-Raphson scheme (right)

regula falsi is based on a bounding technique. An initial interval is calculated , then it is divided and it is checked in which of its subdivision the solution lies. Because the first interval is reduced by the procedure in the inequalities 4.20, the first iteration is already close to the final solution. The implicit return mapping employed with the new model uses an update of the variables which implies the calculation of the derivatives. This can result in a less stable algorithm compared to the textitregula falsi method if a unique solution is contained within the original search interval. The results from either approach are equal within four decimal places (Table 4.1). This is within the set tolerance for the convergence, taking into account the machine's precision (double on 32bit processor). For the intent of this study, the results can be considered equal. Future reference to identical or equal results in the context of of numerical work is based on a limit of four decimal digits.

Table 4.1: Results at the final iteration of the return to the yield surface.

Original elliptic model, 16 iterations	3-invariant model, 17 iterations
$\sigma = \begin{bmatrix} -61.030511 \\ -134.575241 \\ 0.000000 \\ -61.030511 \end{bmatrix} MPa$	$\sigma = \begin{bmatrix} -61.030524 \\ -134.575228 \\ 0.000000 \\ -61.030524 \end{bmatrix} MPa$
$\rho = 5.6363716822 g/cc$	$\rho = 5.6363716822 g/cc$
$\rho_{unloaded} = 5.6075158526 g/cc$	$\rho_{unloaded} = 5.6075158511 g/cc$
$\lambda f = -4.365575e-11$	$\lambda f = 5,835318e-09$

4.6.2 Changes in the Loading Paths According to the Return Mapping Scheme

Four different loading paths were explored for a single integration point by the routine. The initial density was set to 3.3g/cc with no initial stress. An adaptive time step length is used to match the convergence of the constitutive modelling routine. When the return to the yield surface is not successful within a set number of iterations, the length of the time step is divided by 2. Within these tests, the strain increments used in the loading cases are:

loading case 1: [0.000 ;-0.100 ; 0.000 ; 0.000 ; 0.000]

loading case 2: [-0.025 ;-0.050 ;-0.025 ; 0.025 ; 0.025]

loading case 3: [-0.050 ;-0.050 ; 0.000 ; 0.000 ; 0.000]

loading case 4: [0.010 ;-0.120 ; 0.010 ; 0.000 ; 0.000]

The tests are designed to explore different compaction conditions. The first loading case is a uniaxial compression, the second loading case introduces shear, the third one is a biaxial compression and finally, the last test introduces extension in two directions. All the tests are compressive, even the last one despite the extension in two directions. The results from each loading case are shown in Table 4.2.

All loading paths are compressive in P, as expected, as a response to the strain

Table 4.2: Results from the different loading paths.

Loading case 1	Elliptic model	3-invariant model	variation (%)
P (Mpa)	-1241.870	-1241.870	0.000%
Q (Mpa)	98.850	98.850	0.000%
density (g/cc)	7.160	7.160	0.000%
Loading case 2			
P (Mpa)	-1323.910	-1322.510	0.105%
Q (Mpa)	59.980	60.920	-1.552%
density (g/cc)	7.150	7.150	-0.003%
Loading case 3			
P (Mpa)	-1323.910	-1320.170	0.283%
Q Mpa)	59.980	62.470	-3.992%
density (g/cc)	7.150	7.150	-0.007%
Loading case 4			
P (Mpa)	-1194.490	-1194.490	0.000%
Q (Mpa)	113.310	113.310	0.000%
density (g/cc)	7.170	7.170	0.000%

increments. The return to the yield surface is slightly faster on the oedometric path with the *regula falsi* technique, as was shown in Table 4.1 as well. Unfortunately, it is not possible to apply the *regula falsi* to the three-invariant model. The final results from the loading cases are identical in the first and fourth cases but have 1.6% and 4% difference in $\sqrt{J_2}$ in the second and third case. Two factors can be identified that modify the return to the yield surface: the loading history and the introduction of shear deformations. The third case shows that both codes give the same step lengths up to the 7^{th} increment as illustrated in Figures 4.6 and 4.7. The lesser performance in remapping of the Newton-Raphson scheme results in a difference in the time stepping history. The 3-invariant model needs two time steps to go from $t = 7$ to $t = 8$, whereas this is carried out in a single step with the simple elliptic model. Forcing the time step to 0.5 with the simple elliptic model too shows that the divergence is due to history dependency in the loading case 3. However, when shear is introduced in the second loading case, a difference is still present even with matched time step length. The difference in the stress response to the second deformation case (Figures 4.6 and 4.7) and in their final results in Table 4.3 attests to the influence of shear deformations. This is because the *regula falsi* scheme constrains the return to a radial return to the yield surface, whereas the Newton-Raphson scheme does not. When the shear stresses are introduced, the return to the yield surface is not along a principal stress axis, and the difference is a consequence of the difference in the scheme. In both cases the consistency condition is satisfied.

4.6.3 Influence of the Lode Dependency on the Loading Path

To introduce an alteration of the surface with the Lode angle, the parameter β is set to 0.8. This results in the value of the yield stress along a principal stress axis in tension being related to the compressive value by a ratio of 0.8 as a consequence of the formulation of the yield function, expressed in equations 4.21 and 4.23.
The introduction of the function κ results in lower values of the deviatoric stresses as the angle increases. The following loading paths were chosen to perform the test:

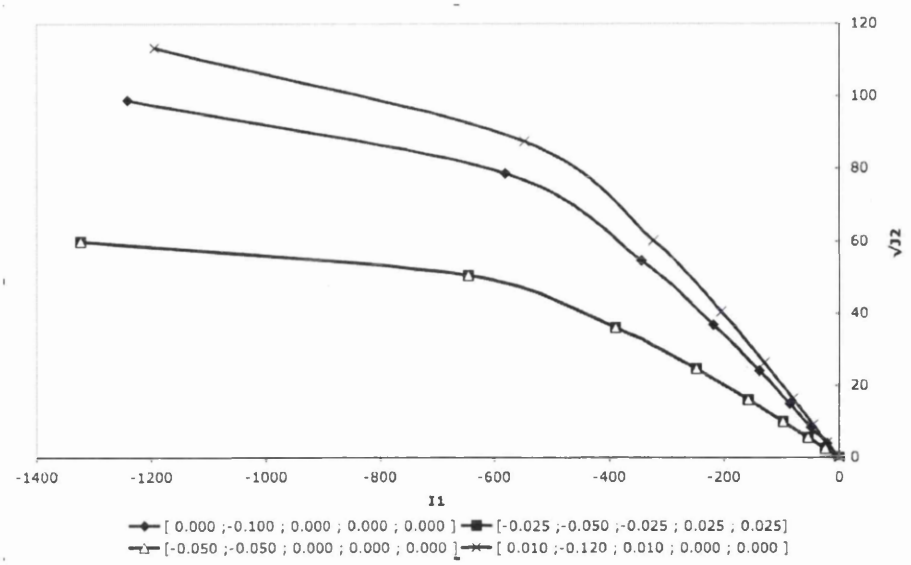

Figure 4.6: Loading paths with a return mapping by *regula falsi*.

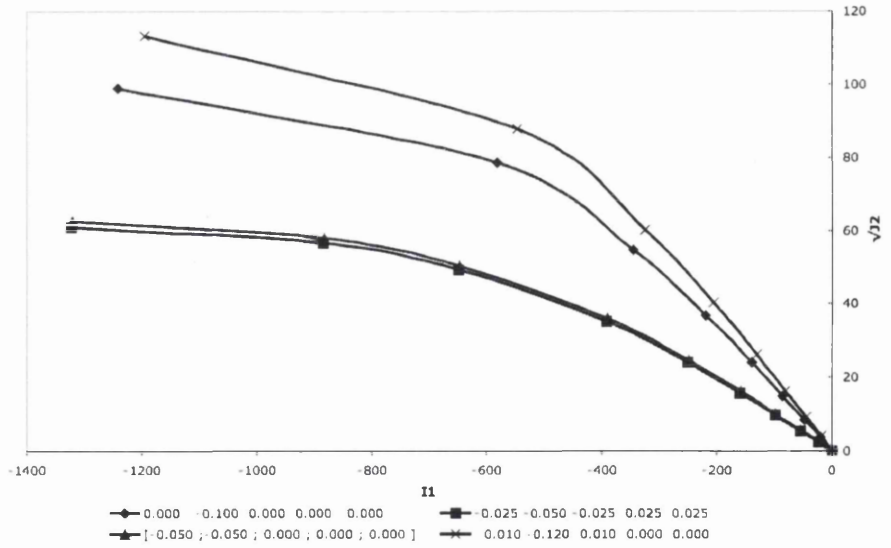

Figure 4.7: Loading paths with a return mapping by a fully implicit Newton-Raphson scheme.

Table 4.3: Results from loading paths 2 and 3 with matched time steps

	Elliptic model	3-invariant model	variation (%)
Loading case 2			
P (Mpa)	-1320.170	-1322.510	-0.177%
Q Mpa)	62.470	60.920	2.542%
density (g/cc)	7.150	7.150	0.005%
Loading case 3			
P (Mpa)	-1320.170	-1320.170	0.000%
Q Mpa)	62.470	62.470	0.000%
density (g/cc)	7.150	7.150	0.000%

loading case 1: [0.000 ; -0.100 ; 0.000 ; 0.000 ; 0.000]
loading case 2: [-0.020 ; -0.100 ; -0.020 ; 0.000 ; 0.000]
loading case 3: [-0.100 ; -0.100 ; -0.100 ; 0.000 ; 0.000]
loading case 4: [-0.2/3 ; -0.100 ; -0.1/3 ; 0.000 ; 0.000]
These tests show a range of loading path: uniaxial in case 1, case 2 reproduces the conditions of the axisymetrical triaxial test presented in Chapter 2, the third case is a hydrostatic compression and the fourth one is a three dimensional stress configuration, which will highlight the effect of the third deviatoric stress invariant. Predictably, the only resulting loading path undergoing changes when $beta = 0.8$ is that of the fourth loading case. This is because it is the only one introducing a value of the angle θ different from 0°. No shear strain is introduced, so the legend in Figure 4.8 does not include them. It can be noted that the use of a yield surface varying with the Lode angle results in a non radial return to the yield surface in the triaxial principal stress plane. This is explained by the enforcement of the perpendicularity condition with the associated flow rule. The normal to the yield surface is radial only for a Lode angle of -30°or +30°. Mathematically this translates into a non symmetrical expression of the term $\boldsymbol{C}\frac{\partial \boldsymbol{n}}{\partial \boldsymbol{\sigma}}$ in equation 4.34. The stress updates are therefore not following a radial path to return to the yield surface. Thus, the value of the Lode angle is not equal to the equivalent angle in strain terms.

In the cases 1 and 2, the Lode angle is 30°. In the third case it is not defined, as the stress is located on the hydrostatic axis. Finally in the fourth case, the Lode angle is 0°with the elliptic model but with the three-invariant model the Lode angle

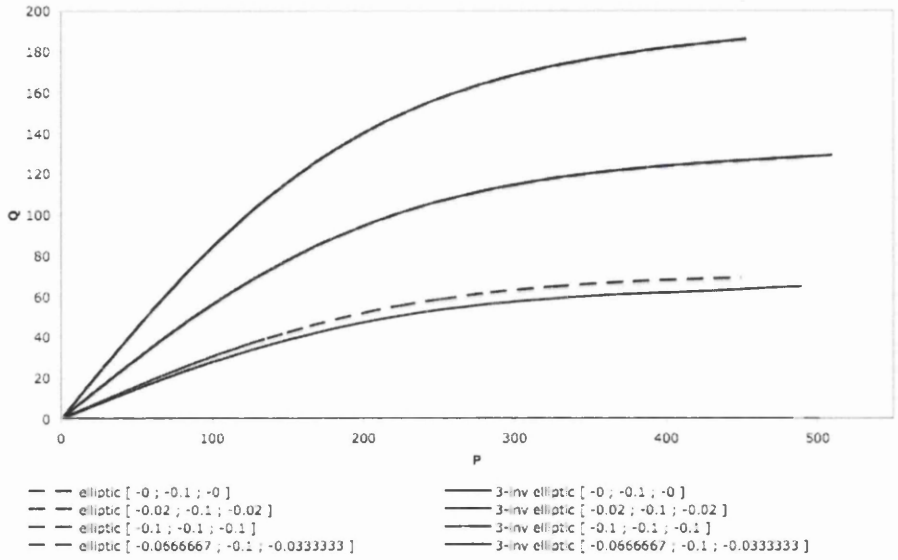

Figure 4.8: Loading paths in the $P-Q$ plane for $\beta = 1$ (equivalent to the modified CamClay) and $\beta = 0.8$ (elliptic with Lode dependency)

is 13.14°. The difference is due to the non radial direction of the return to the yield surface as previously explained. Table 4.4 and Figure 4.9 show the results at 7.0g/cc. The deviatoric stresses are lower by 10% by including the influence of the third invariant. The difference in the Lode angle due to the normality condition and the associated flow rule can be cancelled by using a function for the plastic potential that does not take the third deviatoric stress invariant into account. The derivative of the original elliptic model could, for example be used in the flow rule. This would result in a radial return regardless of the initial loading direction. This modification could be introduced if supported by comprehensive experimental data. The associated model is kept for the present investigation.

The exploitation of a three invariant model presents some challenges. The *regula falsi* cannot be used as it is a bisection method that works only on a scalar, thus the return to the yield surface is radial. For an associated Lode dependent constitutive model, it was demonstrated that the return to the yield surface is not radial, introducing the need for the Newton-Raphson scheme. It does not perform as well as it is dependent on the initial solution, which is the elastic trial. Also, the lesser perfor-

Table 4.4: Results from the loading case 4 at 7 g/cc with the elliptic and three-invariant model.

	Density	P	Q	Lode angle
Original elliptic model	7.00 g/cc	360.80 MPa	66.44 MPa	0.00°
3-invariant model	7.00g/cc	359.84 MPa	60.50 MPa	13.14°

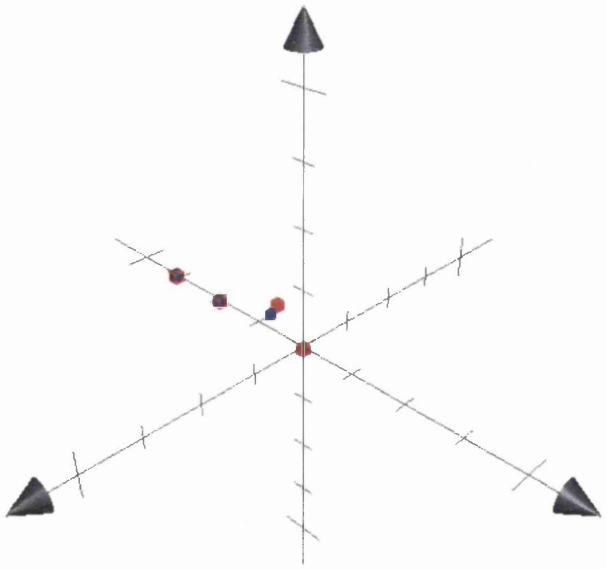

Figure 4.9: Stresses after return to the yield surface at 7.00g/cc, modified CamClay model marked with red cubes and blue spheres for the three-invariant model.

mance of the Newton-Raphson scheme can be compensated by the use of a variable time step. This ensures that the solution is found by the use of smaller time step, thus the scheme is successful although it bears the price of a greater computational cost. Finally, the use of an associated model with a Lode dependent yield surface modifies the direction of the stress response in the triaxial principal stress plane due to the enforcement of the normality condition.

4.7 Choice of the Tangent Modular Matrix Formulation

To establish the most efficient formulation of the tangent modular matrix, a test was carried out. This test is based on the simulation of the compaction of a simple cylinder of ferrous powder, starting from a density of 3.6g/cc and undergoing a 2:1 volume reduction. The simulation is run with a low friction coefficient of 0.01 to introduce some shear stresses, so that all members of the tangent modular matrix are used in the test. In the axisymmetrical conditions, the region is a section of radius 0.5 mm and 1 mm high. The compaction stroke was set to 0.5mm.
A very coarse mesh is used for this test, as this is a test of convergence, not of physical exactitude. This is to keep the simulation time reasonable. The results can however be compared with those obtained from the simulation program used in Modnet and Dienet projects for a comparison with an established and validated code. The mesh is made of unstructured 3-noded triangular elements. The number of nodes is 6 giving 4 elements.
The finite element code uses an automatic step length adjustment scheme. After a set number of successful steps below the specified number of iterations, the step length is multiplied by a user defined factor. If the equilibrium is not satisfied within a maximum number of iterations, the step length is divided. The parameters used for the step length control are listed in Table 4.5.
The analysis was run with the three possible methods of formulating the tangent modular matrix. The effect of the strain perturbation introduced to calculate the tangent modulus according to section 4.5.3 is also investigated by varying it from

Table 4.5: Step length control parameters

Maximum number of iterations per step for step length increase (Ni)	5
Number of steps in less than Ni iterations for step length increase	4
Maximum number of iterations per step	15
Factor for step length increase/decrease	1.5

10^{-4} to 10^{-191}.

The calculations are history dependent as illustrated in section 4.6.1, so this section only concentrates on the convergence with each formulation of the tangent modular matrix by looking at the number of time steps necessary to complete a compaction cycle. This is a relevant indicator of convergence as the time step length is directly controlled by the success or failure to converge within a set number of iterations at each time step.

Three tools are used: a top punch, a die and a bottom punch. The results in Figure 4.10 show that when the tangent modular matrix is calculated by perturbation, there is a range of amplitude of the perturbation for which convergence is optimal. A very large perturbation results, as can be expected, in a poor convergence rate. Above 10^{-4}, the equilibrium equation cannot be satisfied after n steps and convergence is lost. The simulation does not complete for a test with a perturbation of 5.10^{-3}. As the perturbation is decreased, between 10^{-5} and 10^{-16} , the simulation completes in 19 steps. Two more steps are necessary with 10^{-17} and rises sharply. Convergence deteriorates very rapidly below 10^{-17} and the test does not complete below 5.10^{-19}. Comparatively, the classic formulation of the tangent modular matrix yields a poor convergence and the use of the consistent tangent modular matrix formulation further deteriorates convergence. In Figure 4.10, the size of the perturbation is irrelevant to the classic and consistent tangent modular matrix formulations but their results are included as lines for comparison.

To run the test cases, it was verified that the loss of convergence with small perturbation was not due to the terms being impossible to calculate within the machine precision, and all numbers were finite without errors cast by the code.

[1]The perturbation algorithm was used in the Modnet benchmark case study with a perturbation value of 10^{-6} [PM 99]

The results show that the fastest convergence is not obtained by methods that

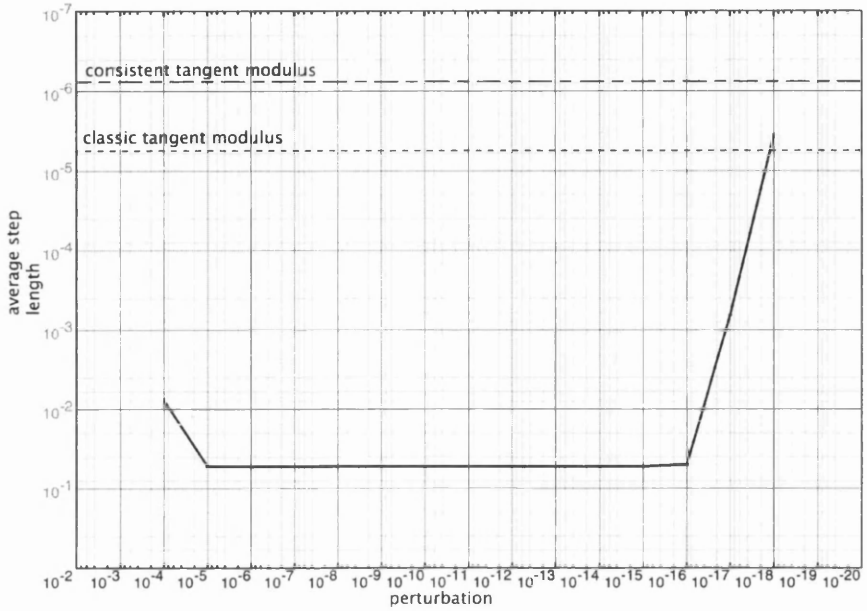

Figure 4.10: Average time step length for different formulations of the tangent modular matrix.

give terms of the tangent modulus closest to the exact derivative . This can be interpreted as the benefit of a smoothing effect by using a finite difference basis for the calculation of the tangent modulus rather than the local value obtained from a Taylor expansion. In this work the simulations are run with the use of a perturbation based calculation of the tangent modulus assigning a perturbation of 10^{-8}.

4.8 Influence of the Lode Dependency

To evaluate the impact of the third deviatoric stress invariant within the constitutive equation, the simulations of two components has been undertaken. The first one is a cylinder. Mosbah *et al.* reported higher forces during ejection and residual stresses than could be expected according to experimental observations, with the conclusion it could be due to the influence of the third deviatoric stress invariant

[MB96]. This test on a simple geometry aims to look at the mechanism which could affect the force levels in the compact and on the tool set. The second numerical experiment is a stepped component. The role of this test is to explore the material response to a more complex geometry and a powder displacement that will induce higher levels of deviatoric stress within the compact. The material parameters used for these simulations were calibrated using the instrumented die test documented in Chapters 2 and 3. They are set out in Appendix B.

4.8.1 Compaction of a Cylinder

The cylindrical geometry of the component keeps the compaction cycle simple. In this particular case, the only factor that can induce non uniaxial displacements of material in the die is friction. Due to friction, density gradients appear throughout the compact that can in turn generate radial movement of the powder.
In this example, the component has a diameter of 18mm and a compacted height of 18mm. The compaction ratio is 2:1 achieved by the stroke of the top punch. The unloading follows by retraction of the top punch then ejection by pushing the compact out of the die with the lower punch. This is illustrated in Figure 4.11.

The simulation was carried out for two values of β: $\beta = 1.0$ and $\beta = 0.8$. The outcome of the simulations show that the Lode angle does not significantly affect the stresses during the compaction phase. The difference between the peak values of the deviatoric stress at the end of the compression is 2.7% (Figure 4.12). The difference in hydrostatic stress is 2.3% (Figure 4.13).This is because, during the uniaxial compaction, little deformation occurs in any other direction than axial. Only friction is susceptible to generate shear stresses, and thus minor radial displacements.

The results at the end of the ejection phase differ more significantly. Introducing the influence of the third deviatoric stress invariant results in a drop in the maximum tensile hydrostatic stress by 5.7% and its maximum compressive value decreases by 11.7%. This is shown in Figure 4.14. The deviatoric stress also decreases by 8.8% (Figure 4.15). These results show that the shrinkage of the elastic domain in the $P - Q$ plane along the tensile deviatoric direction with the Lode angle results in a decrease of the stresses sustained by the powder.

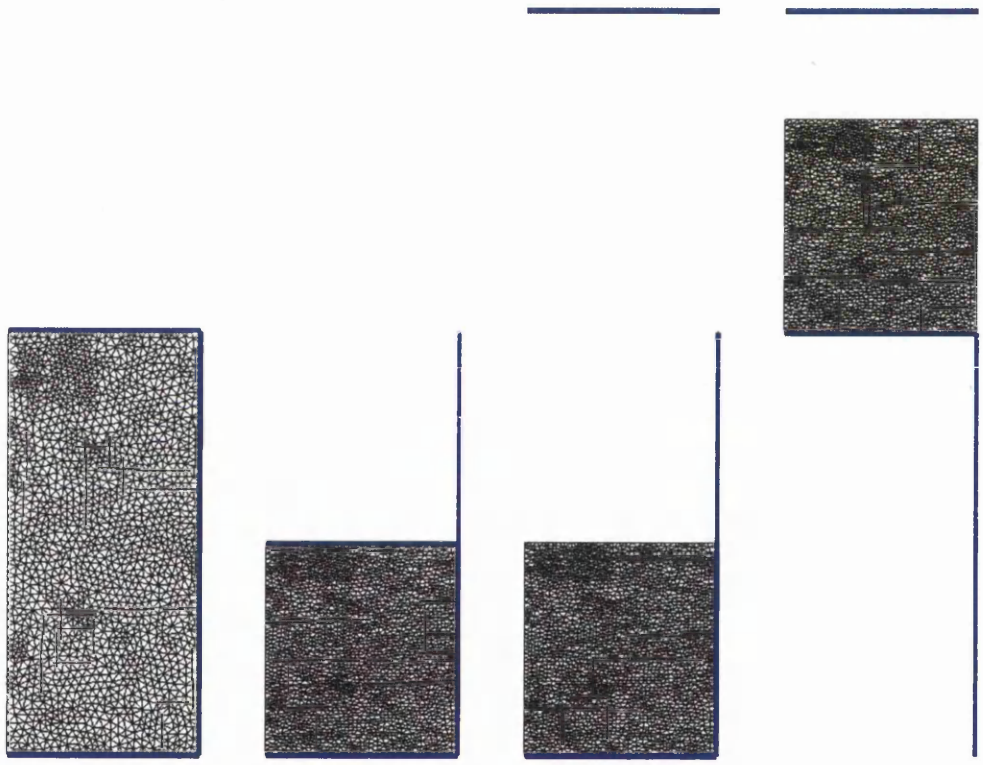

Figure 4.11: Tool kinematics for the compaction of a cylinder. The part is axisymmetrical around the left edge of the shown section.

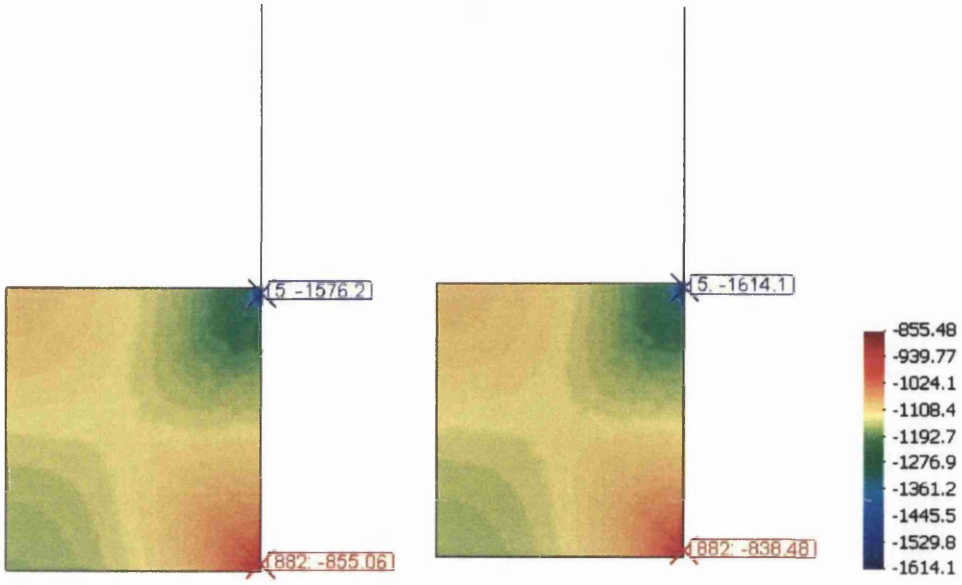

Figure 4.12: First stress invariant at the end of the compaction stroke, left $\beta = 0.8$, right $\beta = 1.0$

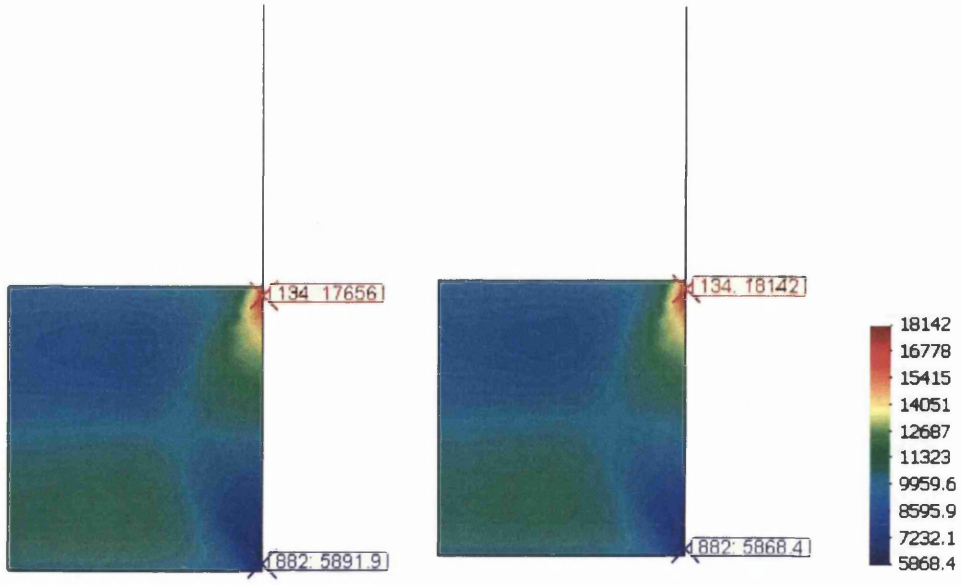

Figure 4.13: Second deviatoric stress invariant at the end of the compaction stroke, left $\beta = 0.8$, right $\beta = 1.0$

The largest difference appears in the residual axial stress (Figure 4.16). The simulation with Lode dependency yields a 31% lower tensile value for the maximum residual axial stress than the Lode independent model. It is also interesting to note that a layer of compressive axial stress forms on the surface of the compact as observed by Luukkonen and Eriksson and also reported in simulation by Jonsèn and Häggblad [LE00, JH05].

More noticeably, including the influence of the Lode angle gives a lower yield limit

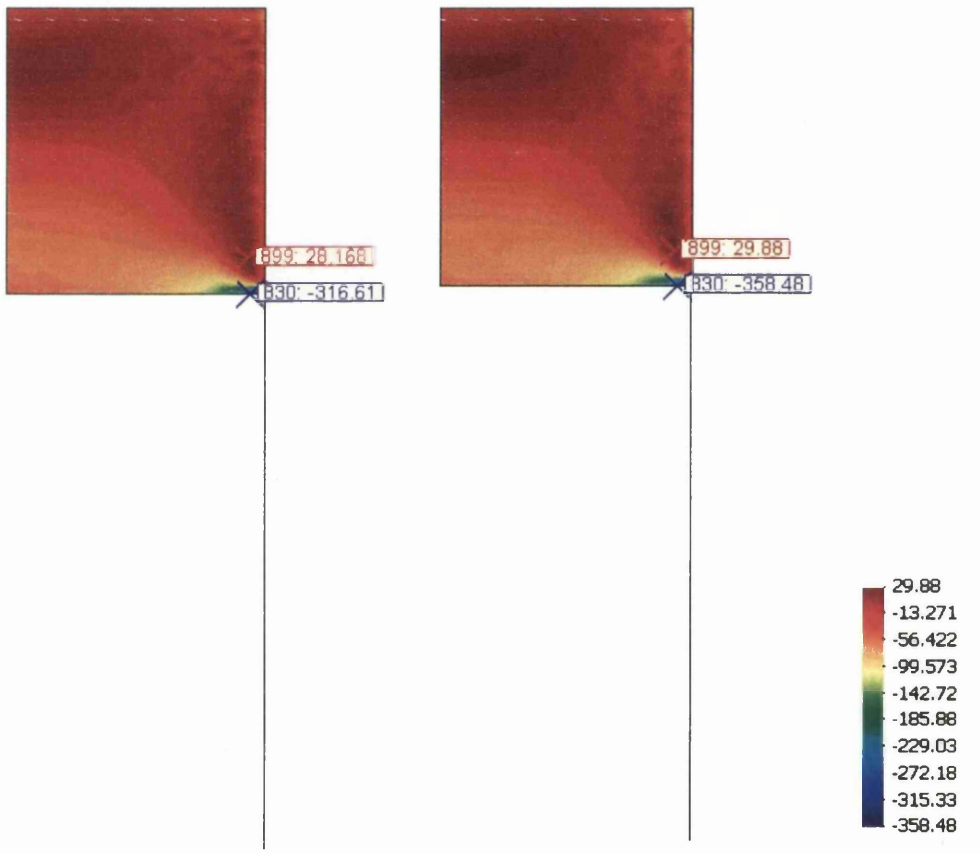

Figure 4.14: First stress invariant at the end of the ejection stroke, left $\beta = 0.8$, right $\beta = 1.0$

as the stress path deviates from a compressive principal stress axis. As a consequence

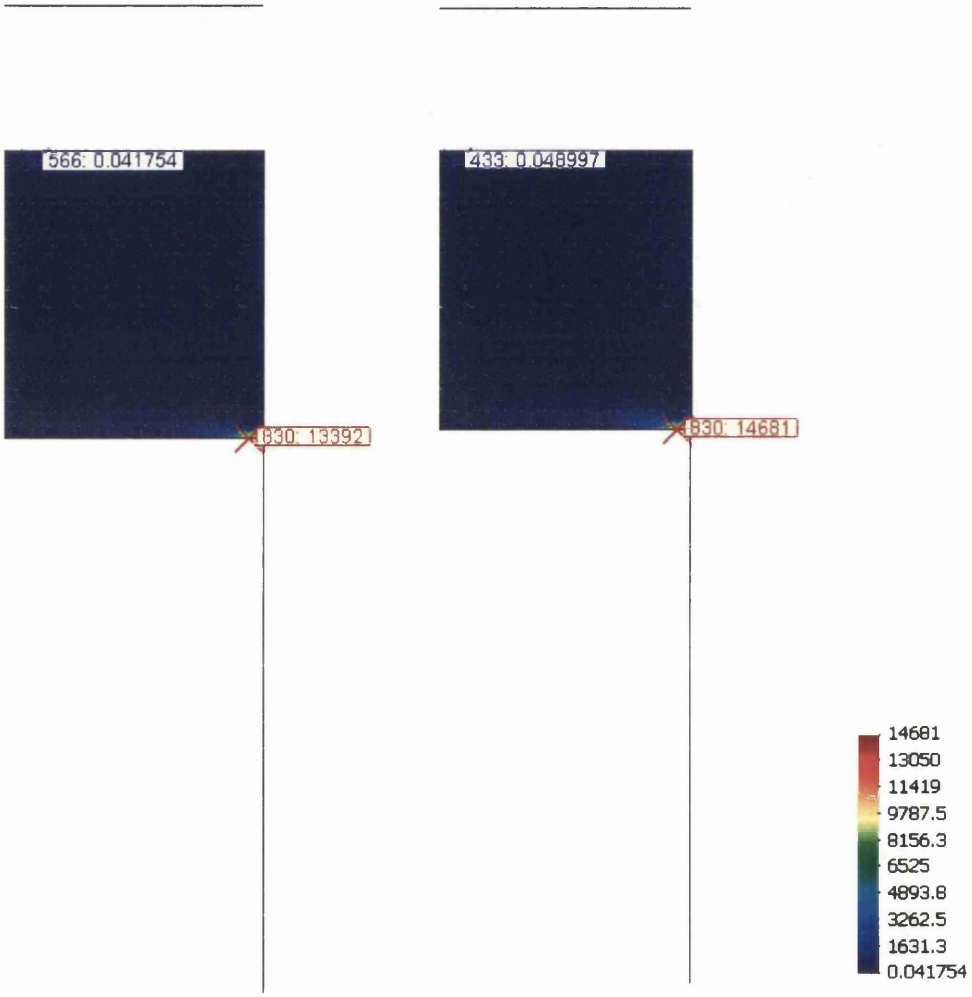

Figure 4.15: Second deviatoric stress invariant at the end of the ejection stroke, left $\beta = 0.8$, right $\beta = 1.0$

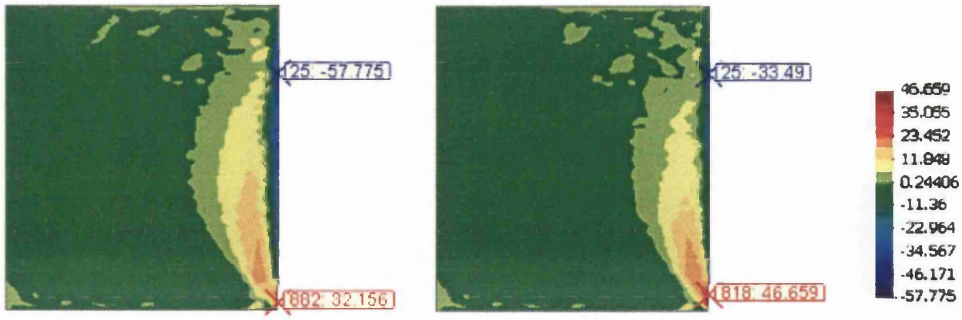

Figure 4.16: Residual axial stress in the cylinder, left $\beta = 0.8$, right $\beta = 1.0$

the material is subjected to 16.2% larger radial displacements towards the core of the component at the top and 13% larger outwards displacements at the bottom. Although a general reduction in the stress level is found, the radial displacements in the component have increased. Larger displacements at lower stresses is the main effect of altering the constitutive relationship according to the Lode angle.
Although the axial forces on the tools are consistently lower when , the variation is negligible during the compaction (131.644kN against 131.602kN). During the ejection a more notable variation can be observed although it is still minor: 4.21kN for and 4.18kN for , a 3% decrease. A more notable difference appears in the radial direction as the compact emerges from the die and the last step of ejection imposing a radial stress on the die showed that it is 11% lower when (166.8MPa against 186.5MPa). This can be linked to the changes in density that take place at the same time. The material is plastically deformed with a recompaction first as it passes the edge of the die, of the order of 0.01%. This is made apparent by the small density peaks in the density plots at the points 1 and 2, Figure 4.18. This is then followed by a loss of density of 0.2% in the case where $\beta = 1$ and 0.45% for $\beta = 0.8$. Figure 4.18 plots the evolution of density at three points along the edge of the compact picked as shown in Figure 4.17. The recompaction only occurs at the lower points, indicating that it is due to a stress concentration as the area on which the radial pressure is applied diminishes.

It appears that the Lode angle has little effect on the stresses in the compact during the compaction. However it facilitates radial material movements by lowering the elastic limit outside the uniaxial compression path during the ejection. The

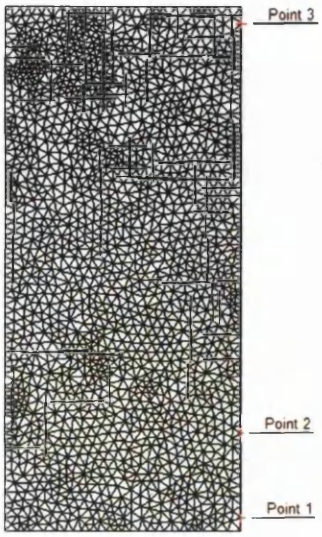

Figure 4.17: Sampling point for Figure 4.18

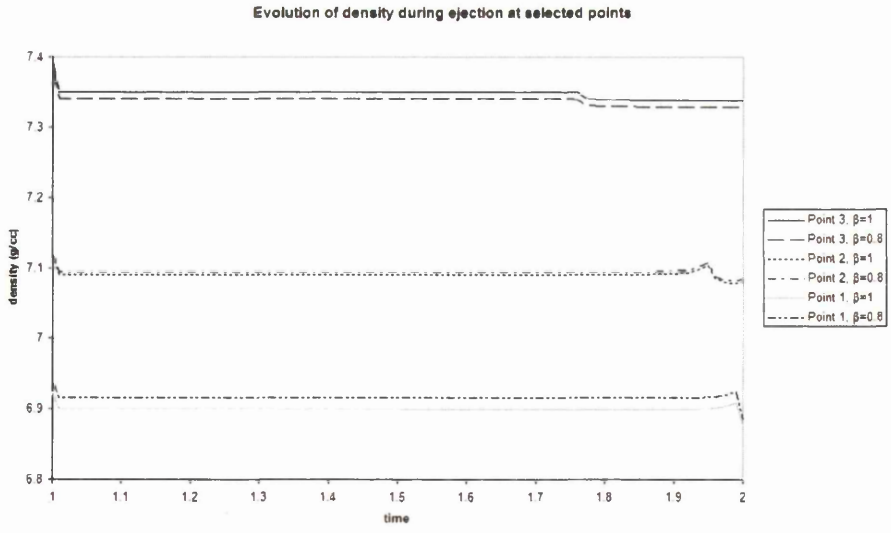

Figure 4.18: Evolution of Density at the points selected in Figure 4.17

hydrostatic and deviatoric stresses show that although the general stress levels in the compact are not deeply affected, the peak values present significant changes. The effect of taking into account the third deviatoric stress invariant in the compaction of a cylinder is reflected by lower deviatoric stress levels and higher pressures.

This first case study shows that the third deviatoric invariant has an influence on the residual stresses and the ejection forces. The material used by Mosbah [MKSK97] was a ferrous powder, but its precise nature is unknown. A direct comparison of the results is therefore not possible. Qualitatively, however the trend shown in the present studies appear to confirm Mosbah's conclusions regarding the potential influence of the third deviatoric stress invariant, resulting in lower tool forces and residual stresses .

4.8.2 Compaction of a Stepped Component

The test case on a stepped component is a case study from the European research program Dienet. Existing results are documented by Coube *et al.* [CJK+05]. The geometry and tool kinematics are exposed respectively in Figure 4.19 and Figure 4.20. The powder is DistaloyAE, the properties of which are available in Appendix B. The die cavity is initially filled with a non uniform density. This is approximated by the use of two regions with respective fill densities of 3.840g/cc and 3.786g/cc, resulting in an average fill density of 3.8g/cc.

The tool displacements, illustrated in Figure 4.20, show that the compaction is carried out by the displacement of the upper and the lower outer punches. The die moves down as well during the compaction, this minimises friction and a lesser length has to be stripped from the side of the step during ejection, thus minimising the risk of breaking off the outer section of the component. The ejection is carried out in two phases, the upper section with the step is first pushed out of the die (time 1.00 to 1.50 in Figure 4.20) then the inner lower punch finishes the ejection by pushing the lower section out of the lower outer punch (time 1.50 to 2.00).

The stresses at the end of the compression stroke (time 1.00) are shown in Figure 4.21 for the axial stress, Figure 4.22 for the radial stress and Figure 4.23 for the

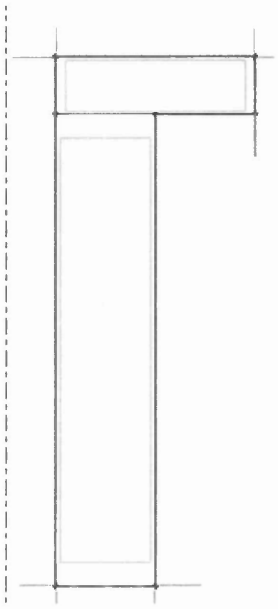

Figure 4.19: Geometry and fill density at the start of the simulation

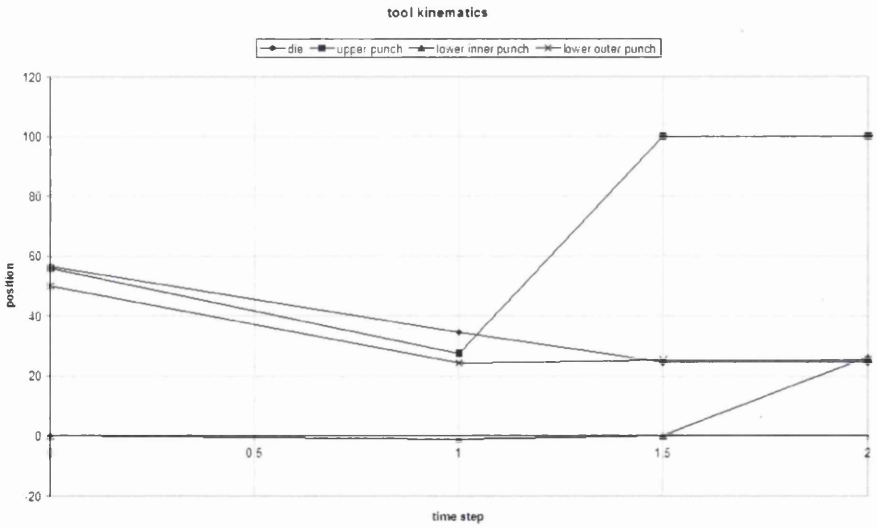

Figure 4.20: Geometry and fill density at the start of the simulation

shear stress. An obvious observation at first is that despite the changes brought by the introduction of the Lode dependency, the stress distributions do not differ fundamentally. The axial and radial stress levels are higher in the upper section of the component due to the higher initial density in that area. Because of this density gradient, the powder in the upper section tends to undergo a lesser compaction at the top of the left column of powder. It is pushed down instead and the high pressure generally observed in the corner of a part is absent and replaced by a pressure point on the inner wall below the level of the step. It formed at the interface between the regions of different initial density as the powder at the top was able to sustain higher axial stress when pushed down. Also, as can be expected, the shear stresses develop along the walls where friction is incurred by the relative displacement between the powder and the tool as the compaction is carried out. Using caused a 1.52% decrease in the peak value of the axial stresses but less than 0.5% in the radial stress at the end of the compaction. The shear stresses and density do not present any notable differences at the end of the compaction. This shows again that the influence of the Lode angle does not yield critical differences during the compression stroke of a compaction cycle.

It is evident from this result that the compaction phase is not greatly affected by

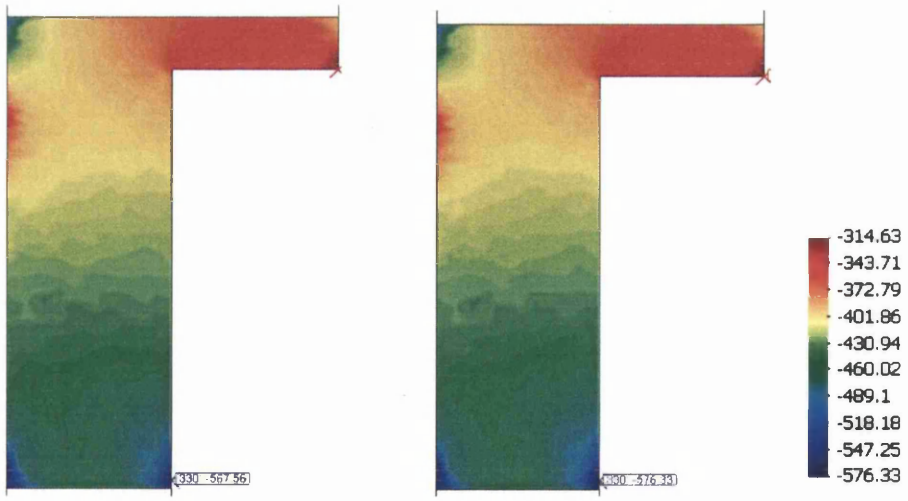

Figure 4.21: Axial stress at the end of the compaction stroke, left $\beta = 0.8$, right $\beta = 1.0$

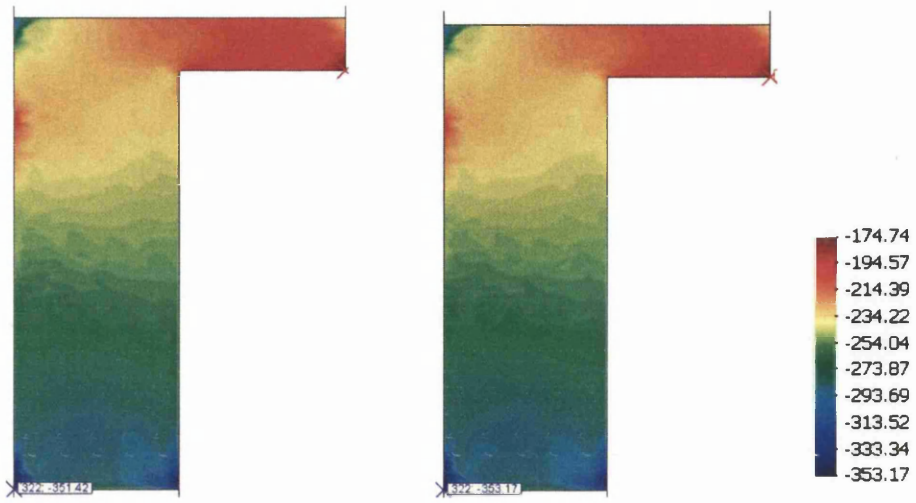

Figure 4.22: Radial stress at the end of the compaction stroke, left $\beta = 0.8$, right $\beta = 1.0$

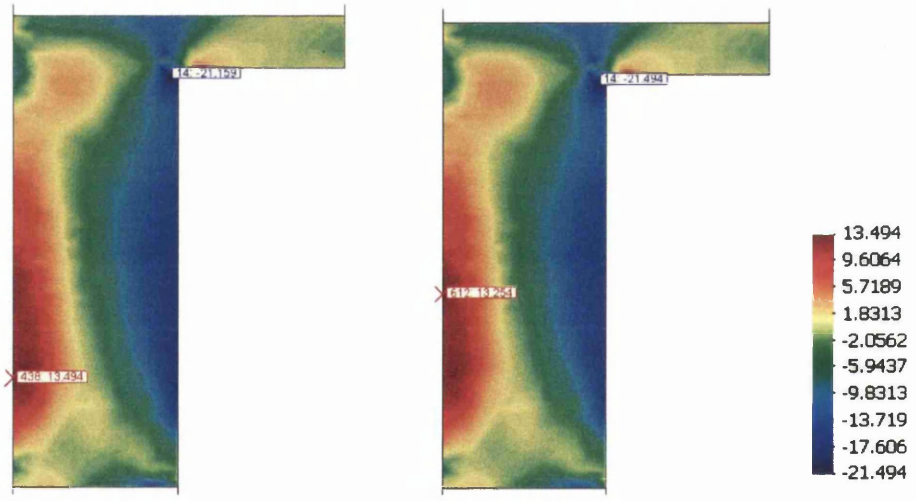

Figure 4.23: Shear stress at the end of the compaction stroke, left $\beta = 0.8$, right $\beta = 1.0$

the variation of β. During the ejection, the difference in axial stress is accentuated between the solutions. The peak values of the axial stress are considerably lower for $\beta = 0.8$, in particular as tensile axial stresses develop. This is illustrated below at 70% of the ejection process. The difference in the peak value is 13.4%. The maximum tensile value of the axial stress does not appear at the same node of the mesh when the value of β changes, however the axial stress at the corner and at the peak along the wall at the centre of the component are within 1% of each other in both cases.

When the part is fully ejected, the residual axial stress exhibits a tensile peak

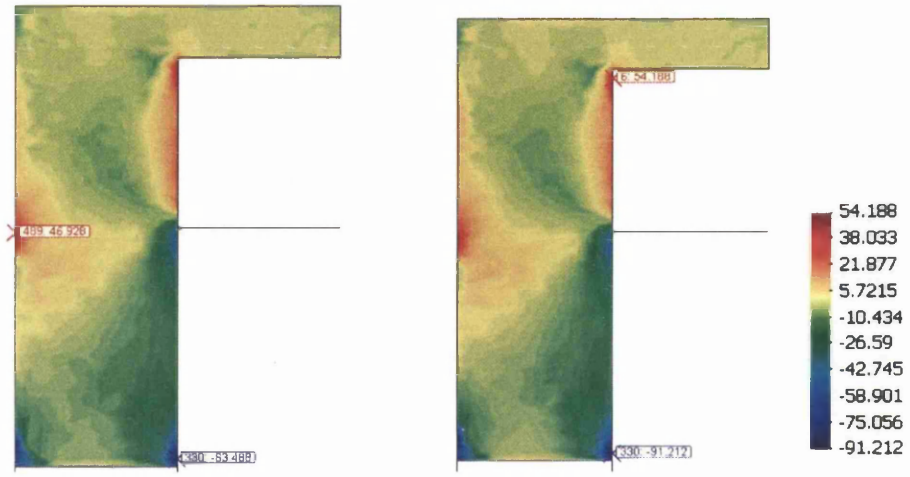

Figure 4.24: Axial stress at 70% of the ejection process, left *beta* = 0.8, right $\beta = 1$

16.6% lower with $\beta = 0.8$ than with $\beta = 1$ (Figure 4.25). This contribute to a 9.1% reduction in the tensile peak value of the pressure shown in Figure 4.26.

The density distribution shown below appears more homogeneous for $\beta = 0.8$, however the spread in density is 8.42% of the average density against 8.51% for $\beta = 1$, showing that any impact on the density is only marginal.

This second case study of the impact of the Lode angle in powder compaction confirms that its main effect occurs during ejection. It results in lower residual stress levels. A lesser force is also predicted for the ejection of the component (5.15kN against 5.17kN).

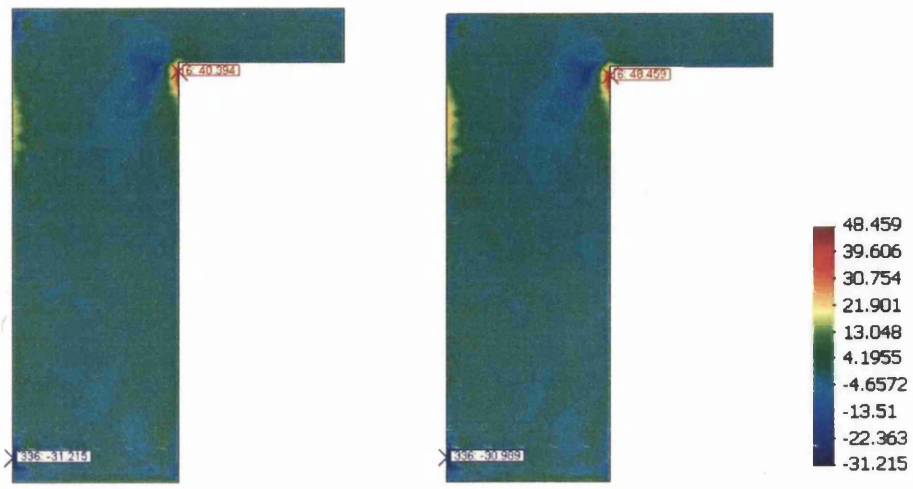

Figure 4.25: Residual axial stress at the end of the ejection, left *beta* = 0.8, right $\beta = 1$.

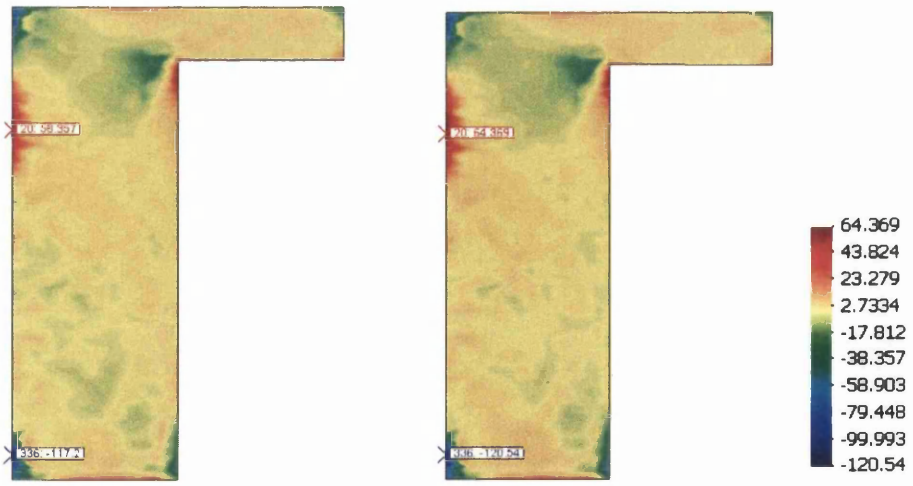

Figure 4.26: Distribution of the first stress invariant at the end of the ejection, left *beta* = 0.8, right $\beta = 1$.

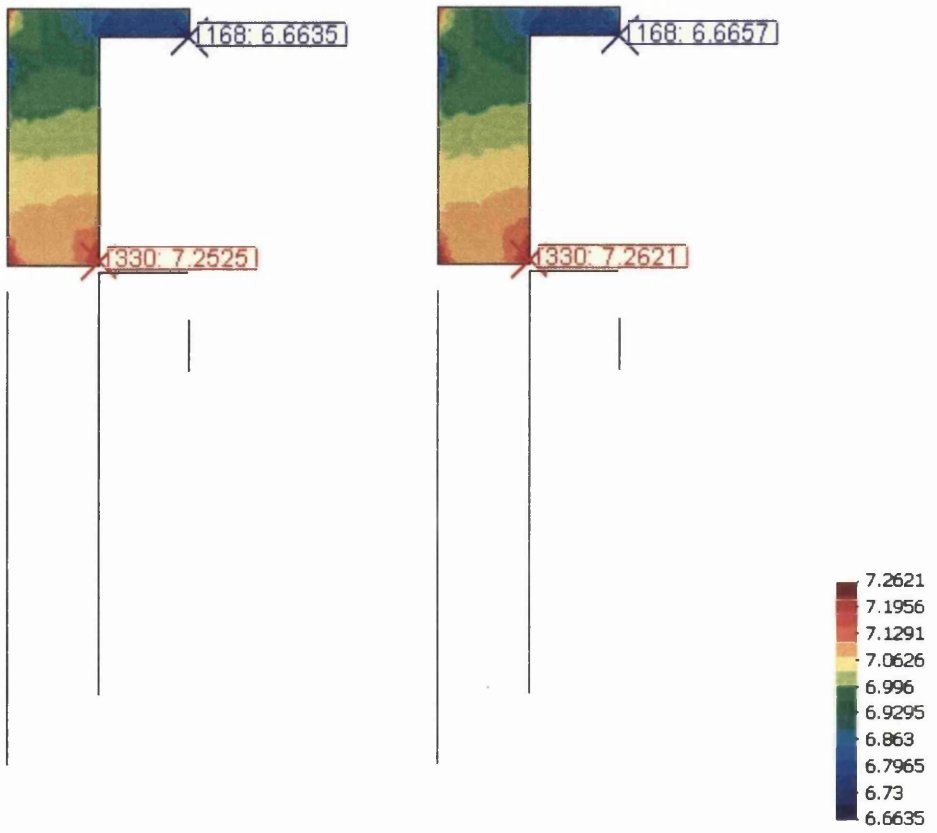

Figure 4.27: Density distribution at the end of the ejection, left *beta* = 0.8, right $\beta = 1$

4.9 Closure

This chapter demonstrates a successful implementation of an associated model with a Lode dependent yield surface. The exploitation of model shows that the stage of the compaction process most affected by the variations of the Lode angle is the ejection. It also shows that including the third deviatoric invariant does not influence greatly the general distribution of stresses and density throughout the compact but that its impact is mainly on the peak values of the stresses (16.6% difference in peak residual axial stress). The impact of a Lode dependency is therefore most critical when studying the stress concentrations rather than for an estimation of density distributions.

The Lode dependency is an essential aspect of the behaviour of powders when investigating the conditions of failure of the powder compaction process, because as the Lode angle moves away from a compressive principal stress axis, one of the principal stresses may be positive. The experimental data in the previous chapter showed with the Brazilian disc test on Alumina samples that such conditions can result in brittle failure. Further work may be concerned with the discrimination of the effects of anisotropy from Lode dependency and their impact on the mode of failure of the powder compacted parts.

Chapter 5

Predicting Fracture Propensity by Numerical Simulations

This chapter focuses on the prediction of fractures in green compacts. The method employed to achieve this is based on experimental observations to establish the conditions under which fractures occur. The cases were chosen from industrial experience and bespoke experiments. These cases were then simulated to analyse the conditions of the compact where fractures are expected to form, with special attention to the stresses and the evolution of density.
A simple criterion was then introduced that aims to identify the regions in which the powder is submitted to conditions that were found to be dangerous for the integrity of the compact. Finally two case studies are presented and lead to the conclusions regarding the use of the proposed fracture propensity criterion and its validity.

5.1 Identification of the Conditions Leading to Fracture

Fractures can develop during the powder compaction process. Important shear stresses or tensile stresses can easily lead to the initiation and growth of cracks in a powder compact. This is due to the characteristics of granular materials. A loss of cohesion can be obtained at relatively low stresses due to the fragility of compacted

parts before sintering. All cohesion in green compacts is obtained by interlocking between the grains of the powder and cold welding. These are not as strong as the crystalline bond established during sintering.
The approach taken in this work to explore the conditions in which fractures can occur is by simulation of test cases. These cases are selected from compaction cycles produced in industry that are known to be likely to produce defective components. The first case is the compaction of a cylinder with different ejection schemes. This case was chosen to explore a solution to ejection cracks adopted in the industry, which consists of keeping a pressure on the top of the compact during the ejection. The second example is based on a case study from the Dienet European thematic research network. Experimental data was collected by an industrial project partner and used here to reproduce numerically the experimental conditions. The observation of the resulting samples was also carried out to explore the fracture patterns and relate them to the results from the simulations. The simulations were run using the model parameters in Appendix B.

5.2 Ejection Cracks

Fractures sometimes appear during the ejection of components. A common form is known as capping. It is a well known problem in industry, in particular for pharmaceutical applications, where the top of tablets can separate from the rest [Pan07, WHM+07]. In materials for mechanical applications, delamination is most common issue, where the compact is split into layers as it comes out of the die. This is the issue investigated in this section. The example studied here is the compaction of a cylinder subjected to different ejection methods. One possibility is to relieve the compact of the axial load exerted by the upper punch and then push it out of the die. Another is to maintain a pressure with the top punch while the compact is ejected and then unload. In the latter case, the load to be maintained on the compact during ejection can also be adjusted. This solution is widely employed in the industry to avoid problems during the ejection. It is believed that the ejection cracks may be caused by tensile stresses. The code employed for the simulations in this study is displacement driven, which means that the displacements of the

tools have to be prescribed rather than the loads. The simulation of the ejection of a partially unloaded component can therefore be carried out by withdrawing the upper punch by a portion of the component's axial elastic recovery. Three different schemes were explored by simulation in the present work:

- The first one was a compression followed by a complete withdrawal of the upper punch and then the ejection.
- The second case undergoes an identical compaction, then a partial unloading takes place. The withdrawal of the upper punch for the partial unloading was calculated from the elastic recovery of the compact in case 1, once unloaded in the die. The profile of the top surface of the compact after recovery is shown in Figure 5.1. Half of the axial recovery was used for the top punch withdrawal (0.0227mm). The figure used is the minimum axial recovery observed at the centre of the compact. It is notable that despite the frictional effects, the largest recovery occurs against the wall. This can be explained by the higher density in that area of the compact resulting in greater accumulated elastic strain. Thus the resulting top surface of the compact is found to be concave.
- The third case that was simulated does not undergo any unloading before the ejection. The top punch was displaced during the ejection so that its distance to the lower punch was constant. Then after completion of the ejection, the load of the top punch was removed.

These three cases are summarised in Figure 5.2. The time scale provided for the duration of each stage was used for the simulation. It is however only a pseudo-time, without any effect as the model is rate independent.

At the end of the compression stroke, the compact is under high pressure and deviatoric stress (Figures 5.4 and 5.5, $t = 1.00$). Pressure achieves the compaction of the powder and the deviatoric stress arises from the friction between the powder and the tool set, in particular the die, resulting in density gradients. At this stage no particular problem is anticipated regarding the integrity of the compact as it follows a normal compaction scheme. The stress distributions observed are regarded as normal.

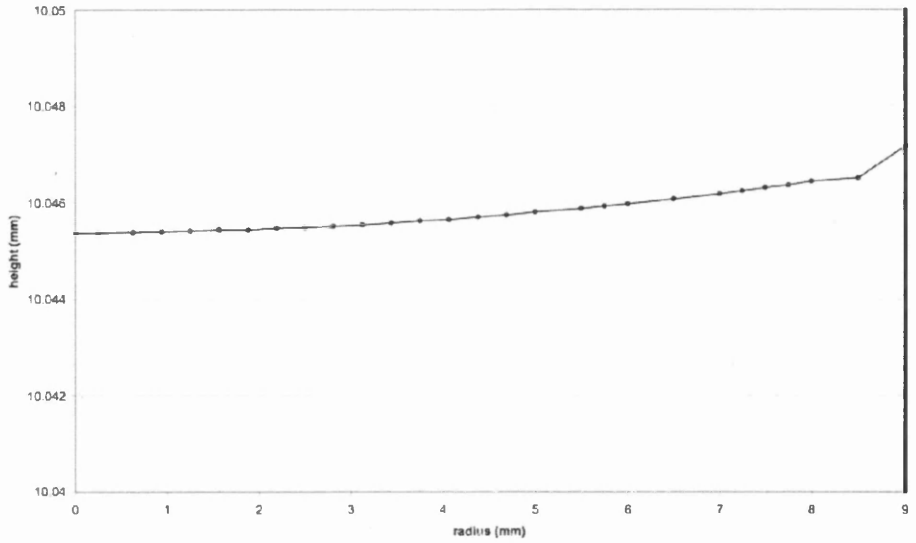

Figure 5.1: Profile of the top surface of the compact after withdrawal of the top punch.

The unloading in cases 1 and 2 results in a respectively total and partial axial recovery of the elastic strains in the compact subject to confinement in the die. Consequently, the maximum pressure drops by 75% in the fully unloaded compact and 40% in the partially unloaded compact (Figure 5.4, $t = 1.25$). The remaining pressure is due to the contribution of radial strains imposed by the die and axial strains that are not fully recovered owing to friction against the die. However it can be seen that the axial stress contribution to the pressure after withdrawal of the upper punch decreases greatly. The average axial stress was calculated as the ratio of the sum of tool forces of the same sign to the cross section of the compact. It is 517.3MPa at the end of the compaction and drops to 262.0MPa with a partial unloading and 16.5MPa with a complete unloading. The distributions reported in Figure 5.3 shows that the variations within each compact after unloading are negligible compared to the difference in stress level that the unloading scheme incurs. The minimum and maximum values of the axial stress also show that tensile axial stresses are developed once the top punch contact is removed. These tensile stresses are located along the top surface of the compact (Figure 5.3, fully unloaded case). This can be seen as an indication of a risk region for the integrity of the compact.

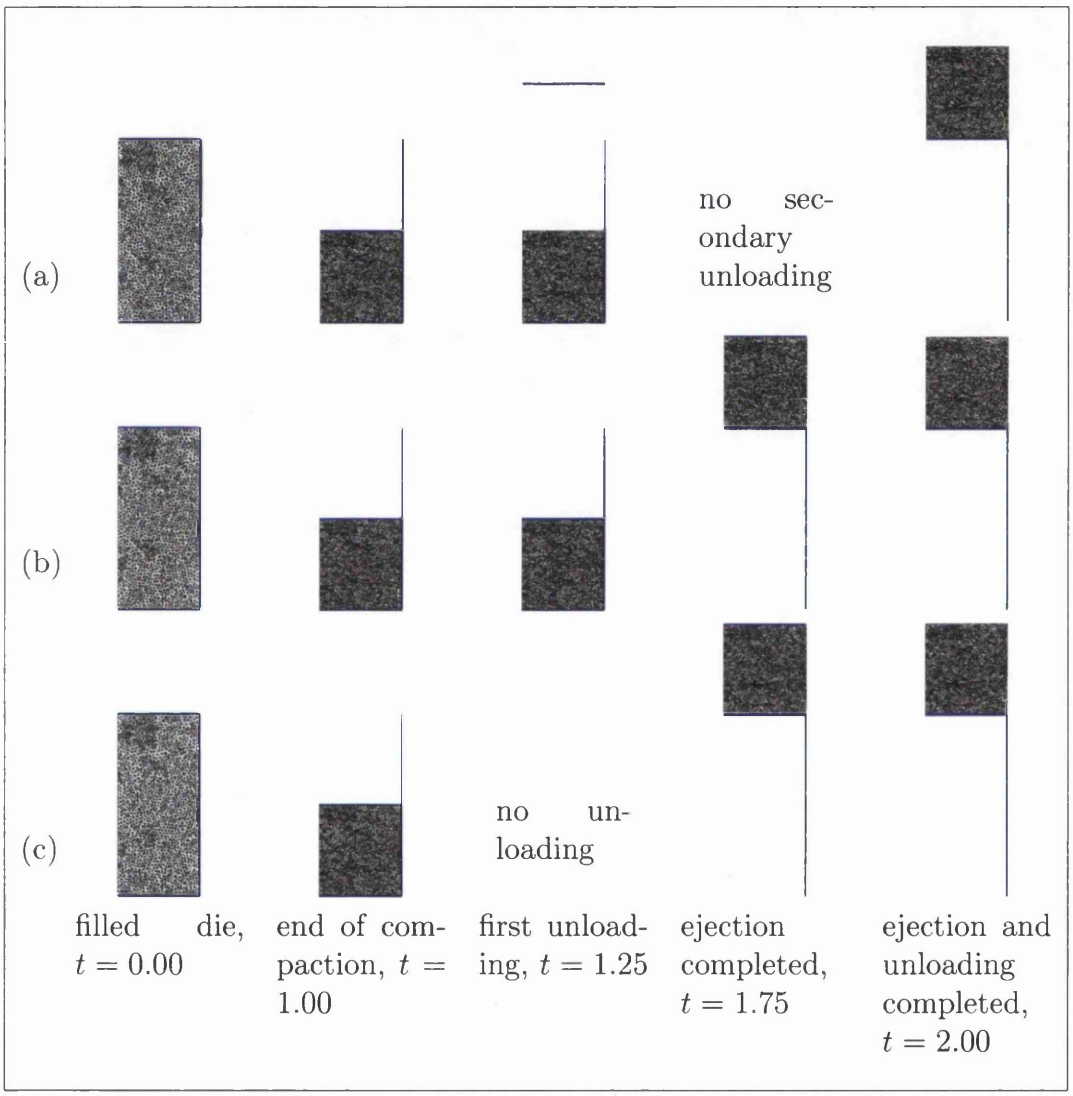

Figure 5.2: Toolset motion.

Capping in particular is the issue to which attention should be drawn at this stage of the fully unloaded ejection scheme as the tensile forces highlighted may result in the separation of the upper surface of the compact from the rest. The capping phenomenon results in a concave fracture surface forming below the top of the compact.

As the unloading takes place, the radial forces decrease proportionally to the axial

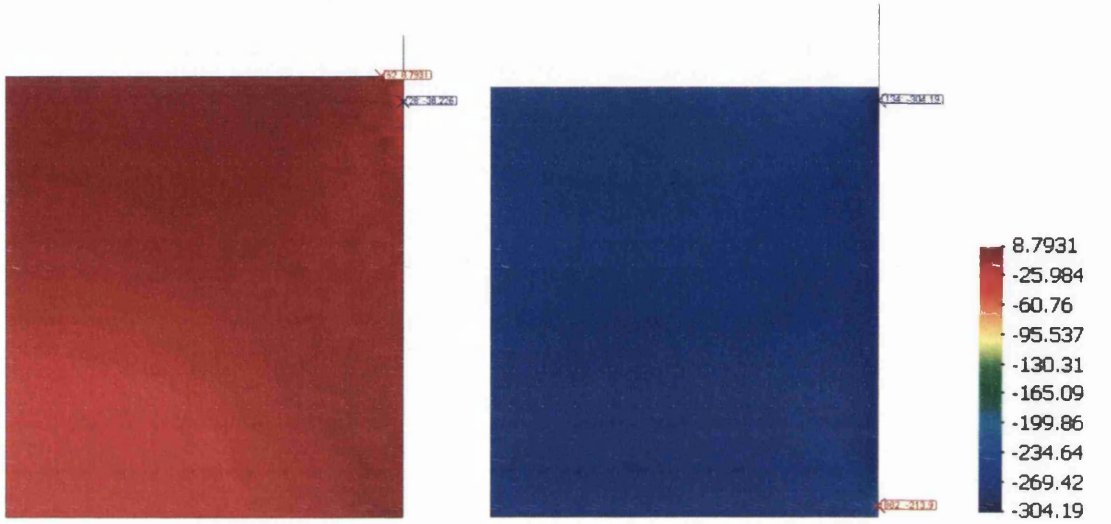

Figure 5.3: Axial stresses at the end of the initial unloading, in the fully unloaded component (left) and the partially unloaded component (right).

forces in both examples with unloading: $\frac{\Delta F_{rad}}{\Delta F_{ax}} = 0.9$. The relaxation of the elastic stresses upon unloading is rendered complex by the presence of the friction preventing a total recovery and the maintained radial constriction in the die. The stress transmission coefficient, which changes with density and the elastic properties of the powder can also be identified as a contributor to establishing this ratio. Thus, this ratio is a characteristic of the powder in the state considered at the end of this compaction rather than a quantity which could be formulated analytically.

As the bottom punch starts pushing the compact out of the die in the case of the ejection without unloading, the friction causes an inversion in the pattern of the shear stresses. Once the load has been removed, the shear stress levels are low, resulting in little change in deviatoric stresses when the ejection starts (Figure 5.5, $t = 1.51$). The friction against the walls is a much more important contribution when the top punch is maintained and the comparison, in Figure 5.5 of the results

at $t = 1.00$ and $t = 1.51$ shows that the trend in deviatoric stress along the die wall is inverted under the influence of the shear stresses.

In the unloaded compacts, the beginning of ejection only has a minor impact on the hydrostatic stress in the compacts that have been previously unloaded. Owing to the friction rising against the ejection forces, the peak deviatoric stress increases by a factor of 1.5 in the partially unloaded compact (Table 5.1) whereas in the fully unloaded compact, the low remaining pressure against the die results in a very small increase (below 0.2%). The ejection takes place at constant speed so the stresses are constant until the compact starts emerging from the die.

The main type of failure that can be highlighted from this case study is delamination. The delamination is the separation in layers of the compact as it is ejected. It occurs due to the tensile stresses developing in the ejected portion of the unloaded component.

Table 5.1: Maximum deviatoric stress Q at key steps of the ejection process for all three cases

	Unloaded	Partially unloaded	Top punch maintained
End of compaction	233.3MPa	233.3MPa	233.3MPa
After Unloading	173.5MPa	74.6MPa	Not Applicable before ejection
Start of ejection	173.7MPa	104.9MPa	182.0MPa

As the compact emerges from the die, a region of tensile mean stress appears at the top of the unloaded component, as tensile stresses develop in the radial and axial directions. The mean stress becomes tensile in a large proportion of the region of the compact that is out of the die, as shown in Figure 5.4.a.

The observations of pressure during ejection of the unloaded components combined with the values of the deviatoric stress (Figure 5.5.a) indicates that the risk of delamination is higher than for the components with top punch pressure maintained. In cases with top punch pressure, the maximum deviatoric stress is not located at the

edge of the die and, most importantly, it is not combined with any tensile hydrostatic stress during the ejection. It is notable that the complete removal of the top punch results in peak shear stresses located in a low pressure area, but an excessive application of top punch pressure results in very high deviatoric stresses. This can lead to problems such as failure of the part by crumbling the compact back into powder as it comes out of the die.

The difference in stress patterns is due to the recovery of elastic deformation. When the top punch is removed, the compact recovers axially, then radially as it comes out of the die resulting in tensile stresses. When the punch is maintained, the axial load remains, at least partially, and the radial stresses are relaxed as the component comes out of the die. The radial stresses can become tensile whereas axial stresses are still compressive. This heterogeneity in stress levels according to their direction results in higher deviatoric stresses, but it also avoid tensile hydrostatic stresses.

After ejection, the components on which top punch pressure was maintained present very different distributions of deviatoric stresses. In the case where partial unloading occurred, the deviatoric stresses are concentrated on the vertical wall of the part, whereas without any top punch withdrawal, the deviatoric stress distribution has a high level region at the core of the compact (Figure 5.5, $t = 1.75$). This is because the axial stresses remain very high throughout the component in the latter case whereas it is only high in the area of higher density at the top right hand corner of the part in the partially unloaded compact as it was already observed that high density regions result in the springback of larger elastic deformations.

The vertical wall of the components ejected under top punch load also presents a surface layer with a gradient of high to low deviatoric stresses from the top to the bottom of the component. The localised stress concentrations forming during the ejection at the edge of the die results in plastic deformations. Consequently, they remain imprinted along the surface of the compact. The maximum value of the deviatoric stress on the surface of the ejected compact is higher in the partially unloaded compact (Figure 5.5.a, t=1.75). This is because the higher remaining deviatoric stresses are in the upper part of the compact. As the top of the compact comes out, the radial stress throughout the part is still high, therefore the partial unloading resulted in a stress unbalance between the radial and axial directions. This essentially highlights the different results of the schemes where pressure is main-

tained on the compact. It also shows the risk of crumbling the outer layer of the compact against the edge of the die during ejection.

The fully ejected components in Figures 5.4 and 5.5, $t = 2.00$ show that with the fully unloaded scheme, a stress concentration occurs as the compact is nearly out of the die resulting in an imprinted residual stress in the corner. With the top punch pressure maintained. deviatoric stresses are generated in the region near the edge of the die as the compact comes out and this results in residual deviatoric stresses shown in Figure 5.5.a and b, $t = 2.00$.

The distribution and maximum values of the stresses within the ejection and unloading stage support the use of top punch pressure as a way of avoiding fractures during ejection. The model also shows that top punch pressure during the ejection needs to be applied appropriately to avoid the high shear stresses detected during ejection that could lead the compact to break as it comes out. The partial unloading scheme chosen as case 2 in this study shows that it is possible to avoid the tensile stresses without generating important deviatoric stresses.

Figure 5.6 shows that the corresponding load maintained on the top of the compact was 46% of the compaction load. This value is within the interval of 40% to 50% used in the industry. The evolution of the force during the ejection is as can be expected. In the schemes with unloading of the compact, the top punch is withdrawn at $t = 1.00$. The ejection is then started at $t = 1.25$. The unloading is accompanied by a stress relief on the die and bottom punch as can be expected. As the compact begins to be pushed out, a minor increase of the axial force on the bottom punch takes place: 285N in the case of the unloaded compact, 1325N for the partially unloaded one and 3188N without unloading. Simultaneously, the inversion of the shear stresses previously observed at the contact between the die and the compact results in the reduction of the force on the upper punch in the cases where the compact is still loaded at the top. From these simulations, it appears that friction does not cause important ejection forces. The difference in the ejection scheme is made visible as the compact emerges from the die. When the compact is unloaded, the decrease in the bottom punch force is linear, whereas it appears hyperbolic when the compact is still loaded. This is because the force from the top punch results in stresses that are distributed in the compact in the form of the deviatoric stresses dominantly located in the portion out of the die. When the compact is unloaded,

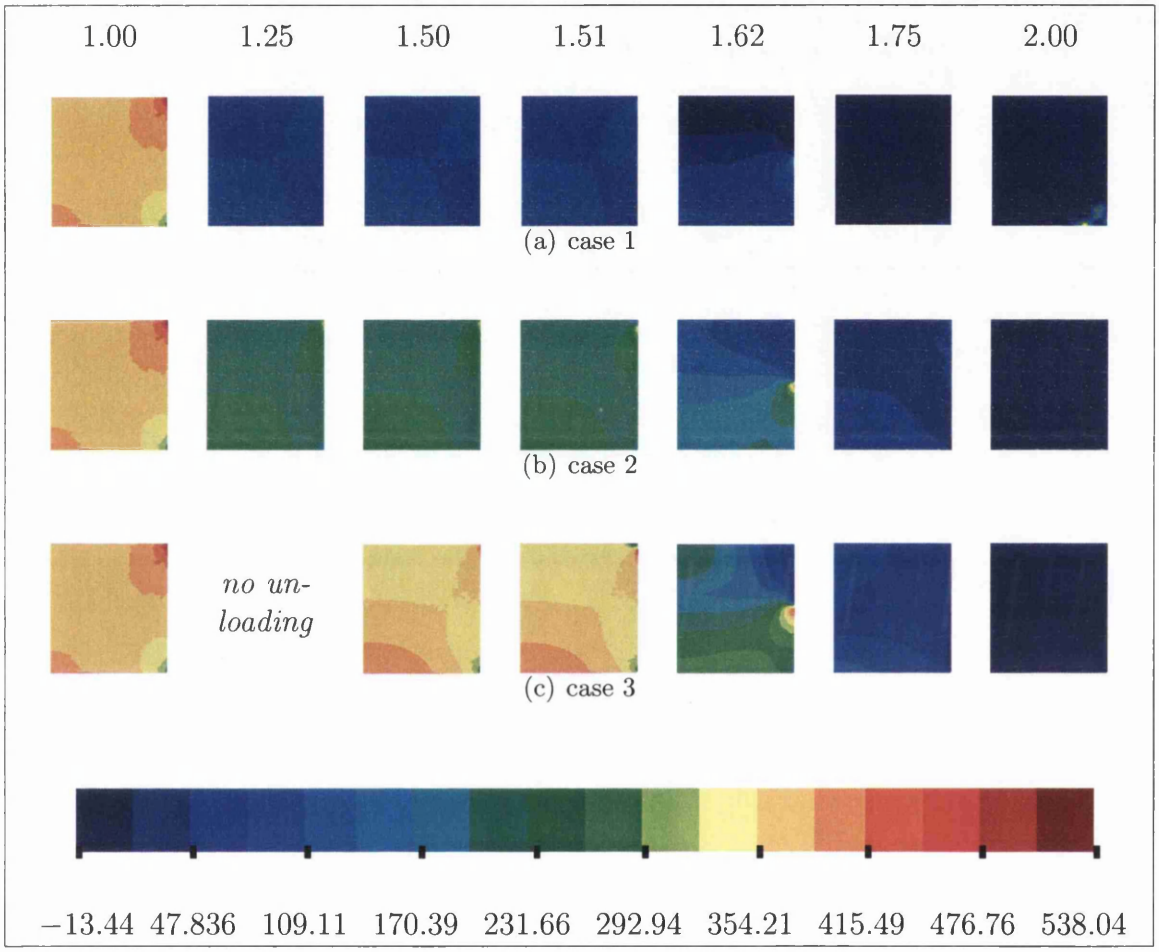

Figure 5.4: Pressure during ejection (MPa)

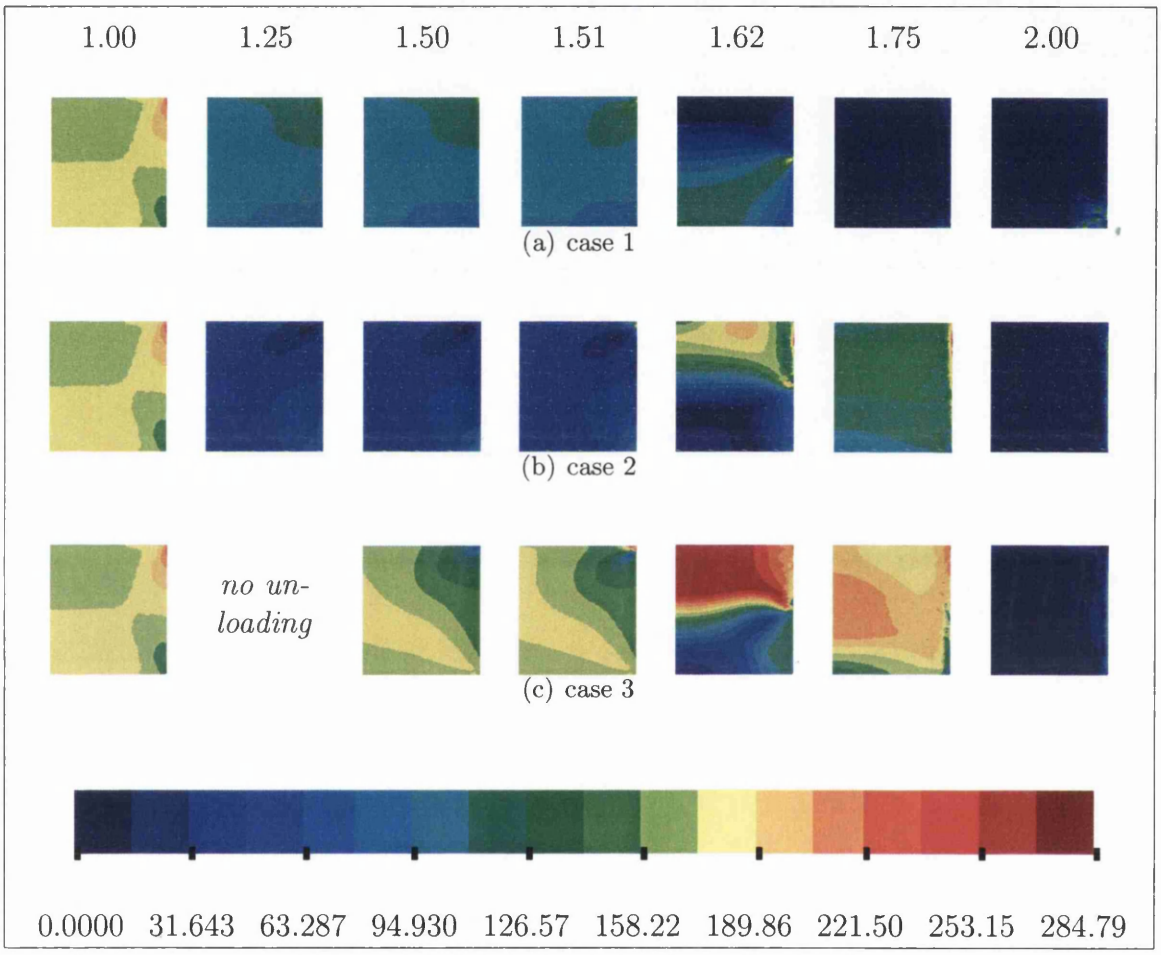

Figure 5.5: Deviatoric stress during ejection(MPa)

the radial stress against the die is more evenly distributed, resulting in a radial force on the die wall evolving proportionally to the portion of the compact remaining in the die.

It is interesting to trace stress evolution at a point of the compact during the un-

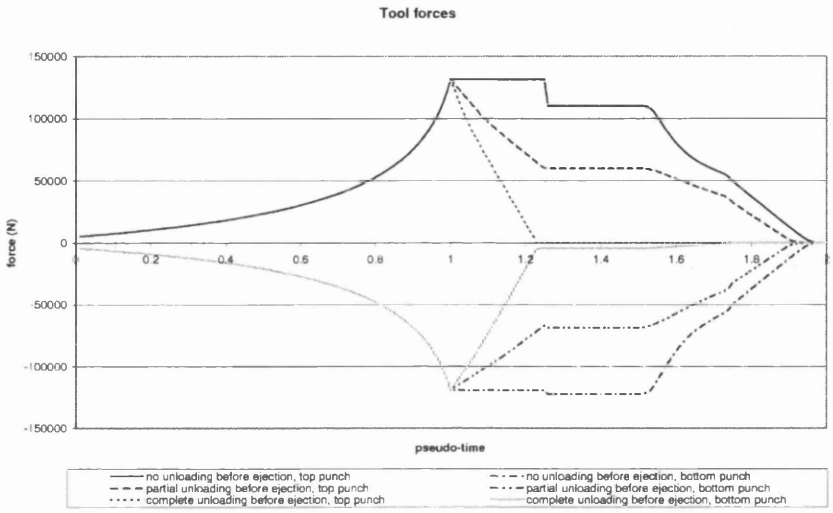

Figure 5.6: evolution of the forces on the top and bottom punches

loading and ejection cycle, particularly along the vertical wall of the compact as it is the area most affected by a change in ejection scheme. The node located at the mid-height of the initial configuration of the mesh was chosen to follow the evolution of the stresses, in particular this is presented in the $P-Q$ plane relevant to the elliptic model (Figure 5.7). In all three cases, the pressure rises until the node passes the edge of the die and then drops suddenly as it is not confined any more (Figure 5.8). Figure 5.7 shows very clearly that the only scheme in which tensile values of P are observed is the ejection scheme without any pressure maintained by the top punch. The deviatoric stress decreases with a sudden peak as the node passes the edge of the die. The peak is due to the shear stress as each section of the compact suddenly recovers the elastic strains radially. It is worth noting that without top punch load, as the node exits the die, the hydrostatic stress becomes tensile. When a partial unloading of the compact is carried out, the trend in deviatoric stress is inverted: it starts from a low value due to the homogeneous stress level between the different

directions as the top punch is maintained. This creates a mainly hydrostatic state of stress. As the node comes out of the die, the shear stress increases with the localised radial recovery because the radial direction is not confined any more resulting in a drop in pressure and an increase in the deviatoric stress. Note that shortly after passing the edge of the die (0.6mm above the edge), a low value of the deviatoric stress is obtained. This is due to a region of low deviatoric stress forming above the edge. When the pressure from the top punch is fully maintained, the same trends are observed, however, an oscillation of the deviatoric stress is observed before the node comes out of the die.

The exact source of this oscillation is not determined. It may be linked to the

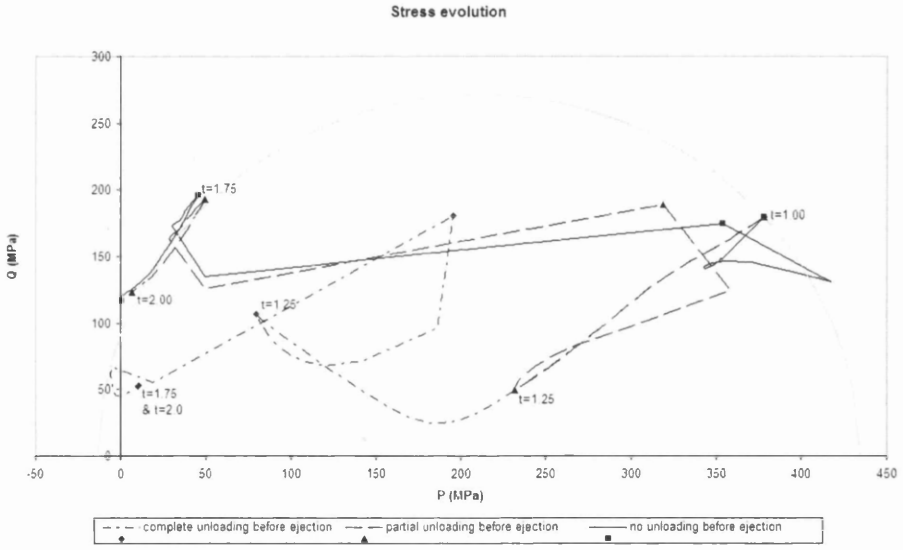

Figure 5.7: evolution of the stress state in the deviatoric plane according to the ejection scheme

material response during ejection, but it can also be due to the numerical scheme employed. A stress update based on the Jaumann rate is used in the constitutive equation, in conjunction with an updated Lagrangian framework for the calculation in relation to the mesh. The stress and strain measures are the Cauchy stress and logarithmic strains respectively. Dienes reported oscillations associated with shear stresses and the use of Jaumann rates in a total Lagrangian framework but concludes that the Jaumann rates can still be used in an updated Lagrangian

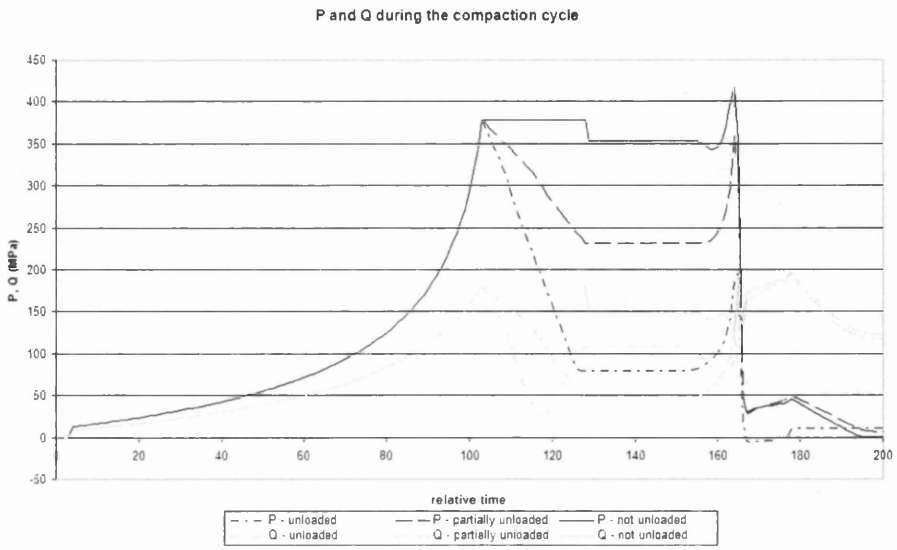

Figure 5.8: evolution of the stress state in the deviatoric plane according to the ejection scheme

framework[Die79]. Simo however, demonstrated that various objective stress rates are particular cases of the Lie derivative and demonstrates that employing this derivative gives a complete frame indifference even with shear stresses inducing rotational terms [SH98]. Finally, Crisfield reported that oscillations in plasticity problems with large deformation can be due to the equations that govern the hardening of the material [Cri97]. It is acknowledged that this phenomenon deserves attention from the research community. It is not the aim of this study to investigate oscillations in numerical methods. The reader is referred to the literature on this particular subject by Truesdell and Noll, Arnold or Marsden and Hughes [TN65, Arn78, JM94]. The present result is therefore considered as it is for this particular work, albeit with the relevant context and issues in mind.

These examples investigated the developments of conditions prone to the initiation of fractures. The correlation between identified risk factors, such as tensile and shear stresses, and the imposed tool kinematics show that the elliptic model can be used to simulate the behaviour of powders outside the usual uniaxial conditions. Qualitatively, the response of the material is consistent with observations in a production

environment. However, the evaluation of the residual stresses is a very difficult exercise and obtaining experimental data regarding the stress distributions during the compaction cycle is not possible with the methods available to date. The numerical values obtained from the simulations could therefore not be evaluated quantitatively.

5.3 Shear Cracks

The investigation of shear crack emergence was carried out by examining faulty components produced experimentally and reproducing their compaction conditions numerically.

5.3.1 Experimental Aspects

The appearance of shear cracks is mainly attributed to non uniform displacement of powder resulting in shearing of the powder. This results in a shear failure or dilatancy, depending on the material's response. Dilatancy is the increase in volume resulting from a shear deformation in granular media. Shear failure is associated with brittle materials, which are generally modelled with granular material constitutive relationships. On the other hand, more ductile models tend to exhibit dilatancy, and models for porous media are appropriate to represent their behaviour. The reader is referred to the differences in the behaviour and shapes of yield surfaces found between the alumina and ferrous powders in Chapter 3. Other conditions, such as the hydrostatic stress and the density at which the shear stresses are encountered can also influence the way in which the material responds.

For the investigation of the shear cracks, a ferrous powder was used, which exhibits a ductile behaviour. This series of experiments has its background in the Dienet thematic network, which was set up as a forum for exchanges between European research organisations and industrials in the field of powder forming. The ferrous case study 2 from the Dienet project was based on a stepped component. Its aim was to establish the performance of powder compaction simulation software with more complex geometries than previously explored. The criteria for performance

were based on density distribution and tool forces.

One of the industrial participants in the Dienet project wished to further explore the conditions under which fracture is likely to occur. To do so, experiments were carried out on a production press. The tools used were equipped with strain gauges to record stresses according to the calibration. Several geometries were compacted with variable height ratios. The tool kinematics employed were deliberately set to create defects in the component. The study was carried out as a partnership between the industry and the University of Wales, Swansea. The present work involved gathering the data from the experiments and processing, then in the reproduction of the experiments by numerical simulations. Eight series of tests were carried out with different aspect ratios illustrated in Figure 5.9. The ratios investigated are listed in Table 5.2. The components were compacted so that both columns of materials undergo a different compression ratio. The compression is therefore qualified as a heterogeneous compaction scheme. Throughout this section, the components are often divided into columns of powder for the analysis of the results. The inner column is the column of powder over the lower inner punch with a height $H2$. It encompasses all the material located between the radii of 5mm and 15mm. The outer column rests over the outer lower outer punch, between the radii of 15mm and 25mm. Its height is $(H_2 - H_1)$.

The exploitation of the results was rendered difficult by the lack of information

Table 5.2: Aspect ratios investigated experimentally, kept as the non simplified fraction of the dimensions in mm at the end of the compaction.

series number	aspect ratio
16	10/20
17	6/26
18	6/16
19	3/16
20	3/23
21	3/8
22	3/6
23	5/12

on the control system of the press. It appears that in some cases, the forces in

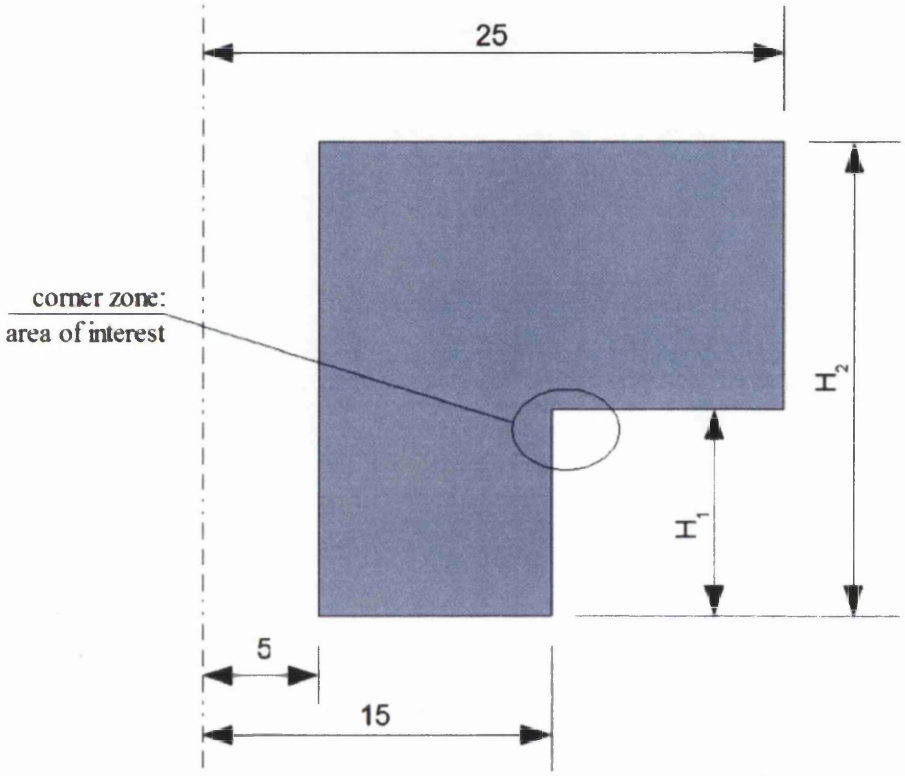

Figure 5.9: Geometry for the stepped components. The aspect ration $\frac{H_1}{H_2}$ is varied between the test series

the tools are not synchronised with the tool displacements. This is because the press used in the experiment is a production press. The speed required for the displacement of the tools within the time allowed by specifying a production rate is not achieved instantaneously, there are transition phases between the stages of the compaction/ejection cycle. For this reason, the tool kinematics set on the interface of the machine does not accurately reflect the true motion of the punches. The evolution of forces and tool displacement for the compaction of components 17, 19 and 20 are presented respectively in Figures 5.10, 5.11 and 5.12. The use of LVDTs would be a good alternative to nominal displacements given by the press.
The compaction cycle is carried out under the sole displacement of the upper punch to create a material flow around the corner. The range of height ratios produced allow an exploration of the behaviour of powder when large movements of material are generated by the motions of the tools during compaction.

Some of the components produced were retrieved from the industrial partner's

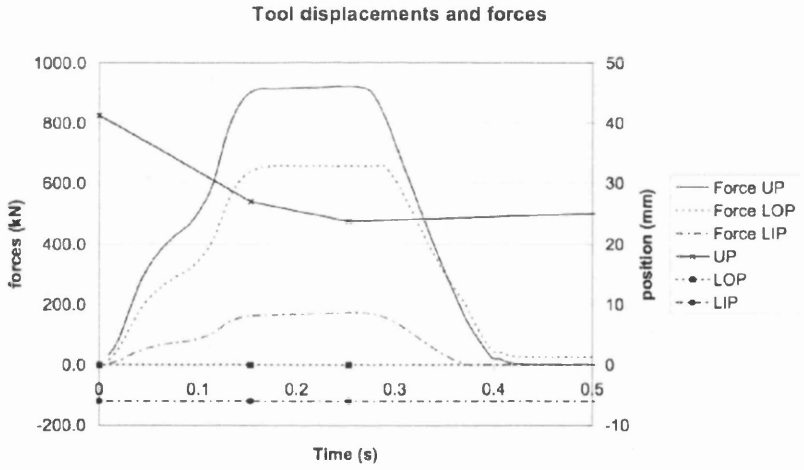

Figure 5.10: Tool forces and displacements for the compaction of component 17.

facilities for examination. Micrographs were taken with particular attention to the inner corner region highlighted in Figure 5.9 where it was observed that, as expected, the defects occurred. The most apparent defect did not appear to be the presence of fractures but regions of low density. This is illustrated in Figures 5.13 to 5.17. A region of low density is observed consistently in the corner zone of the compact from the corner, resulting in the crumbling of a portion of the compact below the corner.

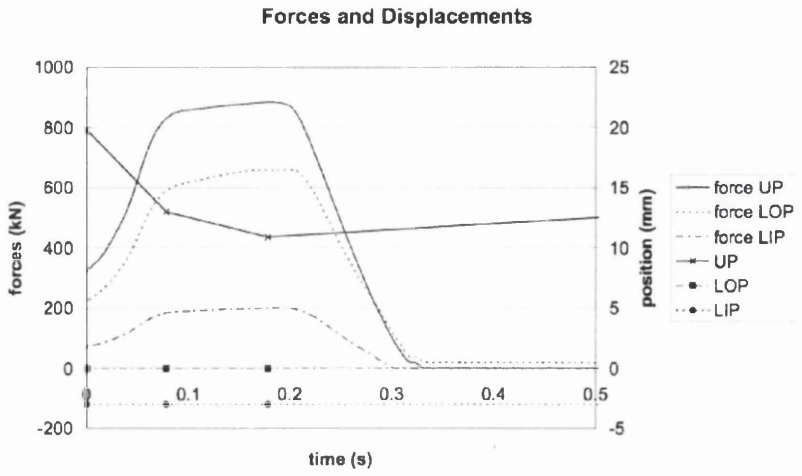

Figure 5.11: Tool forces and displacements for the compaction of component 19.

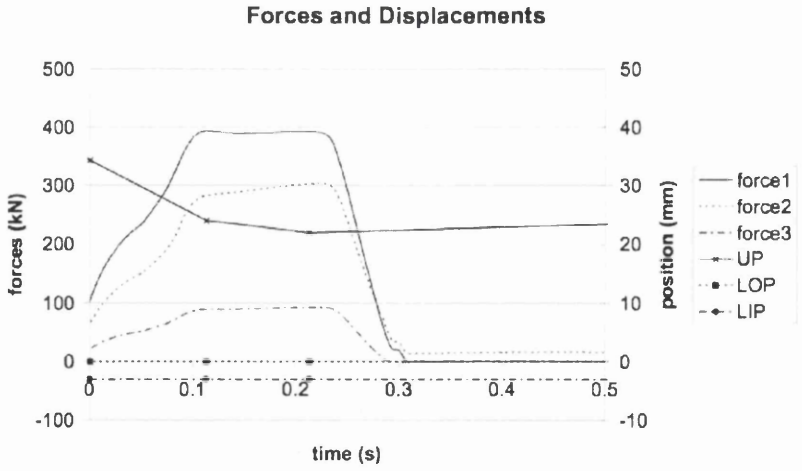

Figure 5.12: Tool forces and displacements for the compaction of component 20.

This is present in all the cases. In two cases (19 and 21), concentric fractures centred around the corner are observed that could be interpreted as shear or so-called dead water cracks (Figures 5.16 and 5.17). The detail of the corner of component 19 also appears to exhibit a fracture emerging radially from the corner and oriented towards the bottom right hand side of the image. No interpretation of powder flow around the corner or observation in the simulations exposed further can explain this. It may simply be a coincidental alignment of the grain boundary in the material.

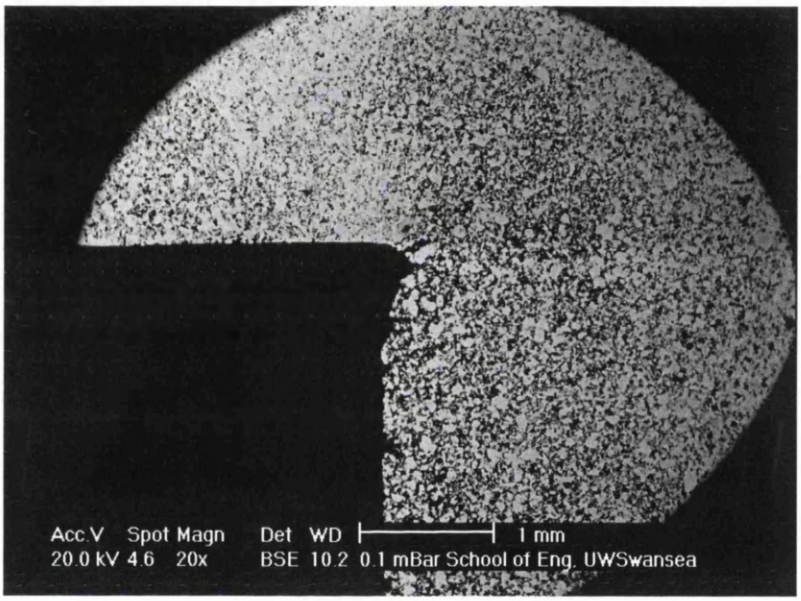

Figure 5.13: Corner of component 17.

5.3.2 Simulations

The numerical work focuses on three particular cases: components 17, 19 and 20. The dimension and tool kinematics used for the simulations are those presented in the previous section. The respective fill densities for the cases 17, 19 and 20 are 3.55g/cc, 3.68g/cc and 3.61g/cc.

The first test case on part 17 is set up with 6072 elements. The element density in the corner is very important. Despite the use of a radius in the corner, the elements

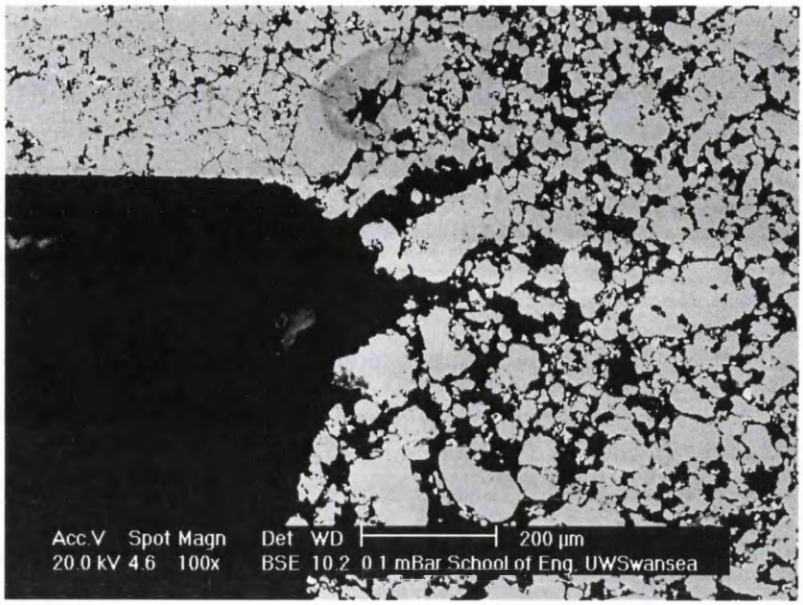

Figure 5.14: Detail of the corner of component 17.

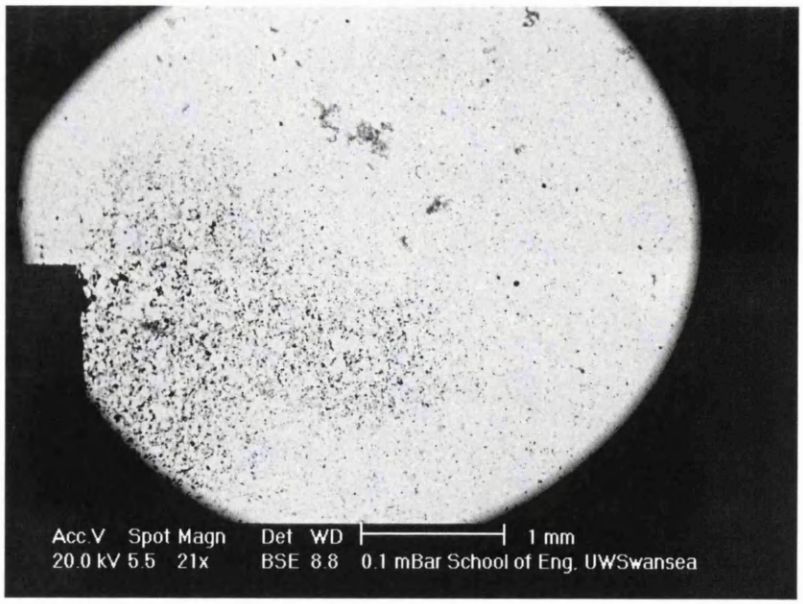

Figure 5.15: Corner of component 19.

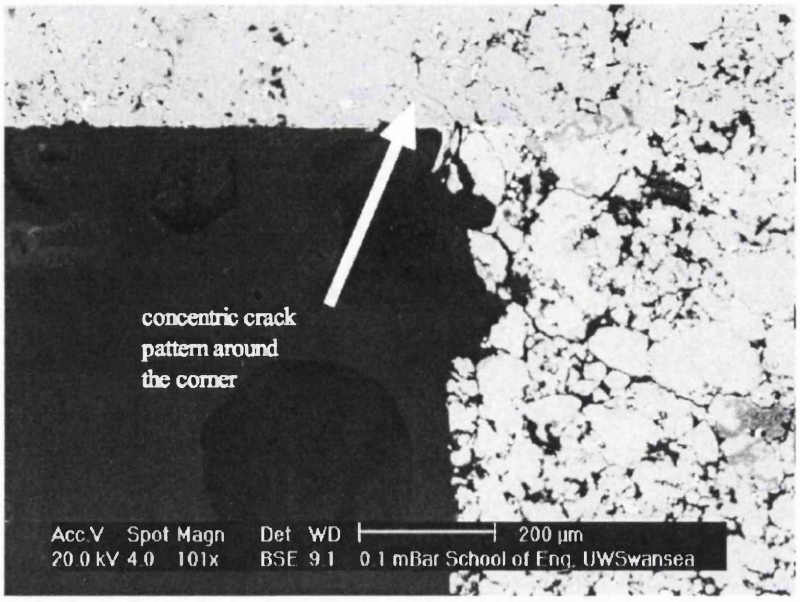

Figure 5.16: Detail of the corner of component 19. Shear marks from the material flow around the corner are apparent

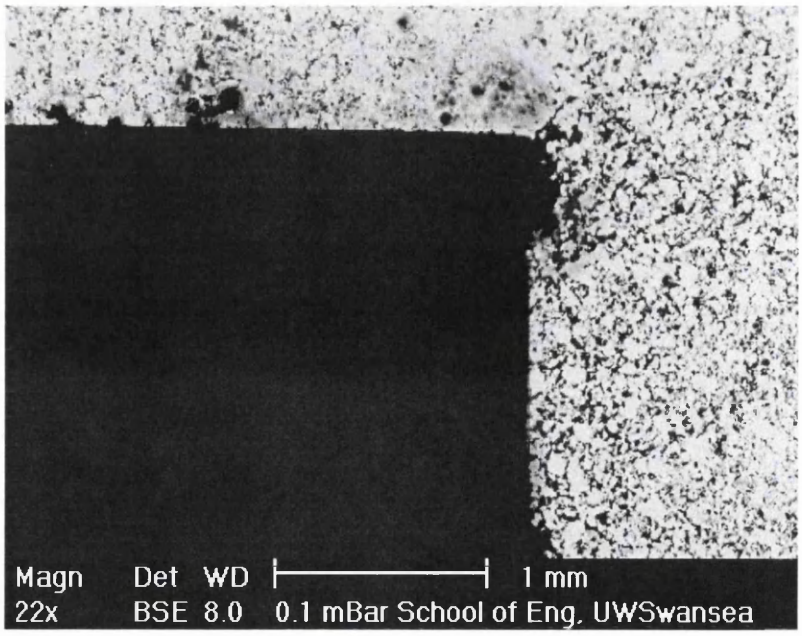

Figure 5.17: Corner of component 20.

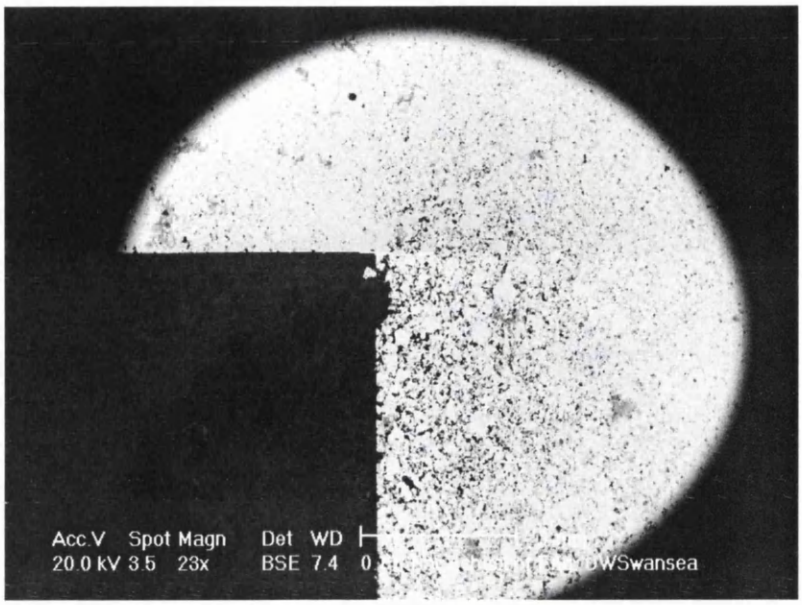

Figure 5.18: Corner of component 21.

Figure 5.19: Detail of the corner of component 21.

become grossly deformed due to the very localised gradient at the corner of the step in the component. The use of larger elements can attenuate this problem to the detriment of the solution's accuracy. In comparison, smaller elements can capture localised phenomena and gradients but are very rapidly distorted to excessive amounts in the simulation leading to calculation failure. To capture the gradients formed at the corner of the step, the length of the elements' side on the boundary was specified as 0.2mm, whereas the size of the elements over the domain is controlled by area, chosen as 0.3mm2. The simulation reached 54.5% of the compaction cycle before gross deformation of the elements made it impossible to progress further. In an updated Lagrangian scheme, this is a difficulty that cannot be overcome without a remeshing strategy. Unfortunately the code does not have the use of such a facility at this time. The fact that the simulation fails before the end of the complete compression stroke is not an obstacle to the exploration of the conditions of fracture initiation. It is also an indication that extreme conditions of deformations are encountered. It is an early indicator that, in practice, the compaction process is also likely to fail.

The density gradients around the corner show that above the lower outer punch, the density is consistently higher than 6g/cc, whereas in the lower part of the compact the density drops below 5.7g/cc. Thus, just above the corner, a very localised high density area is formed. This localised high density is caused at the interface between the columns of powder as the inner column is compacted into the bottom of the die in contact with the powder of the shallower column on the right hand side. Thus the powder in the shallower region is pushed down against the corner. The simulation of a component without a radius highlights this phenomenon by simplifying the material displacement: the radial movements are minimised so that the remaining movement is a compaction against the step and the shearing of the elements that have nodes either side of the corner. The resulting densities are more dispersed with a sharp corner. The material movements and density fields for the comparison of the corner configuration are shown in Figures 5.20 (sharp corner) and 5.21 (0.3mm radius).

The compaction of the component without a radius at the corner makes it possible to observe the influence that the mesh may have on the simulation. In this case, the movement of material around the corner is not reflected as the node situated

at the corner does not move at all. The effect of such a configuration is that the axial stress has a much higher peak (405MPa against 349MPa with a radius) on the horizontal edge of the corner, as the powder cannot slide down into the lower part of the compact. The deformation of the element on the vertical face of the compact immediately below the corner is also very stretched. This affects the quality of the numerical solution. Because of the elongation, the spatial discretisation along this edge also loses quality. Due to the stretched element in the corner, the nodal results show a high density region smeared into the lower part of the compact but the observation of the nodal values shows that the high density region is confined above the corner due to the absence of material flow around the corner to smooth the density distribution. With the radius, the mesh can move around the corner and these effects are minimised. To avoid the effect of the mesh being fixed at the corner, the simulations in this case study are carried out with a radius of 0.3mm at the corner. The better condition of the elements when a radius is present also results in further progression of the simulation. It terminates at 47.5% of the total compaction cycle with a relatively coarse mesh (3341 elements) in the case where no radius is present and 54.5% with a radius despite a finer mesh (6072 elements).

The evolution of density is presented in the sequence of Figures 5.22 to 5.26. On the left of the corner in Figure 5.26, where the column of powder is higher, the density drops sharply as the powder can be compressed into the 6mm deep step. Looking at the earlier stages, it is visible that as the compaction takes place, a loss of density can be observed just below the corner. This phenomenon is dilatancy. It is predicted by the plasticity theory of granular media. It consists of a local increase in volume under shear conditions. This phenomenon can be observed mainly at low densities in powders as reported by McDonald *et al.* [MSCW06] and can also be indirectly detected at higher densities (simple compression test, Chapter 3). The sequence in Figures 5.22 to 5.26 shows the evolution of the density at the corner with the minimum value recorded at each step. As the areas in which dilatancy is present are sheared, the arrangement of the grains of powder changes. The compact spatial configuration that was assumed is disturbed and as grains roll against each other, they occupy a larger volume. This explains why dilatancy is only recorded at low pressures and relatively low densities as plastic deformations and fracture will take place in conditions of higher pressure and density. This phenomenon is present

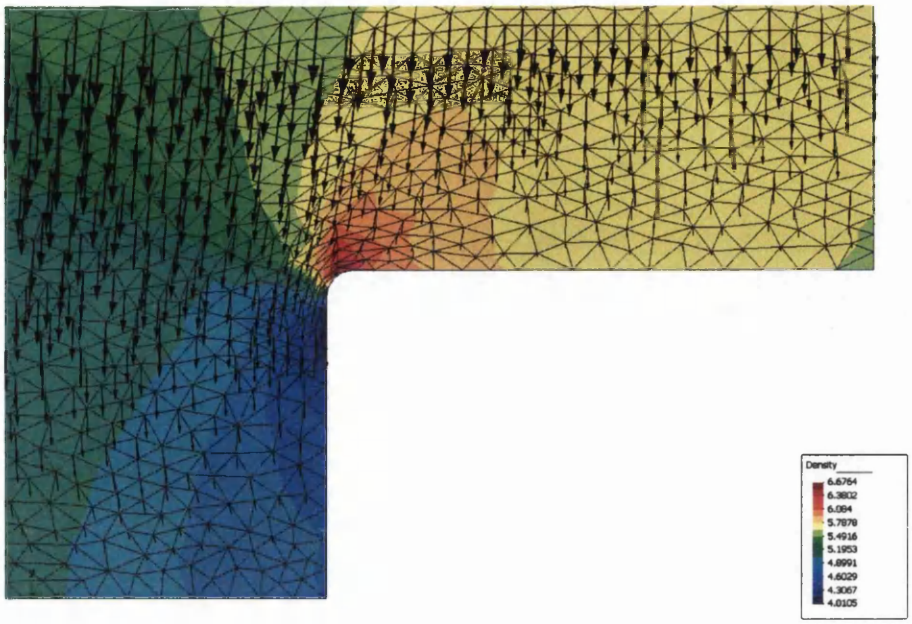

Figure 5.20: Density Contours and displacement vectors in the part 17 without a radius at the corner.

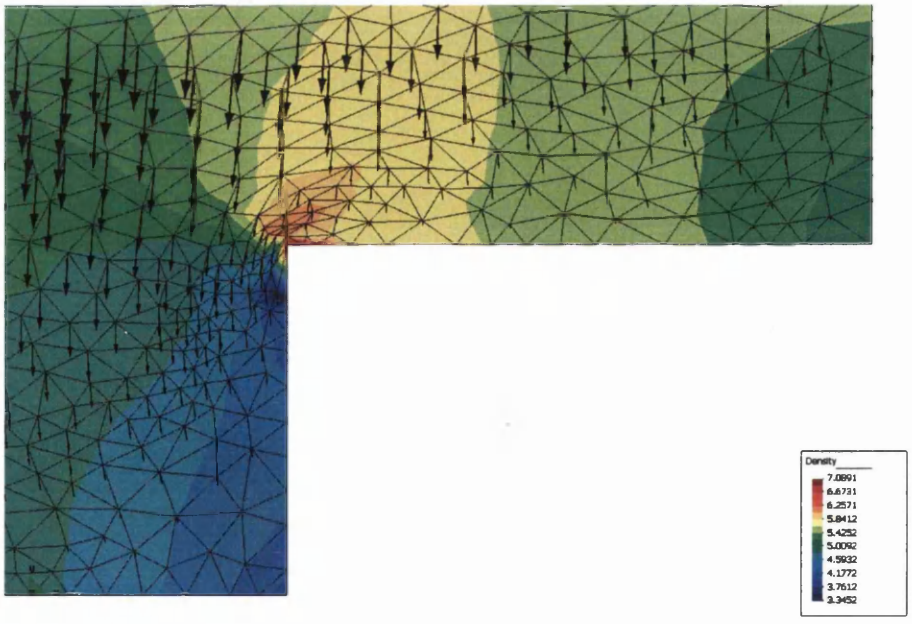

Figure 5.21: Density Contours and displacement vectors in the part 17 with a 0.3mm radius at the corner.

in each case of this stepped component compaction study.

To compare the data obtained from the examples, it is possible to observe

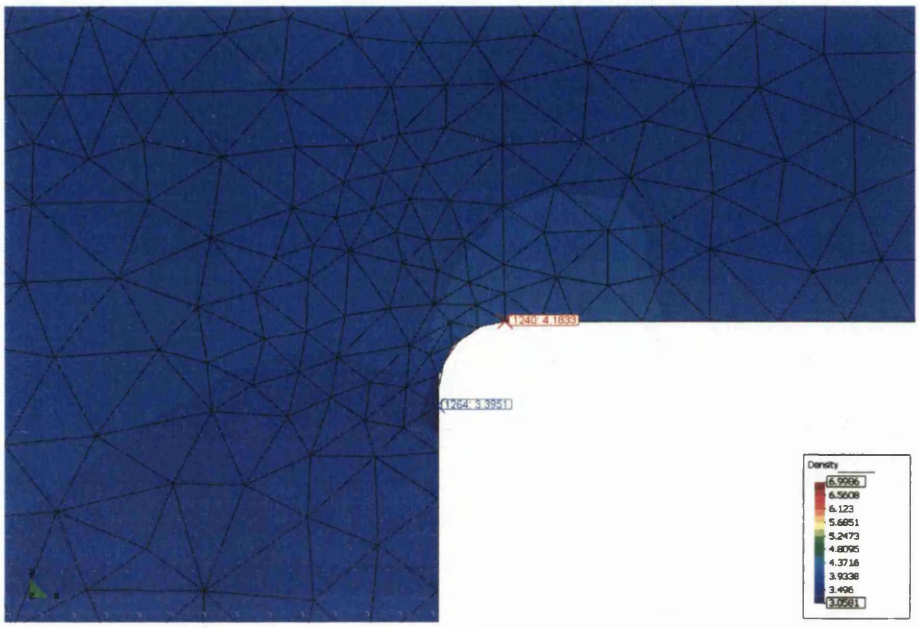

Figure 5.22: Component 17 at 10% of the compaction.

them when they reach the same compaction ratio or average density. The simulations of cases 17, 19 and 20 stopped respectively at 54.5%, 91% and 100% of the compression stroke. Using the compaction ratio would result in the comparison of series 17, 19 and 20 at 52.5%, 70% and 100% respectively with a compression ratio of 1.674:1. However, to reproduce the conditions observed experimentally, the fill densities are different between the simulations: 3.55g/cc (series 17), 3.68g/cc (series 19) and 3.61g/cc (series 20). It was therefore decided that comparing the results of the simulations when they reach the same average density is more appropriate. At 54.5%, 81% and 98% respectively, the simulations 17, 19 and 20 have a common average density of 5.96g/cc, at which the results are deemed comparable.

Figure 5.27 shows that the lowest density is found in the part number 20, although only marginally lower than the lowest value in the other parts, it is particularly important as the compact is at 98% of its compaction. The fully compacted density is 6.06g/cc and this affects the final result dramatically. In the SEM pictures, the component 20 is the one with the largest crumbled area. The other two simulated

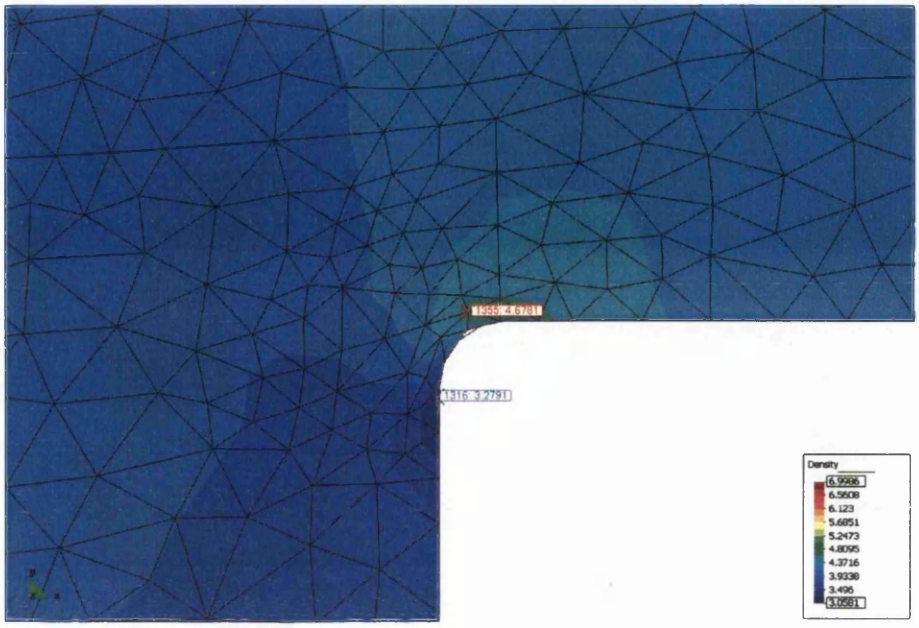

Figure 5.23: Component 17 at 20% of the compaction.

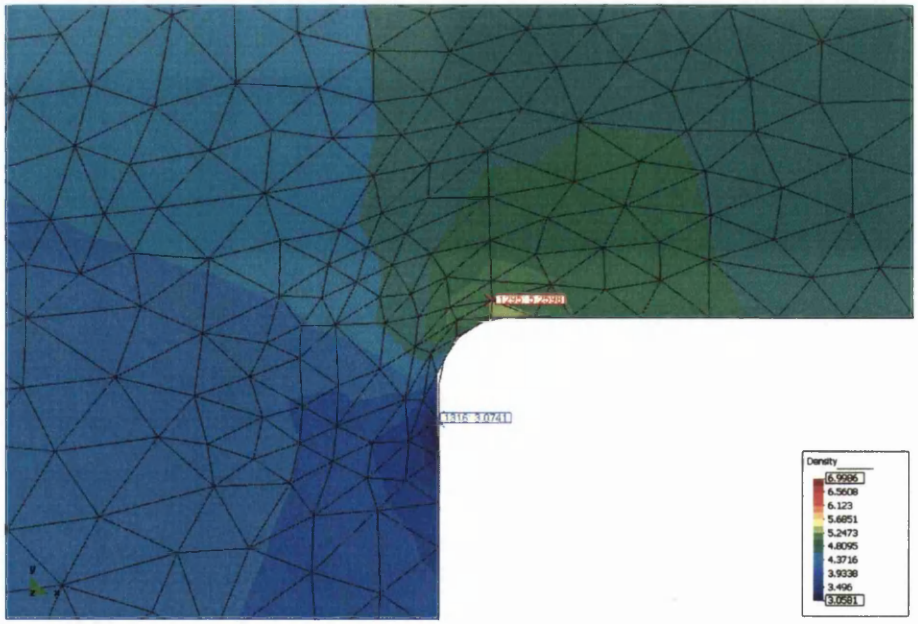

Figure 5.24: Component 17 at 30% of the compaction

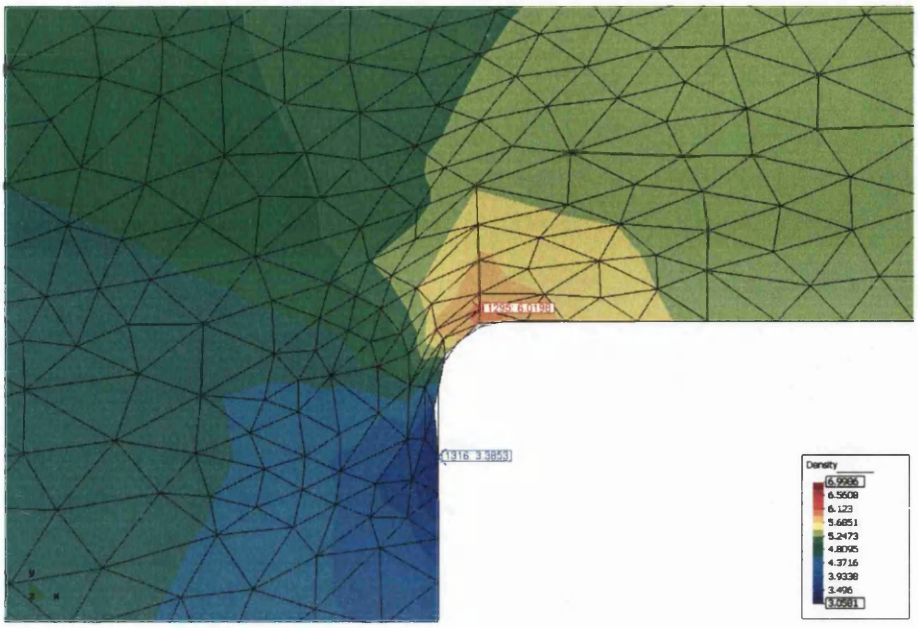

Figure 5.25: Component 17 at 40% of the compaction.

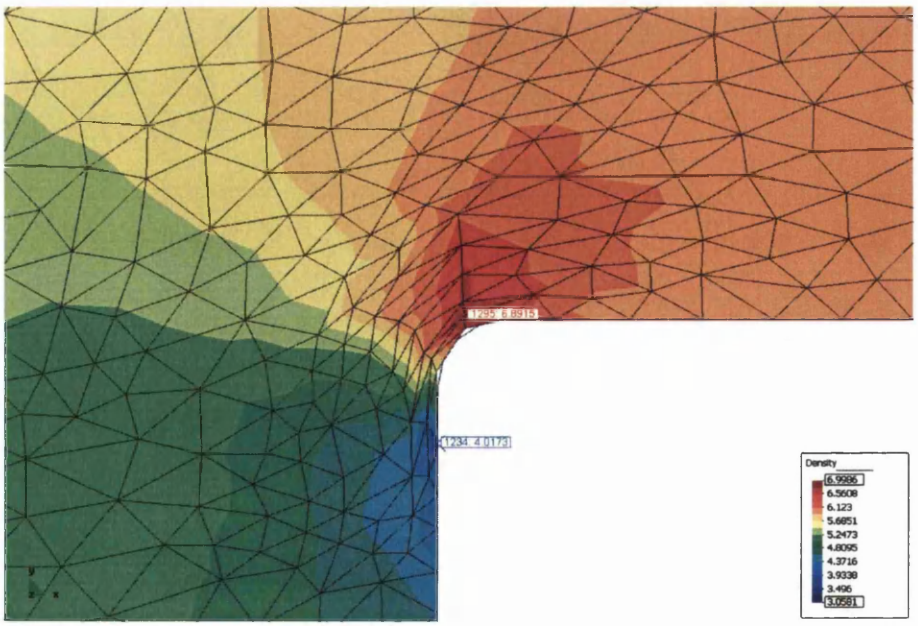

Figure 5.26: Component 17 at 50% of the compaction.

components reach higher density as they are only at 81% and 54.5% of their compaction cycle. This results in higher density throughout the compact. However, a crumbled area is still observed in the SEM images, below the corner. This shows that the area does not reach a sufficient density to sustain the stresses of ejection and the handling necessary to obtain the images. It is also possible that density in this area is so low that no cohesion is achieved by the compaction. Shear stresses, however are higher in the components 17 and 19 (Figure 5.28), just over the corner. This area is affected by concentric shear fracture present on the SEM images (Figures 5.19 and 5.21).

Plotting the evolution of density in Figure 5.34 shows that the component 17 clearly exhibits dilatancy. On the other hand, although dilatancy occurs in the other components, it is not as pronounced and observation of the results shows that it is due to an increase in the volume of the element to which the node belongs, which occurs as the edge of the element returns in contact with the boundary. This can therefore be treated as an effect of the spatial discretisation and not a phenomenon attributable to powder behaviour, such as the dilatancy observed under shear conditions.

This set of simulations shows that dilatancy is predicted by the numerical model but is not a principal cause of cracks in the components studied. The most important cause of fracture is the presence of high shear stresses. The dilatancy phenomenon develops in areas where, instead of cracks developing, the collapse of a region is observed due to a lack of cohesion in the material. As shown by the SEM images and the simulations, dilatancy is not necessarily present to obtain the collapse of region, the densification may simply be locally insufficient.

The dilatancy, however can be interpreted as a sign of material weakening. Its presence at low densities can have little effect as the material may develop cohesion as it is subsequently compacted but a loss of density at a high relative density is a sign that the material is damaged. Indeed, any plastic deformation with a gain in volume can result in the dislocation of the interlocking previously achieved between the particles.

The achievement of cohesion can be seen as a process which only starts from a threshold density and nucleates in a statistical manner, much like solidification in casting processes. For a valid representation of the risk incurred by dilatancy in a continuum model, a threshold density needs to be identified from which the domain

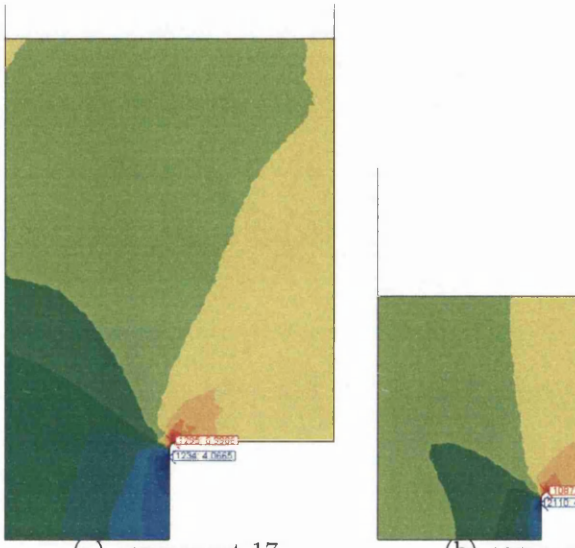

(a) component 17

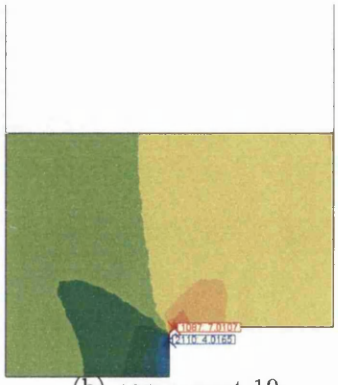

(b) component 19

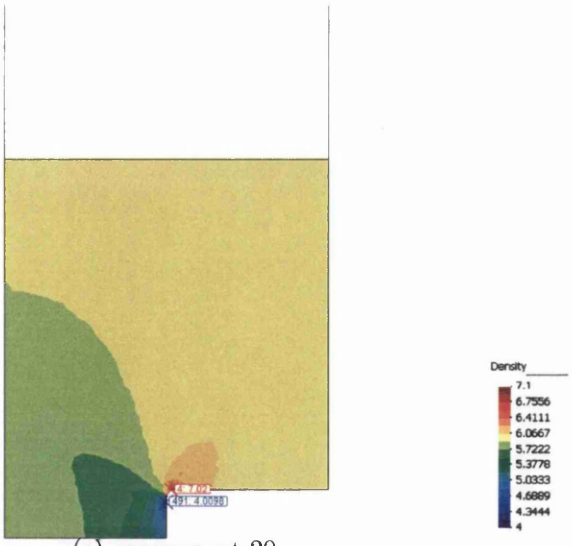

(c) component 20

Figure 5.27: Density contours when the components reach an average density of 5.97g/cc.

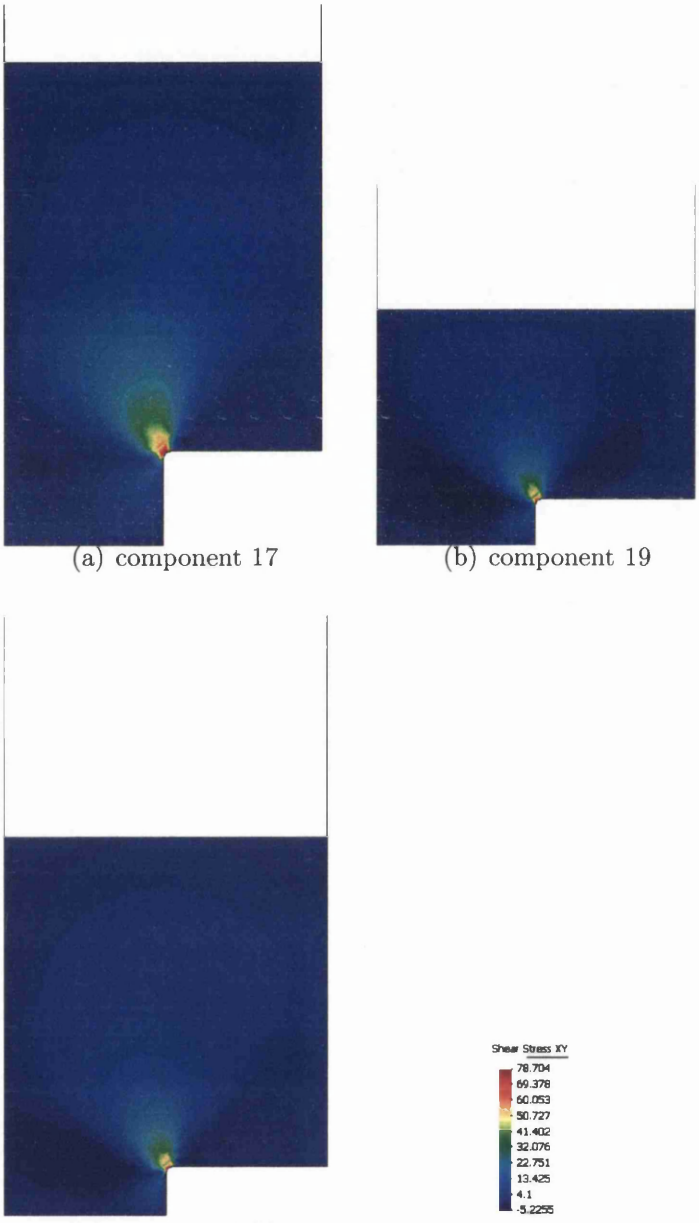

(a) component 17 (b) component 19

(c) component 20

Figure 5.28: Shear stress contours when the components reach an average density of 5.97g/cc.

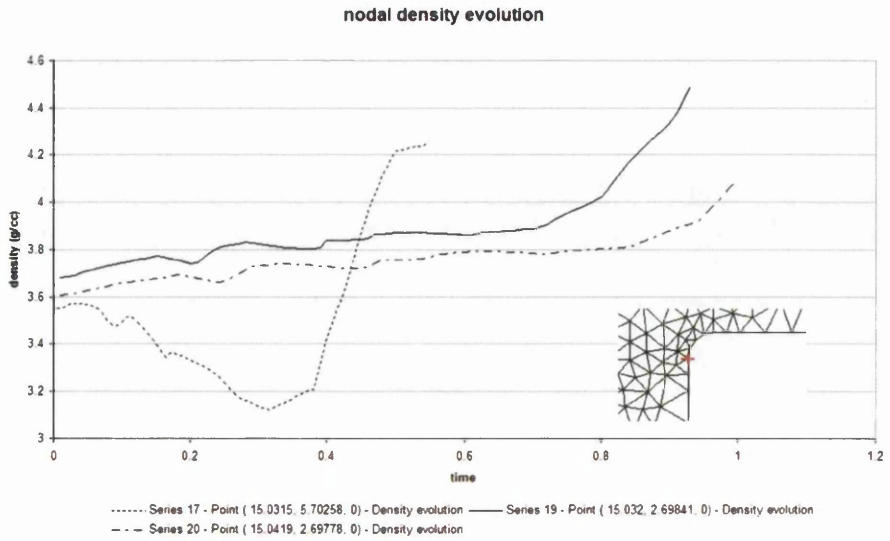

Figure 5.29: Evolution of the density at the node below the corner of component 17, 19 and 20.

is not considered to be granular any more but solid. The failure by dilatancy above this threshold is then considered critical. Thus modelling the initiation of failure needs to take into account the statistical nature of the material behaviour and the transition of the material from non-cohesive (granular) to a cohesive state (porous solid).

5.4 Development of a Crack Initiation Risk Index

This particular crack initiation risk index does not aim to predict the growth of fracture, but it was developed to be an indicative tool to help identify areas which may cause problems in an industrial context.

As highlighted in the second chapter of this thesis, models for crack growth prediction have already been developed [TA06]. These models, however have an important drawback: they can only predict fracture growth when a defect is already introduced. Also they are deterministic in their way of defining fracture. Chapter 3 showed, with the Brazilian disc test in particular, that crack initiation is essen-

tially statistical even if the repeatability of the loading curve is good. This led to the choice of a statistical approach for defect prediction, in which the propensity of crack initiation is investigated rather than the full growth of a fracture. This approach is also coherent with the industrial context of the work as it is of no interest, during a product development, to know how a crack evolves. The key issue is to know whether cracking will occur at all. The Brazilian disc test is a good example of a test that can be used to calibrate a statistical crack propensity criterion. Direct tensile tests and shear tests can also be considered. The main requirement is that the fracture initiation is clearly identifiable in the test.

The cracks can be identified as taking place in the particular region of the stress domain located on the tensile side of the critical state line of the elliptic model. This can be exploited in conjunction with the statistical approach to establish the basis for a crack initiation risk.

To formulate a risk index for fracture occurrence, the Weibull distribution was chosen. This distribution needs an origin at which the event probability is null and the definition of the variable on which the probability depends. A risk region was identified and a base line can be used in the $P-Q$ plane where the risk of fracture can be considered null. The variable which can be exploited from this configuration is the distance between the base line and the stress locus at which the risk is evaluated in the $P-Q$ plane.

This section introduces the crack propensity criterion as an outcome of the work carried out for this thesis. The conditions in which fractures occur have been identified experimentally and it was shown in the previous section that the finite element model used throughout this work can reproduce the conditions that lead to failure and respond appropriately to changes in the tool motions that are used to avoid cracks in the industry. This section makes use of this information to formulate a crack propensity criterion, which encapsulates material variability in the Weibull distribution used to calculate the risk of fracture with a particular set of stress and state variables (subsection 5.4.1), and which also encapsulates the kinematic variability of fracture propensity with the cumulated risk function throughout the material history, presented in subsection 5.4.2. These parameters are calibrated with a logical argumentation as this is used as a proof of concept for the introduction of this new crack propensity criterion. However, some tests can be used to calibrate

it more accurately as mentioned above. The three following subsections present the properties of the statistical model, followed by a subsection on the exploitation of the model. This is then illustrated by two examples in section 5.5.

5.4.1 The Weibull Distribution

The base line needs to be defined in shape and position. The use of the critical state line can be considered for this but the use of an ellipse has advantages. By using a portion of an ellipse concentric with the yield surface, the distance between the stress point and the baseline is along the line passing through the centre of the ellipses and the stress point $P-Q$. This is represented by the axis x in Figure 5.35. It can be assumed that, for purely hydrostatic stresses, a compressive state cannot lead to fracture in the elastic region, whereas a proportion of the compacts may start failing as soon as they are subjected to any tensile stress. This assumption leads to the baseline of the distribution passing through the origin of the $P-Q$ plane.
A second point of the baseline can be chosen because it represents, in an associated model, the limit condition between the compacting and dilating region of the yield surface. When the compact enters the dilating region, its integrity can be considered at risk, whereas under compacting conditions, consolidation occurs, therefore the baseline will go through the point of the yield surface where Q is maximum.
It is then chosen to calibrate the probability distribution so that the likelihood of the compact failing is 0.99 when it reaches the yield condition under a purely hydrostatic tensile stress.
The present distribution (Figure 5.35) is used to illustrate and demonstrate the principles of the model. The present calibration is based on reasoning and a choice of risk at one point. These assumptions can be compared to statistical data collected experimentally. The model makes provisions to accommodate a variation in the distribution parameters according to the angle θ (Figure 5.30).
The baseline is described by:

$$\frac{Q^2}{Q_0^2}+\frac{(P-P_1)^2}{P_1^2}-1=0 \tag{5.1}$$

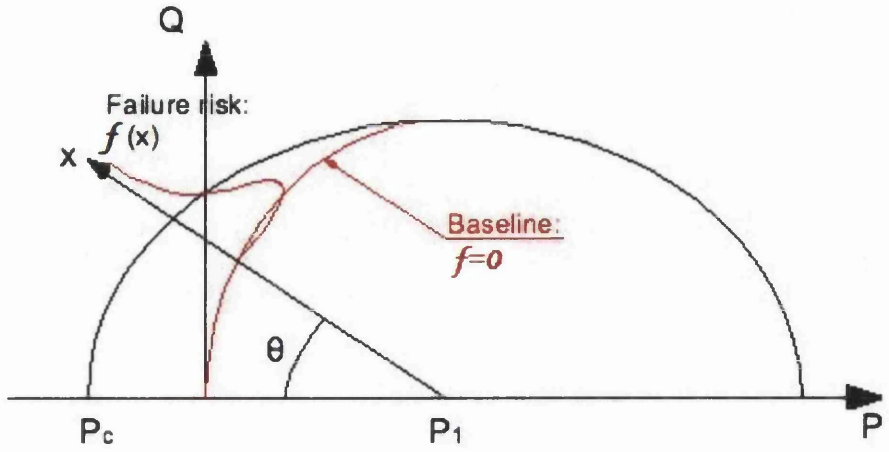

Figure 5.30: Risk of failure — Weibull distribution

At any point (P, Q) of the stress space on the tensile side of the critical state, the probability assessment parameter x of a Weibull distribution can be calculated as the distance from the baseline of the distribution along the line passing through the stress locus (P, Q) and the centre of the ellipse. It is then necessary to find the intersection between that line and the baseline.
The distribution variable x can be calculated as:

$$x = \sqrt{(P - P_1)^2 + Q^2} - \sqrt{(P_{int} - P_1)^2 + Q_{int}^2}$$

The risk of failure is expressed at x as the Weibull probability function for $x > 0$:

$$f(x) = \frac{b}{\alpha}\left(\frac{x}{\alpha}\right)^{b-1} \exp\left(\left(\frac{x}{\alpha}\right)^b\right)$$

In which is a scale parameter, which can be a function of θ, and b is a shape parameter investigated further (Figure 5.38). The cumulated probability function, defining the probability of the event between 0 and x is:

$$Fx = 1 - \exp\left(\left(-\frac{x}{\alpha}\right)^b\right)$$

5.4.2 Calibrating the Distribution

For this first study on predicting the propensity of fracture in powder compacts, a very simple calibration was used. The probability distribution was assumed to be independent of the angle θ (Figure 5.35). The weight can also be kept very simple, so the relative density is chosen. Two parameters are assumed here. Data from observations of failure in production or in a large series of experiments would need to be used.

The shape of the distribution is determined by the exponent b. It is set as 2 in the present study. The corresponding shape of the probability function is shown in Figure 5.31. The scale parameter α can be calculated from a single point of the yield surface at which the probability of failure, $F_{\theta=0}$, is known. It is decided for this case that this point is the point of tensile hydrostatic yield. It can therefore be deduced:

$$F_{\theta=0} = 1 - \exp\left(-\left(\frac{x}{\alpha}\right)\right)$$

in which $F(pc)$ is known and $x = |P_c - P_1|$. Rearranging gives:

$$\alpha = \sqrt{\frac{(P_c - P_1)^2}{-\ln(1 - F_{\theta=0})}}$$

As specified previously, this particular study uses $F_{\theta=0} = 0.99$, therefore:

$$\alpha = \sqrt{\frac{(P_c - P_1)^2}{4.605}}$$

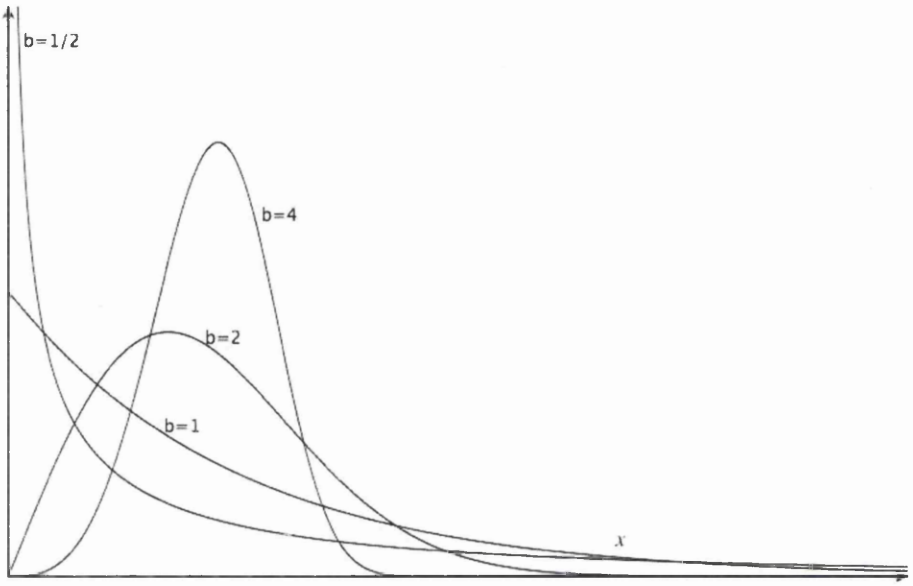

Figure 5.31: Shapes of the Weibull probability distribution with varying shape factor b

5.4.3 Evolution of Damage and Possibility of Recovery of the Material

The index for the risk of fracture occurring needs to take into account that, at low density, the material may not yet have reached a cohesive state, thus powder flow happens without fracture and the risk is very low, but a high risk is incurred when the the stress is in the area of the the $P - Q$ plane that was identified as crack prone. This transition can be reflected by the use of a history dependent function to establish the cumulated risk throughout the compaction cycle and by the use of a weight function based on the density. Finally, the index is based on statistical methods. It should therefore take values between 0 and 1 to indicate the probability of crack occurrence. Based on these considerations, the following function is introduced:

$$R_n = \tanh\left(\frac{W_{n-1}R_{n-1} + W_{max}F(x_n)}{2W_n}\right)$$

where R is the cumulated risk over the history. W is the weight function introduced above, Wmax is its maximum value encountered during the simulation at the point considered. $F(x_n)$ is the probability of a fracture initiating at the time n. The subscripts indicate the time step at which the value of the concerned variable is computed.

The weight function is critical as it governs the ability of the material to recover when recompacted in the cases when a loss of density occurs. This type of phenomenon typically happens at low density. At high density, a fracture is more likely to appear, which cannot recover. The weight function is introduced to reflect this change in behaviour towards damage conditions . The simplest form it can take is equating it to the relative density:

$$W = \eta = \frac{\rho}{\rho_{max}}$$

A more advanced possibility can take into account an evaluation of the density from which cohesion develops and how it grows over a density range. Once the cohesion density is reached, the weight function takes a high value and as a consequence, any risk of fracture at such density will have a greater impact on the damage/fracture index history. A proposed form for such a function is:

$$W(\eta) = 0.5\left(\tanh\left(A\left(\frac{\eta}{B} - 1\right)\right) + 1\right)$$

A can be interpreted as a parameter setting the band of relative density over which density develops and B sets the average relative density at which cohesion appears. The influence of these parameters is illustrated in Figures 5.32 and 5.33.

The parameter B can be determined from the Brazilian disc test for example. In, section 3.3.4, a curve fit on values of fracture initiation stress against density suggests that the lower density at which tensile stress can be sustained is 4.65g/cc as it is the value at which the fitted curve intersects with the density axis. This corresponds to a relative density of 0.627 which can be used for B in the weight function for a DistaloyAE powder mix.

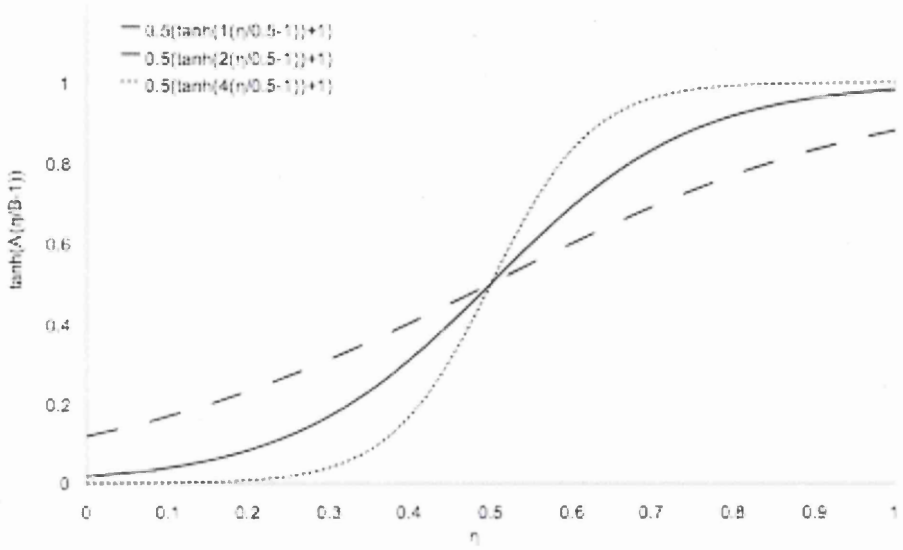

Figure 5.32: Change in the weight function with the parameter A

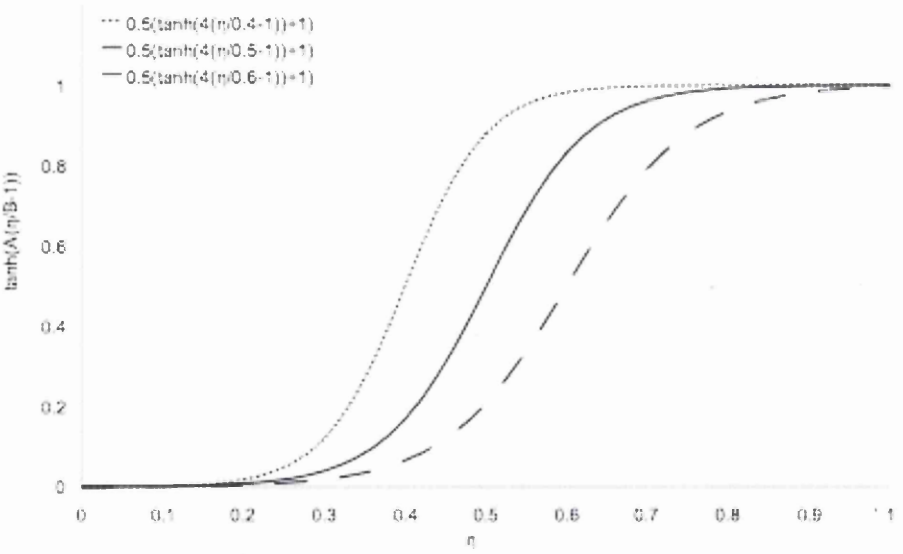

Figure 5.33: Change in the weight function with the parameter B

5.4.4 Definition of the Origin of the Weibull Distribution on the Elliptic Baseline

Defining the x axis requires fitting a line through (P, Q) and the centre of the baseline ellipse, $(P_1, 0)$, thus:

$$Q = aP + b \tag{5.2}$$

$$a = \frac{-Q}{P_1 - P}$$

$$b = Q - aP$$

The intersection is then calculated by satisfying equations 5.1 and 5.2. Substituting equation 5.1 into equation 5.2 gives:

$$\frac{a^2 + 2abP + b^2}{Q_0^2} Q_0^2 + \frac{(P - P_1)}{P_1^2} - 1 = 0$$

$$P^2 \left(\frac{a^2}{Q_0^2} + \frac{1}{P_1^2} \right) + P \left(\frac{2ab}{Q_0^2} - \frac{2P_1}{P_1} \right) + \frac{b^2}{Q_0^2} = 0$$

$$A = \frac{a^2}{Q_0^2} + \frac{1}{P_1^2}$$

$$B = \frac{2ab}{Q_0^2} - \frac{2P_1}{P_1}$$

$$C = \frac{b^2}{Q_0^2}$$

The roots of the polynomial are calculated as

$$P_{i,ii} = \frac{-B \pm \sqrt{B^2 - 4AC}}{2A}$$

with both roots real if the intersection exists. The value of the pressure at the intersection, P_{int}, is P_i or P_{ii} such that is such that P_{int} is smaller than P_1 then Q_{int} is calculated from equation 5.2.

5.5 Examples

The test cases used to investigate the conditions in which fracture may occur were used to analyse the proposed formulation for fracture propensity. The simulations for the cylinder and the stepped component 17 were repeated after implementation of the fracture initiation index. The Weibull distribution shape parameters was defined as b=2 and the scale parameter was calculated at each evaluation of the risk so that 50% of the compacts are considered to have failed if they reach the hydrostatic tensile stress of the yield surface. The scale parameter is assumed independent of the angle θ. Finally, the relative density is used as the weight function.

5.5.1 Test Case: Ejection Crack

The three simulations presented in section 5.1 were used to investigate the behaviour of the fracture initiation criterion. They differ by their unloading and ejection scheme. The first one undergoes a complete unloading in the die before ejection, the second one undergoes a partial unloading and is then ejected, whereas, in the third case, the part is ejected with the top punch maintained in position on the top surface. It is then unloaded after ejection.

At the end of the compression stroke, as expected, no risk is observed for the integrity of the components. During the ejection phase, the risk index remains zero throughout all three components until the compact starts emerging from the die. As the compact emerges from the die, the risk index rises in the component where no top punch pressure was maintained. The area affected matches the area affected by tensile stresses. Figure 5.34 shows the components at 75% of the ejection stroke, which corresponds to half of the compact being out of the die. The areas subjected to tensile stresses are clearly identified by the risk index. As the compact is pushed out, the risk index increases to 1 on its upper surface then goes down again. The reason for the decrease in the risk index is discussed further. The ejection scheme with a partial unloading exhibits points of localised risk not exceeding 0.33 along the vertical wall. In the scheme with the top punch fully maintained on the compact, the risk index remains equal to zero throughout the entire ejection. The result after unloading of the parts shows important areas with a high risk index. These

are the areas where tensile stresses develop. The shear stresses appear to have little effect on the risk index. The calculated risk index distributions are shown in Figure 5.34 at 75% and 100% of the simulated ejection. An important portion of the risk area is within the compact. Although these areas were found to be risk regions, it is unlikely that fracture initiates there, as fracture tend to grow from existing surfaces. According to this, the greater risk region is on the lower part of the outer surface of the component ejected without any top punch pressure.

These examples demonstrate the use of the risk index developed in the previous

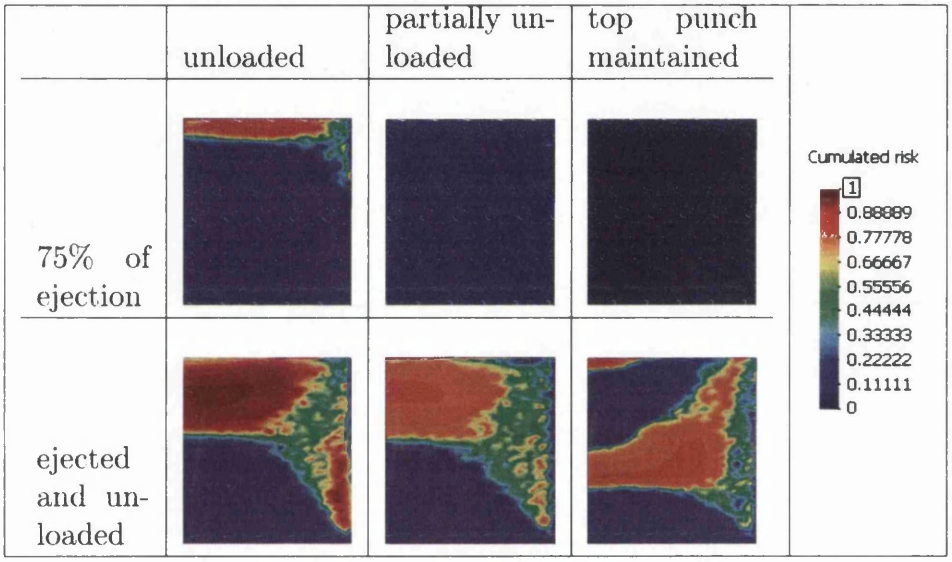

Figure 5.34: Calculated fracture initiation risk index according to the unloading scheme above.

section to identify regions likely to develop defects. It required an adaptation of the finite element program for its implementation: the value of the risk index must be capped to 1 at the stage where the results are interpolated from the integration points to the nodes of the mesh. This procedure carried out by a least square method, which can result in values of the risk index greater than 1 at nodes on the boundary. The use of a finer mesh or higher order elements can be a solution in areas of important gradients, an investigation of error estimation and mesh refinement is available in Khoei's thesis [Kho98].

The risk index, in this particular case yields good results to identify where tensile

cracks can emerge. However due to the very simplified calibration the regions of shear stress do not appear highlighted. This is because the scale factor α is kept independent of the angle θ in the $P - Q$ plane. In the next section, the failure is linked to the emergence of shear stresses, which will highlight the performance of the criterion in such conditions.

5.5.2 Test Case: Shear Crack

Of the tests carried out to investigate the shear cracks, the case 17 was the only one repeated with the implemented crack initiation propensity criterion. This is because it is the only one in which the dilatancy effects have been confirmed as a consequence of shear stresses rather than mesh displacements and because the shear fracture also appears to be present on the micrographs concentrically around the corner.

The highest risk (index level 0.49) occurred at 21% of the compaction (Figure 5.35) and then decreased to 0.3 as density increased as part of the recovery with compaction. It was located in an area of low pressure and low density, below the corner. The area of high shear stress located above the corner with high density is not highlighted. This indicates that if an associated elliptic model is used, covering the dilating region of the yield surface with a fracture risk criterion is not sufficient. It highlights the possibility of the emergence of fractures under a compressive state with high deviatoric stresses.

Superimposing the resulting risk distribution on the SEM image in Figure 5.36 shows that the zone that was predicted to be damaged is located lower than observed on the SEM image. This can be attributed to several factors. Once the material is damaged, it behaves differently due to the lack of cohesion developed. This affects tensile and shear stresses mainly as compressive stresses can still be transmitted. Also, the image shows that the radius of 0.3mm at the corner may have been an overestimation. It was simply specified as a rounded edge for the tool manufacture.

The case studies demonstrated the principle of an empirical criterion defined in the stress space. It highlights the issues associated to detecting fractures. The functions for the baseline and weight used to map the risk of fracture criterion are chosen for

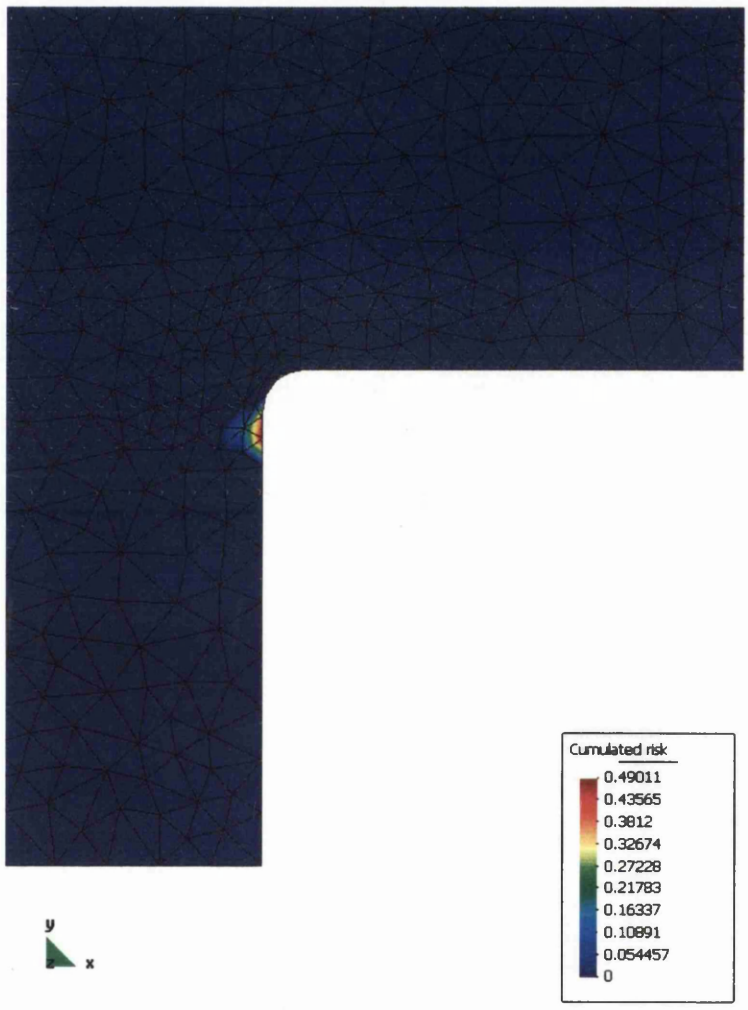

Figure 5.35: Damage risk in component 17.

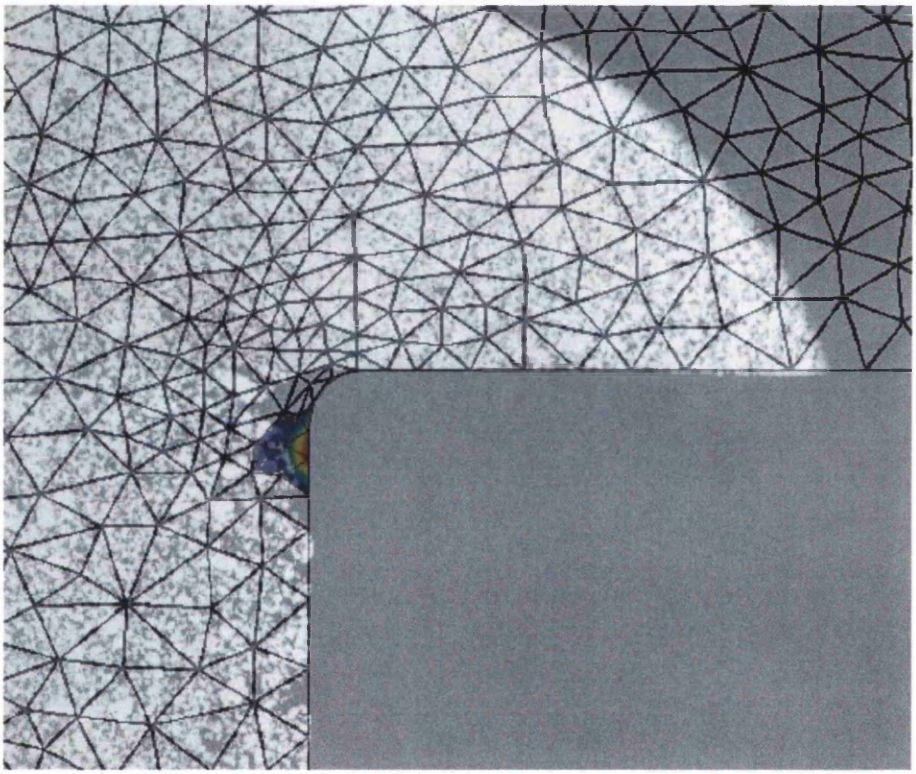

Figure 5.36: Superimposed damage risk in component 17 and SEM image.

a proof of concept. They show that fracture does not only appear under the dilating conditions of the plastic potential or yield function in this associated model.

5.6 Closure

This chapter presented two aspects of fracture investigation. The first part, experimental, investigates the conditions of fractures initiation. Tensile and shear conditions are identified. Also, it was demonstrated that in the case of bad synchronisation in the tool movements, the most likely source of defects is the fact that some regions do not undergo appropriate densification, and this phenomenon can be reproduced by simulation. The resulting low density regions are shown to have crumbled away from the parts.

A crack initiation risk index is introduced. The functions used in this study to define the behaviour of the index are chosen for a proof of concept. The rules defining the risk index are empirical, and the objective is to demonstrate the exploitability of a stress based criterion. The index can be appropriate for industrial use where data collection is combined with simulation tools. The studies presented show that the criterion in its current form is sensitive to low pressure conditions but does not always show high shear stress regions. A modified form of the baseline for the distribution is an expected development that would arise from sampling a large number of failed compacts.

Chapter 6

Conclusions and Recommendations

The work presented in this thesis led to the formulation of a statistical crack propensity criterion. The criterion rests experimental evidence that failure occurrences are difficult to characterise in a deterministic fashion. The proposed formulation takes into account the material history and the initial results show good correlation with experimental observation.

As a part of the study, the influence of the ejection scheme and material movements in the non homogeneous compaction of a stepped component. The ejection study showed that tensile stresses develop when no pressure is maintained and also the presence of a layer of material re-compacted during ejection on the outer wall of component ejected under a top punch load. The non homogeneous compaction of a stepped component highlighted the material movements and dilatancy in conditions of dominant shear stresses.

The Lode dependency of powders was investigated. Based on published experimental data, a Lode dependent model was developed and implemented. The test cases show that important variations can occur in the peak values of the stresses. A 31% difference was observed in residual axial stress between the models. The general aspect of the stress distributions throughout the components is not significantly affected, neither is the density distribution. The tool forces are consistently marginally lower with the Lode dependent model. This highlights that the Lode dependency is

an important factor when looking for the conditions in which failure can occur, but has little interest in toolset design or in the evaluation of density distribution in a component.

The experimental investigation, in Chapter 3, focussed on characterising the low pressure region of the yield surface. As a result, an modified single surface yield model was formulated that can reflect the behaviour of powders at low pressure accurately. To gather the experimental data required, the simple compression test and the Brazilian disc test were used. New image processing techniques were developed to validate the test condition rather than exploit the loading curves, as is the case with conventional data reduction techniques for these tests. This made the more complete exploitation of the test possible, including the calculation of the elastic properties of powder compacts, without measurement methods requiring contact with very fragile green components. Dilatancy could be observed in the simple compression test and the failure of the compacts during the Brazilian disc test was matched with theoretical predictions. Fundamental differences were highlighted between the behaviour of ferrous and ceramic powders, in particular the brittleness of alumina in presence of tensile stresses. The observations on the failure of the compacts also supported the statistical approach for fracture prediction.

The summary of the work carried out for this thesis shows that he work converged to the defect prediction criterion by characterising the stress conditions in which the integrity of compacts is at risk and exploiting this data as a basis. Further developments are possible, in particular with a view to characterise the crack propensity criterion. A more extensive set of tests, including the Brazilian disc test, tensile tests and possibly shear box tests could be carried out. This would make it possible to fit the probability distribution more accurately to the material behaviour. It is also important to establish the cohesion density of the material considered to formulate the recovery function, as a granular material can be subsequently recompacted but a fractured solid will not recover.

Finally, the model established as a conclusion to the third chapter was not numerically tested. A numerical implementation could show how the compacts are affected, in particular ceramics, by a reduced shear strength.

This work aimed to investigate the failure of the powder compaction process and

it was chosen to characterise the phenomena as a continuum to obtain results exploitable for finite element simulation. An alternative approach could be the study of the micromechanical phenomena that lead to the failure or success of a compaction. An extension to this work could exploit micromechanical models, such as the DFEM, to explore the development of cohesion in granular media but also the development of fracture. It may then be possible to know if fracture occurs by breaking the powder particles or loss of the interlocking in the material. Both mechanisms may occur according to the conditions. Numerical predictions could be compared to experimental data to investigate cold welding, held as a contributor to cohesion but little documented in the literature to date. A numerical investigation with the DFEM could also be used to investigate the influence of powder morphology and ductility on their behaviour, providing a micromechanical insight into the differences highlighted in Chapter 3 by bulk characterisation techniques, which suitable for the modelling of powders as a continuum.

Bibliography

[Arn78] V.I. Arnold. *Mathematical Methods of Classic Mechanics.* Springer, Berlin, 1978.

[AST00] ASTM. *Annual Book of ASTM standards*, volume 04.02. ASTM, 2000.

[BAC94] S. Brown and G. Abou-Chedid. Yield behaviour of metal powder assemblages. *Journal of the Mechanics and Physics of Solids*, 42(3), Mar 1994.

[Bar90] J.P. Bardet. Lode dependences pressure-sensitive materials for isotropic elastoplastic. *Journal of Applied Mechanics*, 57:498–506, Sep 1990.

[BBC03] P.O. Bouchard, F. Bay, and Y. Chastel. Numerical modelling of crack propagation: automatic remeshing and comparison of different criteria. *Computer Methods in Applied Mechanics and Engineering*, 192(35-36):3887–3908, Aug 2003.

[BBCT00] P.O. Bouchard, F. Bay, Y. Chastel, and I. Tovena. Crack propagation modelling using an advanced remeshing technique. *Computational Methods in Applied Mechanics and Engineering*, 189(3):723–742, Sep 2000.

[BF06] P. Brewin and L. Federzoni. Dienet: conclusions and achievements. *Powder Metallurgy*, 49(1):8–10, Mar 2006.

[BLM00] T. Belytschko, W.K. Liu, and B. Moran. *Nonlinear Finite Elements for Continua and Structures.* Wiley, Chichester, England, 2000.

[Boc95] G.F. Bocchini. Friction effects in metal powder compaction i: Theoretical aspects. In *Advances in Powder Metallurgy and Particulate Materials*, Seattle, USA, May 1995. MPIF.

[Bor92] D. Bortzmeyer. Modelling ceramic powder compaction. *Powder Technology*, 70(2):131–139, May 1992.

[Cal06] J.A. Calero. PM modelling: overview and industry standpoint. *Powder Metallurgy*, 49(1):10–12, Mar 2006.

[Cam00] I.M. Cameron. *Powder Characterisation for Compaction Modelling.* PhD thesis, University of Wales, Swansea, Swansea, 2000.

[Cap00] J.M. Capus. *Metal Powders: A Global Survey of Production, Applications and Market.* Elsevier, Oxford, 2000.

[CBL+94] G. Coccoz, M. Bellet, R. Lécot, L. Ackermann, and H.-Å. Häggblad. Cold compaction of iron powder: experiments and simulation. In *Powder Metallurgy World Congress*, Paris, France, June 1994.

[CCI+04] O. Coube, Y. Chen, D. Imbault, P. Dorémus, R. Maasen, L. Federzoni, P. Jonsen, J. Tweed, D.T. Gethin, and S Rolland. Computer simulation of die compaction: : Guidelines and an example from the european dienet project. In *Powder Metallurgy World Congress and Exhibition*, Vienna, Austria, Oct 2004. MPIF.

[CG01] I.M. Cameron and D.T. Gethin. Exploration of die wall friction for powder compaction using a discrete finite element modelling technique. *Modelling and Simulation in Materials Science and Engineering*, 9(4):289–307, 2001.

[CIS04] J.C. Cunningham and A. Zavaliangos I.C. Sinka. Analysis of tablet compaction. ii. characterisation of mechanical behaviour and powder/tooling friction. *Journal of Pharmaceutical Sciences*, 93(8):2022–2039, Aug 2004.

[CJK+05] O. Coube, P. Jonsén, T. Kraft, Y. Chen, D. Imbault, P. Dorémus, D.T. Gethin, S. Rolland, and L. Federzoni. Numerical simulation of die compaction : Case studies and guidelines from the european dienet project. In *Euro PM 2005 Congress and Exhibition*, Prague, Czech Republic, Oct 2005. EPMA.

[Cou76] C.A. Coulomb. Essai sur une application des règles des maximis et minimis à quelques problèmes de statique relatifs à l'architecture. *Mémoir de l'Académie des Sciences par Divers Savants*, 7, 1776.

[Cou98] O. Coube. *Modelling and Numerical Simulation of Powder Die Compaction with Consideration of Cracking.* PhD thesis, Université Pierre et Marie Curie, Paris, 1998.

[CR00] O. Coube and H. Riedel. Numerical simulation of metal powder die compaction with special consideration of cracking. *Powder Metallurgy*, 43(2):123–131, Feb 2000.

[Cri96] M.A. Crisfield. *Non-linear Finite Element Analysis of Solids and Structure*, volume 1 - Essentials. Wiley, New York, 1996.

[Cri97] M.A. Crisfield. *Non-linear Finite Element Analysis of Solids and Structure*, volume 2 - Advanced Topics. Wiley, 1997.

[Cun79] P.A. Cundall. A discrete numerical model for granular assemblies. *Géotechnique*, 29(1):47–65, 1979.

[Den02] P.J. Denny. Compaction equations: a comparison of the heckel and kawakita equations. *Powder Technology*, 127(2):162–172, Oct 2002.

[Des69] P. Desayl. Strength of concrete under combined compression and tension - determination of interaction curve at failure from cylinder split test. *Materials and Structures*, 3 (2)(2), 1969.

[Des80] C.S. Desai. A basis for yield, failure and potential functions in plasticity. *International Journal for Numerical and Analytical Methods in Geomechanics*, 4(4):361–375, Oct 1980.

[DFA+01] Z.-Y. Deng, T. Fukasawa, M. Ando, G.-J. Zhang, and T. Ohji. Microstructure and mechanical properties of porous alumina ceramics fabricated by the decomposistion of aluminium hydroxide. *Journal of the American Ceramic Society*, 84(11):2638–2644,, Nov 2001.

[DGM+95] P. Dorémus, C. Geindreau, A. Martin, L. Debove, R. Lécot, and M. Dao. High pressure triaxial cell for metal powder. *Powder Metallurgy*, 38(4):284–287, 1995.

[Die79] J.K. Dienes. On the analysis of rotation, stress rates in deforming bodies. *Acta Mechanica*, 32(4), 1979.

[Dor03] P. Dorémus. Characterisation of distalloy ae for the dienet program. Technical report, Dienet European thematic research network, 2003.

[DP52] D.C. Drucker and W. Prager. Soil mechanics and plastic analysis or limit design. *Quarterly of Applied Mechanics*, 10(2), 1952.

[DS71] F.L. DiMaggio and I. Sandler. Material model for granular soils. *ASCE, Journal of Engineering Mechanics Division*, 97(3):935–950, May 1971.

[DTA01] P. Dorémus, F. Toussaint, and O. Alvain. Simple tests and standard procedure for the characterisation of green compacted powder. *NATO Science series, sub-series III, Computer and Systems Science*, 176:29–41, May 2001.

[E. 05] E. Yu. Vyal' and A.M. Laptev. Use of certain binders to increase the strength of green compacts. *Powder Metallurgy and Metal Ceramics*, 44(11-12):614–618, Nov 2005.

[ELM88] P. Edwards, P. Lyvers, and O.R. Mitchell. Precision edge contrast and orientation estimation. *IEEE Transactions on Pattern Matching and Machine Intelligence*, 10 (6)(6):927–937, Nov 1988.

[EPM07a] EPMA. *http://www.epma.com/.* EPMA website, Sep 2007.

[EPM07b] EPMA, JPMA and MPIF. *http://www.pmdatabase.com/.* PM Database, Sep 2007.

[Ern99] E. Ernst. Cracks and their formation in powder compaction. In *Powder Compaction: An intensive short course*, Bremen, Germany, Oct 1999. EPMA.

[Fah96] M.K. Fahad. Stresses and failure in the diametral compression test. *Journal of Materials Science*, 31(14):3723–3729, Jan 1996.

[Fle95] N.A. Fleck. On the cold compaction of powders. *Journal of Mechanics and Physics of Solids*, 43(9):1409–1431, Sep 1995.

[GDR+01] D.T. Gethin, M. Dudko, R.S. Ransing, R.W. Lewis, and A.J.L. Crook. Numerical comparison of a deformable discrete element model with an equivalent continuum analysis for the compaction of ductile porous material. *Computers and Structures*, 79(13):1287–1294, May 2001.

[GLR03] D.T. Gethin, R.W. Lewis, and R.S. Ransing. Plasticity theory for porous solids. *Modelling and Simulation in Materials Sciences and Engineering*, 11(1):101–114, Jan 2003.

[Gre72] R.J. Green. Plasticity theory for porous solids. *International Journal of Mechanical Sciences*, 14(4), 1972.

[Gri20] A.A. Griffith. The phenomena of rupture and flow in solids. *Philosophical Transactions of the Royal Society*, 221:163–198, 1920.

[GTG+01] D.M.M. Guyoncourt, J.H. Tweed, A. Gough, J. Dawson, and L. Pater. Constitutive data and friction measurements of powder using instrumented die. *Powder Metallurgy*, 44(1):25–33, Jan 2001.

[Gur77] A.L. Gurson. Continuum theory of ductile rupture by void nucleation ad growth: part i - yield criteria and flow rules for porous ductile media. *Journal of Engineering Materials Technology*, 99(1), 1977.

[Guy05] D.M.M. Guyoncourt. Measurement of friction on part ejection - report aeat/ld81000/07. Technical report, AEA Technology, 2005.

[Hö91] H.-Å. Häggblad. Constitutive models for powder materials. *Powder Technology*, 67(2):127–137, Aug 1991.

[Hec61] R.W. Heckel. Density-pressure relationships in powder compaction. *Transactions of the Metallurgical Socitey of AIME*, 221(4), 1961.

[Her95] H. Hertz. Über die Berührung elastischer Körper. *Gesammelte Werke*, 1, 1895.

[HO94] H.-Å. Häggblad and M. Oldenburg. Modelling and simulation of metal powder die pressing with use of explicit time integration. *Modelling and Simulation in Materials Science and Engineering*, 2(4):893–911, Jul 1994.

[Hon59] G. Hondros. The evaluation of poisson's ratio and the modulus of materials of a low tensile resistance by the brazilian (indirect tensile) test with particular reference to concrete. *Australian Journal of Applied Sciences*, 10:243–268, Jan 1959.

[Jen64] A.W. Jenike. Storage and flow of solids. *Bulletin of the University of Utah*, 53(26), 1964.

[JH05] P. Jonsèn and H.-Å. Häggblad. Modelling and numerical investigation of the residual stress state in a green metal powder body. *Powder Technology*, 155:196–208, 2005.

[JH07] P. Jonsèn and H.-Å. Häggblad. Fracture energy based constitutive models for tensile fracture of metal powder compacts. *International Journal of Solids and Structures*, 44(20), 2007.

[JM94] T.J.R. Hughes J.E. Marsden. *Mathematical Foundations of Elasticity.* Dover, New-York, 1994.

[Jon06] P. Jonsèn. *Fracture and Stress in Powder Compacts.* PhD thesis, Luleøa University of Technology, Luleøa, Sweden, 2006.

[KAAL06] A.R. Khoei, A.R. Azami, M. Anahid, and R.W. Lewis. A three-invariant hardening plasticity for numerical simulation of powder forming processes via the arbitrary lagrangian-eulerian fe model. *International Journal for Numerical Methods in Engineering*, 66(5):843–877, Apr 2006.

[KDW06] M. Kabatova, E. Dudrova, and A.S. Wronski. Fracture micromechanics of static subcritical growth and coalescence of microcracks in sintered fe15cr02mo07c steel. *Powder Metallurgy*, 49(6):363–368, Dec 2006.

[Kho98] A.R. Khoei. *Finite element modelling and adaptive remeshing in static and dynamic analysis of metal powder forming processes.* PhD thesis, University of Wales, Swansea, Swansea, UK, 1998.

[Kho05] A.R. Khoei. *Computational plasticity in Powder Forming Processes.* Elsevier, Oxford, 2005.

[KL71] K. Kawakita and K.-H. Lüdde. Some considerations on powder compression equations. *Powder Technology*, 4(2):61–68, Jan 1971.

[KMB02] A.R. Khoei, M. Mofid, and A. Bakhshiani. Modelling of powder compaction process using an endochronic plasticity model. *Journal of Materials Processing Technology*, 130-131:175–180, Dec 2002.

[Koe71] M. Koerner. Triaxial compaction of metal powder. *Powder Metallurgy International*, 3(4), 1971.

[Kor06] D. Korachkin. *Measurement Methods for the Determination of Powder Properties for Compaction Modelling.* PhD thesis, University of Wales, Swansea, Swansea, UK, 2006.

[Kra03] T. Kraft. Optimizing press tool shapes by numerical simulation of compaction and sintering-application to a hard metal cutting insert. *Modelling and Simulation in Materials Science and Engineering*, 11(3):381–400, Apr 2003.

[KSA07] A.R. Khoei, M. Samimi, and A.R. Azami. Reproducing kernel particle method in plasticity of pressure-sensitive material with reference to powder forming process. *Computational Mechanics*, 39(3):247–270, Feb 2007.

[KSAS06] A.R. Khoei, A. Shamloo, M. Anahid, and K. Shahim. The extended finite element method (x-fem) for powder forming problems. *Journal of Materials Processing Technology*, 177(1-3):53–57, Jul 2006.

[LE00] P. Luukkonen and T. Eriksson. Residual stresses in green bodies of steel, powder and their relaxation during heat treatment. In *20th AMS Heat, Treating Society Conference*, St. Louis, Missouri, USA, 2000.

[LGYR05] R.W. Lewis, D.T. Gethin, X.S. Yang, and R.C. Rowe. A combined finite-discrete element method for simulating pharmaceutical powder tabletting. *International Journal for Numerical Methods in Engineering*, 62(7):853–869, Jan 2005.

[LS87] R.W. Lewis and B.A. Schrefler. *The Finite Element Method in the Deformation and Consolidation of Porous Media.* Wiley, New York, 1987.

[MB96] P. Mosbah and D. Bouvard. Finite element simulation of die compaction and ejection of iron powder. *Advances in Powder Metallurgy and Particulate Materials*, 61(2), Jun 1996.

[MK79] W.C.P.M. Meerman and A.C. Knaapen. A high-pressure triaxial testing cell. *Powder Technology*, 22(2), 1979.

[MKSK97] P. Mosbah, J. Kojima, S. Shima, and H. Kotera. Influence of the third stress invariant on iron powder behaviour during compaction. In *Proceedings of the International Workshop on Modelling of Metal Powder Forming*, Grenoble, France, Jul 1997. EPMA.

[MNZ79] Z. Mroz, V.A. Norris, and O.C. Zienkiewicz. Application of an anisotropic hardening model. *Géotechnique*, 29(1), 1979.

[Mos95] P. Mosbah. *Etude Expérimentale et Modélisation du Comportement de Poudres Métalliques.* PhD thesis, Université Joseph Fourrier, Grenoble, France, 1995.

[MPI07] MPIF. *http://www.mpif.org/.* MPIF website, Sep 2007.

[MSCW06] S.A. McDonald, L.C.R. Schneider, A.C.F. Cocks, and P.J. Withers. Particle movement during the deep penetration of a granular material studied by x-ray microtomography. *Scripta Materialia*, 52(2):191–196, Jan 2006.

[MSSO99] K. Mori, Y. Sato, M. Shiomi, and K. Osakada. Prediction of fracture generated by elastic recovery of tools in multi-level powder compaction using finite element method. *International Journal of Machine Tools and Manufacture*, 39(7):1031–1045, Jul 1999.

[New04a] Newsview. Gentle Breeze powers PM post Vienna. *Metal Powder Report*, 59(10):10–11, Nov 2004.

[New04b] Newsview. Light for PM at the end of the tunnel as the China question looms? *Metal Powder Report*, 59(7):12–14, Aug 2004.

[NZ72] G.C. Nayak and O.C. Zienkiewicz. Elasto-plastic stress analysis. a generalization for various constitutive relations including strain softening. *International Journal for Numerical Methods in Engineering*, 5(5):113–135, 1972.

[OH80] D.R.J. Owen and E. Hinton. *Finite Element in Plasticity.* Pineridge Press, Swansea, 1980.

[Pan07] P.C. Panos. Understanding the interfacial strength of bilayer pharmaceutical tablets. In *International Conference on Powder Metallurgy and Particulate Materials*, Denver, USA, May 2007. PowderMet2007.

[Pav98] E. Pavier. *Caractérisation du comportement d'une Poudre de Fer pour le Procédé de Compaction.* PhD thesis, Institut National Polytechnique de Grenoble, Grenoble, France, 1998.

[PD99] E. Pavier and P. Doremus. Triaxial characterisation of iron powder behaviour. *Powder Metallurgy*, 42(4):345–352, Apr 1999.

[PF01] R. Panelli and F.A. Filho. A study of a new phenomenological compaction equation. *Powder Technology*, 114(1-3):255–261, Jan 2001.

[PM 99] PM Modnet Computer Modelling Group. Comparison of computer models representing powder compaction process. *Powder Metallurgy*, 42(4):301–311, Apr 1999.

[PZC03] A.T. Procopio, A. Zavaliangos, and J.C. Cunningham. Analysis of the diametrical compression test and the applicability to plastically deforming materials. *Journal of Materials sciences*, 38(17):3629–3639, Sep 2003.

[QZS+03] R. Qiuhua, S. Zonhqi, O. Stephanson, C. Li, and B. Stillborg. Shear fracture (mode ii) of brittle rock. *International Journal of Rock Mechanics and Mining Sciences*, 40(3):355–375, Apr 2003.

[RGK+00] R.S. Ransing, D.T. Gethin, A.R. Khoei, P. Mosbah, and R.W. Lewis. Powder compaction modelling via the discrete and finite element method. *Materials and Design*, 21(4):263–269, Aug 2000.

[RLG04] R.S. Ransing, R.W. Lewis, and D.T. Gethin. Using a deformable discrete-element technique to model the compaction of mixed ductile and brittle particulate systems. *Philosophical Transactions of the Royal Society of London A*, 362(1822):1867–1884, Sep 2004.

[RSL95] R.S. Ransing, M.N. Srinivasan, and R.W. Lewis. Icada: Intelligent computer aided defect analysis for casting. *Journal of Intelligent Manufacturing*, 6(1):29–49, Feb 1995.

[RST63] K.H. Roscoe, A.N. Schofield, and A. Thorairajah. Yielding of clays in state wetter than critical. *Géotechnique*, 13(3):211–240, 1963.

[Rus90] J.C. Russ. *Computer Assisted Microscopy.* Plenum Press, New York, 1990.

[SC07] I.C. Sinka and A.C.F. Cocks. Constitutive modelling of powder compaction - ii. evaluation of material data. *Mechanics of Materials*, 39(4):404–416, Apr 2007.

[SCML00] I.C. Sinka, A.C.F. Cocks, C.J. Morrison, and A. Lightfoot. High pressure triaxial facility for powder compaction. *Powder Metallurgy*, 43(3):253–262, Mar 2000.

[SH98] J.C. Simo and T.J.R. Hughes. *Computational Inelasticity.* Springer, New-York, 1998.

[SK98] S. Shima and H. Kotera. Study of of constitutive behaviour of powders for application to simulation of compaction processes. In *Powder Metallurgy World Congress and Exhibition*, Valencia, Spain, Oct 1998. MPIF.

[SM86] S. Shima and K. Mimura. Densification behaviour of ceramic powders. *International Journal of Mechanical Sciences*, 28(1), 1986.

[SO76] S. Shima and M. Oyane. Plasticity theory for porous metals. *International Journal of Mechanical Sciences*, 18(6):285–291, 1976.

[SRKW+77] S. Strijboz, P.J. Rankin, R.J. Klein-Wassink, J. Binnik, and G.J. Oudemans. Stresses occuring during one-sided die compaction of powders. *Powder Technology*, 18(2):187–200, Nov 1977.

[SW68] A.N. Schofield and P. Wroth. *Critical state soil mechanics.* McGraw-Hill, London, 1968.

[TA06] S.M. Tahir and A.K. Ariffin. Simulation of crack propagation in metal powder compaction. *International Journal for Computational Methods in Applied Mechanics and Engineering*, 7(4):293–302, Jul-Aug 2006.

[TLGA93] D.V. Tran, R.W. Lewis, D.T. Gethin, and A.K. Ariffin. Numerical modelling of powder compaction processes: a displcaement based finite element method. *Powder Metallurgy*, 36(4), 1993.

[TN65] C. Truesdell and W. Noll. *The Non-Linear Field Theories of Mechanics.* Springer, Berlin, 1965.

[VL84] K.C. Valanis and C.F. Lee. Endochronic theory of cyclic plasticity with applications. *Journal of Applied Mechanics*, 51(2):367–374, 1984.

[Wal23] E.E. Walker. The properties of powders. part vii. the distribution of densities in columns of compressed powder. *Transactions of the Faraday Society*, 19:73–82, Jul 1923.

[Wes39] H.M. Westgaard. Bearing pressures and cracks. *Journal of Applied Mechanics*, 49, 1939.

[WHM+07] C.-Y. Wu, B.C. Hancock, A. Mills, A.C. Bentham, S.M. Best, and J.A. Elliott. Numerical and experimental investigation of capping mechanisms during pharmaceutical tablet compaction. *Powder Technology*, in press, available online, 2007.

[Zen98] D.C. Zenger. Common causes of cracks in PM compacts. *International Journal of Powder Metallurgy*, 34(4), 1998.

[ZHL77] O.C. Zienkiewicz, C. Humpheson, and R.W. Lewis. *A Unified Approach to Soil Mechanics Problems (Including Plasticity and Viscoplasticity).* Wiley, New York, 1977.

[ZT00] O.C. Zienkiewicz and R.L. Taylor. *Finite Element Method, Fifth Edition*, volume 2: Solid Mechanics. Butterworth-Heinmann, 2000.

Appendix A

Derivatives for the Development of the Three-Invariant Model

The derivatives omitted in Chapter 4, necessary for the implementation of the three-invariant model are laid out in this appendix.

A.1 Standard Derivatives

In the case of a 2-D problem in which the stresses are $\boldsymbol{\sigma} = \begin{bmatrix} \sigma_{xx} & \sigma_{yy} & \sigma_{zz} & \sigma_{xy} \end{bmatrix}^T$, the derivatives of the stress invariants are:

$$\frac{\partial I_1}{\partial \boldsymbol{\sigma}} = \begin{bmatrix} 1 \\ 1 \\ 1 \\ 0 \end{bmatrix}$$

$$\frac{\partial J_2}{\partial \boldsymbol{\sigma}} = \begin{bmatrix} \bar{\sigma}_{xx} \\ \bar{\sigma}_{yy} \\ \bar{\sigma}_{zz} \\ 2\bar{\sigma}_{xy} \end{bmatrix}$$

$$\frac{\partial J_3}{\partial \boldsymbol{\sigma}} = \begin{bmatrix} \bar{\sigma}_{yy}\bar{\sigma}_{zz} + \frac{1}{3}J_2 \\ \bar{\sigma}_{xx}\bar{\sigma}_{zz} + \frac{1}{3}J_2 \\ \bar{\sigma}_{xx}\bar{\sigma}_{yy} - \bar{\sigma}_{xy}^2 + \frac{1}{3}J_2 \\ -2\bar{\sigma}_{zz}\bar{\sigma}_{xy} \end{bmatrix}$$

$$\frac{\partial^2 I_1}{\partial \boldsymbol{\sigma}^2} = \mathbf{0}_{4\times 4}$$

$$\frac{\partial^2 J_2}{\partial \boldsymbol{\sigma}^2} = \frac{1}{3}\begin{bmatrix} 2 & -1 & -1 & 0 \\ -1 & 2 & -1 & 0 \\ -1 & -1 & 2 & 0 \\ 0 & 0 & 0 & 6 \end{bmatrix}$$

$$\frac{\partial^2 J_3}{\partial \boldsymbol{\sigma}^2} = \frac{2}{3}\begin{bmatrix} \bar{\sigma}_{xx} & \bar{\sigma}_{zz} & \bar{\sigma}_{yy} & \bar{\sigma}_{xy} \\ \bar{\sigma}_{zz} & \bar{\sigma}_{yy} & \bar{\sigma}_{xx} & \bar{\sigma}_{xy} \\ \bar{\sigma}_{yy} & \bar{\sigma}_{xx} & \bar{\sigma}_{zz} & -2\bar{\sigma}_{xy} \\ \bar{\sigma}_{xy} & \bar{\sigma}_{xy} & -2\bar{\sigma}_{xy} & -\bar{\sigma}_{zz} \end{bmatrix}$$

A.2 Derivatives of the Hardening Terms

$$I_0 = -6K_1 \left(\ln \left(1 - \frac{\rho - \rho_0}{\rho - \rho_{max}} \right) \right)^{K2}$$

$$I_c = K_{c0} + K_{c1} I_0 + K_{c2} I_0^2$$

$$M = \left(\frac{-6Q_{max}}{I_0} \tanh \left(\frac{K_3 I_0}{-6Q_{max}} \right) \right)^2$$

$$\frac{\partial I_0}{\partial \rho} = \frac{6K_1 K_2}{\rho - rho_{max}} \left(\ln \left(1 - \frac{\rho - \rho_0}{\rho - \rho_{max}} \right) \right)^{K_2 - 1}$$

$$\frac{\partial I_c}{\partial \rho} = K_{c1} DI_0 \rho + K_{c1} I_0 DI_0 \rho$$

$$\frac{\partial M}{\partial \rho} = \frac{2\sqrt{M}}{I_0} \frac{\partial I_0}{\partial \rho} \left(\frac{6Q_{max}}{I_0} \tanh \left(\frac{K_3 I_0}{-6Q_{max}} \right) + \frac{K_3}{\cosh^2 \left(\frac{K_3 I_0}{-6Q_{max}} \right)} \right)$$

A.3 Derivatives of the Yield Function/Plastic Potential

$$\boldsymbol{n} = \frac{\partial f}{\partial \boldsymbol{\sigma}} = C_1 \frac{\partial I_1}{\partial \boldsymbol{\sigma}} + C_2 \frac{\partial J_2}{\partial \boldsymbol{\sigma}} + C_3 \frac{\partial J_3}{\partial \boldsymbol{\sigma}} \tag{A.1}$$

$$C_1 = \frac{\partial f}{\partial I_1} = M\kappa^2 \left(2I_1 - I_0 - I_c \right)$$

$$C_2 = \frac{\partial f}{\partial J_2} = 27 + M\kappa \frac{\partial \kappa}{\partial J_2} \left(I_1 - I_0 \right) \left(I_1 - I_c \right)$$

$$C_3 = \frac{\partial f}{\partial J_3} = M\kappa \frac{\partial \kappa}{\partial J_3} \left(I_1 - I_0 \right) \left(I_1 - I_c \right)$$

$$\frac{\partial \boldsymbol{n}}{\partial \boldsymbol{\sigma}} = \frac{\partial^2 f}{\partial \sigma^2} = C_2 \frac{\partial J_2}{\partial \boldsymbol{\sigma}} + C_3 \frac{\partial J_3}{\partial \boldsymbol{\sigma}}$$

$$+C_{11} \frac{\partial I_1}{\partial \boldsymbol{\sigma}} \left(\frac{\partial I_1}{\partial \boldsymbol{\sigma}} \right)^T C_{22} \frac{\partial J_2}{\partial \boldsymbol{\sigma}} \left(\frac{\partial J_2}{\partial \boldsymbol{\sigma}} \right)^T C_{33} \frac{\partial J_3}{\partial \boldsymbol{\sigma}} \left(\frac{\partial J_3}{\partial \boldsymbol{\sigma}} \right)^T$$

$$+C_{23} \frac{\partial J_2}{\partial \boldsymbol{\sigma}} \left(\frac{\partial J_3}{\partial \boldsymbol{\sigma}} \right)^T C_{32} \frac{\partial J_3}{\partial \boldsymbol{\sigma}} \left(\frac{\partial J_2}{\partial \boldsymbol{\sigma}} \right)^T C_{12} \frac{\partial I_1}{\partial \boldsymbol{\sigma}} \left(\frac{\partial J_2}{\partial \boldsymbol{\sigma}} \right)^T$$

$$+C_{21} \frac{\partial J_2}{\partial \boldsymbol{\sigma}} \left(\frac{\partial I_1}{\partial \boldsymbol{\sigma}} \right)^T C_{13} \frac{\partial I_1}{\partial \boldsymbol{\sigma}} \left(\frac{\partial J_3}{\partial \boldsymbol{\sigma}} \right)^T C_{31} \frac{\partial J_3}{\partial \boldsymbol{\sigma}} \left(\frac{\partial I_1}{\partial \boldsymbol{\sigma}} \right)^T$$

$$C_{11} = \frac{\partial^2 f}{\partial I_1^2} = 2M\kappa^2$$

$$C_{22} = \frac{\partial^2 f}{\partial J_2^2} = 2M \left[\frac{\partial \kappa}{\partial J_2} \frac{\partial \kappa}{\partial J_2} + \kappa \frac{\partial^2 \kappa}{\partial J_2^2} \right] (I_1 - I_0)(I_1 - I_c)$$

$$C_{33} = \frac{\partial^2 f}{\partial J_3^2} = 2M \left[\frac{\partial \kappa}{\partial J_3} \frac{\partial \kappa}{\partial J_3} + \kappa \frac{\partial^2 \kappa}{\partial J_3^2} \right] (I_1 - I_0)(I_1 - I_c)$$

$$C_{23} = \frac{\partial^2 f}{\partial J_2 \partial J_3} = 2M \left[\frac{\partial \kappa}{\partial J_2} \frac{\partial \kappa}{\partial J_3} + \kappa \frac{\partial^2 \kappa}{\partial J_2 \partial J_3} \right] (I_1 - I_0)(I_1 - I_c) = C_{32}$$

$$C_{12} = \frac{\partial^2 f}{\partial I_1 \partial J_2} = 2M\kappa \frac{\partial \kappa}{\partial J_2} (2I_1 - I_0 - I_c) = C_{21}$$

$$C_{13} = \frac{\partial^2 f}{\partial I_1 \partial J_3} = 2M\kappa \frac{\partial \kappa}{\partial J_3} (2I_1 - I_0 - I_c) = C_{31}$$

$$\kappa = \frac{1-\beta}{2} \left(1 - \frac{3\sqrt{3}}{2} \frac{J_3}{} J_2^{3/2} \right) + \beta$$

$$\frac{\partial \kappa}{\partial J_2} = \frac{9(1-\beta)\sqrt{3}}{8J_2^{5/2}} J_3$$

$$\frac{\partial \kappa}{\partial J_3} = \frac{-3(1-\beta)\sqrt{3}}{4J_2^{3/2}}$$

$$\frac{\partial^2 \kappa}{\partial J_2^2} = \frac{-45(1-\beta)\sqrt{3}}{16J_2^{7/2}} J_3$$

$$\frac{\partial^2 \kappa}{\partial J_3^2} = 0$$

$$\frac{\partial^2 \kappa}{\partial J_2 \partial J_3} = \frac{\partial^2 \kappa}{\partial J_3 \partial J_2} = \frac{9\,(1-\beta)\,\sqrt{(3)}}{8 J_2^{5/2}}$$

A.4 Derivatives of n with Respect to the Hardening Coefficients

$$\frac{\partial \boldsymbol{n}}{\partial \epsilon_{pv}} = \frac{\partial \boldsymbol{n}}{\partial \rho} \frac{\partial \rho}{\partial \epsilon_{pv}}$$

When using equation A.1 to express $\boldsymbol{n}$, the derivatives of C_1, C_2 and C_3 are required.

$$\frac{\partial C_1}{\partial \rho} = -M\kappa^2 \left(\frac{\partial I_0}{\partial \rho} + \frac{\partial I_c}{\partial \rho} \right) + \kappa^2 \left(2I_1 - I_0 - I_c \right) \frac{\partial M}{\partial \rho}$$

$$\frac{\partial C_2}{\partial \rho} = -M\kappa \frac{\partial \kappa}{\partial J_2} \left((I_1 - I_c) \frac{\partial I_0}{\partial \rho} (I_1 - I_0) \frac{\partial I_c}{\partial \rho} \right) + 2\kappa \frac{\kappa}{J_2} (I_1 - I_0)(I_1 - I_c) \frac{\partial M}{\partial \rho}$$

$$\frac{\partial C_3}{\partial \rho} = -M\kappa \frac{\partial \kappa}{\partial J_3} \left((I_1 - I_c) \frac{\partial I_0}{\partial \rho} (I_1 - I_0) \frac{\partial I_c}{\partial \rho} \right) + 2\kappa \frac{\kappa}{J_3} (I_1 - I_0)(I_1 - I_c) \frac{\partial M}{\partial \rho}$$

Regrouping the terms gives:

$$\frac{\partial \boldsymbol{n}}{\partial I_0} = -M\kappa \left[\kappa \frac{\partial I_1}{\partial \boldsymbol{\sigma}} + 2\,(I_1 - I_c) \left(\frac{\partial \kappa}{\partial J_2} \frac{\partial J_2}{\partial \boldsymbol{\sigma}} + \frac{\partial \kappa}{\partial J_3} \frac{\partial J_3}{\partial \boldsymbol{\sigma}} \right) \right]$$

$$\frac{\partial \boldsymbol{n}}{\partial I_c} = -M\kappa \left[\kappa \frac{\partial I_1}{\partial \boldsymbol{\sigma}} + 2\,(I_1 - I_0) \left(\frac{\partial \kappa}{\partial J_2} \frac{\partial J_2}{\partial \boldsymbol{\sigma}} + \frac{\partial \kappa}{\partial J_3} \frac{\partial J_3}{\partial \boldsymbol{\sigma}} \right) \right]$$

$$\frac{\partial \boldsymbol{n}}{\partial M} = \kappa^2 \left(2I_1 - I_0 - I_c \right) \frac{\partial I_1}{\partial \boldsymbol{\sigma}} + 2\kappa \left(I_1 - I_0 \right) \left(I_1 - I_c \right) \left(\frac{\partial \kappa}{\partial J_2} \frac{\partial J_2}{\partial \boldsymbol{\sigma}} + \frac{\partial \kappa}{\partial J_3} \frac{\partial J_3}{\partial \boldsymbol{\sigma}} \right)$$

$$\frac{\partial \boldsymbol{n}}{\partial \epsilon_{pv}} = \left(\frac{\partial \boldsymbol{n}}{\partial I_0} \frac{\partial I_0}{\partial \rho} + \frac{\partial \boldsymbol{n}}{\partial I_c} \frac{\partial I_c}{\partial \rho} + \frac{\partial \boldsymbol{n}}{\partial M} \frac{\partial M}{\partial \rho} \right) \frac{\partial \rho}{\partial \epsilon_{pv}}$$

Appendix B

Material Properties for the Simulations

The material properties of the ferrous powder DistaloyAE, used for the simulations in chapters 4, 5 and in the simulations of Appendix C are listed in this appendix. They are for use with the modified CamClay model as laid out in Chapter 4.

The equation of the yield surface is:

$$f = \frac{(P - P_1)^2}{P^2} + \frac{Q^2}{Q_0^2} - 1$$

The calibration procedure laid out in section 3.5 is used to establish the value of P_1 and Q_0 over a density range. The coefiicient K_1, K_2, K_3 and Q_{max} are then computed by using the optimisation routine in Microsoft Excel to fit the functions the map P_1 and Q_0 against the density.

$$P_1 = K_1 \left(\ln \left(1 - \frac{\rho - \rho_0}{\rho - \rho_{max}} \right) \right)^{K_2}$$

$$Q_0 = Q_{max} \tanh \left(\frac{K_3 P_0}{Q_{max}} \right)$$

The coefficients for the DistaloyAE are:

$$\begin{aligned} K_1 &= 63.87622 MPa \\ K_2 &= 1.231336 \\ K_3 &= 1.846485 \\ Q_{max} &= 286.5595 MPa \end{aligned}$$

The limit values of the density are the loose powder density: $\rho_0 = 3.2 g/cc$ and the maximum green density: $\rho_{max} = 7.4 g/cc$.

The characteristic curves are in Figures B.1 and B.2. It was shown in Chapter 3 that it is not possible to calibrate the model with the simple compression test or the Brazilian disc test to obtain the cohesion term. It is necessary, however to have cohesion to carry out simulations that include the ejection. For this purpose, after inspection of the data obtained through the model developed it was decided that it is appropriate to adopt: $P_0 = 1.06 P_1$ for the modified CamClay model.

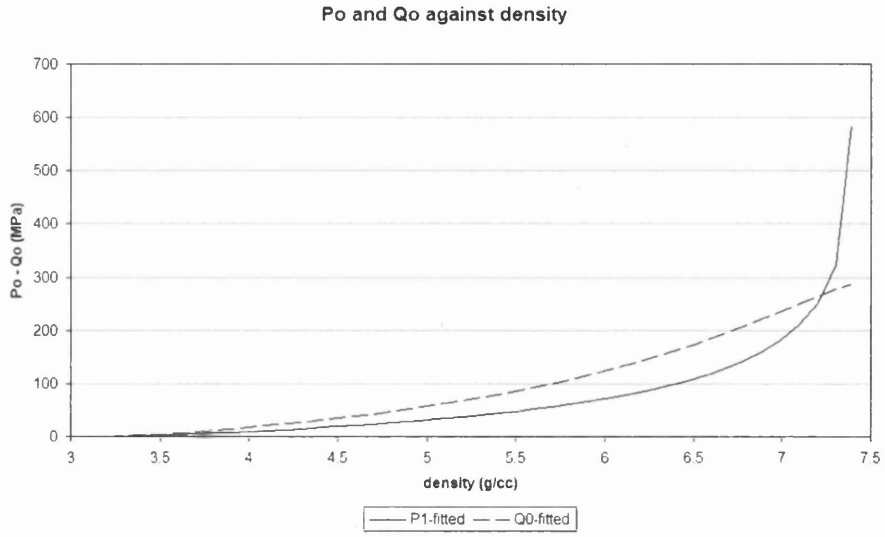

Figure B.1: Fitted function for P_0 and Q_0 against the powder density

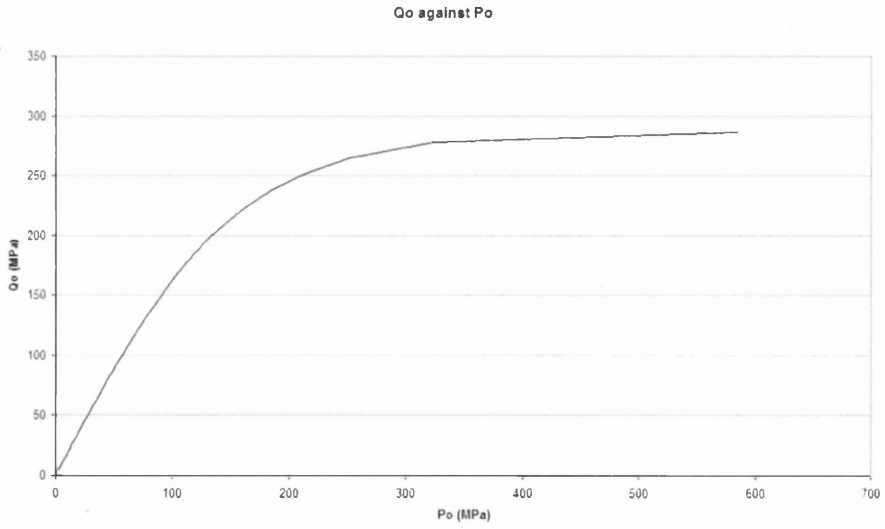

Figure B.2: Q_0 against P_1

Appendix C

Numerical Simulations of the Simple Compression test and the Brazilian Disc Test

The results presented in this appendix are obtained from the simulation of the simple compression test and the diametral compression test. They are included for reference within the main text but it is acknowledged that refinements may be required.

C.1 Simple Compression Test

A cylinder of powder was compacted to an average density of 6.78g/cc. Its diameter and compacted height are 18mm. The mesh is composed of 2503 linear triangular elements of uniform size. The density distribution is shown in Figure C.1. The top punch was then raised and the die stripped down. The compact is then submitted to a load from the top punch without any confinement, thus reproducing the simple compression test.

The results are plotted below as the first stress invariant and the second deviatoric

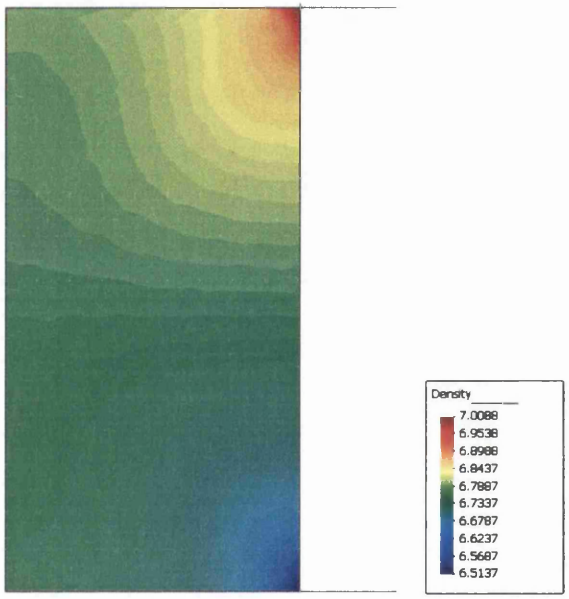

Figure C.1: Density distribution at the end of the compaction

stress invariant, which are respectively measures of the pressure and the deviatoric stress.

The evolution of the stress invariants (Figure C.2) shows that the pressure and deviatoric stresses increase until 60% of the top punch stroke. They then start to decrease slowly. In particular, a band of high deviatoric stress is formed from the upper outer corner to the centre of of the component when the displacement of the top punch is 0.442mm. This band of high deviatoric stress is present before the maximum load is reached (47.86kN at 0.468mm). The loading curve in Figure C.3

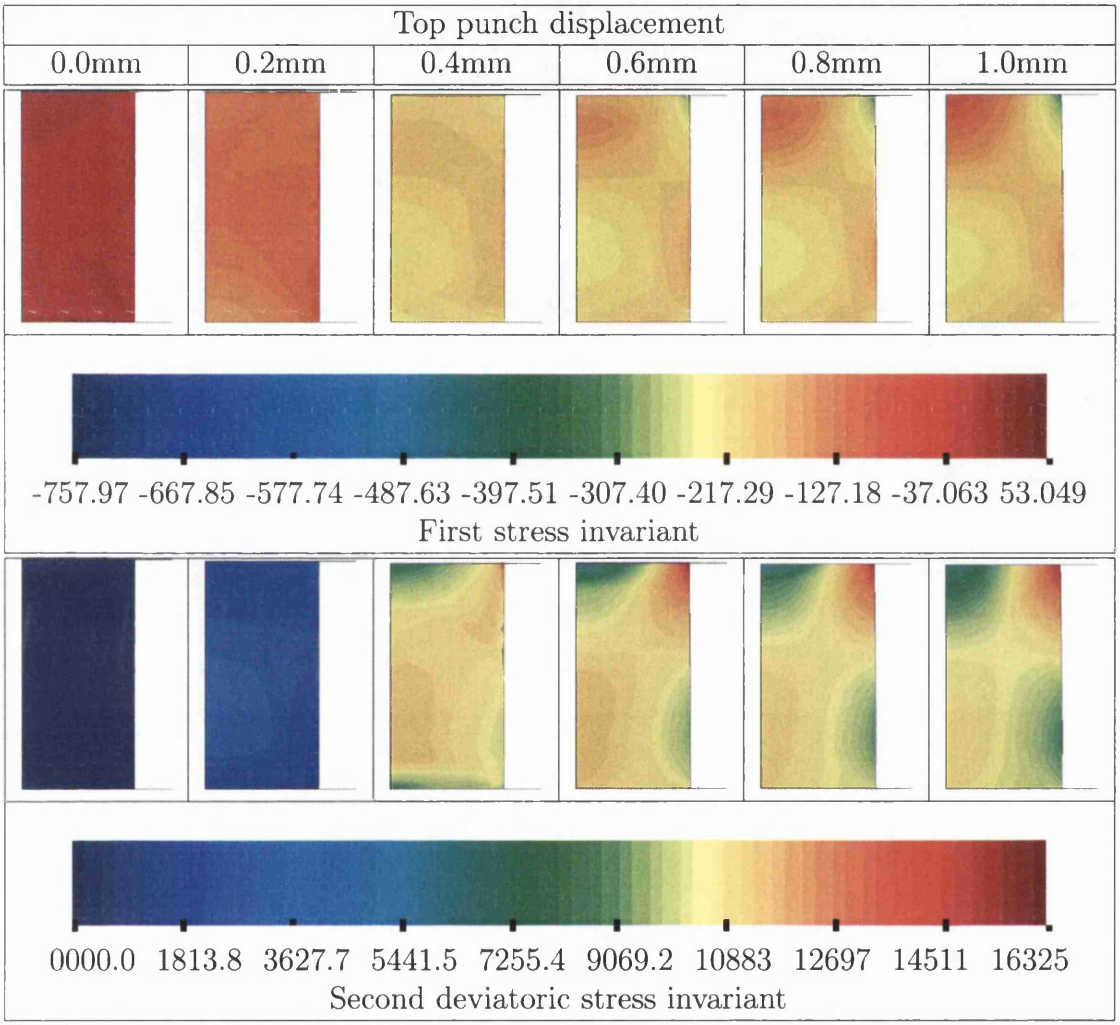

Figure C.2: Stress invariants during the simple compression test

shows the main features of the experimental loading curves with a settlement at the beginning of the compression, then a linear region followed by an inflexion and decrease in the top punch load. The rupture of the component is not simulated so the final collapse with the reduction of the top punch load is not complete. Following the density of the node 192 (FigureC.4) is also an indicator that yielding occurs in the component before the maximum load. At this particular node, located at the centre of the high deviatoric stress band, the density decreases from a top punch displacement of 0.378mm. Figure C.5 shows that the radial displacements do not only evolve with the radius in the component but also with the axial coordinate. This indicates that barrelling takes place. The barrelling is not symmetrical between the top and the bottom of the compact. This shows that the density distribution at the beginning of the test influences the profile of the compact. It is safe to assume that it also influences the pattern in which the compact fails.

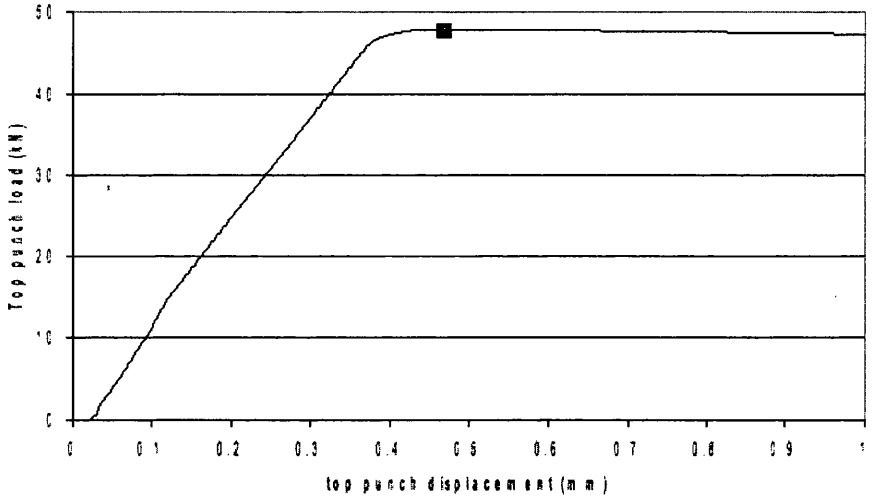

Figure C.3: Top punch load during the simple compression test

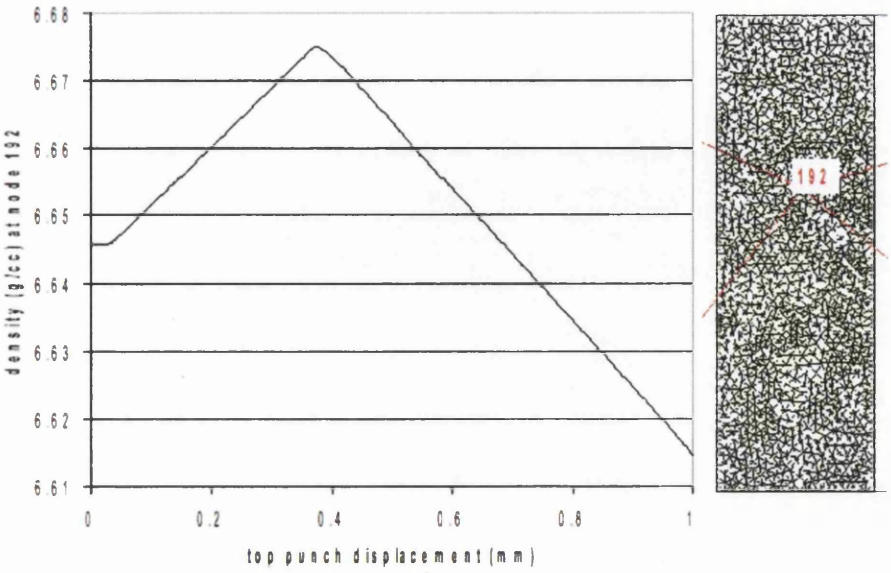

Figure C.4: Evolution of density at node 192 (shown on the right)

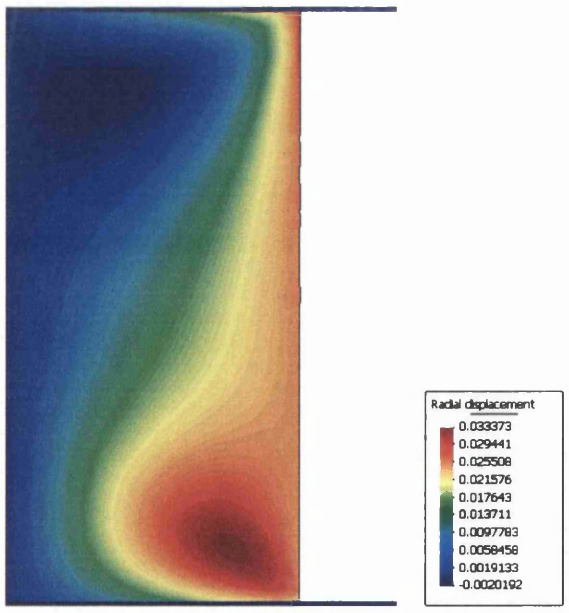

Figure C.5: Radial displacements at the end of the simple compression test

C.2 Brazilian Disc Test

The diametral compression test was simulated for a powder compact. The initial density was set as 7.2g/cc. The compact has an 18mm diameter and its its thickness is set as 1mm for the simulation. The plain stress conditions are used for the analysis. The contacts at the top and the bottom of the cylinder are set as 3mm wide, so that the ratio of contact width to sample diameter is 0.167.

The simulation of the diametral compression test shows that dilatancy sets early in the test after a tool displacement of 0.012mm (Figure C.6). The resulting strain increment highlight the possibility that fracture may occur from other points than the centre of the compact along the compressed diameter. This result still needs refinements on the mesh and contacts but the results concur with the results by Procopio [PZC03], which states that this is due to the influence of plastic deformations incurred around the contact.

The evolution of stresses (Figure C.7) and density (Figure C.8) show that a part of the dilation at the centre is carried out elastically until the yield surface is reached. The stresses then start decreasing as the bearing capacity of the powder is reducing by the density loss.

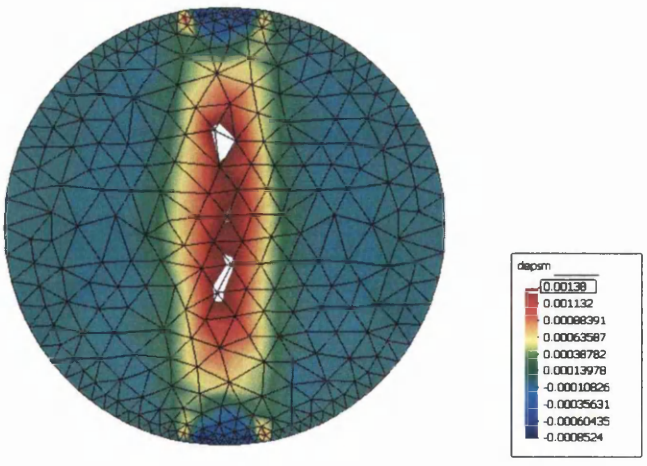

Figure C.6: Dilatancy in the diametral compression test threshold on volumetric plastic strain increments set to highlight areas where dilatancy starts

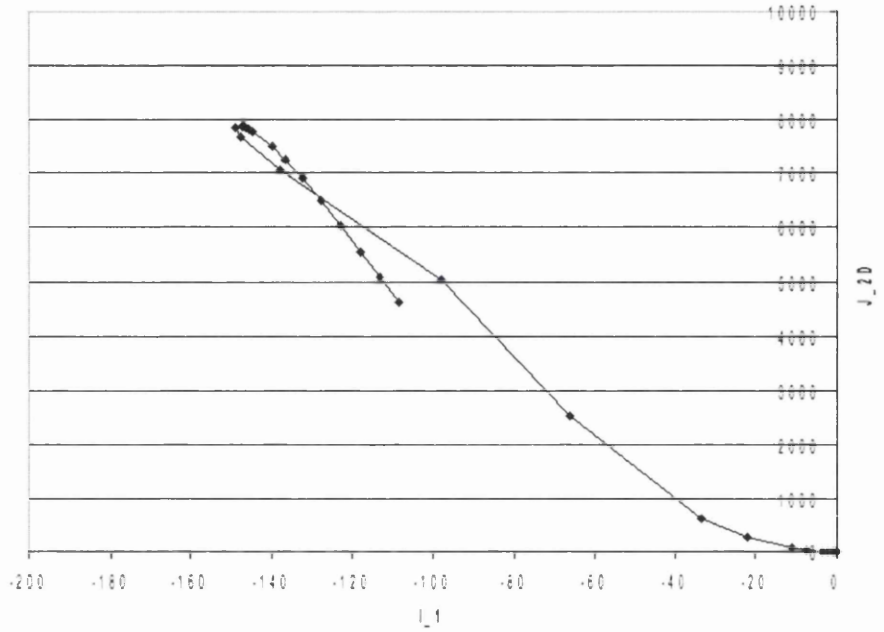

Figure C.7: Evolution of the stress invariants at the centre node

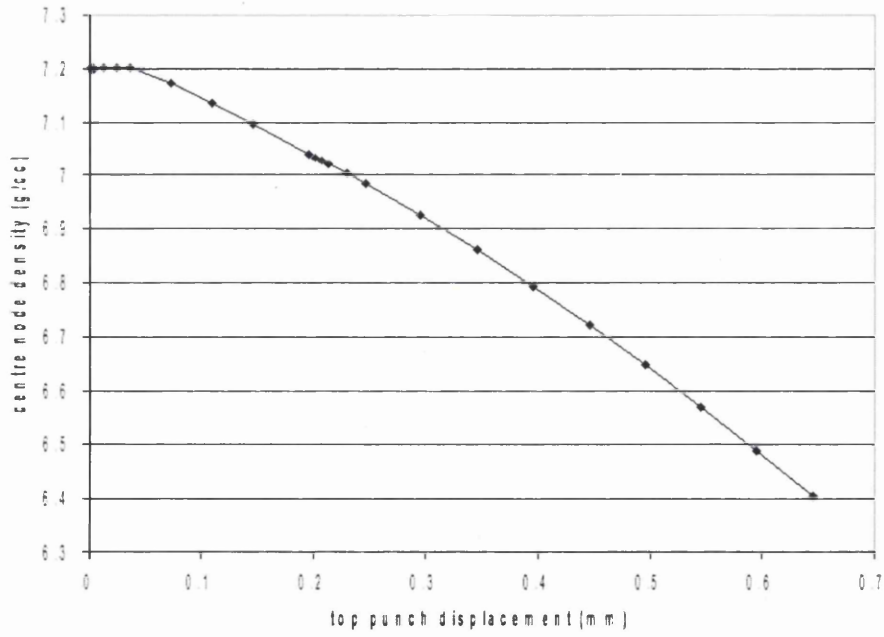

Figure C.8: Evolution of density at the centre node